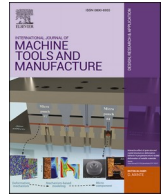




Contents lists available at ScienceDirect

International Journal of Machine Tools and Manufacture

journal homepage: <http://www.elsevier.com/locate/ijmactool>

Powder Bed Fusion of nickel-based superalloys: A review

Salomé Sanchez^a, Peter Smith^a, Zhengkai Xu^a, Gabriele Gaspard^{a,c}, Christopher J. Hyde^a, Wessel W. Wits^b, Ian A. Ashcroft^a, Hao Chen^d, Adam T. Clare^{a,*}^a Faculty of Engineering, University of Nottingham, Advanced Manufacturing Building, Jubilee Campus, Nottingham, NG7 2RD, United Kingdom^b University of Twente, Drienerlolaan 5, 7522 NB, Enschede, Netherlands^c Department of Mechanical Engineering, EPFL, Route Cantonale, 1015, Lausanne, Switzerland^d Department of Mechanical, Materials and Manufacturing Engineering, University of Nottingham Ningbo China, Ningbo 315100, China

ARTICLE INFO

Keywords:

Additive manufacturing
 Powder bed fusion
 Laser powder bed fusion
 Electron beam melting
 Nickel-based superalloys
 Mechanical properties
 Microstructure evaluation
 Tensile
 Hardness
 Shear
 Fatigue
 Creep
 Toughness

ABSTRACT

Powder Bed Fusion (PBF) techniques constitute a family of Additive Manufacturing (AM) processes, which are characterised by high design flexibility and no tooling requirement. This makes PBF techniques attractive to many modern manufacturing sectors (e.g. aerospace, defence, energy and automotive) where some materials, such as Nickel-based superalloys, cannot be easily processed using conventional subtractive techniques. Nickel-based superalloys are crucial materials in modern engineering and underpin the performance of many advanced mechanical systems. Their physical properties (high mechanical integrity at high temperature) make them difficult to process via traditional techniques. Consequently, manufacture of nickel-based superalloys using PBF platforms has attracted significant attention. To permit a wider application, a deep understanding of their mechanical behaviour and relation to process needs to be achieved. The motivation for this paper is to provide a comprehensive review of the mechanical properties of PBF nickel-based superalloys and how process parameters affect these, and to aid practitioners in identifying the shortcomings and the opportunities in this field. Therefore, this paper aims to review research contributions regarding the microstructure and mechanical properties of nickel-based superalloys, manufactured using the two principle PBF techniques: Laser Powder Bed Fusion (LPBF) and Electron Beam Melting (EBM). The ‘target’ microstructures are introduced alongside the characteristics of those produced by PBF process, followed by an overview of the most used building processes, as well as build quality inspection techniques. A comprehensive evaluation of the mechanical properties, including tensile strength, hardness, shear strength, fatigue resistance, creep resistance and fracture toughness of PBF nickel-based superalloys are analysed. This work concludes with summary tables for data published on these properties serving as a quick reference to scholars. Characteristic process factors influencing functional performance are also discussed and compared throughout for the purpose of identifying research opportunities and directing the research community toward the end goal of achieving part integrity that extends beyond static components only.

Build direction and axis definition are almost uniformly defined as below (as shown in Fig. 1)

1. Introduction

Additive manufacturing (AM) can be defined as “a process of joining materials to make objects from 3D model data, usually layer upon layer, as opposed to subtractive manufacturing methodologies”. This technique has drawn significant attention due to its flexibility in design and fabrication. Commercially, AM has the potential to save both money and

time while delivering enhanced functionality with respect to conventional subtractive manufacturing techniques. This becomes apparent when highly customised parts with high value and low volume are required. Several researchers have previously reviewed the potential advantages of AM, as well as its positive impact on society [1]. These studies concluded that this process is driving a revolution to manufacturing technology.

In the last two decades there has been a dramatic increase in the number of publications associated with Nickel-based materials in AM (see Fig. 2).

* Corresponding author.

E-mail addresses: salome.sanchez3@nottingham.ac.uk (S. Sanchez), peter.smith2@nottingham.ac.uk (P. Smith), xu_zhengkai@simtech.a-star.edu.sg (Z. Xu), gabriele.gaspard@alumni.epfl.ch (G. Gaspard), christopher.hyde@nottingham.ac.uk (C.J. Hyde), wessel.wits@nl.thalesgroup.com (W.W. Wits), ian.ashcroft@nottingham.ac.uk (I.A. Ashcroft), Hao.Chen@nottingham.edu.cn (H. Chen), adam.clare@nottingham.ac.uk (A.T. Clare).

<https://doi.org/10.1016/j.ijmactools.2021.103729>

Received 12 December 2020; Received in revised form 7 April 2021; Accepted 7 April 2021

Available online 17 April 2021

0890-6955/© 2021 The Author(s).

Published by Elsevier Ltd.

This is an open access article under the CC BY-NC-ND license

(<http://creativecommons.org/licenses/by-nc-nd/4.0/>).

Nomenclature			
AB	As Built	HT	Heat Treatment
BD	Build Direction (will be aligned with the Z-axis in Figures, unless otherwise specified, see Fig. 1)	IN	Inconel
CAD	Computer Aided Design	LCF	Low cycle Fatigue
DA	Direct Ageing	LPBF	Laser Powder Bed Fusion
EBM	Electron Beam Melting	OM	Optical Micrography
EBSD	Electron Back Scatter Diffraction	PBF	Powder Bed Fusion
EDM	Electrical Discharge Machining	PREP	Plasma Rotated Electrode Process
FCC	Face Centred Cubic	RA	Recrystallisation Annealing
HA	Homogenisation and ageing	RT	Room temperature
HCF	High Cycle Fatigue	SEM	Scanning Electron Microscopy
HIP	Hot Isostatic Pressing	SR	Stress Relieved
HSA	Homogenisation and solution treatment and ageing	ST	Solution treatment
		STA	Solution treatment and Ageing
		TEM	Transmission Electron Microscope

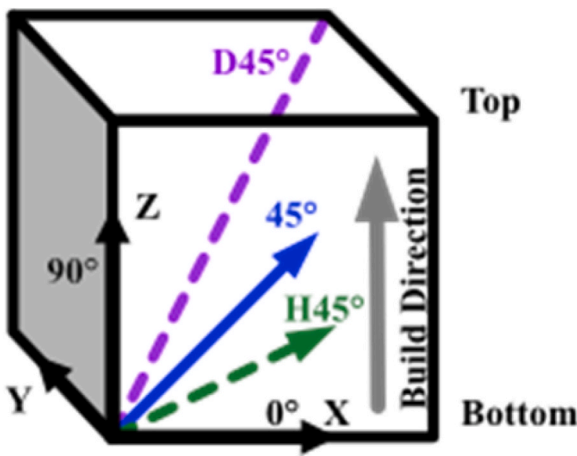


Fig. 1. Layout of the build directions and principle planes commonly used when highlighting anisotropy in PBF specimens. Noting the orientation of this primitive is commonly considered to align with the machine coordinate system.

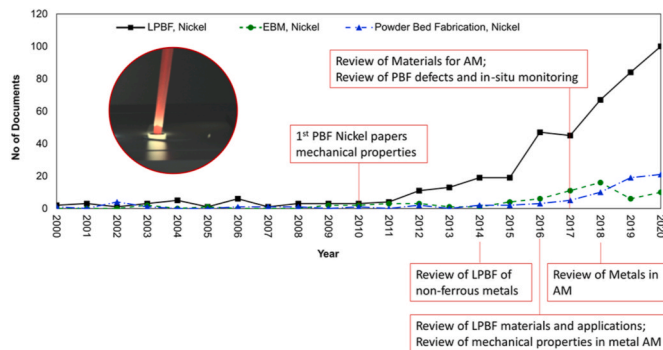


Fig. 2. Number of publications on Additive Manufacturing of nickel-based superalloys (from Scopus database) with major milestones [2–8]. This shows an increase in publications associated with Nickel-based materials in Additive Manufacturing.

There are several prior reviews regarding AM, particularly Powder Bed Fusion (PBF), of metals. The reviews in the literature to date provide a general overview of metal AM techniques, focusing on the processing methods, corresponding microstructures, mechanical properties and their applications with a variety of materials [3,9–12]. Murr et al.

compared the two main metal PBF techniques, i.e. Laser Powder Bed Fusion (LPBF) and Electron Beam Melting (EBM), and their processing of commonly used structural materials [13], while Korner et al. reviewed EBM and the process-property links in metallic materials [14]. Song et al. reviewed the differences in microstructures and mechanical properties between LPBF manufactured components and their conventionally manufactured counterparts [15]. Sames et al. reviewed a series of metal AM techniques, focusing on their issues and their mechanisms, as well as creating models to simulate them [16]. Basak and Das reviewed the microstructure evolution in commonly used metal alloys processed with various metal AM techniques [17]. In the literature, review papers on the general mechanical properties of LPBF manufactured components can be found [18–20]. These tend to focus on the microstructure and mechanical performance of additively manufactured Ti–6Al–4V components [21,22] and nickel-based superalloys [23,24]. Wang et al. reviewed LPBF manufactured Inconel (IN) 718 components, mainly concentrating on its microstructure and mechanical properties [25]. This is perhaps the most similar work to the review undertaken here which only represents a fraction of the state-of-the-art now available in the literature. Aboulkhair et al. comprehensively reviewed aluminium alloys [26]. Zhang et al. reviewed the applications of LPBF titanium alloys and of titanium matrix composites in biomedical engineering [27]. It is worth mentioning that there are also review papers on novel design [28] and material systems [29] applied to additive manufacturing. However, there is yet to be presented a comprehensive review on the subject of mechanical properties of PBF Nickel-based superalloys which provides an authoritative and comprehensive resource to scholars in this field. Therefore, the motivation for this paper is to present a comprehensive review of the mechanical properties of PBF nickel-based superalloys. This will provide researchers with a better understanding of the state-of-the-art and the effect of PBF processing parameters on the mechanical properties. A summary of the research undertaken for different mechanical properties will be given at the end of this review to help practitioners to identify what categories of material evaluation have been performed and to identify gaps in research. Finally, both the opportunities and shortfalls of PBF in the processing of Nickel-based superalloys will be discussed. Since our understanding of the fundamental metallurgy and process itself develops at a rapid rate it essential that the community has a point of reference from which to draw.

1.1. Powder bed fusion techniques

This paper focuses on the two principle PBF techniques: LPBF and EBM. PBF is one of the most popular AM techniques for metal part fabrication. This process consists of two stages: firstly, the powder is spread uniformly on the working area, then an energy source (a laser

beam for LPBF and an electron beam for EBM) selectively melts the powder bed according to a 3D model and hence build the final component [30]. The two main differences between these fabrication methods are their power sources and power transmission systems. Two diagrams representing a typical LPBF and EBM systems are presented in Fig. 3 [9]. Both methods and process nuances have already been properly reviewed by other researchers and Table 1 summarises the relevant differences between the two systems [9,16,30]. This method can be used to process a variety of materials, ranging from metals to ceramics, for many applications, such as aerospace, biomedical and automotive. For a broad review of the materials available for all types of AM platform the reader is referred to Bourell et al.'s review of the topic [31].

1.2. Nickel-based superalloys and the role for AM

This section will highlight the characteristics of nickel-based superalloys, why they are appropriate for PBF use and examples of their applications, particularly in the aerospace sector.

1.2.1. Characteristics of nickel-based superalloys

Nickel-based superalloys, as a family of modern aerospace engine materials [34,35], which possess a combination of high-temperature strength, toughness, creep and oxidation/corrosion resistance. For these reasons, this class of alloys has been widely used in components operating in critical environments [36]. The first generation of nickel-based superalloys, designed for high-temperature applications in jet engines, included Nimonic 75, developed by Henry Wiggin Ltd, UK, in the 1940s [34]. Since then, nickel-based superalloys have been continuously produced, studied and used in building turbine blades, turbine discs, seals, rings, and other components in gas turbines. Nowadays, there are nearly 1.8 tonnes of nickel-based superalloys in a typical jet engine. These materials have greatly contributed to the increase of the continuous operating life of jet engines to above 20,000 h [37]. While coating technologies (e.g. Zirconia based thermal barrier coatings, TBCs) have also served to enhance high temperature performance the role of the substrate nickel-based superalloy cannot be overstated. Fig. 4 shows the weldability and therefore the utility of nickel-based superalloys in fabrications. This is a useful indicator of how challenging high integrity AM will be for a given material. Effectively, the process window becomes greatly reduced above the broken red line.

Nickel-based superalloys are used in many applications, such as land-based gas turbines, nuclear power plants and chemical containers. A summary of some common applications for nickel-based superalloys are reported in Table 2.

Table 1
The major differences between Laser Powder Bed Fusion and Electron Beam Melting. This provides an insight into process characteristics [9,16,30].

Aspects	LPBF	EBM
Power source	Laser	Electron beam
Power range	20 W–1 KW	Several KW, much higher than the laser power
Energy beam spot size	50 μm –180 μm	50 μm –200 μm
Power transmission system	High-frequency scanning mirrors	Electromagnetic lenses and magnetic scan coil
Scan speed range	Up to 15 m/s	Up to 10 m/s
Powder bed thickness range	20 μm –100 μm	50 μm –200 μm
Powder bed temperature range	Significant substrate heating is not usual and can range from 20 °C [32] to 975 °C [33]	Can be very high, slightly below the materials' melting temperature
Build chamber condition	Normally filled with protective gases, with an oxygen content less than 0.1%	Vacuum, <10 ² Pa

Fig. 5 summarises the types of nickel-based superalloys studied in PBF research. It is clear from this figure that IN718 and IN625 are the most explored in PBF studies. Their composition can be found in Table 8 in the Appendix.

1.2.2. Nickel-based superalloys and PBF in the aerospace Industry

The aerospace industry represents a significant prize for AM machine producers, since a significant amount of components have a high part value and are produced using high value materials [40]. Indeed, nickel-based aerospace components are characterised by complex geometries and low production volumes. Furthermore, given the characteristic excellent mechanical properties of Nickel-based superalloys, designed to work in safety critical applications, these parts are difficult and expensive to machine with conventional machining techniques [41–44]. As a result, particular attention must be paid to the selection of tooling, coolants, and processing parameters, leading to increasing production costs [40]. On the contrary, PBF's ability to manufacture complex geometries allow the incorporation of new and additional functionalities to components. Hence, this area is an appropriate way to demonstrate the potential of using PBF in conjunction with nickel-based superalloys.

Work by Yadroitsev et al. demonstrated the capability of LPBF in producing complex filters constituted of free-form structures from IN625 [45]. The parameters of the unit cell, or even of individual cells, can be

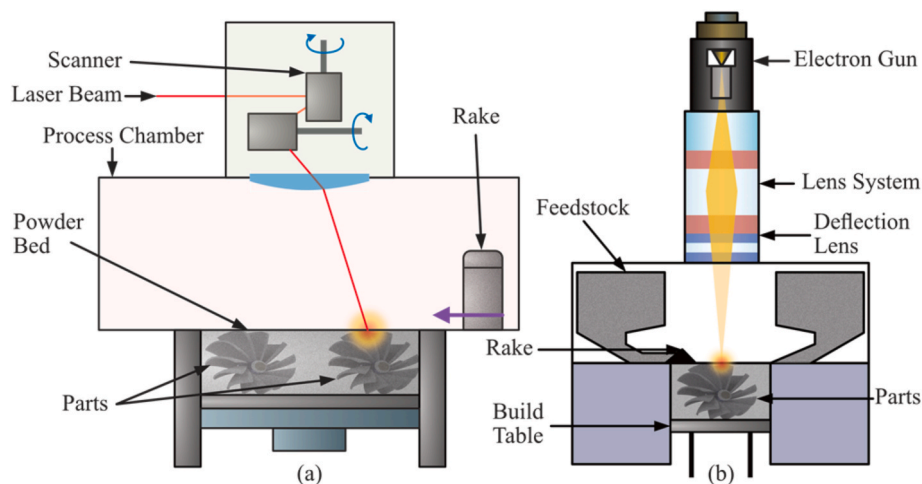


Fig. 3. Diagram of the two main Powder Bed Fusion processes. (a) Laser Powder Bed Fusion. (b) Electron Beam Melting systems. The two main differences (power sources and power transmission systems) are visible. After [9].

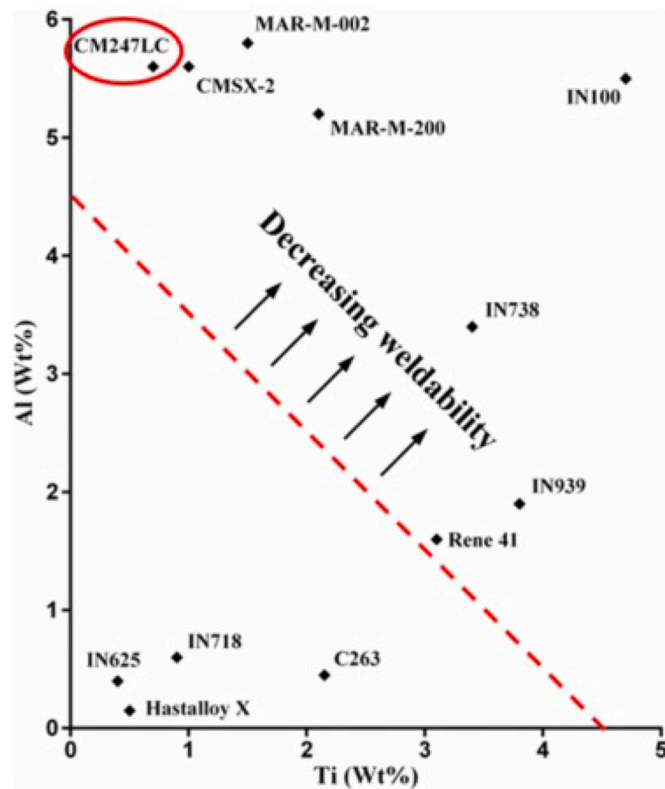


Fig. 4. 'Weldability' diagram for a range of nickel-based superalloys as a function of their Ti and Al alloy element composition. Figure from Catchpole-Smith et al. [38]. Weldability is considered poor above the dashed line and deteriorates with increasing Ti and Al content. This work will inform future research on alloy compositions.

easily modified at the modelling stage and optimised for specific applications with features below 1 mm (Fig. 6). This demonstrates an immediate opportunity for AM technologies which cannot be achieved through conventional machining methods.

A further advance was demonstrated by Bernstein et al., who developed and built a prototype turbine blade characterised by a leading edge with inbuilt cooling channels obtained via LPBF (Fig. 7) [42]. The measured average cooling hole size (0.3945 mm) was slightly smaller than the nominal size (0.5 mm), highlighting tolerancing challenges remaining to be conquered in LPBF. The standard deviation for these hole diameters was small (0.0206 mm), indicating LPBF has potential as an accurate and effective technique to produce these features. Despite some promising results, this process cannot yet compete with the feature resolution obtained by laser processes or electrical discharge machining (EDM), which are common methods for cooling hole introduction. Indeed, Li et al., amongst others, have demonstrated that by using a laser or EDM drilling process it is possible to obtain holes with a diameter <150 μm . However, common industrial processes for civil aircraft require cooling hole diameters in the range 300–500 μm [46]. This is a fundamental technology limitation which governs turbine blade and nozzle guide vane thermodynamic performance. However, focus on AM research for aerospace applications has so far been focused on static components. The reasons behind this becomes evident with exploration of the mechanical properties exhibited by AM materials, a topic explored in much more detail later in this review.

Since LPBF has shown promising initial results in the realising complex structures in aero-engine components, more and more companies are expressing intentions to invest in this technology. A review of metal AM use in the commercial aviation industry was written by Gisario et al. [47] and a review of the material characteristics of AM IN718 for high temperature applications was written by Yong et al. [48].

Table 2

Common applications of nickel-based superalloys [39]. This shows the numerous areas where additively manufactured nickel-based superalloys could be used.

Applications	Examples	Typical alloys
Aerospace Industry	Aircraft gas turbines: disks, combustion chambers, bolts, casings, shafts, exhaust systems, blades, vanes, burner cans, afterburners, thrust reversers, Space vehicles: aerodynamically heated skins, rocket engine parts	IN600, IN601, IN617, IN625, IN706, IN718, IN738, IN754, IN X-750, Nimonic 115, Nimonic 75, Nimonic 80, Nimonic 90, Rene 41, Waspaloy, Hastelloy X
Chemical and petrochemical industries	bolts, fans, valves, reaction vessels, tubing, transfer piping, pumps	IN600, IN625, IN690, IN718, IN725, IN925, Rene 41, Waspaloy
Pulp and paper mills	tubing, doctor blades, bleaching circuit equipment, scrubbers	Hastelloy G, IN600, IN671, IN706, IN718, Rene 41, Waspaloy
Nuclear power systems	control rod drive mechanisms, valve stems, springs, ducting	Hastelloy G, IN600, IN625, IN706, IN718, Rene 41, Waspaloy
Marine architecture	ships, submarines	IN600, IN625, IN718, Rene 41, Waspaloy
Electronic Parts	resistors	IN706, IN718, Nichrome, Waspaloy
Steam turbine power plants	bolts, blades, stack gas reheaters	IN706, IN X-750
Metals processing mills	ovens, furnace, afterburners, exhaust fans	IN600, IN625, IN706, IN718, N06008, Nichrome, Rene 41, Waspaloy
Heat-treating equipment and Metal processing	trays, fixtures, conveyor belts, baskets, fans, furnace mufflers, hot-work tools and dies	IN600, IN706, Nimonic 80, Rene 41, Waspaloy, Waspaloy
Automotive industry	spark plugs, glow plugs (in diesel engines), catalytic converters, combustion systems Reciprocating engines: turbochargers, exhaust valves, hot plugs, valve seat inserts	IN625, Waspaloy
Medical applications	dentistry uses, prosthetic devices	Vitallium, Ni–Cr and Ni–Ti alloys
Pollution control equipment	scrubbers, flue gas desulfurization equipment (liners, fans, stack gas reheaters, ducting)	IN718
Coal gasification and liquefaction systems	heat exchangers, repeaters, piping	IN690

As an example, NASA has tested some LPBF built rocket injectors, demonstrating that these parts can withstand heat and pressures generated during space rocket launches [49]. MTU Aero Engines also announced that the borescope bosses for their PurePower PW1100G-JM engines will now be produced using LPBF [50]. Further, the Netherlands Aerospace Centre together with the University of Twente developed a novel micro-pump assembly for space application, composed of no moving parts, such as hydraulic valves [51]. The manufacturing of this micropump was only possible using LPBF, due to the complex internal features which could not be obtained by other means. GE Aviation played a fundamental role in the introduction of AM to the aerospace industry, in particular through the acquisition of both SLM Solutions and Arcam, two major AM companies specialising in LPBF and EBM, respectively. As a proof of principle, GE Aviation built a working miniature version of a jet engine using entirely LPBF [52]. Even though the scale was far smaller than commercial engines, this prototype was able to reach 33,000 RPM in functional testing and marks a significant step towards a more widespread use of LPBF in aero-engines manufacturing. They also created a sensor housing using only LPBF, which made it the first 3D printed part to be approved for use by the FAA

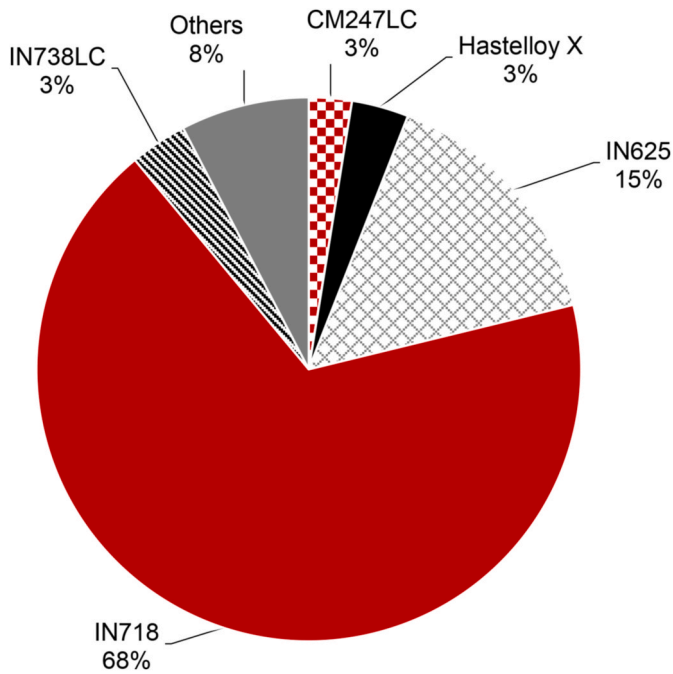


Fig. 5. Pie chart showing the nickel-based superalloys studied in powder bed fusion research to date, from 290 studies. Inconel 718 and Inconel 625 are the most studied alloys given their level of usage primarily in the aerospace markets where there are immediate opportunities for aerospace.

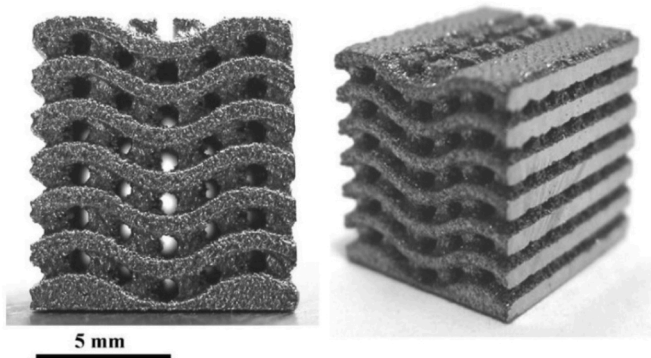


Fig. 6. Inconel 625 filter with placement specific pore orientation and cross-sectional area. These samples were manufactured by powder bed fusion, demonstrating the ability of powder bed fusion to manufacture highly optimised geometries with features < 1 mm. This is an exemplary use of Laser Powder Bed Fusion technology [45].

[53]. Other demonstrators, like turbine blades, were printed using EBM IN738LC and were assembled onto a disk for spin pit testing to validate the mechanical integrity and design of the blades [54].

In summary, AM is a promising technique for the manufacturing of nickel-based components. However, the knowledge gaps, which currently restrain PBF from wider scale exploitation, remain significant. Failure to fully understand the microstructural and functional response of AM nickel-based superalloys will severely limit the applications for this technology/material combination. As such, we must obtain a fundamental understanding of the origin of defects in both material and process.

2. PBF process control and quality inspection

In order to efficiently transfer the PBF processes to industry,

adequate and solid inspection methods for both the building process and build quality must be selected. Some of the techniques proposed for this purpose are discussed in this section and will provide the scholar with reference methodologies.

2.1. Microstructural characterisation

The most common methods for the analysis of PBF nickel-superalloys include Optical Micrography (OM), Scanning Electron Microscopy (SEM) and Electron Back Scatter Diffraction (EBSD), which are described briefly below. All of these are common to well equipped metallography laboratories. In order to use those methods, samples need to be carefully prepared. A review on the preparation of metallic materials has also been written by Zhang et al. [55] which will assist nickel-based superalloy and AM researchers in developing characterisation strategies. Here, the main observations under these techniques are highlighted. Arriving at appropriate specimen conditions often requires appropriate grinding, polishing, and etching. The reader can refer to Zhang et al.'s review [55] on this topic for more information.

Porosity in PBF specimens is a classic 'first indicator' to investigate and although the Archimedes principle is suggested by ASTM standards for carrying out porosity measurements for PBF materials [56], OM is typically used by the research community to observed these at a x50 magnification or less (Fig. 8). The lateral resolution of OM is in the order of 200 nm [57]. If a higher resolution is required (smaller pore size) use of electron microscopy is required. Specimen cross-sections are often analysed using an image analysis software, such as ImageJ, and porosities can be quantified albeit destructively. Perevoshchikova et al. proved that these porosity values were comparable to those obtained with the Archimedes method [58]. In softer materials caution must be taken in order not to obscure pores by material smearing upon polishing. Melt pools can also be identified using OM (Fig. 29) under an appropriate etch. However, microstructure at the grain scale is usually not observed using OM since salient features in PBF nickel-based superalloy specimens are typically 5–30 μm . As such, higher resolution imaging techniques, such as SEM, are required if understanding beyond the macro (weld tracks, pores) is required.

SEM is widely used to characterise PBF nickel-based superalloys sample microstructures. Along with back scattered electron micrographs, the material's surface topography, grain structure, phases and precipitates can be observed. In fact, the fast heating and cooling cycles produced during PBF, often make precipitates small (in the range of nm) which may be beyond the limit of SEM. Since the composition, spatial frequency and size of these are critical in determining alloy performance. Characterisation of these (and controlling their formation) is critical in process.

EBSD can provide more detailed information regarding the material's crystallographic texture as an accompaniment to electron microscopy. An EBSD orientation map of an As-Built (AB) LPBF IN718 specimen is given in Fig. 19 [59]. EBSD is exceptionally useful in relating the textural formation in AM with the associated process parameters and material composition. Data sets emerging from EBSD are highly valuable when considering the recrystallisation behaviour of AM specimens. Terner et al. also used EBSD to estimate residual stress in LPBF IN625 by assessing misorientation or strain levels from local misorientation by means of orientation imaging, and found that EBSD was adequate to qualitatively assess residual stress in a material [60]. Allied to EBSD are a number of emergent techniques which make use of laser ultrasonics. Rossin et al. used resonant ultrasound spectroscopy to characterise and detect LPBF part microstructure variability [61]. Further Smith et al. demonstrated the use of Spatially Resolved Acoustic Spectroscopy for characterisation of AM components [62]. While these techniques are in their infancy they have clear potential to be used alongside AM in the production environment.

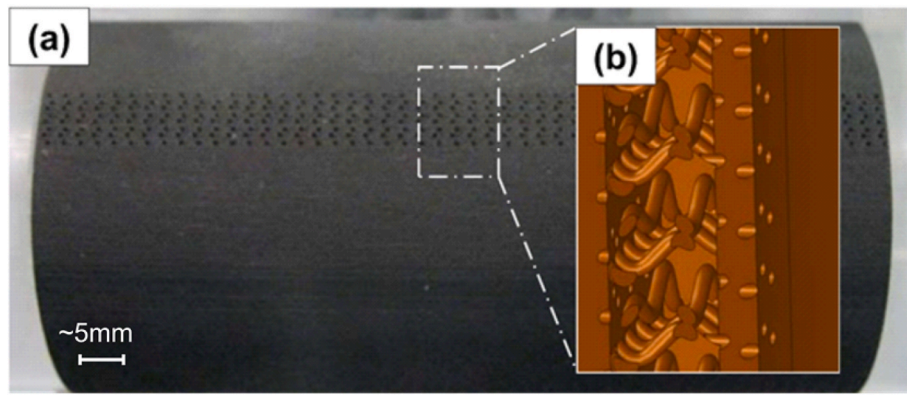


Fig. 7. Example of novel cooling channels in a leading edge. (a) the overview. (b) Computer Aided Design model of the internal structure of the cooling channels [42]. The average measured cooling hole size (0.39 mm) was slightly smaller than the nominal size (0.5 mm), highlighting tolerancing challenges still to be conquered in Laser Powder Bed Fusion.



Fig. 8. Optical micrographs of a laser powder bed fused specimen [58]. Porosity and other defects are clearly present in the material. These can be easily detected using optical micrography. However, caution should be taken when considering softer materials as smearing can serve to obscure pores. (Process parameters used: 295 W, 2250 mm/s 0.11 mm layer height.)

2.2. X-ray diffraction

X-ray diffraction (XRD) can be used not only to determine the crystalline structure of polycrystalline materials but also to measure residual stresses [63]. In Fig. 9, the XRD spectra for an IN718 powder and an AB LPBF specimen are reported, giving a general overview of the phase distribution in the material. As expected, the main phase present was the γ face-centred cubic (FCC) NiCr phase [64]. From the peak analysis it is

observed that the γ' and γ'' peaks can overlap with the γ , becoming difficult to separate the different contributions. Therefore, other techniques, such as Transmission Electron Microscope (TEM), became necessary to identify and quantify these two precipitates.

Some examples of XRD use in literature include Xia et al. who studied the impact of additional strengthening particles (tungsten carbides WC) on LPBF IN718 specimens and used XRD to characterise the phase distribution in some LPBF IN718+WC composites [65]. γ -Ni, $\text{Ni}_2\text{W}_4\text{C}$, NbC

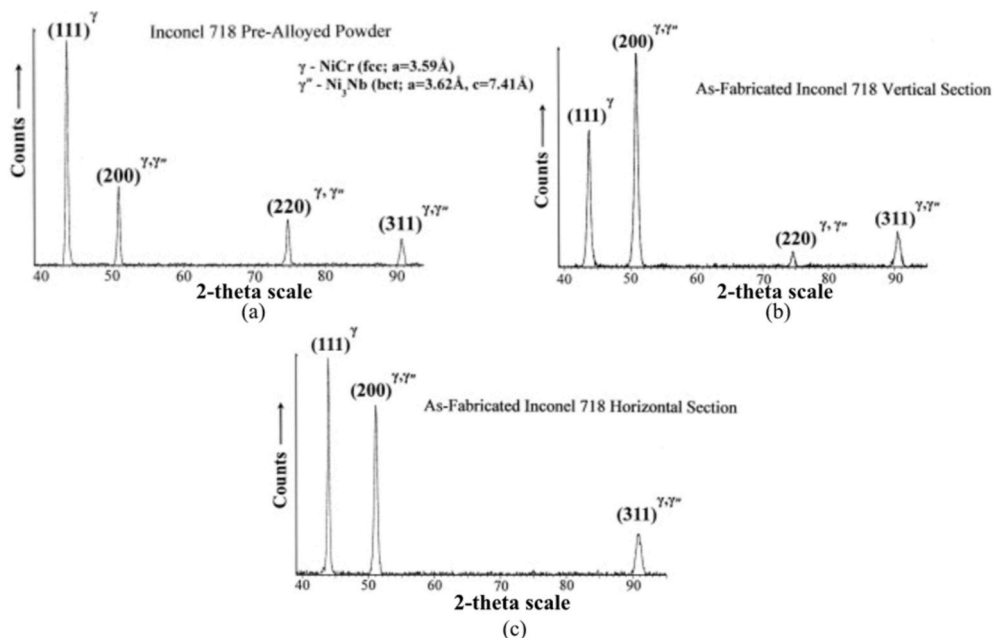


Fig. 9. X-ray Diffraction results for a laser powder bed fused Inconel 718 specimen. (a) Powder. (b) As-built vertical section. (c) As-built horizontal section [64]. As expected, the main phase present is the γ face-centred cubic NiCr phase and it is observed that the γ' and γ'' peaks can overlap with the γ , becoming difficult to separate the different contributions.

and the residual WC particles were found as the main phases. A shift in the diffraction peaks was highlighted, which was probably due to the lattice strain generated by the presence of larger W atoms. These induced stresses were thought to be responsible for the observed material strengthening. In the study by Raghavan et al., spectra from specimens treated with different HT were compared [66]. The XRD spectra obtained from the specimens (Fig. 10) showed that increasing the solution temperature decreased the number of secondary phases (γ' , γ'' and carbides).

Popovich et al. used XRD to investigate the effect of post-processing techniques on LPBF IN718 specimens [67]. A large amount of δ and γ'' phases were generated during the heat treatment (HT), whereas two types of carbides (NbC and TiC) were produced after Hot Isostatic Pressing (HIP) and HT (Fig. 11). Consistent with prior studies, it also highlighted the limitations and inadequacy of the XRD spectra for quantifying and differentiating phases such as δ and γ'' , characterised by overlapping peaks.

XRD can be used not only qualitatively, but also quantitatively in determining specimens phase distribution. As an example, in a further study by Popovich et al., XRD was used to analyse the chemical composition of LPBF IN718 specimens at different stages of manufacturing (reported in Table 3) [68]. It was found that the total amount of strengthening particles in the AB specimen slightly increased compared to the original powder, increasing the strength more than predicted. During homogenisation, δ particles were fully dissolved, partially lowering specimen strength. However, if this was followed by an ageing treatment, the total volume of strengthening phases reached the value of ~ 33 vol%, namely three times more than AB specimens. The strengthening effect of these precipitates was confirmed by tensile

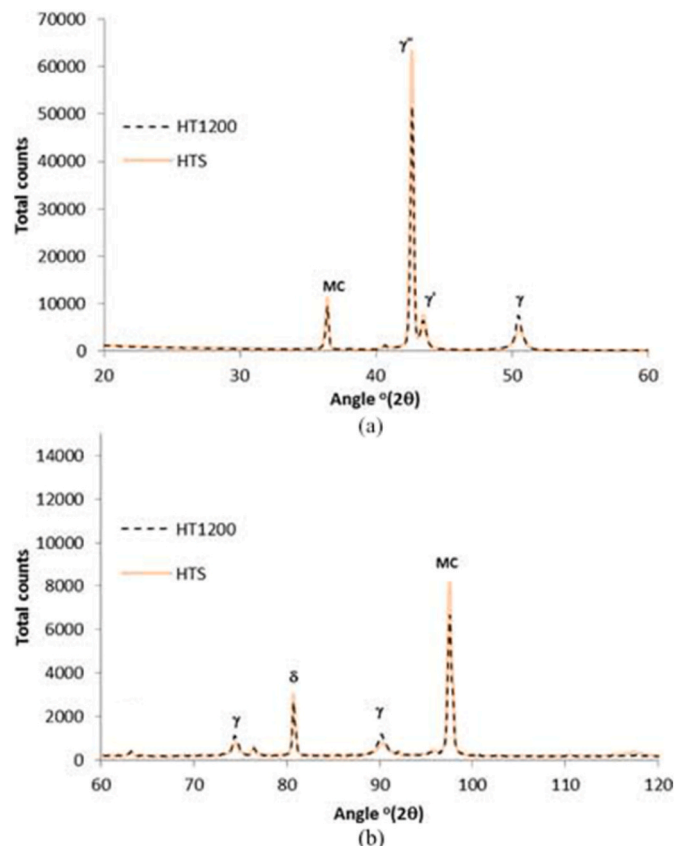


Fig. 10. Comparison between the X-ray Diffraction spectra of two differently heat-treated Laser Powder Bed Fused Inconel 718. (a) Between a 2θ angle of 20° - 60° . (b) Between a 2θ angle of 60° - 120° [66]. This showed that increasing the solution temperature decreased the number of secondary phases (γ' , γ'' and carbides).

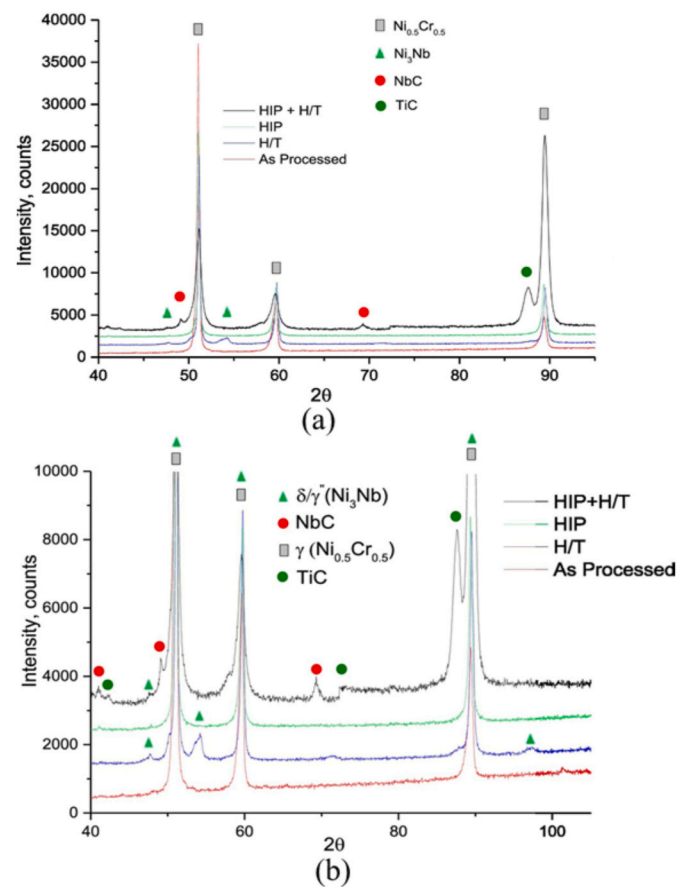


Fig. 11. X-ray Diffraction spectra of as-built and post-processed Inconel 718 specimens. (a) Full spectra. (b) An enlarged image [67]. This demonstrates the inadequacy of the X-ray Diffraction spectra for quantifying and differentiating phases such as δ and γ'' , characterised by overlapping peaks.

Table 3

X-ray Diffraction results for laser powder bed fused Inconel 718 quantitative composition [68]. Illustrating that X-ray Diffraction can be used not only qualitatively, but also quantitatively in determining specimens phase distribution.

Sample	Phases	Composition/vol%
Original powder	γ - Ni	90.0
	γ' - Ni ₃ Al	3.5-3.9
	γ'' - Ni ₃ Nb	4.3-4.5
	δ - Ni ₃ Nb	1.8-2.0
AB condition	γ - Ni	86.8
	γ' - Ni ₃ Al	1.9
	γ'' - Ni ₃ Nb	8.0
	δ - Ni ₃ Nb	3.3
Homogenisation	γ - Ni	90.1
	γ' - Ni ₃ (Al,Ti)	1.9
	γ'' - Ni ₃ Nb	8.0
Homogenisation + ageing	γ - Ni	67.3
	γ' - Ni ₃ (Al,Ti)	8
	γ'' - Ni ₃ Nb	4
	δ - Ni ₃ Nb	3.5
	γ' - Ni ₃ Al	17.2

testing: fully HT specimens showed a tensile strength of 1350 MPa, compared to 1002 MPa for AB equivalents.

XRD can also be used to measure the residual stresses generated during PBF. Residual stress is commonly observed in PBF as localised stresses are induced upon cooling. Goel et al. observed, using neutron diffraction, that residual stresses were higher in LPBF than in EBM AB IN718 samples [69]. Sanz et al. analysed the residual stresses in some

LPBF IN718 specimens and explored how they were affected by different post-processing strategies [70]. These measurements indicated that the stresses, of tensile nature, drastically undermined performance. Shot peening (amongst other methods) can be used to induce high compressive stresses in the surface and hence counterbalance this effect (Fig. 12) [70]. However, much like additional HT intrusive post-processing steps serve to undermine the economic case for using PBF.

2.3. X-ray computed tomography

X-ray Computed Tomography (XCT) uses X-rays to take multiple two-dimensional cross-sectional images of an object from different orientations, allowing observation within [71]. With the help of XCT, the built-in defects as well as those generated during the mechanical testing can be characterised without destroying the specimen. In a study by Tillmann et al., the porosity of LPBF IN718 was evaluated using OM and XCT [72]. The comparison between the two measurements showed a significance difference between the two measurements (Table 4). This difference was imputed by the limit of the XCT resolution. In fact, porosities with a diameter smaller than 8 μm were not detected by this technique, measuring therefore a smaller amount of porosities. This is a fundamental limitation since defects at this size, and appropriate population, can undermine part integrity significantly.

XCT analysis also revealed that a region with a high porosity density was located between skin and core. The formation mechanism of these defects was explained in an previous study [73]. Smith et al. also observed that most of the cavities generated during PBF were found near the surface under the conditions they explored (Fig. 13) [74]. The reconstructed 3D volumes clearly show that the build direction (BD) also has an impact on cavities distribution. However, this may be a result of unfavourable processing conditions as opposed to a general deficiency in processing nickel-based superalloys.

Xu et al. performed a series of staged thermal-mechanical tests, investigating the defects evolution in some LPBF IN718 specimens during creep testing [75]. This was achieved by performing XCT at different stages of the test. Fig. 14 shows the porosity distribution along the specimen length at different stages: before testing, at 7.3% strain, at 11.5% strain and after failure. The increase in porosity during creep is straightforward, and the weakest point (Peak 1' in Fig. 14) could also be easily identified through the use of XCT.

Having introduced the primary techniques and common observations associated with PBF of Nickel-based superalloys is it now possible

Table 4

Specimens relative density using Optical Micrographs and X-ray Computed Tomography [72]. The comparison between the two measurements showed a significance difference between the two measurements, highlighting the limitation of X-ray Computed Tomography resolution.

Optical microscopy (average)	Transverse section	Longitudinal section
	0.13 \pm 0.06%	0.09 \pm 0.07%
XCT (average)	Full volume 0.069 \pm 0.012 vol%	

to more closely inspect the microstructures which result from the process.

2.4. PBF process monitoring

Monitoring the PBF building process is necessary to follow and control the process, understand how defects are developed and how they could be removed. This topic has been reviewed extensively by Everton et al. [76]. Robust and widely deployable in-process monitoring capability.

Thermal imaging is one of the most used techniques for melt pool characterisation [77,78] and defect distribution [79]. Criales et al. and Arisoy et al. recorded the movement of a single laser scan during a LPBF IN625 building (Fig. 15) [77,80]. From these thermographs, melt pool sizes, particles spattering tendency, thermal gradients, heating and cooling rates were extracted.

Spatter generated during laser scanning can create serious defects in the PBF samples surfaces and bulk [81]. Foster et al. demonstrated the validity of using thermal imaging for in-situ monitoring of spatter locations [82]. In the thermographs, spatter trajectories were identified from grey scaling and contour plots as shown in Fig. 16. Tan et al. also showed the potential of using neural-network based image segmentation for spatter extraction during LPBF [83]. Alternative monitoring methods also include high frame rate camera to monitor melt pools [84,85], reflectometer-based instrument to measure the dynamic laser energy absorption during the scan [86] and Back Scattered Electron detection system to record the in operando signal during EBM [87].

XCT has been commonly used as a technique for post build analysis (see section 2.3) but can also carry out online measurements. For example, Leung et al. presented the successful application of XCT in capturing pores generation and spatter distribution in single laser track scanning [88]. Finally, other reviewers categorized the defects generated in PBF specimens while monitoring the building process [89,90].

Overall, in-process monitoring has many benefits in terms of understanding the PBF process and controlling the quality of parts produced. This continues to be an important research area for PBF machine technology.

3. Microstructural observations

AM is a layer-wise technique which differs in many aspects from conventional manufacturing techniques such as casting, forging, or rolling. Hence the microstructures observed here are distinct from rolled or wrought equivalents. A review of the microstructural differences between PBF and conventional materials was written by Song et al. [15]. This different approach generates some characteristic microstructures, leading to distinctive material properties. It is also possible, through various PBF techniques, to provide a spectrum of microstructures which may be more or less suited for a given application. This section will highlight typical PBF microstructures and show how process parameters give rise to these. A review on the use of LPBF γ' -strengthened nickel-based superalloys was written by Adegoke et al. highlights the effect of process parameters on the microstructure and defects of these alloys [24].

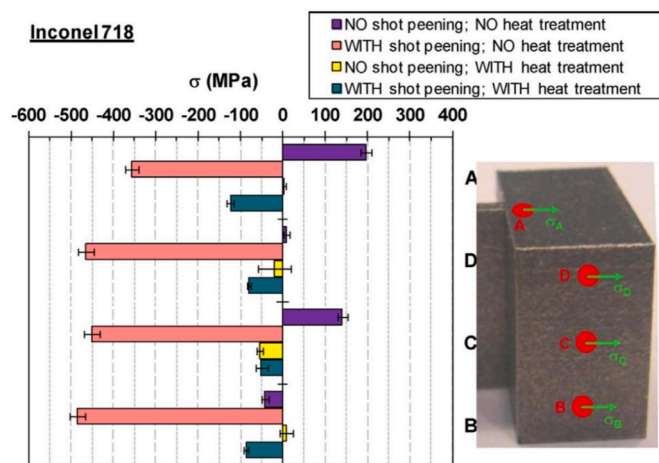


Fig. 12. Residual stress conditions in specimens treated with different post-processing techniques (heat treatment and shot peening) [70]. This illustrates the use of X-ray Diffraction for residual stress measurements as well as the effect of shot peening for inducing compressive residual stresses.

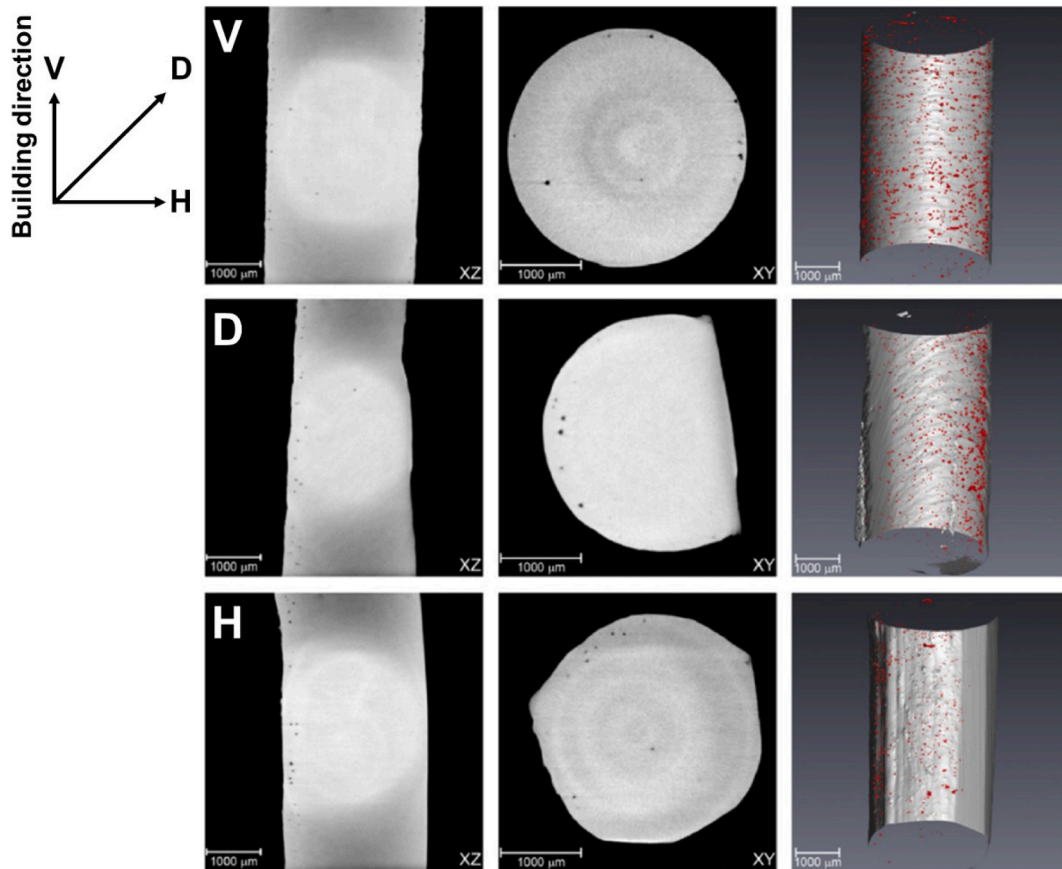


Fig. 13. X-ray Computed Tomography images of specimen cross-section in 2D and reconstructed 3D volumes. V, D and H indicated the different specimen positioning strategies during the building process (which is shown in the top right-hand corner of the image) [74]. The reconstructed 3D volumes clearly show that the build direction has an impact on cavities distribution.

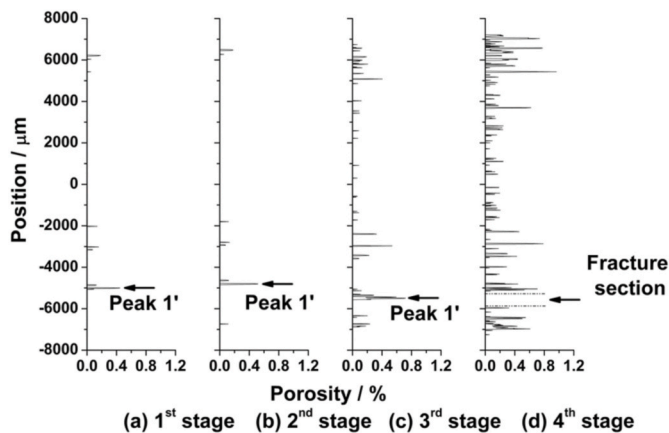


Fig. 14. Porosity distribution in the specimen at different stages of creep testing [75]. Showing the potential of using X-ray Computed Tomography to determine where failure will occur in a specimen and for investigating evolution during tests.

3.1. Typical PBF microstructures

This section will describe typical LPBF and EBM microstructures and how these are linked to process parameters. PBF microstructures have specific process defects. Reviews on these defects and how process parameters affect them have been presented by Malekipour et al. and Grasso et al. [7,91]. Fig. 17 shows some of the typical defects in PBF processes. For more details, the reader is referred to the papers

mentioned.

Fig. 18 presents an overview of the microstructures observed in AB LPBF IN718 specimens [92]. The morphology of melt pools can be clearly observed in the XZ plane (Fig. 18a), while the laser scan tracks are recognisable in the XY plane (Fig. 18b) [92]. Fig. 19 shows an EBSD image with individual laser scan tracks with a width of $\sim 75 \mu\text{m}$ on the XY plane [59]. AB samples have a strong $\langle 100 \rangle$ crystallographic texture in the build direction [93]. Small equiaxed grains with an average size of $10 \mu\text{m}$ can be recognized at the track the overlapping regions between the tracks [59]. These microstructural differences in the two directions are responsible for the mechanical anisotropy of PBF nickel-based superalloys components, which represents a tremendous challenge to researchers.

The dendritic growth directions (yellow arrows in Fig. 18c) follow the build direction (z). However, the growth of dendrites on both sides of the track interfaces does not show any preferential direction (Fig. 18d) [92]. In contrast, another study found that the newly-formed crystals grow into cellular dendrites in a direction which is either parallel to the original direction or rotated by 90° [94]. This allows the grains to interpenetrate from one layer to another. Chlebus et al. investigated the features in the dendritic (Fig. 20a) and interdendritic (Fig. 20b) regions of AB LPBF IN718 specimens [58]. The fast heating and cooling cycles produced during PBF, results in small interdendritic regions (in the range of nm). Microsegregation of some alloying elements, such as Nb, Mo and C, are also produced during the dendrite formation, because of the rapid cooling rate. Some chemical composition inhomogeneities can be observed in Fig. 20a, indicated by arrow 2 [58]. This segregation promotes the formation of NbC carbides and Laves phase in the interdendritic region, as shown in Fig. 20b [58].

EBM specimens show slightly different microstructures compared to

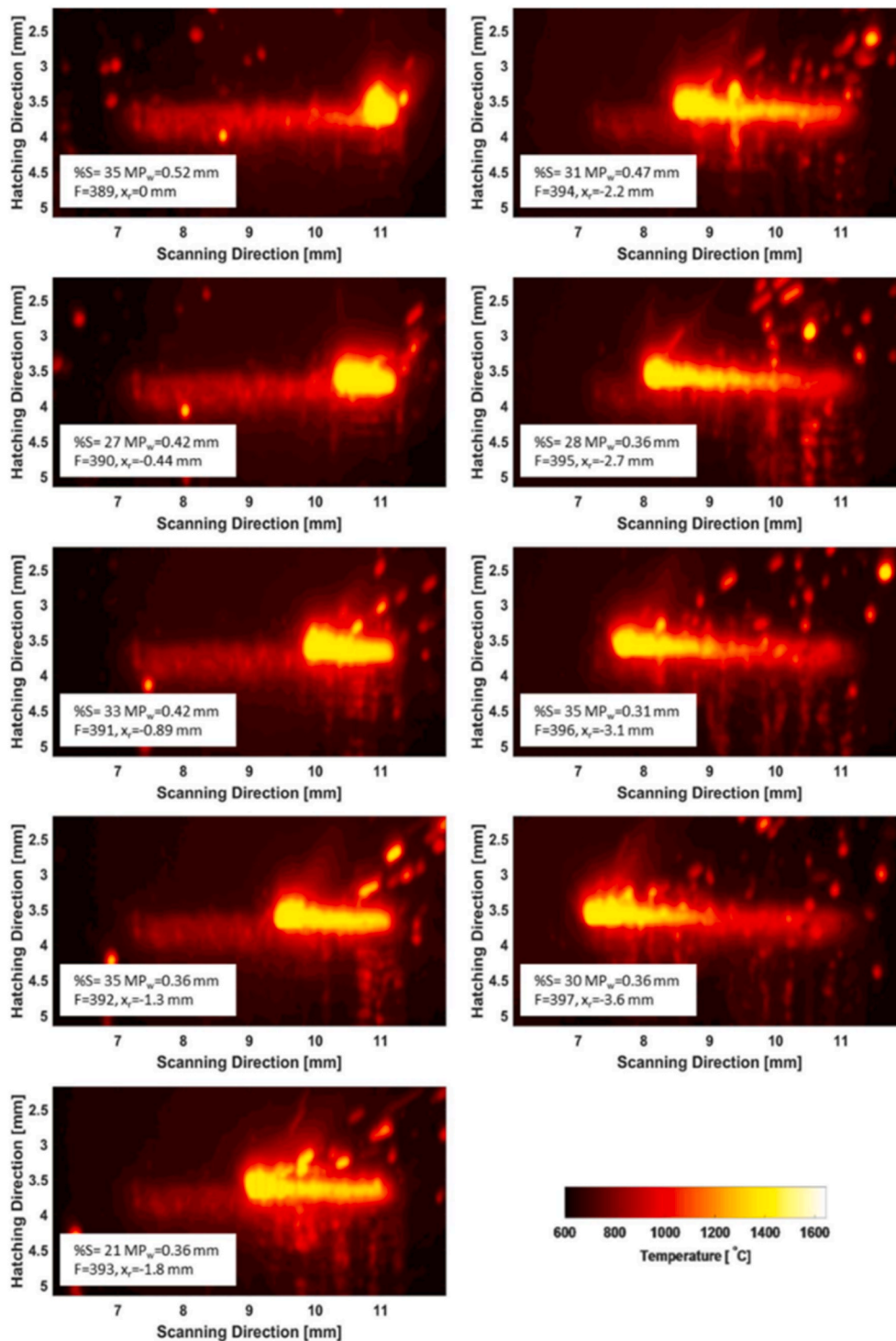


Fig. 15. Series of thermographs recording the building process of a single track [77]. From these thermographs, melt pool sizes, particles spattering tendency, thermal gradients, heating and cooling rates were extracted, illustrating the utility of thermal graphs to monitor Powder Bed Fusion processes quantitatively.

the LPBF equivalents. Kirka et al. analysed the microstructure and chemical compositions of EBM IN718 specimens [96]. Different phases were identified using EDS, their chemical compositions are reported in Table 5. The micrographs of AB EBM specimens (Fig. 21) show that EBM specimens have a lower dislocation density (than LPBF materials), Laves phases and MC carbides in AB state and large disk-shaped γ'' particles (average size of 80 nm).

Sames et al. observed a variation in microstructure along the build direction of the AB EBM IN718 specimens (Fig. 22) [97]. The

needle-shaped δ particles at the top were much coarser than those at the bottom. Additionally, the material in this area showed a greater contrast upon etching, indicating a more severe secondary element segregation. Deng et al. provided more detailed information about the precipitate morphologies as well as the microstructural variations occurring during EBM of IN718 [98]. All these results indicated that thermal cycling varied during the build, influenced by the number of layers already deposited. Hence localised HTs are a common phenomenon in PBF and should be considered in-process optimisation.

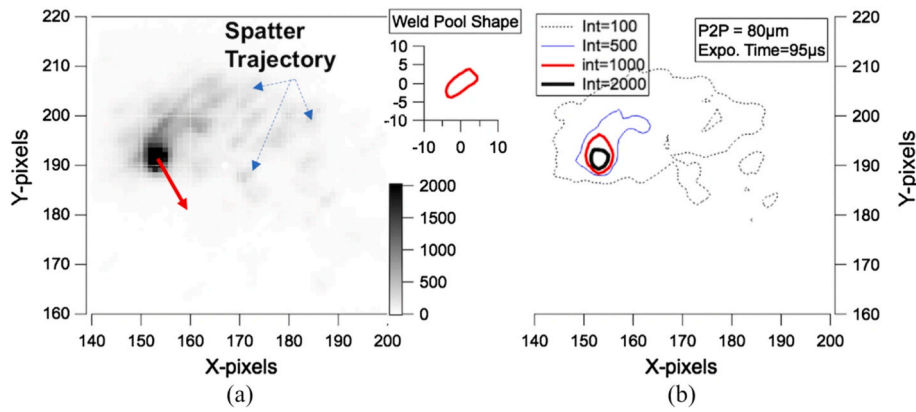


Fig. 16. Analysis of thermographs. (a) Grayscaleing the image captured by infrared cameras. (b) The corresponding contour plot. This shows the usefulness of using infrared cameras to locate spatter generated during the building process [82].

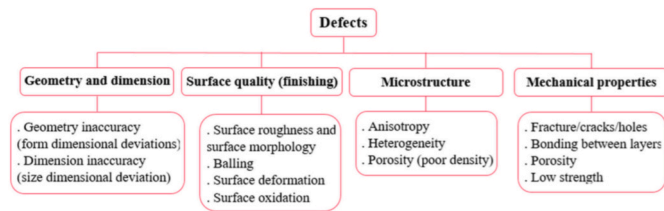


Fig. 17. Summary of defects present in powder bed fusion processes. This can serve as reference for commonly used terminology by practitioners [91].

Polonsky et al. studied the presence and morphology of fusion defects in EBM IN718 specimens [99]. Columnar grains, with a primary

aspect ratio smaller than 0.2 and oriented in the build direction, were found to surround the defects on the XY plane (Fig. 23a). Instead, the regions above the defects had small equiaxed grains with almost no discernible texture. This shows that defects drive the recrystallisation phenomena and influence the resulting microstructure.

Table 6 summarises the commonly observed differences in microstructure between LPBF and EBM and Fig. 24 illustrates some of these differences.

Since powder fusion and recrystallisation of the melt pool are the central phenomenon in PBF, different building parameters and post-processing techniques will lead to different characteristics, which can be quantified using the different methods described previously. Exploration of these in more detail is a key concern.

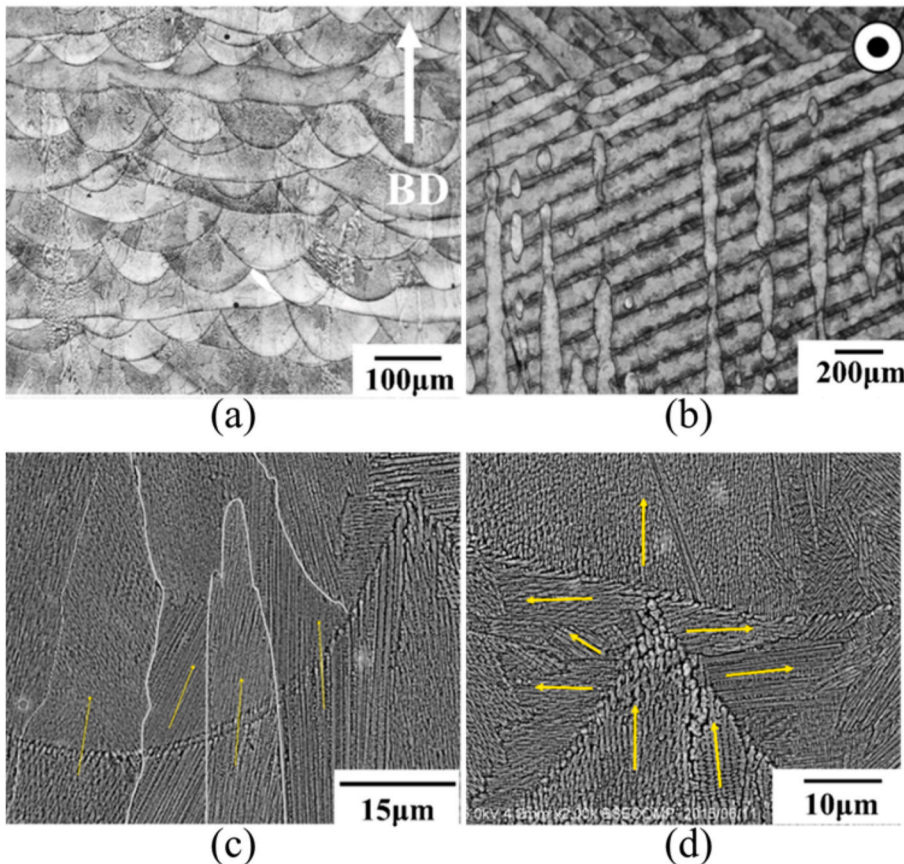


Fig. 18. Images of as-built Laser Powder Bed Fused Inconel 718 specimens. (a) Side view. (b) Top view. (c) The melt pool boundaries between layers. (d) The melt pool boundaries between adjacent tracks from the side. The arrow in (a) indicates the build direction (BD) and the circle in (b) indicates the plane is perpendicular to the build direction. Melt pools in (a) and laser scan tracks in (b) are clearly visible. The yellow arrows in (c) and (d) represent the dendrite growth direction. They follow the build direction in (c) and have no preferred direction in (d) [92]. These images illustrate the particular anisotropic microstructure resulting from the Powder Bed Fusion processes. (For interpretation of the references to colour in this figure legend, the reader is referred to the Web version of this article.)

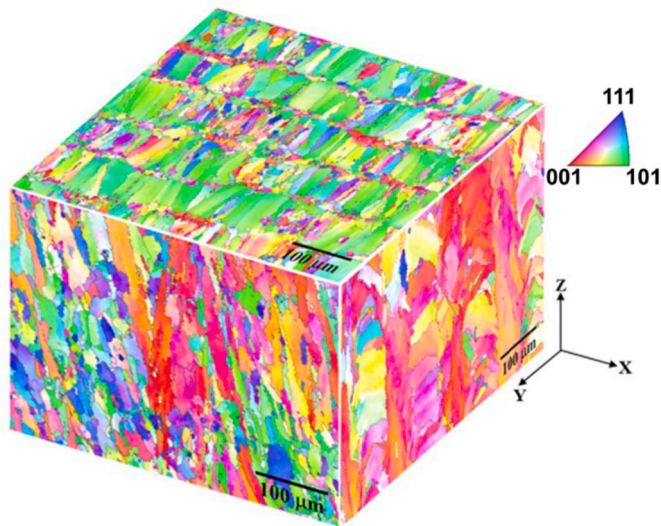


Fig. 19. Electron Backscatter Diffraction maps of an as-built Laser Powder Bed Fused Inconel 718 specimen [59]. This shows the dominant direction of grain growth and strong $\langle 100 \rangle$ crystallographic texture in the build direction, which is characteristic of Powder Bed Fusion processes. Individual laser scan tracks with small equiaxed grains track the overlapping regions can also be seen in the XY plane (perpendicular to the building direction).

3.2. Process parameters driven phenomenon

PBF process parameters naturally have an effect on the print quality and the resulting microstructure. Indeed, using optimised process parameters can suppress the formation of voids and build defects, such as micro-cracks, in LPBF [101–103] and EBM [104]. Review papers on the process-microstructure relationship for LPBF of metallic materials has been presented previously and the reader is directed to these accordingly [105–107]. Kumara et al. also investigated phase transformations of PBF IN718 [108]. An overview of the different effects of build parameters on PBF of nickel-based superalloys microstructure is given below.

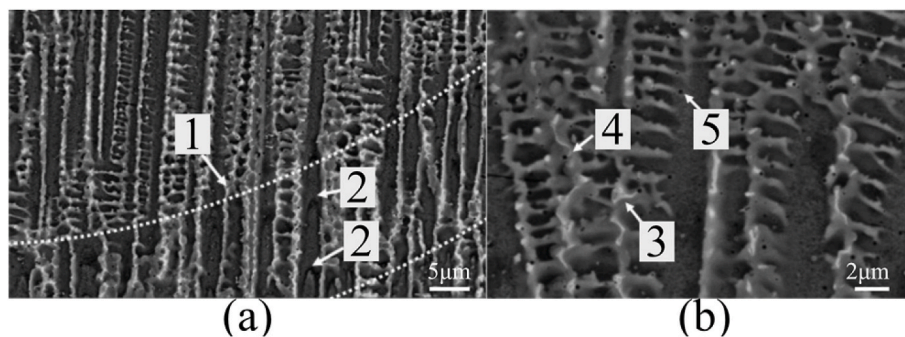


Fig. 20. Typical examples of Scanning Electron Microscopy images of phenomenon in Additively Manufactured nickel-based superalloys. (a) An overview of the interface between adjacent layers. (b) The interdentritic region. Mark 1 indicates the layer-layer melt pool boundary, 2 indicates the dendritic cell tips, 3 and 4 highlight some $\gamma +$ Laves phase eutectic, 5 points a MC carbide [95]. These features are caused by the rapid heating and cooling during the Laser Powder Bed Fusion process.

Table 5

Chemical composition of phases marked in Fig. 21 (wt %) [96]. This provides further proof of the present of Laves phase and MC carbides in the as-built state of Electron beam melted Inconel 718.

Items	Phase	Ni	Nb	Ti	Fe	Cr	Mo	Si	C
1	MC	0.43	89.91	6.01	0.15	0.62	–	–	2.73
2	Laves	42.20	22.87	0.11	13.54	11.24	9.53	0.5	–
3	MC	0.4	90.38	6.31	0.17	0.7	0.71	–	0.99
4	Laves	38.8	28.55	0.23	11.70	9.40	11.19	0.77	–
5	γ matrix	56.19	4.14	0.68	18.99	15.91	3.80	0.04	–

3.2.1. Powder characteristics driving build quality

Powder quality plays a key role in determining PBF components final quality. Powders can be rotary, gas or water atomized and exhibit different morphologies, particle size distributions, flowability, surface roughness and chemical composition. These can vary from supplier to supplier [109]. Sutton et al. reviewed the most commonly used powder characterisation techniques, paying attention to the impact of powder quality on final material properties [110]. A similar review by Tan et al. also focused on powder characterisation techniques, but with a particular emphasis on powder granulometry [111]. This was identified as a key method to ensure a high performance of the feedstock, leading to high quality and, importantly, dense parts.

Studies have found that chemical composition had the strongest impact on the microstructure, as higher content of certain elements resulted in the precipitation of detrimental elements and prevented recrystallisation during HT, which decreased mechanical performance, particularly fatigue [109]. Another work also found that the segregation of alloying elements in LPBF Hastelloy X during solidification resulted in variations in composition which caused cracking in the build direction [112]. By investigating four powders with different contents of various alloying elements, Mancisidor et al. achieved a defect free material [112].

The recyclability of nickel-based powders has been studied by several researchers [113–116]. These generally observed that, as long as the recycled powder is well sieved and stored, little or no difference in properties was found between the specimens manufactured using recycled and fresh powder over ~ 10 build cycles. However, it was found that the presence of minor alloying elements in the metal powder, can influence the crack formation mechanism in PBF specimens [117].

Sames et al. evaluated the properties of components manufactured using powders obtained from various production methods, namely gas atomiser, rotary atomiser, and plasma rotated electrode process (PREP) [118]. From the SEM observations, PREP powder showed a smoother surface and almost no internal trapped gas, compared to the others (Fig. 25a–c). These voids in the starting powder particles may lead to an increased number of porosities in the final PBF part, which is the case for the powders obtained with the first two methods (Fig. 25d and e).

Another study compared powder atomisation methods and found that LPBF parts made using water atomized powder resulted in higher sample porosity than for gas atomized powder. This was thought to be

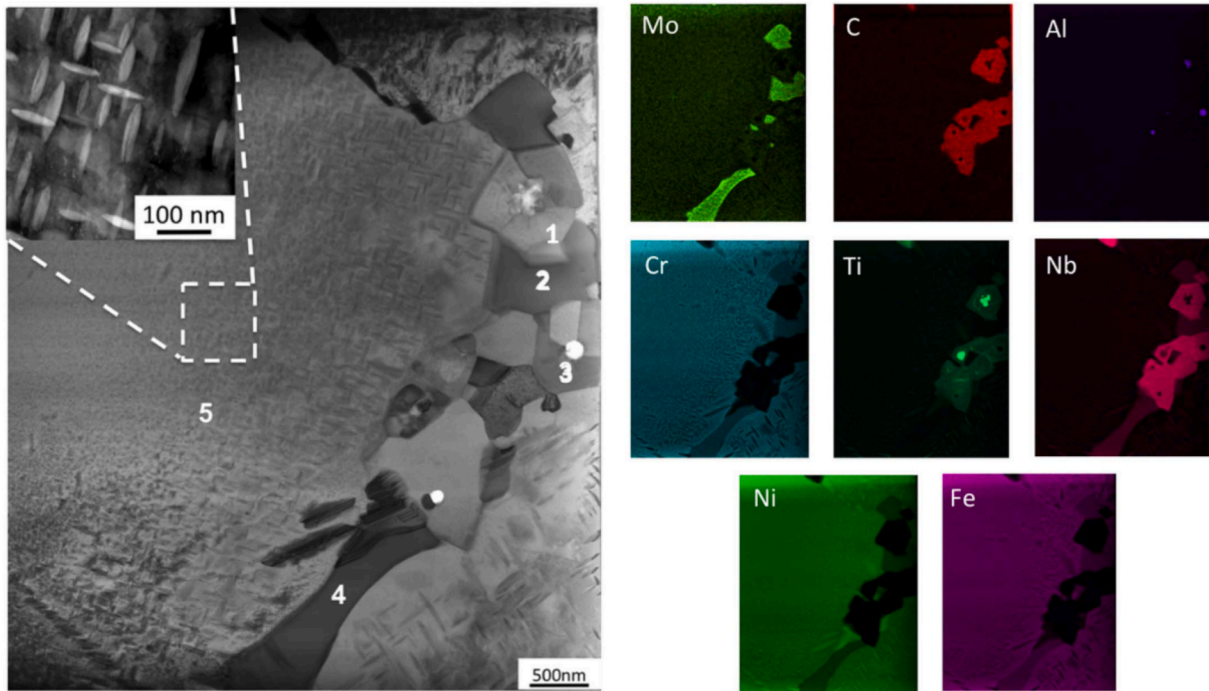


Fig. 21. As-built Electron Beam Melted Inconel 718 microstructure and Electron Diffraction Spectroscopy results (quantified in Table 5) [96]. This shows that Laves phases and MC carbides are present in the as-built state, as well as large disk-shaped γ'' particles.

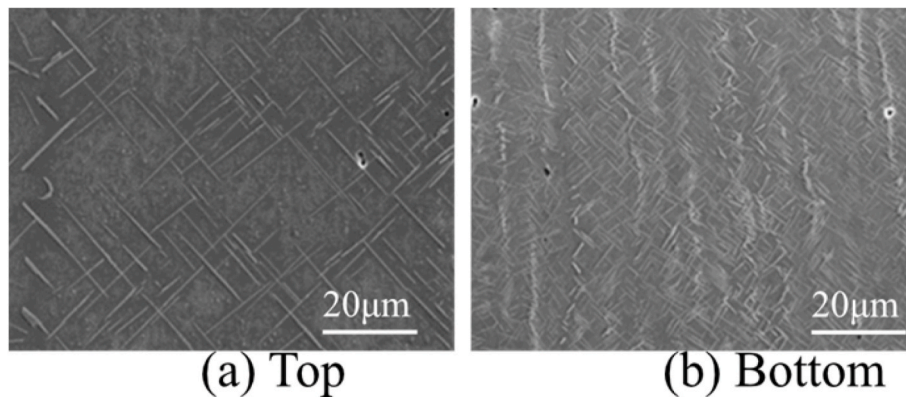


Fig. 22. Scanning electron micrographs of an as-built Electron Beam Melted Inconel 718 sample. (a) The top of the sample (few thermal cycles). (b) The bottom of the sample (many thermal cycles) [97]. This shows a variation in microstructure along the build direction, particularly regarding δ particles which are coarser at the top (a).

caused by the more irregular morphology of water atomized powder and hence better packing density but this observation is far from conclusive [119]. However, there are still limitations to gas atomized powder, such as hollow and/or satellite balls [120]. It was also found that the laser absorption rate can be increased by increasing the surface roughness of powder particles [120].

In terms of particle size, work has found that the presence of powder particles smaller than 10 μm resulted in severe agglomeration and impeded LPBF process through spreading problems [121]. Additionally, a method of rapidly characterising powders (morphology, flowability and size distribution) was developed in order to evaluate the influence of different alloy compositions on LPBF processability [122].

It is clear that many parameters combine to define powder quality, which in turn affects the PBF process and the resulting mechanical properties. Hence, it is essential to understand and control powder quality in order to produce adequate parts. Therefore, the role of the powder is critical in determining both the interaction with the incident

energy beam but also in assuring spread-ability upon the powder bed. Furthermore, the recyclability of powder and its effects on mechanical properties and in-situ alloying [123,124] are emerging topics and should be investigated. There is significant opportunity to explore this space further as in many cases the economic viability of PBF processes is driven by new powder cost but also how easily it may be recycled.

3.2.2. Controlling build environment

A review of the build environment in PBF was written by Poorganji et al. [125]. All PBF build chambers usually operate under vacuum or an inert gas (e.g. Argon or Nitrogen) in order to avoid oxidation of the part and powder. Traore et al. researched the influence of gas atmosphere on nickel-based superalloys [126]. However, despite processing in an Argon atmosphere with <0.2%, oxidation may still occur resulting in oxide inclusions in built parts and oxide spatter particles, which were in the size range to be recycled [127]. Zhao et al. investigated the role of the build environment on melt pool dynamics in EBM and LPBF [128].

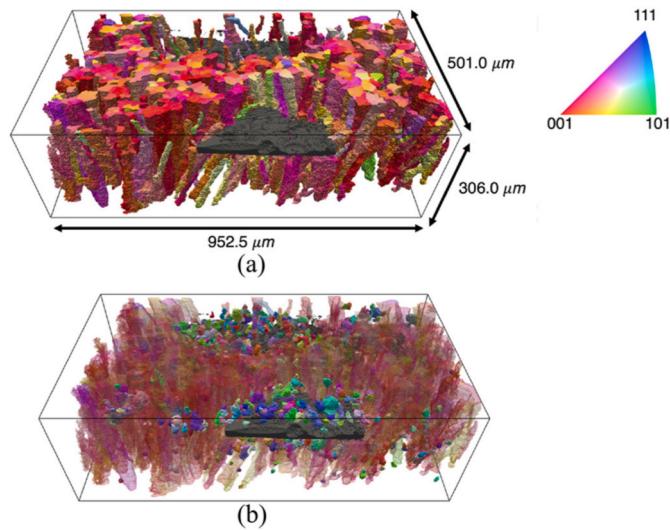


Fig. 23. Electron Backscatter Diffraction data of grains surrounding a defect. (a) The columnar grains surrounding the fusion defect. (b) The equiaxed grains above the defect [99]. This shows that defects also affect the build process and resulting microstructural morphology in Powder Bed Fusion processes.

Table 6

Summary of common microstructural differences between Laser Powder Bed Fused and Electron Beam Melted material. The reader is advised to use this with caution as process technology evolves. This table is intended as a broad guide only and observations will vary between process configurations.

Characteristics	LPBF	EBM
Porosity	Both have similar densities in AB or post-processed conditions (~99.9% with appropriate processing parameters)	
Grain morphology	Elongated grain parallel to the build direction with ill-defined grain boundaries and very fine columnar cellular structures at higher magnifications. Some equiaxed grain formation perpendicular to the build direction which can be recognized at overlapping regions between tracks.	More columnar grain formation than LPBF parallel to the build direction. Perpendicular to the build direction, grains have a more uniform and equiaxed pattern.
Precipitates	Microsegregation of some alloying elements (e.g. Nb, Mo and C) promotes the formation of NbC carbides and Laves phase in the interdendritic region and precipitates on the grain boundaries.	Laves and MC carbides present in AB condition. Disk-shaped γ'' particles, much larger than those found in LPBF, exhibit a directional growth parallel to the build direction. Microstructural variation along the build direction is also present (with δ precipitates much coarser at the top than near the substrate).
Texture	AB samples have a strong $\langle 100 \rangle$ crystallographic texture in the build direction.	Texture in the $\{100\}$ planes along the build direction.

The LPBF build environment, which has the high atmospheric pressure and multiple laser reflections, is the source of more build quality issues, such as vapor recoil pressure on the melt surface, than the EBM build environment. Furthermore, an investigation was conducted on the differences in surface morphology and composition during multicycle EBM with IN718 powder reuse and there was a significant change after exposing the powder to the build chamber environment [129]. Additionally, increased oxidation rates were observed initially for the EBM N06002 alloys in comparison with wrought [130]. A study confirmed

Al_2O_3 particles were formed in IN718 alloys during PBF, which act as nucleation sites for the precipitation of Nb/Ti carbides, leading to the formation of unique core-shell composites with Al_2O_3 in the centre and Ti/Nb at the periphery [131].

Microstructures can also be influenced by controlling the EBM process temperature [132]. At 915 °C, large δ needles were formed (Fig. 26a). By increasing SEM magnification (Fig. 26b) a finer δ -phase (~200 nm) distributed at the grain boundaries, as well as some isolated MC carbides (~1.5 μm), were observed. On the other hand, the microstructure obtained at 990 °C appeared relatively clean. Slightly coarser carbides (~3 μm) as well as fine δ particles were also found at the grain boundaries (Fig. 26c and d).

Overall, this shows that the build environment needs to be adequately controlled to obtain defect-free and desired microstructures.

3.2.3. Energy beam driven phenomenon

Laser parameters, such as the laser power, scan speed, hatch distance and scan strategy, are some of the main factors influencing PBF microstructures. 'Stripe', 'Meander', 'Total fill' and 'Chessboard' (also known as 'Island') strategies are some of the main scan strategies used in LPBF currently (Fig. 27). Different and customised strategies, including multi-laser [133], residual heat factor [134] and 'unit-cell' strategies [135], are also being developed in order to obtain and control microstructural characteristics, such as grain morphology, density, defects, cracking, and surface quality.

In a study on EBM by Helmer et al., the area energy density E [J mm^{-2}] was used as a comparison parameter to evaluate the overall effects of laser power P [W], scan speed v [m s^{-1}] and hatch distance H [μm] on grain morphology [136]. To allow a comparison, the energy density applied to two specimens was similar, respectively 1.8 J mm^{-2} for the first and 1.9 J mm^{-2} for the second specimen [94]. As expected, different values of scan speed and hatch distance produced two clearly distinct grain morphologies, as shown in Fig. 28. Additionally, in another study by Karimi et al., it was found that the electron beam focus offset also directly affected the grain morphology [137]. Fernandez-Zelaia et al. also showed that the morphology and texture of the mesoscale can be controlled by the melting sequence [138]. Similar results were found for LPBF processes [139]. Indeed, in a LPBF study, using a flat top laser beam changed grain morphology to a wide and planar geometry with a 150% increase in grain size, compared to 200 W Gaussian beam [140]. Sow et al. also compared a 80 μm diameter Gaussian laser spot and a 500 μm diameter top-hat laser beam and found that the 500 μm diameter top-hat laser beam increased productivity, suppressed spatter and produced fully dense IN625 parts [141].

Fig. 29 compared the features of two LPBF IN718 specimens, produced with different laser power (250 W and 950 W) [67]. The shape and size of melt pools can be easily recognized in the OM, highlighting a clear influence of the laser power. Indeed, lower power generates smaller melt pools and results in a reduced HT of underlying layers. This, combined with a consequent faster solidification, leads to smaller grains. For LPBF IN738LC, using higher laser power increased the depth of keyholes, causing instability and increasing pore formation due to the periodic collapse of the keyholes [142]. Furthermore, laser volume energy density was found to be the main parameter affecting cracking and porosity. For example, increasing the laser volume energy density resulted in an increase in number and size of cracks in the SRR99 nickel-based superalloy [143] and minimal solidification cracking was observed in IN738LC with narrow melt pools with a strong melt pool overlap [143]. In LPBF René 104 superalloy was built with 3 different strategies (meander, stripe, chessboard) and these were found to have a significant effect on cracking and relative density [142]. The scan strategies with more partitions were shown to increase the emergence of cracks while the overlapping zone increased the size, number and frequency of cracks [142]. Likewise, residual stresses were shown to be caused by scan-strategy induced microstructure [144] and it was found that a more uniform scan strategy resulted in less residual stresses

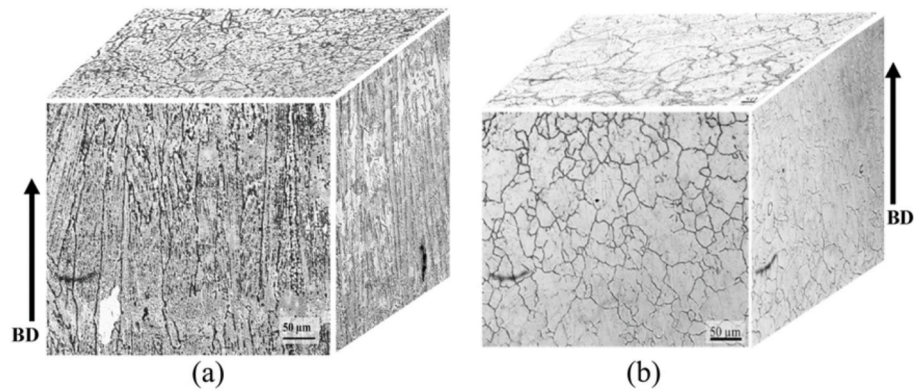


Fig. 24. Microstructural cubes of hot isostatically pressed Inconel 625. (a) Processed by Electron Beam Melting. (b) Laser Powder Bed Fusion. Showing the differences in microstructure produced by the different processes [100], such as grain morphology and size.

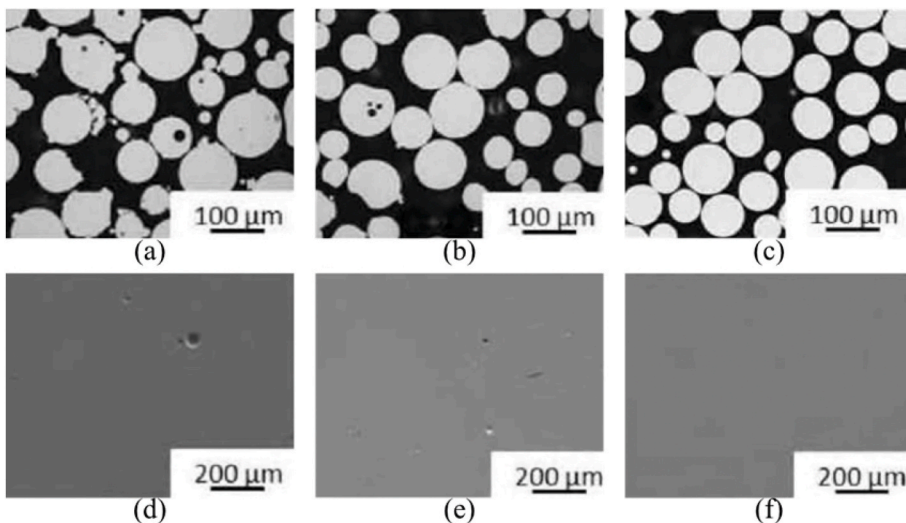


Fig. 25. Powders and corresponding laser powder bed fused specimens [118]. (a) Gas atomized powder at 100 μm scale. (b) Rotary atomized powder at 100 μm scale. (c) Plasma rotated electrode processed powder at 100 μm scale. (d) Gas atomized powder at 200 μm scale. (e) Rotary atomized powder at 200 μm scale. (f) Plasma rotated electrode processed powder at 200 μm scale. From the Scanning Electron Microscopy observations, plasma rotated electrode processed powder showed a smoother surface and almost no internal trapped gas, compared to the others, illustrating the importance and effect of powder types on the resulting microstructure of powder bed fused materials.

[145]. Lee et al. studied the formation of cracks in EBM Mar-M247 parts and concluded that cracks usually form along interdendritic grain boundary at the end of solidification, due to the coexistence of liquid films and residual thermal stresses [102]. Peng et al. demonstrated that EBM induced cracks in DZ125 superalloy, classified as “liquid-state cracks”, were also widely spread at interdendritic grain boundary [103]. Similar conclusions about crack formation mechanisms were drawn. It is clear from the above that the formation of cracks, or hot cracking, is an issue in PBF, but with appropriate processing parameters, these can be reduced or eliminated. Chauvet et al. studied the formation of cracks in EBM of non-weldable nickel-based superalloys and found a correlation between hot cracks and high angle grain boundaries [146]. He also found that the presence of a liquid film during the last stage of solidification and thermal stresses trigger hot cracking [146]. Marchese et al. also confirmed that high thermal residual stresses resulted in hot cracks during LPBF of Hastelloy X [147].

Part density is also influenced by the laser parameters. Indeed, a study found that the relationship between density and laser input energy during LPBF of GH3536 was found to comply with a quadratic function and presented an inverted U-shaped distribution [145]. Furthermore, results showed that in a given scanning strategy, the density decreased as the scanning speed increased for a fixed fluence [148].

Insufficient laser overlap (large hatch spacing) can deteriorate the surface of materials [149]. Indeed, the laser energy input improved density and surface quality of Ni-Cr-B-Si, with a fine grain microstructure and strengthening precipitates [150]. Attard et al. investigated

these effects and produced a controlled functionally graded microstructure by varying the process parameters [151].

Finally, it is clear that the combination of scan strategies, laser power and other process parameters affect the microstructure and final mechanical properties of PBF components. In order to optimise PBF process parameters, some researchers are using the Taguchi regression method [152,153] and Artificial Neural Networks [154].

3.3. Post-processing for component performance

Given the microstructural anisotropy and the defects generated during manufacturing, post-processing is necessary to improve the properties of most AB LPBF components. Post-processing, which includes heat treatments, surface treatments and machining processes, is a prime method to create more favourable microstructures. The purpose of post-processing is to enhance both the form and integrity of the bulk and surface of a component to elevate performance characteristics. While the intent in all AM processes is to create a component within a single step, it is inevitable that, where shortfalls are apparent, additional measures must be taken. This is not entirely inconsistent with established manufacturing routes. For example, it is a pedestrian activity in modern manufacturing to machine a casting. However, in the case of AM where subsequent processing is required the business and design case for this technology will be undermined. Hence, while often currently essential, the research community must endeavour to achieve geometrical tolerance and material condition in process. Lim et al. wrote a

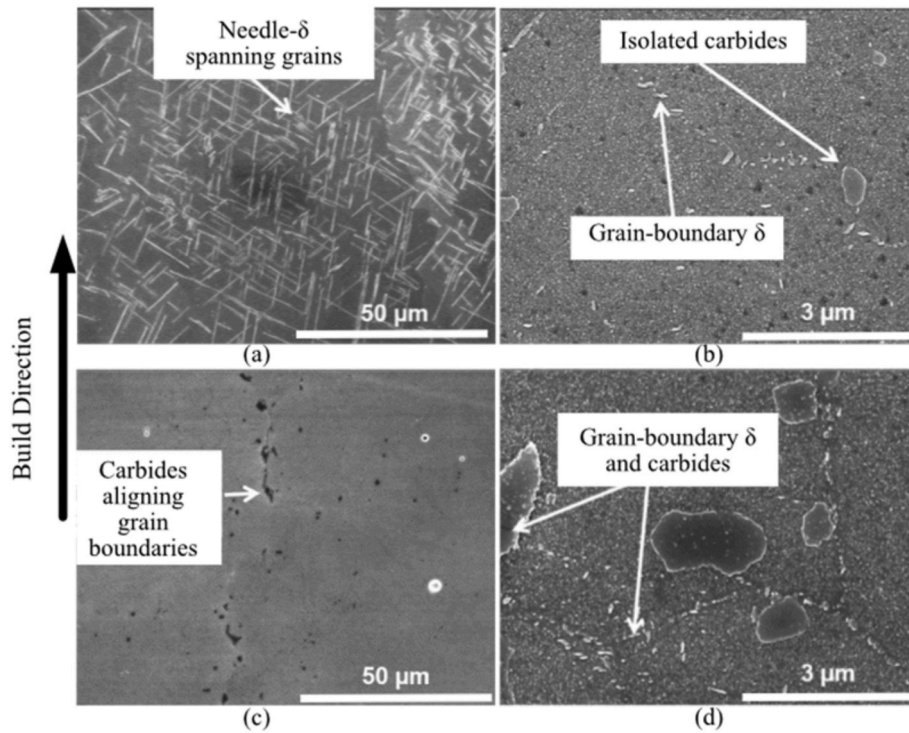


Fig. 26. Scanning Electron micrographs of Electron Beam Melted Inconel 718 built with different base plate temperatures [132]. (a), (b) 915 °C. (c), (d) 990 °C. This shows the influence of process temperature on the precipitation of secondary phases.

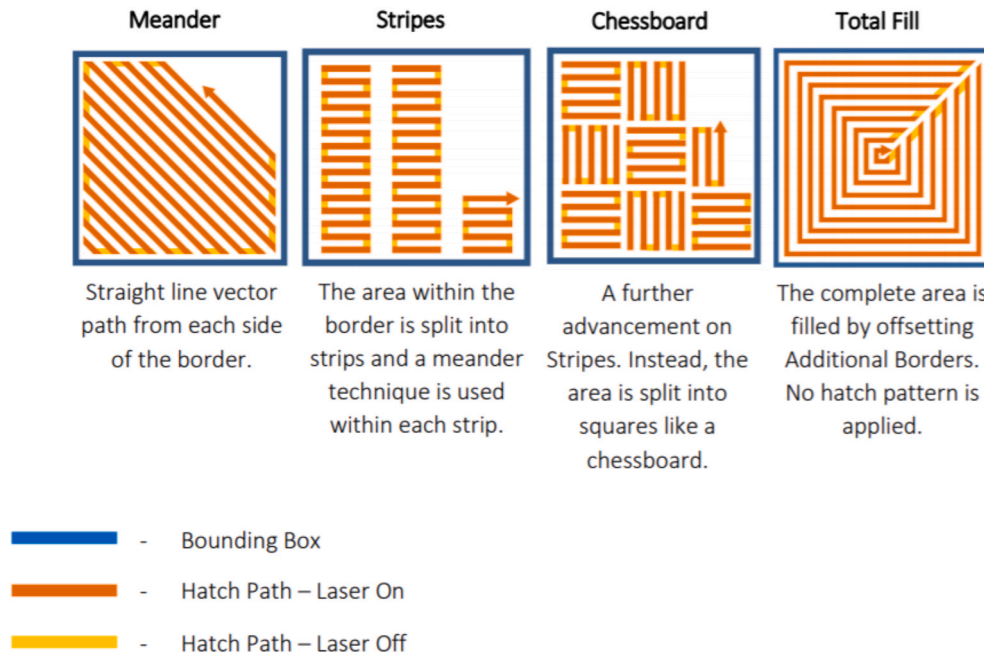


Fig. 27. Typical scan strategies as demonstrated in the Renishaw ‘QuantAM’ material editor. These result in markedly different microstructures and mechanical properties.

review on reducing residual stress in metal PBF parts [155] which informs us that while stresses may be substantially reduced by process optimisation they cannot be removed entirely within the PBF process itself.

3.3.1. Heat treatments for enhancing mechanical properties

In industry, almost all functional AM parts in mission critical applications are post-processed using HT. HT allows the modification of the

microstructure through controlled heating and cooling of materials. By modifying the microstructure, materials can obtain enhanced mechanical properties. Indeed, performance of AM material is poor because of surface integrity defects and unfavourable microstructural formation [156] with secondary phases such as Laves phases that embrittle grain boundaries and are detrimental for mechanical properties [95]. Hence, HTs are used to increase grain size [157], obtain a more equiaxed microstructure, dissolve detrimental phases, such as Laves [158], to form

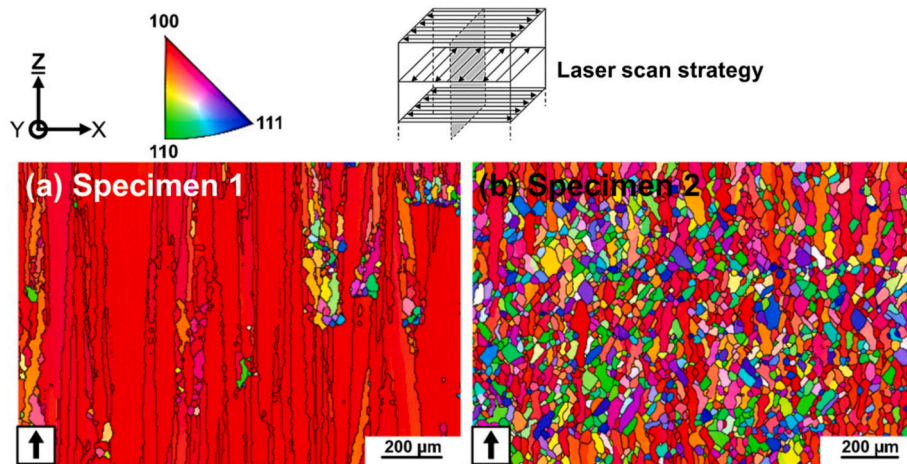


Fig. 28. Electron Backscatter Diffraction maps of Electron Beam Melted specimens manufactured with different parameters. (a) Parameters: $E_1 = 1.8 \text{ Jmm}^{-2}$, $v = 2.2 \text{ ms}^{-1}$, $H = 150 \text{ } \mu\text{m}$. (b) Parameters: $E_2 = 1.9 \text{ Jmm}^{-2}$, $v = 8.8 \text{ ms}^{-1}$, $H = 37.5 \text{ } \mu\text{m}$ [136]. This illustrates that varying process parameters can result in drastically different microstructures and textures.

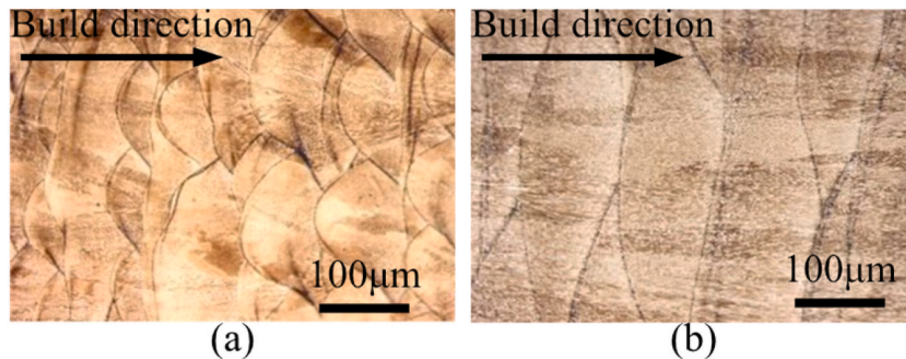


Fig. 29. Optical micrographs of etched Laser Powder Bed Fused Inconel 718 specimens manufactured with varying laser power [67]. (a) Power = 250 W. (b) Power = 950 W. The melt pools across layers can be clearly observed and show that a difference in laser power can significantly affect the melt pool shape.

strengthening precipitates such as δ -phase, γ' and γ'' [156,159], and to remove defects [160] to improve mechanical properties. Although sometimes AB microstructure is more beneficial for certain properties, like in the case of Parizia et al. who found that AB IN625 presented better oxidation resistance than its HT counterpart [161]. There are different types of HT, each giving different microstructures. Usually, samples are first stress relieved, which reduces texture and residual stress in samples [162]. Then, solution treatment (ST) is used to enhance the mechanical properties [163] by dissolving detrimental phases [164, 165]. Subsequently, samples are sometimes aged (single or double ageing) to favour the precipitation of strengthening phases [158]. Samples can be Solution treated then Aged (STA) or Directly Aged (DA). Thermal techniques, such as homogenisation and HIP treatments are also used. Homogenisation is usually used prior to HIP and is similar to stress relief as it reorients columnar grains [157]. Zhao et al. observed that during homogenisation of LPBF IN718, the grains would continue recrystallisation whereas the suction-cast alloy showed abnormal grain growth, which showed the potential of engineering the microstructure of AM materials through HTs to obtain superior mechanical properties than in conventionally manufactured alloys [166]. HIP results in recrystallisation, grain coarsening and change from highly textured columnar grains to randomly oriented equiaxed grains which are larger than after homogenisation [64,157,167,168]. Moreover, a slightly weaker texture is obtained, compared to STA [168], although it is still strong [167]. HIP was also found to be effective at closing defects, resulting in a higher density [169].

Different HT standards exist for conventionally manufactured

material, however, as no PBF-specific HT standards have been defined at this time, significant research has gone into exploring the effects of wrought HT and modified HT on PBF microstructure.

The Standard Specification for Additive Manufacturing Nickel Alloy (UNS N07718) with Powder Bed Fusion [170] gives guidelines for thermal processing of PBF nickel-based superalloys. For HIPing, components should be processed in an inert atmosphere at no less than 100 MPa, within the range of 1120 °C and 1185 °C within $\pm 15 \text{ } ^\circ\text{C}$, and held for 240 min $\pm 60 \text{ min}$ followed by cooling under and inert atmosphere below 425 °C [170]. For HT, it states that components should be solution treated and aged following the AMS2774 standard for Heat Treatment of wrought nickel alloy and cobalt alloy parts [171]. This standard gives the range of possible heat treatments to use for different geometries of nickel-based superalloys. It should be noted that none of these HT are specific for AM, but rather are for conventional manufacturing processes. This highlights the need for the development of PBF specific microstructures. Some practitioners, such as Huang et al. and Aydinöz et al., have started to research this area [163,172]. For example, Huang et al. investigated the effect of solution time, solution temperature, cooling method and ageing process on the mechanical properties of LPBF IN718 and identified that there was a minimum solution time for a given temperature to obtain similar microstructures and mechanical properties (Fig. 30).

3.3.1.1. Grain structure. Although grain boundaries normally occupy a small fraction of material volume, they play a crucial role in controlling material properties. The sensitivity associated with this behaviour drives

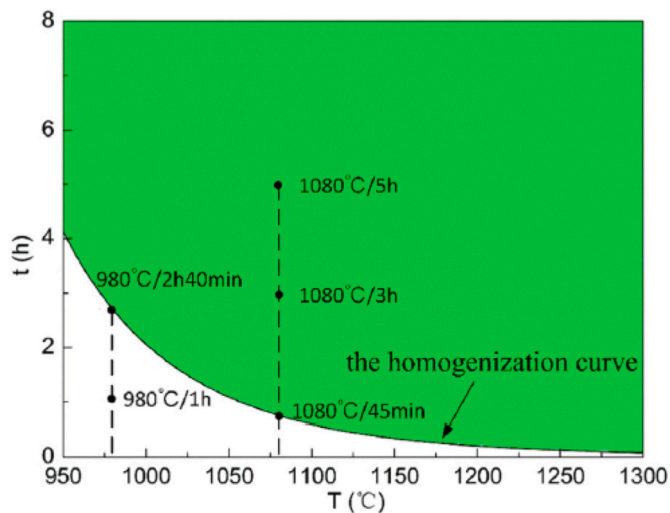


Fig. 30. Variation of required solution time for solution temperature for Laser Powder Bed Fused Inconel 718 [163]. This shows that there is a minimum solution time for a given solution temperature which results in similar microstructures and properties. This further highlights the requirement for the development of Powder Bed Fusion specific heat treatments as the standard heat treatments designed for conventionally manufactured materials are unsuitable.

significant efforts in optimising processes. Fig. 31a and b compare the microstructures of an HT and HIP + HT LPBF IN718 specimens [173]. Obvious evidence of the scan strategy used is eliminated in both cases [173]. From the measurements, it was found that the average grain size for HT specimens was $15.5 \pm 2.0 \mu\text{m}$, namely 30% smaller than HIP + HT equivalents.

Holland et al. investigated the evolution of the grain boundary network in AB and HT LPBF IN718 specimens [174]. It was observed that non-specific grain boundaries dominated in the AB specimens, whereas after HT the number of special grain boundaries increased significantly from 9% to around 60%. This second class of grain boundaries includes twin boundaries and twin-related grain boundaries, able to improve material strength and resistance to intergranular degradation. Another study on LPBF IN625 provided similar results [175]. It was also found that above a certain annealing temperature (1150°C), these grain boundaries developed in prevalence significantly.

“Grain boundary misorientation” is defined as the difference in crystallographic orientations between adjacent grains of the same phase. This microstructural feature can be characterised through EBSD. Gribbin et al. evaluated the misorientation angle (Fig. 32) in some HT and HIP + HT LPBF IN718 specimens [176]. The distribution of the misorientation angles for HT specimens was broad, indicating no preferential growth direction. On the other hand, for HIP + HT specimens, the distribution showed a prominent peak at 60° , indicating an equiaxed grain structure with a high twin content caused by annealing. The detrimental effect on fatigue performance previously observed by Zhang et al. correlates well with the misorientation effect [177].

In a further study by Chauvet et al., it was found that grain boundaries with a high misorientation angle were prone to crack propagation in AB and HT EBM samples (Fig. 33) [146]. Han et al. obtained similar results in this regard [178]. Research also concluded that the difference in interdendritic liquid pressure between the dendrite tip and root, as illustrated in Fig. 34, would cause an insufficient feeding of molten material at the dendrite root, promoting void generation and therefore highly affecting the part hot cracking behaviour.

Tomus et al. compared the grain morphology of LPBF Hastelloy X specimens processed with various post-processing techniques [179]. The HT consisted in a single solution step ($1175^\circ\text{C}/2\text{h}$), while HIP was performed using the same time and temperature, with an applied stress

of 150 MPa. Fig. 35a,c,e,g display a series of EBSD images illustrating the grain morphology in the XZ plane for AB, HT, HIP and HIP + HT specimens, respectively. HT and HIP effectively reduced the strong texture in the build direction in the AB specimen [180]. Another study found that HIP of LPBF Hastelloy X ‘closed’ internal cracks, reduced porosity and generated equiaxed grains [181]. This was also observed in CMSX-4 [77]. Fig. 35b,d,f,h illustrates the grain morphology perpendicular to the build direction (XY plane). HIP specimens showed a smaller grain size, because of recrystallisation. Similarly to previous results, individual laser scan tracks and small equiaxed grains were also observed in the XY planes [59]. Further studies on post-processing techniques indicated that HIP cannot be considered as an efficient tool to heal EBM induced cracks [182].

3.3.1.2. Precipitate formation. Fig. 31a and b compare the microstructures of an HT and HIP + HT LPBF IN718 specimens and showed that ‘white’ precipitates are clearly visible at grain boundaries [173]. EDS observations (Fig. 31) indicated that these are rich in Mo, Nb, W and Si, with stoichiometric ratios of $(\text{MoNbW})_5\text{Si}_3$ [173]. However, the precipitates in both specimens were similar in size ($\sim 2.5 \mu\text{m}$) [173]. Similarly, Sames et al. investigated the effects of in-situ HT on γ'/γ'' phases in EBM IN718 specimens [183]. The γ'/γ'' phases in the AB specimen showed an elongated disk shape, with a diameter of $\sim 20 \text{ nm}$ and a thickness of $\sim 10 \text{ nm}$ (Fig. 36a). From the micrographs comparison in Fig. 36, both the diameter and thickness of these strengthening particles increased during the in-situ HT. Since strengthening phases have an optimal size range and corresponding mechanical properties, this process was found to be effective in improving material strength [183] by impeding the dislocation movement at the grain boundaries [173].

Furthermore, Divya et al. investigated the HT effects on dislocations and strengthening particles in LPBF CM237LC specimens [184]. In the AB specimens (Fig. 37a), dislocations entangled and tended to accumulate at the grain boundaries. As shown in Fig. 37d, the HT decreased the dislocation network density, especially at the grain centre. These observations are in accordance with results by Tucho et al. [185]. At the same time, the HT significantly increased the size of the γ' phase. In fact, before HT, two distinct types of γ' phase could be observed: one with a size of $\sim 5 \text{ nm}$ (Fig. 37b) and another, much larger, with a size $\sim 50 \text{ nm}$ (Fig. 37c). After the HT (Fig. 37d and e), the primary γ' particles reached a size of over 500 nm , while the secondary γ' particles, characterised by a cuboidal morphology, had a size of $\sim 200\text{--}400 \text{ nm}$. Fine tertiary γ' particles were spread in the region between the secondary γ' particles. The influence on γ' particles size may be the basis of the strengthening mechanisms caused by HT. During a 3-step HT on LPBF Haynes 282, γ' precipitation was found at 950°C during TEM in-situ HT [186]. After HT, the morphology and size of γ' precipitates were comparable to powder metallurgy samples and annealing twins were present [78]. HT was also optimised for LPBF CMSX-4 to obtain segregation of γ/γ' microstructure [52].

Kuo et al. evaluated the effects of different HT strategies on the δ -phase in LPBF IN718 specimens [92]. In the AB specimen, δ -phase was found distributed parallel to the build direction, segregated in the interdendritic region due to the Nb segregation during the build process (Fig. 38a). This was hypothesized to be a consequence of Nb segregation which occurred during the LPBF process. Specimens which underwent a solution treatment and aging (STA) ($980^\circ\text{C}/1\text{h}$ then $718^\circ\text{C}/8\text{h} + 621^\circ\text{C}/10\text{h}$) possessed a much coarser δ -phase than their non-solution-treated equivalents (Fig. 38b and c, respectively). This difference can be related to the dissolution of γ'' phase and the consequent formation of needle-shaped δ -phase during this first thermal treatment. However, these elongated particles are undesirable since they degrade material mechanical properties, causing “ δ -phase embrittlement”.

Stoudt et al. presented a time-temperature-transformation diagram for the δ -phase in LPBF and wrought IN625 specimens [187]. The

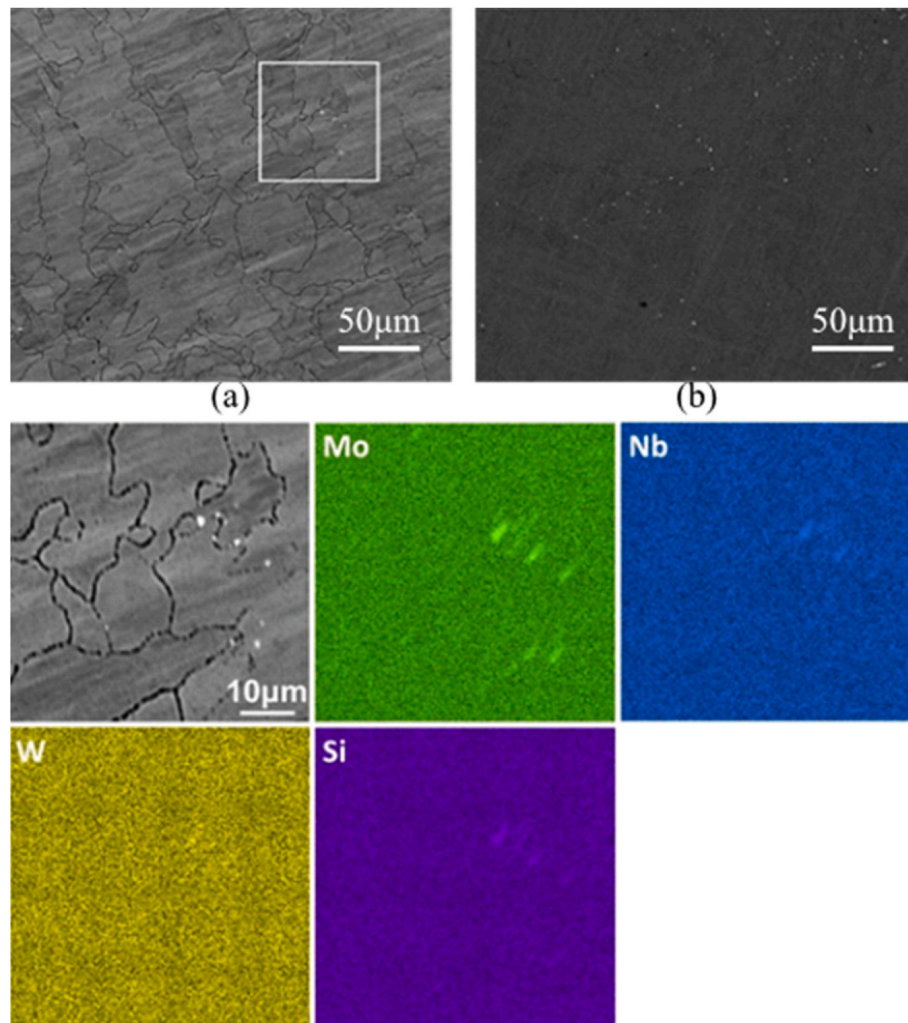


Fig. 31. Microstructure of Laser Powder Bed Fused Inconel 718 specimens with varying thermal treatments [173]. (a) Heat treated sample microstructure with Electron Diffraction Spectroscopy results of the section squared in (a). (b) Hot Isostatically Pressed and heat treated sample. This shows obvious evidence of the elimination of scan strategy effects through thermal treatments.

formation of δ -phase during a LPBF process was found to be much faster than in the conventional wrought process. Moreover, it was observed that the stress-relief HT, normally used in industry for IN625 (870 °C/1h, red dot in Fig. 39), would promote the formation of δ -phase during LPBF and not for wrought equivalents. Zhang et al. also proved that conducting this same HT at 800 °C can lead to the nucleation and growth of δ -phase [188]. The calculated activation energy for the growth of the δ -phase was found to be $(131 \pm 0.69) \text{ kJ mol}^{-1}$. Another study also designed a two-step ST with a two-step aging treatment which facilitated the precipitation of δ phase at the grain boundaries [189]. These results highlight the fact that HT conditions for LPBF processes need to be re-evaluated and distinguished from those used for conventional manufacturing methods.

Laves phases are another common precipitate which is known to be detrimental to the mechanical properties of nickel-based superalloys. Indeed, Laves phases subtract Nb from the two main strengthening phases, namely γ'' and δ . Pröbstle et al. explained that, in agreement with other studies, only the Laves phases were visible on TEM of AB LPBF IN718 (Fig. 40) because of the rapid heating and cooling cycles, which suppressed other secondary phase precipitation [190]. Hence, HT is necessary to dissolve these and create more wrought like microstructures.

TEM micrographs and diffraction patterns for each specimen are shown in Fig. 41. In the solution treated specimen (Fig. 41a), the

associated diffraction pattern (Fig. 41b) indicated that there were no secondary phases. This means that the Laves phases, which are commonly observed in AB specimens (Fig. 40), were fully dissolved during the solution treatment. In the HIP specimen, intense recrystallisation occurred (Fig. 41c and d) due to the high temperature and deformation induced, dissolving all substructures present after build. As for the previous case, no secondary phases were revealed from the diffraction patterns, suggesting a complete dissolution of secondary phases during HIP. As stated, a combination of solution treatment and ageing represents one of the most commonly used HT strategies for IN718. Both TEM micrographs and diffraction patterns for this strategy (Fig. 41e and f) revealed the presence of γ'' particles with a size $\sim 30 \text{ nm}$. Similarly, for HIP + ageing treated specimens, reflections of γ'' phases were observed in the diffraction pattern (Fig. 41i). From the TEM micrographs (Fig. 41g and h), needle-shaped δ particles were individuated at the grain boundaries. These observations were similar to those made by Kuo et al. [92]. However, in this case, the needle-shaped δ precipitates were also found to lower the specimen strength. These results confirmed that the precipitation of δ particles reduced the amount of γ'' present in the surrounding area (Fig. 41h).

Despite the general consensus that Laves phases are detrimental to mechanical properties and need to be dissolved, recent studies have found that the size, morphology and distribution of Laves phases can prove beneficial to the mechanical properties of PBF nickel-based

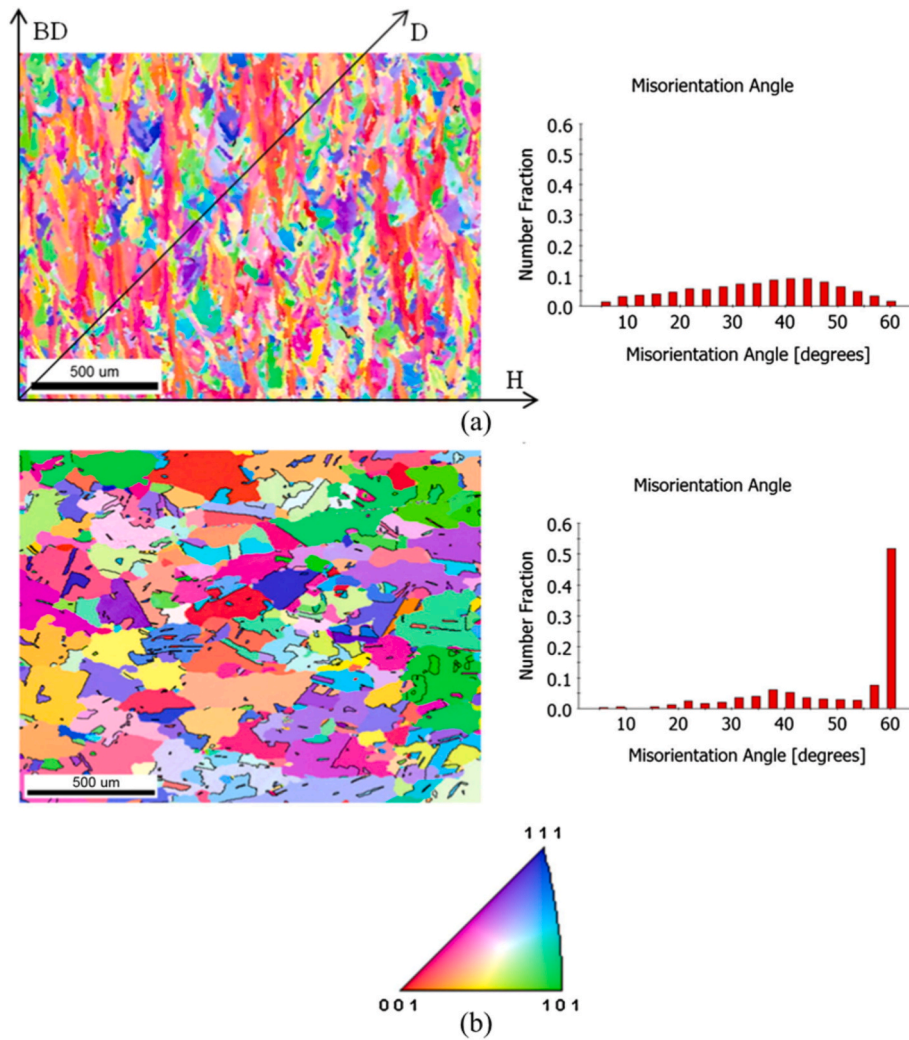


Fig. 32. Electron Backscatter Diffraction maps of Laser Powder Bed Fused Inconel 718 specimens showing grain morphology and misorientation angle distributions [176]. (a) Heat-treated sample. (b) Hot Isostatically Pressed and heat treated sample. The broad distribution in the heat treated sample indicates no preferred growth direction as compared to the Hot Isostatically Pressed and heat treated sample.

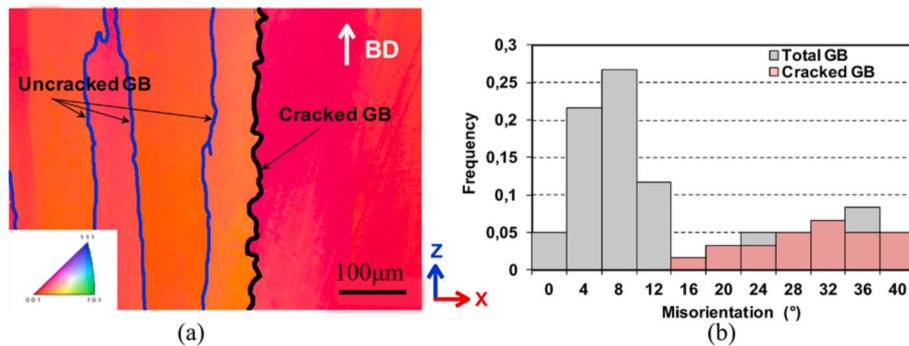


Fig. 33. This figure demonstrates that grain boundaries with a high misorientation angle are prone to crack propagation in as-built and heat treated Electron Beam Melted samples [146]. (a) An Electron Backscatter Diffraction map showing the cracked grain boundary along the high angle grain boundary (misorientation > 15°). (b) The distribution of grain boundary misorientation and cracked grain boundaries.

superalloys [191–193]. For example, Sui et al. managed to dissolve the sharp corners and grooves of the Laves phase through HT, causing it to change from a long-stripped to a granular shape [191]. They then found in another study that the granular Laves phases were more beneficial to the plastic deformation of PBF IN718 than long-stripped Laves phases and that a certain amount of Laves phase was the best match between

strength and ductility of the sample [192]. Similarly, Xiao et al. found that fine discrete Laves phase improved the tensile properties of LPBF IN718, even outperforming wrought IN718, and had good elongation, whereas long-chain-like Laves phase had a more brittle nature and suboptimal properties [193].

Overall, an optimised HT can control the size, shape and distribution

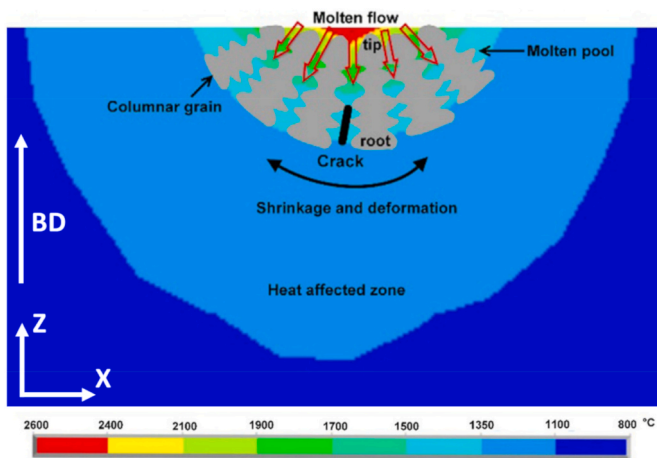


Fig. 34. Illustration of the hot cracking mechanism in the Laser Powder Bed Fusion process [178], demonstrating crack formation and growth within a single melt pool. This shows that the difference in interdendritic liquid pressure between the dendrite tip and the root causes an insufficient feeding of molten material at the dendrite root, promoting void generation and therefore highly affecting the hot cracking behaviour of the part.

of precipitates to cater to mechanical properties desired. More work should be undertaken to explore this aspect.

3.3.1.3. Residual stress. Tucho et al. demonstrated that thermal cycling during the building process induced residual stresses in the material (a common observation in energy beam processes), producing plastic deformation and dislocation networks (Fig. 42a) [185]. However, since these are caused by internal stresses, the dislocation networks can be removed using an appropriate HT, as shown in Fig. 42b.

Overall, with the appropriate HT, it is possible to obtain a microstructure which resembles that of a cast nickel-based superalloy, as was the case for LPBF high-strength alloy VZHL21 after progressive stages of post-treatment [194] and Hastelloy X after solution annealing [181]. However, a combination of ductility dip cracking and strain age cracking mechanisms were identified as the primary causes of cracking in LPBF CM247LC following post-build thermal treatments [195]. This shows that HT still requires optimisation in order to obtain a defect free LPBF material.

3.3.2. PBF surface integrity following machining

Machining is often required to obtain the desired geometry following PBF. AM components present new machining challenges given material inhomogeneity and intricate geometries. Given the implicit part-to-part variation traditional datum acquisition challenges associated with casting are apparent. However, given the limitations of current class PBF systems it is likely that additional value add to AM components will be derived by machining processes.

Machining processes affect materials' microstructure, surface quality and induce residual stress. As stated previously, PBF materials have different microstructures, surface roughness and residual stresses than conventionally cast or wrought nickel-based superalloys. A review on the machinability of conventionally manufactured nickel-based superalloys was conducted by Ezugwu et al. and discusses the issues with the machining of nickel-based alloys and the cause of tool wear and failure [196]. Hence, the effects of machining will be different and it is important to understand their impact in order to control part quality. A study compared the effect of different post-processing techniques - namely barrel finishing, ultrasonic shot peening, ultrasonic impact treatment and shot peening - and their effects on surface roughness, hardness and residual porosity [197]. Ultrasonic impact treatment had the best reduction in surface roughness (by 57.4%) and in residual porosity (by 84%), while shot peening improved hardness the most (by

66.5%) [197]. Shot peening also refined subsurface grains in EBM IN718 and improved surface texture and oxidation performance [198]. A different study also showed that shot peening and ultrasonic impact treatment improved the surface texture parameters and residual stresses of HIP LPBF IN718 [199]. Further, Kuner et al. also found that polishing an AB EBM Hastelloy resulted in slower oxidation kinetics compared to the non-polished sample [200] and Karthick et al. observed a superior surface finish, reduced porosity and improved compressive residual stress in samples that were post-processed using grinding followed by low plasticity burnishing compared to other samples [201].

Furthermore, the use of electropolishing surface treatment with anhydrous electrolyte solution was studied to improve the surface quality of LPBF IN718 [202]. The results clearly indicated the potential benefit of introducing highly regulated electrolyte flow in the polishing of AM metal parts [202]. The effect of LPBF Hastelloy X microstructure on Electromechanical dissolution characteristics was also studied and showed that compared to wrought, LPBF finer grains, denser sub-grain boundaries and dislocations contributed to the formation of a more stable and thicker passivation film [203].

Studies have shown that the PBF microstructure of nickel-based superalloys has implications for the machining process as well. For example, there are peculiar interactions between build orientation and machining strategy [204]. It has been shown that the surface topography and integrity of LPBF IN625 was affected by the relative orientation of cutting direction to the build direction and scan strategy orientation [205]. Indeed, Patel et al. showed that machining with the feed in the build direction generated the greatest cutting force (as shown in Fig. 43) of the orientations tested [205]. Similarly, another study found that feeding the cutter against the build direction resulted in lower peak forces with larger deviations while feeding along the build direction resulted in higher peak forces with lower deviations [206]. Further, LPBF IN718 with HIP and HT were found to have better minimum specific cutting energy, minimum tool wear and minimum surface roughness during milling than wrought IN718 [207]. The peak milling cutting force was found to be dependent upon the feed direction as well as the layer-wise scan rotation employed in fabricating LPBF IN625 [206]. Hence, these studies reveal that, in a similar theme as "Design for Manufacture", the need to select PBF build parameters for post-processing needs to be considered [204].

No studies on the effect of EBM microstructure on machining parameters and vice versa were reported to date. Hence, this area should be developed further. Another development area is the use of hybrid machines which build and machine the part during the same process [208,209]. For example, using a new hybrid method which combines LPBF and Laser Shock Peening, a 95% decrease in CM247LC cracks was obtained [102]. Hence, more research should be conducted on hybrid machines as they have the potential to further control the microstructure and mechanical properties of PBF materials.

3.4. Modelling of nickel-based superalloys in PBF

Numerical modelling is a useful tool to understand the fundamental mechanisms and predict the possible outcomes of PBF processes. A review on the research progress of LPBF nickel-based superalloys simulation was conducted by Qiu et al. [210]. Other reviews investigate multi-scale modelling for PBF [211], the classification of AM modelling [212], microstructure modelling of metal AM materials [213], multi-physics continuum modelling approaches for metal powder [214, 215], have also been presented. Some typical models used in modelling AM microstructure include: thermal modelling, phase field modelling, kinematic modelling and cellular automata. These models can be used individually or coupled with other models to model PBF process and microstructure.

Thermal models can determine the temperature in the material during AM processes and calculate fluid flow and porosity. These models are some of the most used in AM modelling. Zhang et al. simulated the

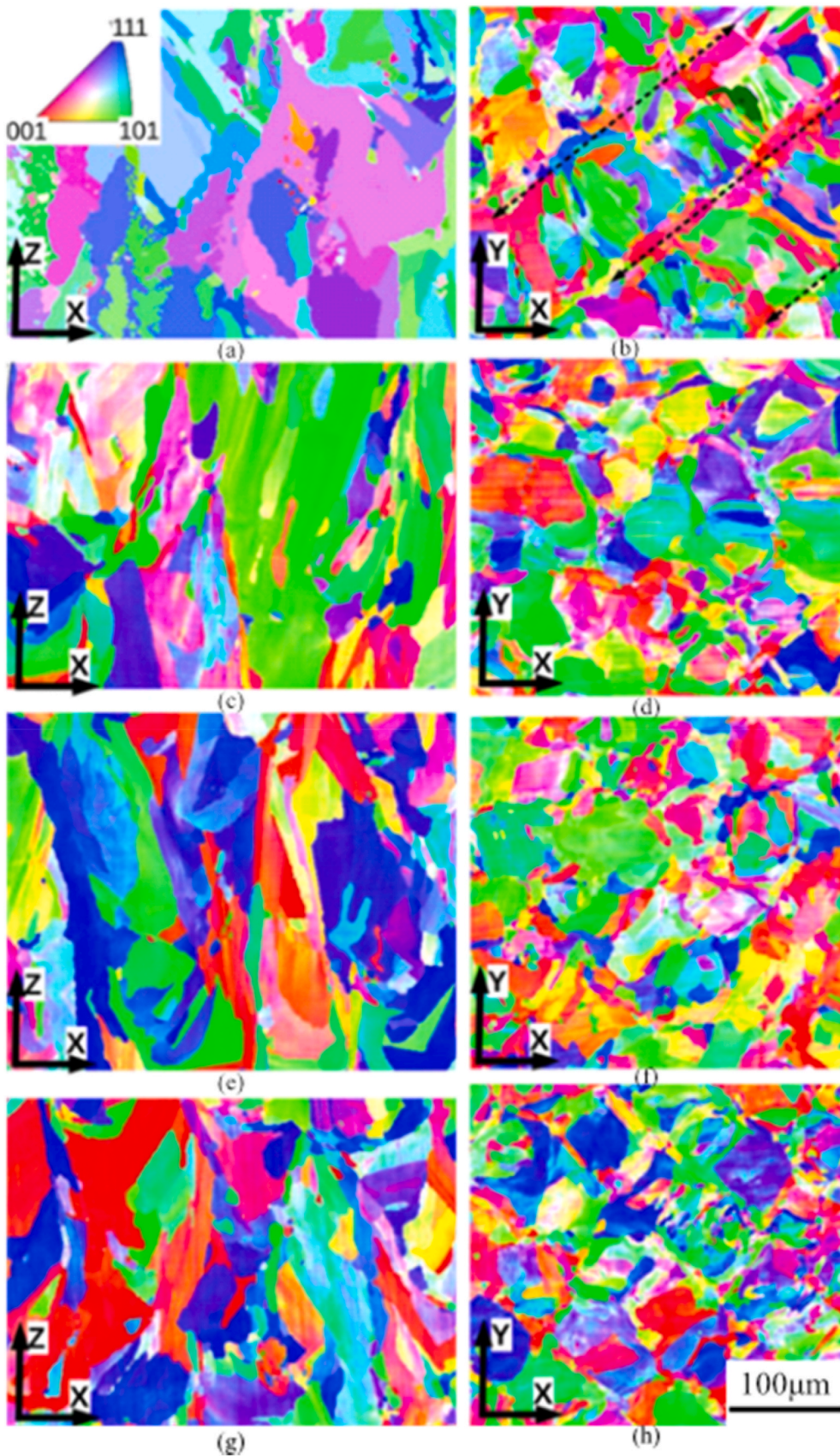


Fig. 35. Grain morphology of planes parallel (XZ) and perpendicular (XY) to the build direction with varying thermal treatments [179]. (a) As-built specimen parallel to the build direction. (b) As-built specimen perpendicular to the build direction. (c) Heat treated specimen parallel to the build direction. (d) Heat treated specimen perpendicular to the build direction. (e) Hot Isostatically Pressed specimen parallel to the build direction. (f) Hot Isostatically Pressed specimen perpendicular to the build direction. (g) Hot Isostatically Pressed and heat treated specimen parallel to the build direction. (h) Hot Isostatically Pressed and heat treated specimen perpendicular to the build direction. Heat treatment and Hot isostatic pressing effectively reduced the strong texture in the build direction in as-built specimens.

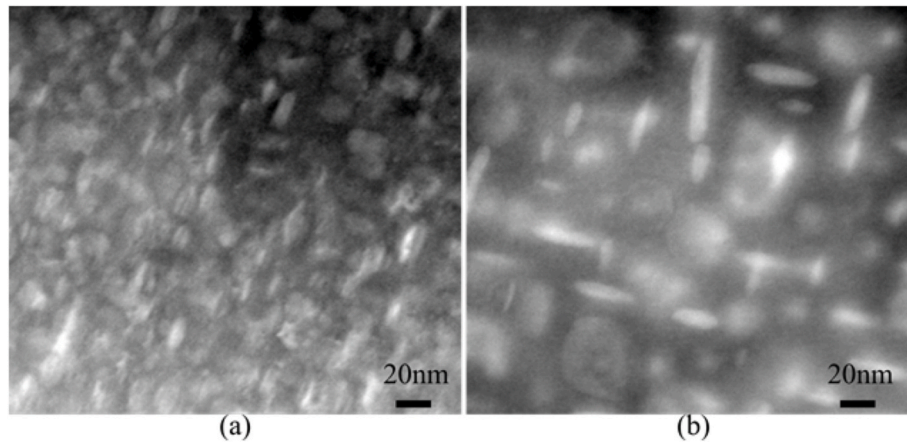


Fig. 36. Transmission Electron Microscopy visualisation of γ'' precipitates in Electron Beam Melted Inconel 718 specimens [183]. (a) As-built samples (low cooling rate). (b) In-situ heat treated samples. This illustrates the effect of heat treatment on the size of strengthening precipitates, γ'' in this case.

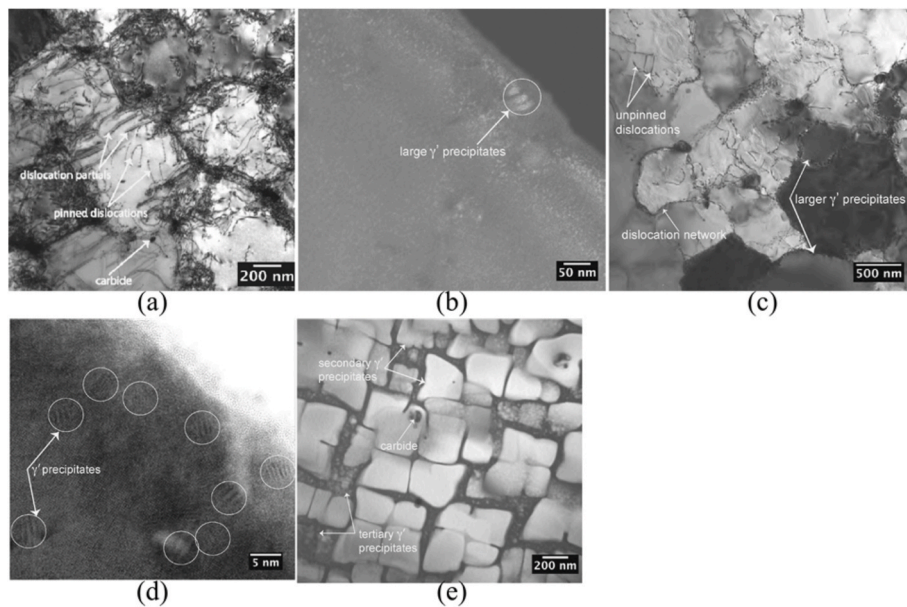


Fig. 37. Dislocations and γ' phases in Laser Powder Bed Fused CM247LC specimens [184]. (a), (b), (c) As-built. (d), (e) Heat treated This shows that dislocations are entangled and tend to accumulate at the grain boundaries. Heat treatment also decreases the dislocation network density, especially at the grain centre.

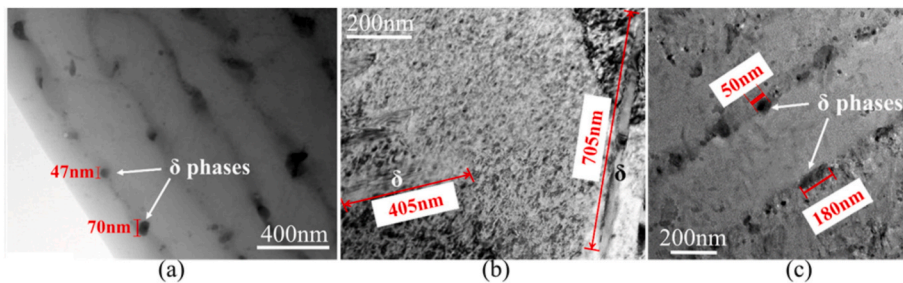


Fig. 38. δ -phases in the interdendritic region of Laser Powder Bed Fused Inconel 718 specimens [92]. (a) As-Built with Nb segregation during the Laser Powder Bed Fusion process. (b) Solution + ageing treated. (c) Direct aged. The solution treated and aged specimen contained much coarser δ -phase than their non-solution-treated equivalents due to the dissolution of γ'' phase and the consequent formation of needle-shaped δ -phase during this first thermal treatment. This shows that thermal treatments affect the presence, size and morphology of precipitates in Powder Bed Fused materials.

temperature gradient and the cooling rate at the edge of the melt pool for LPBF IN718 using COMSOL Multiphysics™ 5.0 software [216]. A similar study was conducted by Kirka et al., simulating the thermal profile of a laser track on solidified materials [96]. The results showed that up to five layers underneath can be remelted when a new layer is processed. This can be observed from the dendritic structure refinement found in the last remelted region and its homogenisation in the heat

affected zone. Xia et al. also investigated the melt pool temperature contour in the manufacturing process of IN718+WC with LPBF [65]. This helped to explain the formation mechanism of Ni_2W_4C primary dendrite and (Nb, M)C carbides. Temporal evolution of the temperature distribution for the single bead experiments was simulated for EBM IN718 using FEA with thermal conduction and recoalescence taken into account [217]. Contrary to the experimental observations, the

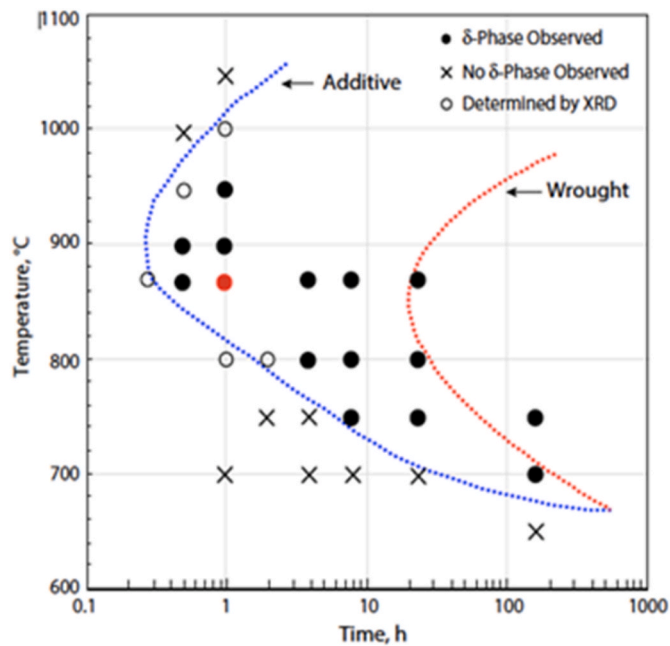


Fig. 39. A time-temperature-transformation diagram for the formation of δ -phase in Laser Powder Bed Fused and wrought Inconel 625 components. The red dot indicates the industry recommended stress-relief Heat Treatment conditions [187]. This shows that the formation of δ -phase is much faster during Laser Powder Bed Fusion than for the wrought process. The stress relief heat treatment (red dot) was shown to promote the formation of δ -phase during Laser powder bed fusion but not for wrought equivalents. (For interpretation of the references to colour in this figure legend, the reader is referred to the Web version of this article.)

constructed microstructure consisted mostly of equiaxed and mixed grains [217].

Phase field modelling can model both solid and liquid material phases in the same model and is used to observe microstructure evolution (e.g. grain coarsening and dendrite growth). Pinomaa et al. used this method to simulate the kinetics of solidification, including the development of microstructural features including grain morphology, solute distribution, and formation of metastable phases – was able to accurately model temperature distribution, history, thermal gradients and cooling rates of a LPBF nickel-based superalloy [218].

Transport phenomena models are also used to study solidification, residual stresses, distortion, defect formation and the evolution of microstructure and properties of AM alloys, as reviewed by Wei et al.

[219]. Huynh et al. [220] simulated the stress distribution in novel test pieces to prove desired results could be achieved with customized geometries.

These different models can also be used to understand and predict the effect of PBF process parameters on the material microstructure or mechanical properties. For example, Raghavan et al. aimed to create a simulation to predict the effects of various EBM processing parameters on some IN718 specimens microstructure [221]. As expected, both the thermal gradient and solid-liquid interface velocity, generated during melt pool solidification, influenced the final grain morphology (Fig. 44). The same process was then simulated varying some process parameters, such as preheat temperature, spot ON time, beam diameter and spot beam current (Fig. 45), analysing their impact on the morphology produced.

Other studies use models to determine the PBF manufacturability of certain nickel-based superalloys, like Yang et al., who determined the feasibility of manufacturing by LPBF of nickel-based SX-superalloys by calculating the solidification conditions (temperature field, thermal gradient and solidification speed) of multi-track samples using an established finite element model based on the columnar to equiaxed transition [222].

Using models to optimise PBF parameters is also being researched. A universal and simplified model has been proposed to predict the energy density suitable for LPBF of a variety of metallic materials including nickel-based superalloy, using the relationship between energy absorption and consumption during LPBF [223]. Results confirmed that the model can predict suitable laser energy densities needed for processing materials without tedious trial and error experiments [223]. A full process energy prediction diagram for LPBF GH3536 alloy, based on the simulated molten pool depth and width, is also proposed as a method for the selecting process parameters [224]. Yan et al. also showed that using data-driven multi-scale and multi-physics models can be used to derive process-structure-property relationships for AM and optimise process parameter [225].

Finally, other researchers concentrate their efforts on the simulation of other aspects of the PBF process: powder bed melting [226–234], melt pool fluid dynamics [235,236], phase transitions [237] and microscale thermodynamic and kinetic mechanisms [235,236,238,239]. By simulating the microstructure development during PBF buildings, can provide useful insights to the morphology and distribution of dendrites and precipitates in the final part [240–242]. The simulation of residual stresses has also produced some results [243–246] of note but is also a clearly developing field prime for expansion.

The authors would also like to highlight the current gulf in capability between modelling times and the effective process speeds. There remain significant challenges to overcome therefore in arriving at models which

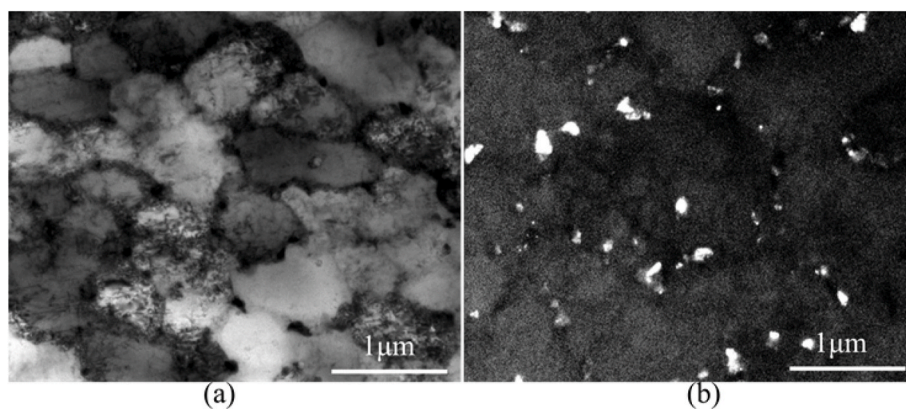


Fig. 40. Transmission Electron Microscopy images showing the laves phase in the as-built Laser Powder Bed Fused Inconel 718 [190]. (a) Bright field. (b) dark field. Only Laves phases are visible due to the fast heating and cooling cycles, which suppressed other secondary phase precipitation during Laser Powder Bed Fusion.

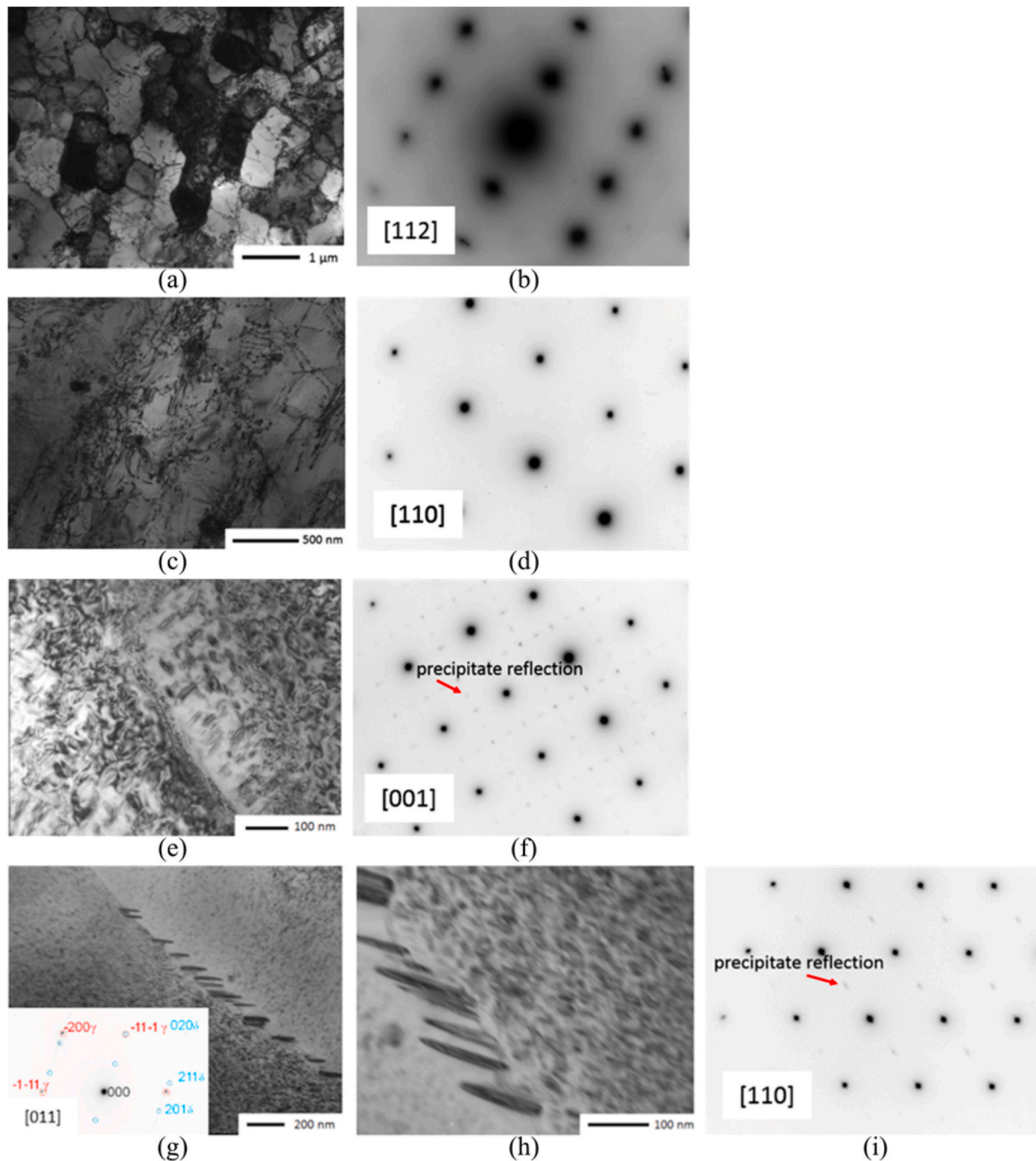


Fig. 41. Transmission Electron Microscopy images and diffraction pattern of Laser powder bed fused specimens [172]. (a), (b) Solution treated. (c), (d) Hot Isostatically Pressed. (e), (f) Solution treated and aged. (g)–(i) Hot isostatically pressed and aged. After solution treatment, diffraction shows the dissolution of Laves phases usually present in as-built condition. Following Hot Isostatic Pressing, grains are recrystallised and secondary phases dissolved. After solution and ageing treatment, the Transmission Electron Microscopy images and diffraction patterns reveal the presence of secondary phases, such as γ' . This demonstrates that solution and ageing treatments are able to precipitate secondary phases.

are sufficiently computationally efficient to allow ‘on-the-fly’ model and control architectures to be deployed.

4. Mechanical properties

The characterisation of mechanical properties is essential before AM components can safely be used in applications beyond the static. A review of the mechanical properties of metal AM parts was written by Lewandowski et al. [4] should the reader require broader context. Fig. 46 shows the mechanical properties of PBF nickel-based superalloys

studied to date. At the current stage, studies have mainly focused on tensile and hardness performance and less on shear, toughness, fatigue and creep properties. Table 7 captures which studies looked into the different mechanical properties. It also lists the common standards usually used to test the mechanical properties. However, it should be noted that it is common for researchers to adapt standards to specific needs of AM part testing. The controlling factors for the mechanical properties of LPBF manufactured nickel-based superalloys are analysed as follows.

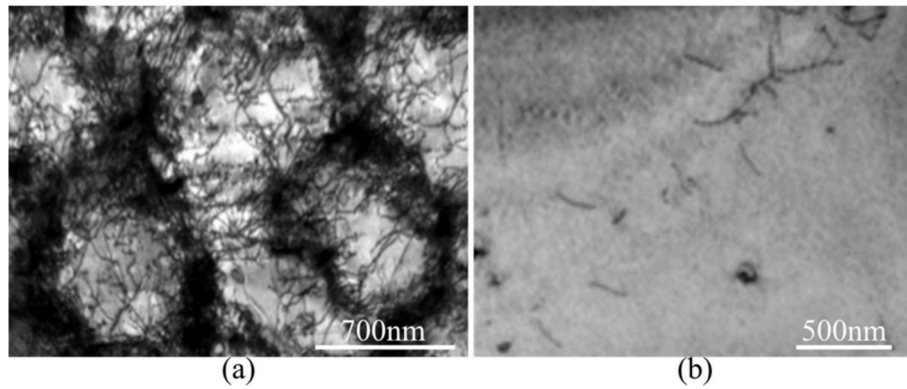


Fig. 42. Bright field TEM images showing dislocations in Laser powder bed fused IN718 specimens [185]. (a) As-built. (b) Heat treated. This reveals the presence of Laves phase.

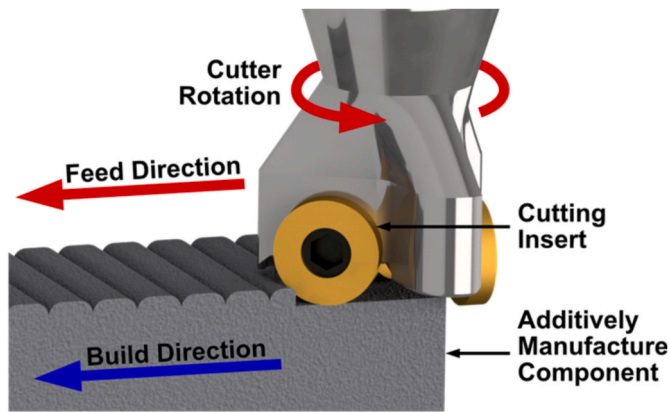


Fig. 43. This shows the effect of the PBF build orientation on the subsequent machining. The greatest cutting force is generated when the feed direction is parallel to the build direction, which gives rise to anisotropy at machined faces.

4.1. Tensile properties

Tensile testing is one of the more commonly used mechanical tests which allows the determination of the elasticity modulus, yield strength, ultimate tensile stress, ductility and stress and strain relationship for the material. These are ordinarily undertaken in a uniaxial form and as such, do not closely resemble real world loading cases. Tensile tests can easily be performed at room temperature according to standards listed in Table 7. Since nickel-based superalloys are used at elevated temperatures, their high-temperature tensile properties also need to be carefully

considered according to the relevant standards. For example, some studies tested IN718 specimens at 650 °C [67,258,277,296], IN738LC at 850 °C [249,251,267], Hastelloy at 750 °C [255,284], in IN625 at 815 °C [333] and IN625 at 538 °C [292] and 760 °C [263,269]. A study found that high temperature tensile tests resulted in intergranular cracking [331].

Some of the most commonly used tensile testing specimen geometries are defined by the ASTM standards (Fig. 47a–c) and the ISO and EN standards (Fig. 47d). Specific countries also have their own standards, which were developed by referring to the ASTM and ISO standards. Using the standard testing procedures allows the AM specimens tensile properties to be obtained and compared between different authors. Gonzalez et al. compared the tensile properties of specimens fabricated with LPBF, EBM and binder jetting [100]. The results indicated that all AM methods surpassed the ASTM F3056-14 standard mechanical properties requirements and that LPBF specimens possessed slightly better performance and isotropy than the other two processes.

4.1.1. The influence of powder composition, quality and thickness on tensile properties

Powder quality also plays an important role in the PBF process. Sames et al. compared the tensile properties of specimens manufactured with gas atomized, rotary atomized, and plasma rotated electrode process (PREP) powders [118]. The former two contain trapped gas, leading to increased porosities in the specimen, while PREP powders resulted in higher relative density and thus, higher tensile strength. Nguyen et al. compared the influence of the use of fresh and recycled powder on final properties [115]. Recycled powder particles had a slightly larger average size, lower Hall flow rate and lower packing density, with respect to the fresh powder. This was due to particles' tendency to stick together and deform during the building process. Despite the differences

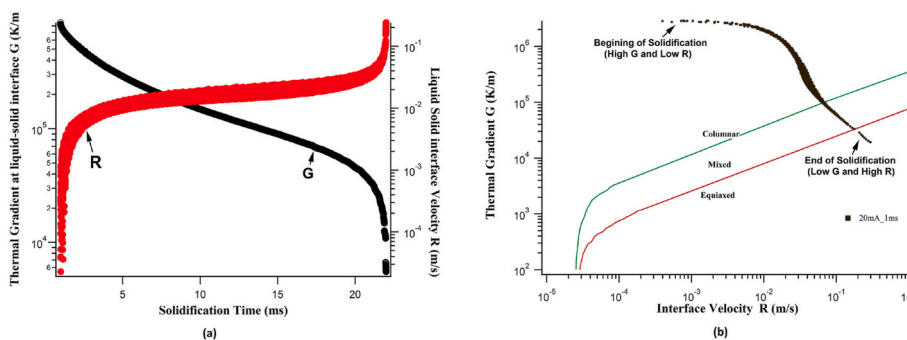


Fig. 44. Thermal gradient and solid-liquid interface velocity generated during melt pool solidification [221]. (a) Relationship between Temperature Gradient (G)/Liquid-solid interface velocity (R) and solidification time. (b) Example of solidification path. This shows that both the thermal gradient and solid-liquid interface velocity, generated during melt pool solidification, influenced the final grain morphology.

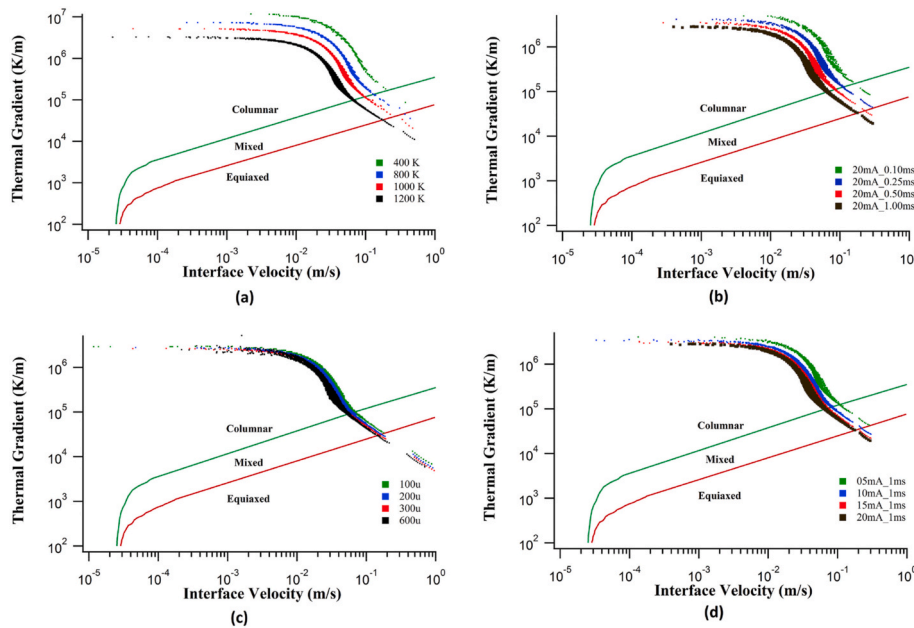


Fig. 45. Effects of process parameters on grain morphology by controlling the temperature gradient (G) and liquid-solid interface velocity (R) of the melt pool [221]. (a) Preheat temperature. (b) Spot ON time. (c) Beam diameter. (d) Spot beam current. All of these parameters influence the final melt pool morphology.

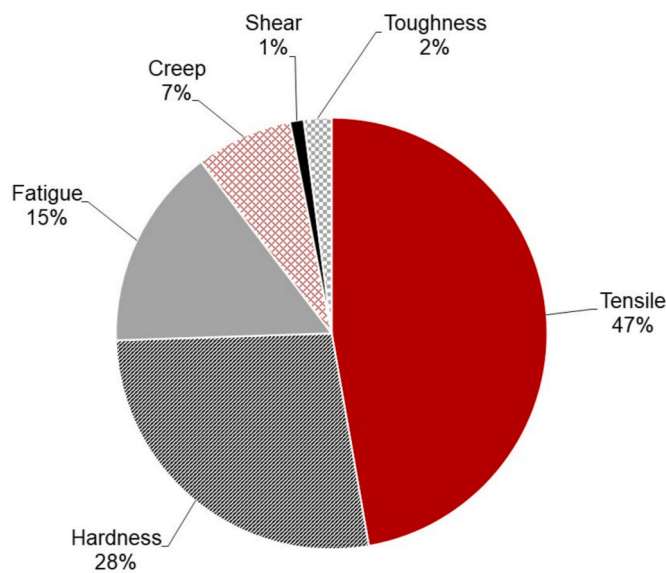


Fig. 46. Pie chart summarising the mechanical properties investigated in powder bed fused nickel-based superalloys research, across 290 papers. Almost half of the studies investigated tensile properties, while a third studied hardness properties. Other properties, especially shear and toughness, have been the subject of limited studies.

in powder quality, their effect on the mechanical properties was insignificant in this case. However, Gasper et al. demonstrated the mechanisms by which Hastelloy X powders degrade in powder bed fusion [127].

Another study looked at the effect of minor alloying elements on microcrack formation in LPBF Hastelloy X and the influence of hot cracking on tensile and compressive properties [334]. They found that a reduction in minor alloying elements resulted in the elimination of hot cracking in AB LPBF Hastelloy X but reduced the overall tensile strength by 140 MPa [334]. Similarly, the effect of graphene nanoplatelets (GPNs) reinforced K418 nickel-based superalloy composites, fabricated by LPBF, on the tensile properties was studied [338]. Some work

revealed that introducing a 1 wt% titanium carbide (TiC) nanoparticles in LPBF Hastelloy X eliminated microcracks and increased yield strength by 98 MPa [340].

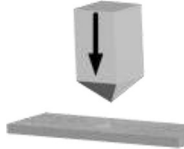
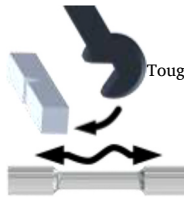
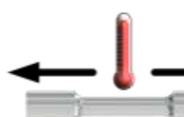
Fabricating metal matrix composites with PBF can augment material properties. Indeed, Yao et al. showed that the tensile strength of AB LPBF IN718 specimens could be improved by adding TiC nano-particles, which hindered dislocation movements [271]. However, the transformation of these particles from MC to M₂₃C₆ carbides during HT, counteracted the already existing strengthening mechanism, resulting in a reduced tensile strength, and improved ductility. Alternatively, Xia et al. chose WC particles to strengthen the LPBF IN718 specimens [65]. By increasing the scan speed, WC particles and dendritic structures became much finer, increasing the tensile strength and reducing the ductility. Other particles have also been tested to reinforce PBF specimens, including graphene nanoplatelets [262] and carbon nanotubes [266].

Furthermore, the thickness of the powder layer can also affect tensile performance. Indeed, Sufiiarov et al. [274], observed that a thinner layer thickness contributed to better tensile strength since it could provide better bonding between adjacent layers. However, Nayak et al. observed that the tensile performance of 100 μm layers was similar to that of thinner layers [416]. Zhou et al. manufactured functionally graded materials with strong bonding between 316L and IN718 powders. A relatively strong shear strength (581 ± 11 MPa) was obtained, probably due to the strong metallurgical bonds generated during LPBF [265]. Furthermore, Muñoz-Moreno et al. characterised the bulk elastic properties and shear moduli of AB and HT LPBF CM247LC components using resonant ultrasound spectroscopy [311]. The difference between the shear modulus of the AB (85 GPa) and HT specimens (87–88 GPa) was found to be negligible. Whereas Sabelki et al. found that both HT and build direction affected the torsional properties of LPBF IN718 [342]. The evaluation of shear strength is important for many components working in safety critical scenarios. Nevertheless, the number of studies related to the shear strength of PBF manufactured nickel-based superalloys is very limited.

4.1.2. Build orientation results in anisotropic tensile properties and controls the failure mode

Build direction is yet another important factor that highly affects

Table 7
Summary of the standards used during mechanical testing and references that investigated these different mechanical properties.

Mechanical Property	Standards	References
 Tensile	Room temperature: - ASTM E8/E8M - ISO 6892-1; EN 10002-1 - Swedish SS112111-7A35 - German DIN 50125 - Chinese grain T 228.1 Elevated temperature: ASTM E21 ISO 6892-2 EN 10002-2 Chinese grain boundaries/T 228.2 ASTM B769	[58,64–68,74,92,95–97,100,104,115,117,118,148,165,172,173,176,178–180,183,216,220,247–341]
	Vickers (ASTM E92) Knoop (ASTM E92) Rockwell (ASTM E18) Brinell (ASTM E10)	[59,64,65,67,70,72,95,121,146,148,150,160,165,179,180,183–185,195,197,216,275,277,278,281,284–287,289,290,292–295,300,302–305,307,308,310,311,321,324,330,335,343–380]
 Shear	Charpy V-notch technique ASTM E23 ISO 148	[68,113,274,381–383]
 Hardness	Toughness	
 Fatigue	ASTM E466 ASTM E606 ASTM E647	[172,176,178,220,252–257,296,312,313,319,322,327,328,333,337,370,373,384–404]
 Creep	ASTM E139 ISO 204	[75,190,249–251,275,295,326,333,384,388,405–415]

specimens mechanical properties and results in microstructural and mechanical anisotropy [417]. Chlebus et al. investigated the tensile properties of specimens built in four directions (Fig. 48) [95]. The results indicated that the specimens built in the $45^\circ \times 45^\circ$ direction possessed the best tensile strength in both AB and HT conditions. Moreover, specimens built in transverse directions were always stronger than the longitudinally built equivalents. This was explained by the angle between the loading direction and grain growth direction, which can greatly affect specimen tensile behaviour.

Ni et al. also compared the tensile strength of longitudinally and transversely built IN718 specimens considering the Schmid factor, which is used to describe the relationship between slip planes and slip direction [259]. This research found that the transversely built specimens possessed better tensile strength, which was in accordance with Chlebus et al. [95]. In another study, the differences in strength between longitudinally and transversely built specimens were believed to be caused by the angle between the loading direction and the orientation of the pores present between adjacent planes, due to lack-of-fusion [260]. The fractures for the longitudinally and transversely built samples were controlled by two different failure modes: the ‘opening mode’ (Mode I), which occurs when the loading direction is normal to the defect/pore orientation, leading to fast failure, and the ‘in-plane shear mode’ (Mode II), which happens when the loading direction is instead parallel to the

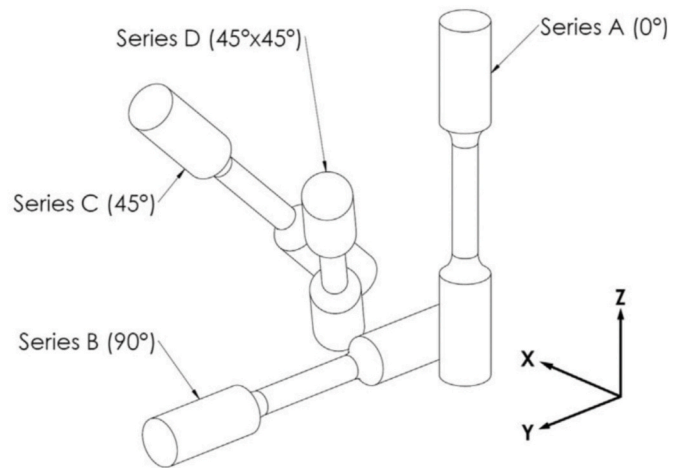


Fig. 48. Demonstration of the commonly applied layout of powder bed fused specimens with respect to the machine axis [95]. These layouts, or build orientations, affect the subsequent mechanical properties.

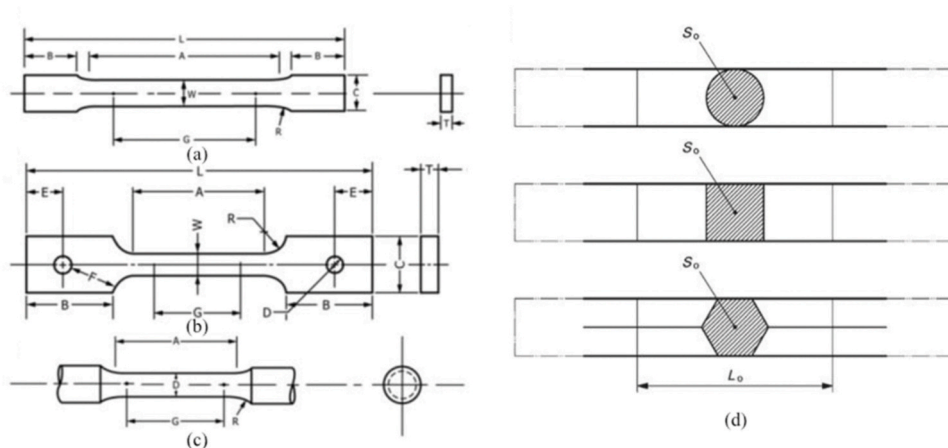


Fig. 47. Commonly used tensile testing geometries defined by different standards. (a), (b), (c) ASTM standards. (d) ISO/EN standards. Using these geometries and following standards allows comparison between results from different authors.

pores orientation, typical of transversely built specimens. Similar results were obtained in a series of studies performed at room and elevated temperatures [249,261,263,277,296] with AB [247,257,258,274,276,279,288] and post-processed specimens [64,92,264].

However, other studies reported that specimens built in the longitudinal direction had better mechanical resistance. Indeed, Tomus et al. found that, when tested at 900 °C, specimens built in the longitudinal direction performed better [117]. This was also the case for LPBF of Haynes 282 at 900 °C and 20 °C [104]. However, specimens built in the transverse direction were found to possess higher tensile strength at room temperature and 700 °C. No solid explanation for these observations was given in this study. Similar results obtained by Kirka et al. could not explain the origin of the differences between longitudinally and transversely built specimens [297]. The authors reported that, by increasing the build height, transverse specimens became stronger and more ductile. This might have been caused by the consistent heat input which transformed γ'' precipitates into brittle δ -phase, in the bottom of the structure. Finally, a comprehensive study relating the build direction to the anisotropic behaviour of LPBF specimens was performed by Hovig et al. [314].

4.1.3. Scan strategies and the effect on tensile properties

The tensile properties of PBF manufactured specimens are mainly controlled by the build parameters, with scan strategy (the path that the energy beam takes) being one of the most important. Indeed, beam power and hatch spacing were found to be the principle factors driving tensile strength [336]. Kirka et al. compared a point heat source fill scan strategy, with the conventional raster scan strategy applied in EBM [298]. The former strategy contributed to a more equiaxed microstructure, almost eliminating tensile strength anisotropy. Based on this result, Zhou et al. applied an improved alternative scanning strategy to a functionally graded component, which resulted in improved tensile strength [265]. Additionally, Geiger et al. compared the effects of three different scan strategies (labelled A, B and C and illustrated in Fig. 49) on LPBF IN738LC components [267]. The EBSD results (Fig. 49) showed that different scan strategies generate different microstructural features, which cannot be fully eliminated by HT. The tensile testing results showed that scan strategy B always developed the highest Young's modulus among all the applied strategies. Moreover, sample tensile properties are also affected by their locations on the building plate and shielding gas flow.

4.1.4. Heat treatments for improved tensile properties

In order to produce more homogeneous microstructures and improve components mechanical properties, post-processing is still necessary at the present stage. HTs' main purposes are: decrease anisotropy, dissolve potentially crack-initiating particles and form strengthening precipitates. For more information about typical thermal treatments of PBF nickel-based superalloys and achievable optimum properties, the reader is directed towards the AMS2774 standard for Heat Treatment of wrought nickel alloy and cobalt alloy parts [171], which is currently recommended for thermal treatment of PBF nickel-based superalloys by the Standard Specification for Additive Manufacturing Nickel Alloy (UNS N07718) with Powder Bed Fusion [170]. The effects of HT on PBF specimen tensile properties have been widely studied [66,74,92,95,165,183,186,249,251,266,283,285,289,311,339,418].

Two standard HTs for conventional materials were applied by Zhang et al. [165]. The first one consisted of two steps: a solution treatment (980 °C, 1 h/air cooling) + double aging (720 °C, 8 h/furnace cooling at 55 °C/h to 620 °C, 8 h/air cooling) and the second HT started by a homogenisation treatment (1080 °C, 1.5 h/air cooling), followed by the same two steps as the first HT. Both methods contributed to the recrystallisation of dendritic structures and the precipitation of γ' and γ'' particles. As a result, both HTs increased material tensile strength. It was also observed that in the two-step HT, which is normally used for forged materials, undissolved Laves phases were still present. This illustrated

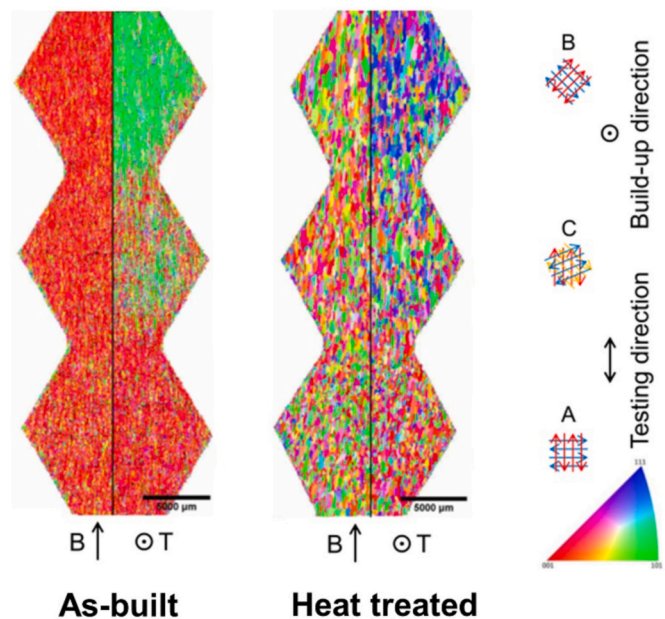


Fig. 49. Electron Backscatter Diffraction results show the effects of scan strategies A, B and C (illustrated on the right-hand side of the figure) on specimens microstructures [267]. This illustrates that different scan strategies generate different microstructural features, which cannot be fully eliminated by heat treatment. The different scan strategies also affect the mechanical properties. The tensile testing results showed that scan strategy B always developed the highest Young's modulus among all the applied strategies.

that the three-step HT was better performing, even though it produced slightly lower tensile strength. On the contrary, in a study where LPBF specimens were reinforced with carbon nanotubes [266], the recrystallisation of fine microstructures caused by the HT slightly decreased the yield strength. That was not the case when an in-situ HT technique - achieved by taking advantage of the powder bed preheating function in EBM machines - was used. In fact, the results showed that this in-situ HT led to much coarser microstructures, a larger number of intergranular cracks and poorer tensile strength when compared to conventional EBM specimens [183]. Additionally, Sames et al. investigated the impact of cooling rates in EBM [97]. The slowly cooled specimens possessed a much higher tensile strength respect to the fast-cooled equivalents, at the cost of lower elongation. A 3-step HT on LPBF Haynes 282 increased yield strength and ultimate tensile strength [186].

HIP is a commonly used technique to eliminate the micro-porosities and mitigating the impact of microstructural anisotropy. In the literature is usually applied with or compared to other HT processes [64,172,173,179,250,260,269,284,287,297,418]. For example, Tomus et al. studied the tensile properties of LPBF Hastelloy X specimens in AB, HT, HIP and HIP + HT conditions [179]. The results showed that the HIP improved specimen relative density from 99.2% to 99.8% in AB condition to 99.9%. Although it also led to carbides precipitating at the grain boundaries, the amount of carbides was believed to be too low to affect specimen mechanical properties. A study on HIP of IN738 showed that it improved the tensile strength of parts built vertically and horizontally but decreased the strength in the 45° samples [418]. Furthermore, all post-treated specimens possessed similar tensile strengths, while being lower than the AB. This was attributed to the rearrangement of dislocations during post-processing. Confirmation to that was found in another study by Kreitzberg et al., where HIP LPBF specimens possessed the lowest yield strength (Fig. 50), both at room and elevated temperatures, compared with other LPBF samples tested [269]. From these results, it was concluded that higher porosity lead to higher tensile strength.

In a study by Yao et al. [271], the AB and HT tensile test fracture

surfaces of LPBF IN718 and TiC reinforced LPBF IN718 specimens were evaluated. All specimens presented dimpled fracture surfaces, indicating a ductile failure. It was also observed that the dimples in the HT specimens were larger and shallower, indicating lower ductility than the AB specimen. The homogenized STA LPBF IN718 samples achieved higher strength than the AMS wrought specifications and good plasticity as well [328].

Although tensile strength is a significant mechanical property in many situations, compressive strength is also of importance. Typically, complex structures including lattices will undergo both tensile and compressive loading in operation. Therefore, AM lattice structures, which are designed for tailored mass, surface area, modulus and strength, are usually characterised with compression tests [216]. Strondl et al. compared the tensile and compressive yield strength of EBM IN718 specimens [96]. The results indicated that the tensile strength was higher than the compressive resistance, especially in HT conditions. Smith et al. demonstrated that LPBF IN718 specimens possessed slightly higher compressive yield stresses [65]. However, none of the studies explained the cause of these differences. The hot compression behaviour of IN718 specimens was studied by Mostafa et al. for LPBF components applications in the forging process [317]. The results indicated that the tensile behaviour is highly strain-rate dependent.

Fig. 51 summarises the tensile strength properties for all of the studies reported to date. Each point represents the tensile property results for a sample from a paper. It should be noted that most samples had different processing and post-processing conditions, as well as different testing procedures. For example, some of the low laying points in the figure correspond to high temperature tensile testing by Popovich et al. [68]. Violin plots require a lot of data and the lesser number of studies

available for EBM and Young's Modulus is the reason why they do not have plots. From Fig. 51b, it is clear that EBM nickel-based superalloys are much less investigated than for LPBF. The average tensile strengths of EBM IN718 and IN625 are also slightly below their LPBF counterparts. The research gaps, in terms of which materials are studied, are also apparent in Fig. 51.

Fig. 51 was based on Table 9 in the Appendix section which lists the published data for the tensile properties of PBF manufactured nickel-based superalloy.

4.2. Hardness properties

Hardness is a measure of a material resistance to localised permanent deformation such as small dents or scratches [420]. Hardness measurements are easy to perform, which is one of the reasons why they are one of the most frequently used mechanical property characterisation tests to provide an indicator to material condition. The processing parameters and HT can significantly influence LPBF specimens hardness [421]. As well as the building parameters, powder properties such as particle size distribution, flowability and rheology also affect specimen final hardness [121]. Supports were also shown to have a marginal effect on the local microstructure and hardness due to the low heat input in LPBF [380].

4.2.1. Build orientation and hardness measurements

Yen et al. showed that the build orientation affected hardness properties directly [290]. Additionally, Chlebus et al. demonstrated that planes parallel to the build direction had a slightly higher hardness than perpendicular ones [95]. This was imputed to the interfaces overlapping

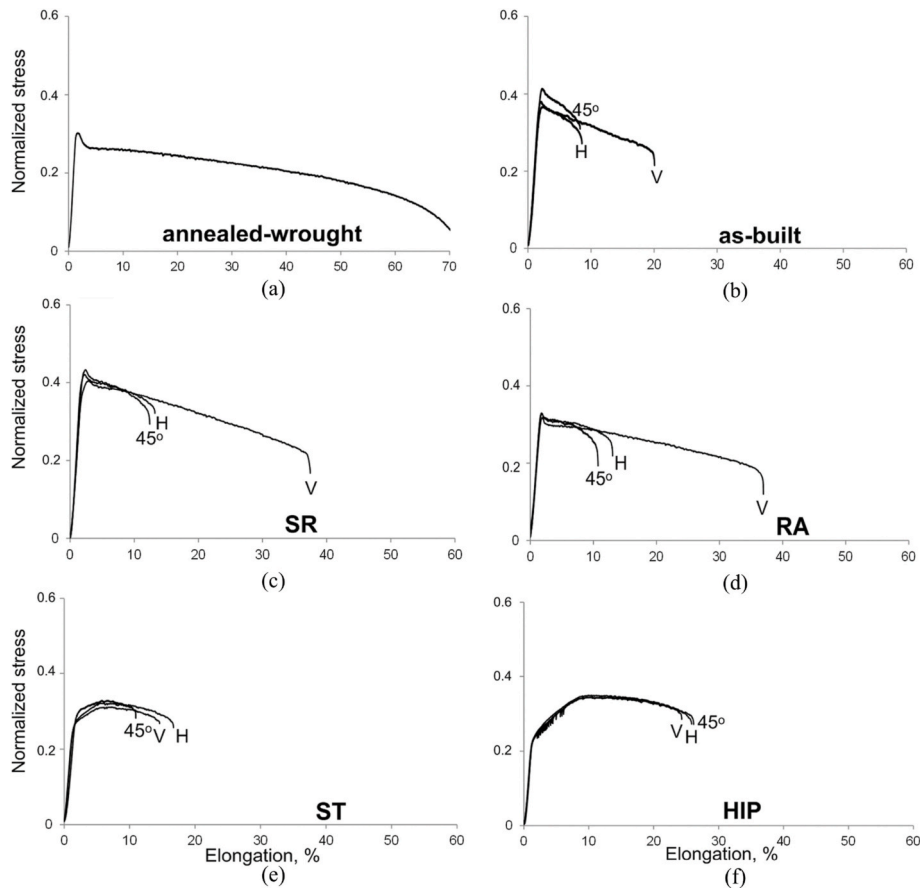


Fig. 50. Tensile stress-strain diagrams obtained at 760 °C for different thermal treatments [269]. (a) Annealed-wrought. (b) As-built. (c) Stress relieved (SR). (d) Recrystallisation annealed (RA). (e) Solution treated (ST). (f) Hot isostatically pressed. Hot isostatically pressed Laser Powder Bed Fused specimens possessed the lowest yield strength, highlighting the effect of different thermal treatments on the resulting mechanical properties of powder bed fused specimens.

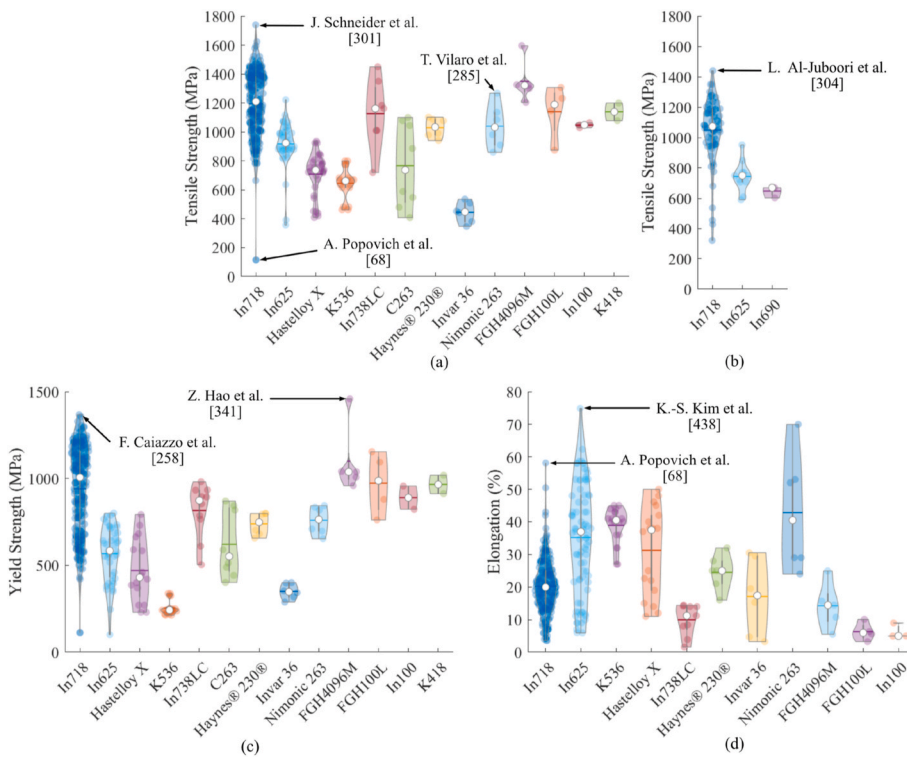


Fig. 51. Violin plots of research conducted in different nickel-based superalloys on Tensile properties. From 137 papers. (a) Tensile strength of Laser Powder Bed Fused alloys. (b) Tensile strength of Electron Beam Melted alloys. (c) Yield strength of Laser Powder Bed Fused alloys. (d) Elongation of Laser Powder Bed Fused alloys. The white dot is the median, horizontal lines are the mean, the height represents the range, the width is the amount of data, and the vertical lines in the middle are the inter-quartile range. The materials are arranged in order of how much data was available. These figures include the vast range of sample conditions used in works covered in this review and so direct comparison between studies should be undertaken with caution. This shows that Inconel 718 and Inconel 625 have been studied most comprehensively within the literature. The average tensile strengths of Electron Beam Melted Inconel 718 and Inconel 625 are also slightly below their Laser Powder Bed Fused counterparts. The violin plots were created using free to access matlab code [419].

between deposited layers, which tended to crack more easily, as well as weaker grain boundary strengthening planes perpendicular to the build direction. Strößner et al. and Murr et al. both obtained similar results [277,354] while Tomus et al. believed that the difference in hardness between the different planes was so small that it could be ignored [179]. Naturally there are differences in the experimental methods adopted here which are potentially significant in giving rise to these differences in results.

Variations in hardness with respect to the build direction, indicated that the hardness is affected by specimens microstructural anisotropy. Indeed, Chauvet et al. demonstrated that the size of γ' phase decreased gradually along the build direction, due to the thermal history of LPBF [146]. This variation in γ' size was consistent with the measured hardness gradient (Fig. 52a). In the study by Wang et al., hardness was found to decrease with increasing columnar structure width [278].

4.2.2. Energy density, scan strategy, scan speed and hardness properties

When evaluating the comprehensive effects of a series of processing

parameters, energy density needs to be considered. However, the influences of energy density on final properties are difficult to assess since many studies led to contradictory conclusions based on differing experimental methods. Experimental results, showed in Fig. 53a, by Rong at al. seem to collocate that linear energy density has an optimum in a range between 173 J/m and 303 J/m [343]. However, in another study (Fig. 53b) by Jia et al., a proportional relationship between the linear energy density (in a range between 180 J/m and 330 J/m) and the hardness was observed [344]. The conclusion to that result was that a higher linear energy density resulted in a more homogenous microstructure, thus increasing the hardness [344]. Conversely, other studies found that the materials hardness decreased by increasing linear energy density (in a range between 400 J/m and 1200 J/m) [67,281,345,346]. In particular, one study indicated that this was due to a coarsened microstructure [345], while others thought that the cause had to be identified in a finer microstructure and less brittle precipitates [67,281]. Furthermore, in a study by Yen et al. no direct relationship between the hardness and volumetric energy density was observed [290].

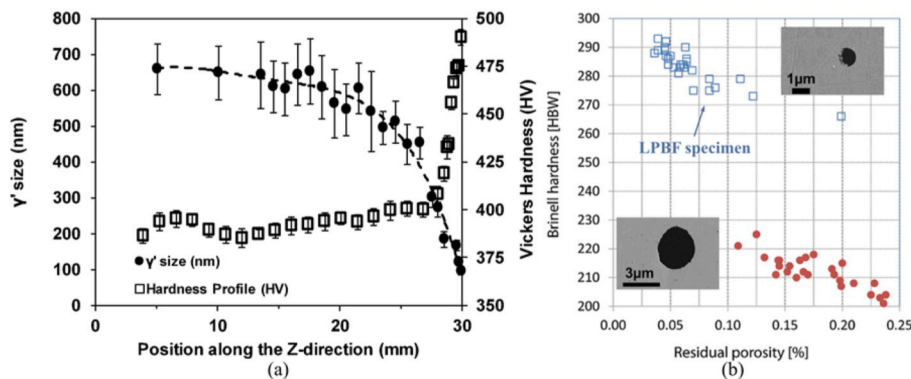


Fig. 52. The size of γ' phase decreased gradually along the build direction, due to the thermal history of Laser Powder Bed Fusion, which affected the hardness properties. (a) Diagram showing the distribution of γ' size and hardness along the build direction [146]. (b) Diagram showing the relation between hardness and porosity [353]. This shows that parameters like build height also affect mechanical properties.

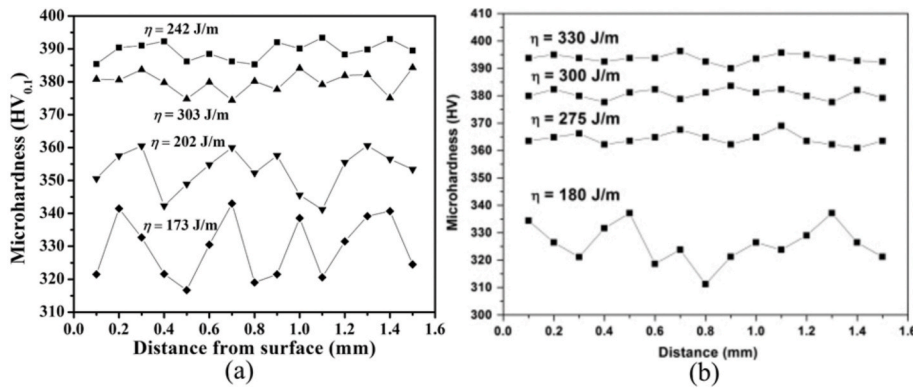


Fig. 53. Effects of linear energy density on hardness. (a) By Rong et al. [344]. (b) By Jia et al. [344]. This shows contradicting evidence from the different authors with Rong et al. arguing that linear energy density has an optimum in a range between 173 J/m and 303 J/m to obtain the best hardness properties [343] and Jia et al. saying that there is a proportional relationship between the linear energy density (in a range between 180 J/m and 330 J/m) and the hardness observed [344]. This illustrates some of the variability in findings between different studies, further highlighting repeatability challenges in powder bed fusion.

Yang et al. noticed that the melt pool mode, such as keyhole and conduction mode (Fig. 54), in the LPBF process also influenced specimens hardness [369]. Two different microstructures were found in the central and peripheral zone for keyhole mode specimens, while the conduction mode specimens were more uniform. The main features of different melt pool regions are listed in Fig. 54. The central zone in the keyhole mode, which mainly benefited from finer dendritic and γ'/γ'' precipitates, had a higher hardness (249 HV/359 HV) than the marginal mode (249 HV/321 HV) and conduction mode (260 HV/330 HV).

Additionally, Gu et al. observed a direct relationship between grain morphology and hardness in the melt pool [368]. The hardness in different locations of the melt pool was measured (Fig. 55b and c) and the results were listed in Fig. 55d. They showed that the top surface of the melt pool was full of fine cellular dendrites and equiaxed grains with an average hardness of 387 HV while the bottom of the melt pool was dominated by unidirectional columnar dendrites with an average hardness of 337 HV. The edge of the melt pool, instead, was characterized by the presence of multidirectional columnar dendrites and an average hardness of 340–350 HV. The centre of the melt pool had an average hardness slightly higher of about 363 HV. From this, it was concluded that the morphology of the grains in the melt pool, which is controlled by the temperature gradient and the cooling rate, defined the hardness.

Lu et al. considered the effects of island scan strategies [286]. A smaller island size contributed to higher solidification rates, meaning that the increased residual heat effectively heat treated the solidified materials, leading to a higher hardness. However, another study found that higher values of hardness and compressive yield strength were obtained from the samples produced using Meander scanning strategies as opposed to an Island approach [148].

Choi et al. indicated that there was an optimum scan speed to produce the highest hardness [59]. The effect of scan speed was studied by Xia et al., the results indicated that higher scan speeds were generally correlated to higher hardness [65]. Indeed, higher scan speeds produced finer primary dendrites and more homogeneously dispersed granular carbides, which both contributed to higher deformation resistance. Furthermore, Choi et al. indicated that there was an optimum scan speed to attain high hardness [59]. However, at higher scan speeds, discontinuous laser tracks and non-fully melted powder were found to increase the porosity. On the other hand, lower scan speeds gave rise to excessive energy input and material vaporization, trapping vapours in the solidified structures. Higher porosity led to lower hardness as the pores would easily collapse when loaded. As proof, LPBF IN625 porosity was found to be consistent with the hardness gradient [59,353]. Rong et al. observed a similar trend but they justify the decrease in hardness at lower scan speeds with a coarsened microstructure [345]. In contrast, Karimi et al. found no direct relationship between EBM specimens hardness and porosity [367].

4.2.3. Optimal heat treatment for improved hardness

Post-processing techniques also have a significant influence on specimens' hardness. Zhang et al. heat treated LPBF IN718 specimens according to standards AMS 5662 and AMS 5383 [165]. Both methods increased the hardness than their AB equivalents due to the uniform precipitation of γ' and γ'' strengthening particles during ageing. Similar results and explanations were published in several other studies for LPBF [70,95,184,216,277,287,347,349,350,352] and EBM specimens [294, 295]. Deng et al. suggested that grain size growth might lower the hardness [294], while another study on HT LPBF Nimonic 263 samples by Vilaro et al. explained that the dislocation density and precipitation of γ' particles worked together to influence the hardness [285]. As such, grain size is not the only factor to influence hardness.

A study reported that annealing LPBF IN718 at 600 °C for 2h did not affect the grain size or the microhardness of the sample [379]. Whereas under the solid solution process of 950 °C, the fine homogeneous δ -phase and γ' phase in the grain or near the grain boundary had an important effect on the X–Y surface hardness value (476–500 HV) of the alloy [374]. Under the solid solution process of 950 °C, the fine homogeneous δ -phase and γ' phase in the grain or near the grain boundary had an important effect on the surface hardness value (HV476–500) of LPBF IN718 [375]. Hence, some studies concluded that there was an optimum annealing temperature to obtain the highest hardness [275, 348]. Below the optimum temperature, residual stresses were relieved with no precipitation formation, leading to lower hardness. However, Deng et al. suggested that residual stress could harden the material to some extent [289]. Above the optimum temperature, δ particles were dissolved, leaving the sample without their strengthening mechanism, decreasing the hardness [348].

Additionally, Tucho et al. demonstrated that the effects of solution HT on the hardness of LPBF IN718 were dependent upon both temperature and hold time [185]. In order to achieve full recrystallisation, a solution temperature higher than 1100 °C was necessary. It was also found by Sun et al. that HT was not only able to improve EBM IN718 specimens hardness, but also remove any gradient of this along the build direction (Fig. 56) [308].

Other post-processing techniques were found to have positive effects on hardness. An in-situ HT technique applied on EBM IN718 specimens achieved much higher material hardness than an equivalent HT [183]. However, in a study on LPBF IN718 by Tillmann et al., it was observed that while specimen density and microstructure isotropy was highly improved by HIP, hardness decreased compared to the AB equivalents [72]. This was possibly due, at least in part, to grain growth. Murr et al. obtained similar results in their study on EBM of IN625 [292]. They noticed that HIP not only changed the crystallographic structure but also dissolved the γ'' precipitates, leading to a decrease in hardness. Another technique used different ion irradiation fluences and found that as the fluence was increased, so did the nano-hardness of IN625.

Fig. 57 summarises the Hardness properties for all of the studies done

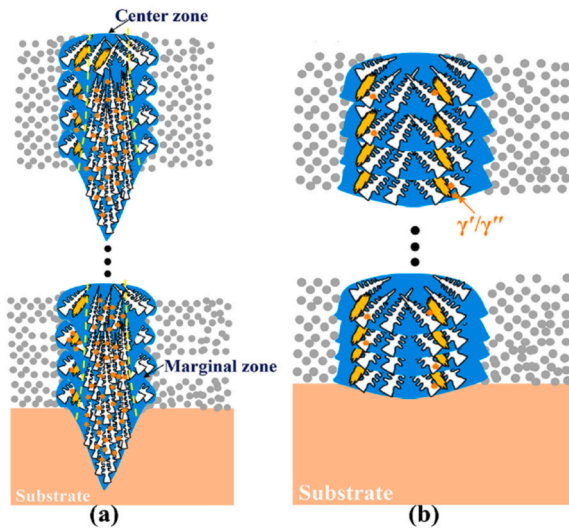
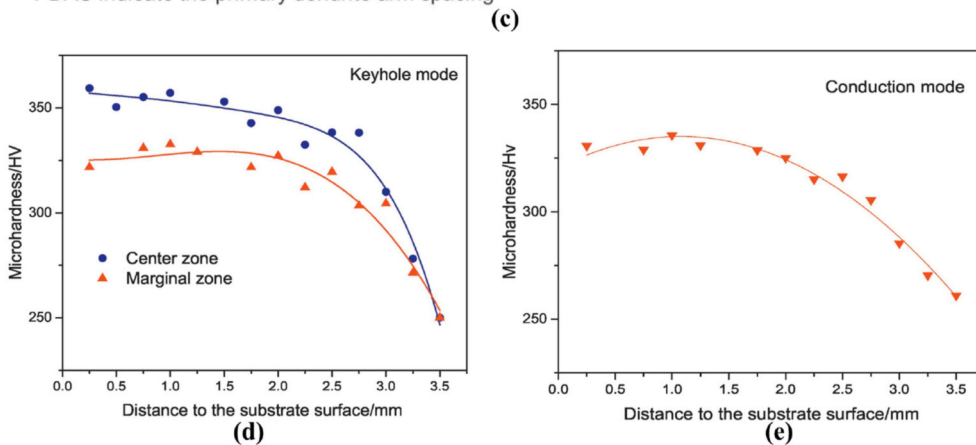


Fig. 54. Illustration of the heterogeneity of powder bed fusion material properties. (a) Diagram of keyhole mode. (b) Diagram of conduction mode thin wall. (c) Summary of the features in keyhole mode and conduction mode thin walls. (d) Microhardness distribution in the keyhole mode. (e) Microhardness distribution in the conduction mode thin walls [369]. The central zone in the keyhole mode, which mainly benefited from finer dendritic and γ'/γ'' precipitates, had a higher hardness (249 HV/359 HV) than the marginal mode (249 HV/321 HV) and conduction mode (260 HV/330 HV).

Feature	Keyhole mode		Conduction mode
	Center zone	Marginal zone	Center zone/ Marginal zone
PDAS (μm)	0.3 ± 0.1	3.0 ± 0.3	2.6 ± 0.3
Cooling rate (K/s)	$\sim 10^7$	$\sim 10^4$	$\sim 10^4$
Main precipitates	γ'/γ''	Laves	Laves
Area fraction of main precipitates	Bottom	22.7%	7.6%
	Middle	18.5%	11.8%
	Top	13.9%	14.5%
Texture	(001)	-	-

PDAS indicate the primary dendrite arm spacing



to date. Each point represents a hardness value for a sample from a paper. It should be noted that most samples had different processing and post-processing conditions, as well as different testing procedures. The research gaps, in terms of which materials are studied, are also apparent in Fig. 57 since the materials are arranged in order of how much data was available.

Data for EBM materials is not shown in this graph as there was not enough data reported to justify a similar type of figure. The reader is directed to Table 10 in the Appendix which compiles published data for the hardness of PBF manufactured nickel-based superalloy, including the EBM data.

4.3. Toughness properties

In many structural applications, material fracture toughness, a measure of material resistance to unstable crack propagation, needs to be carefully evaluated. The delay period associated with inhibition of crack propagation is a further key requirement in safety critical applications. However, crack propagation is also evaluated in both creep and fatigue scenarios.

4.3.1. Powder layer and build orientation effects on toughness

Ardila et al. and Gruber et al. studied the effect of recycled powder on the fracture toughness of LPBF and EBM IN718 specimens [113,383].

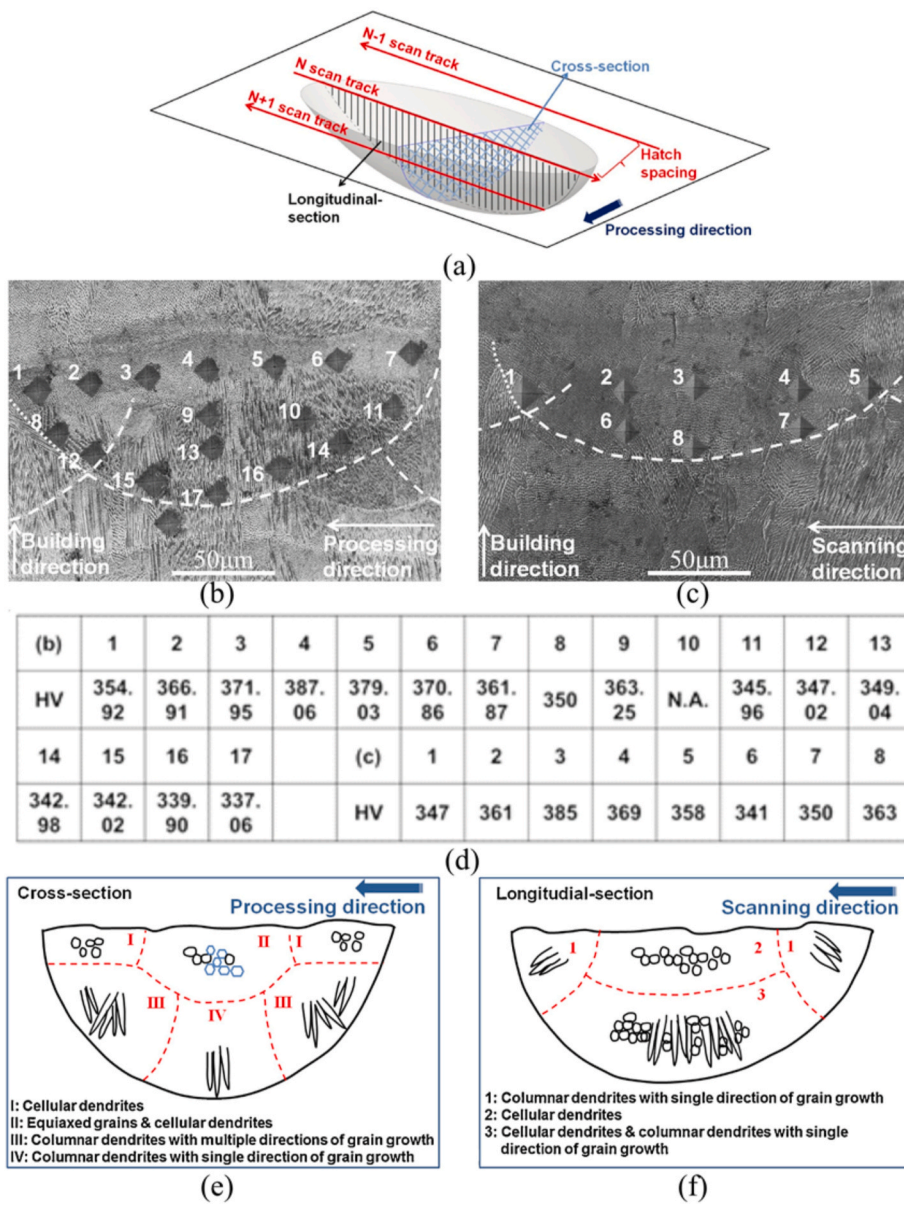


Fig. 55. The difference in hardness and grain morphology between the different regions of the melt pool [368]. (a) Diagram of a melt pool. (b) Cross-section of the melt pool. (c) Longitudinal-section of the melt pool. (d) Hardness measurement results. (e) Grain morphologies in different areas in cross-section. (f) Grain morphologies in different areas in longitudinal-section of the melt pool. The difference in hardness between the different regions concluded that the morphology of the grains in the melt pool, which is controlled by the temperature gradient and the cooling rate, defined the hardness. This also illustrates the heterogeneity of Laser Powder Bed Fused material, not only throughout the sample, but also at melt pool level.

For LPBF, the powder was recycled 14 times, with a Charpy test performed at 5 different junctures between these cycles. Results (Fig. 58) showed that the energy needed to fracture the LPBF IN718 specimens fluctuated around 10 J, with no noticeable influence from the powder degree of recycling. For EBM, excessive oxidation of the recycled powder was identified as the cause for insufficient melting and weak bonding in the specimen, with a consequent reduction in toughness.

Sufiiarov et al. investigated the influence of layer thickness on the fracture toughness of LPBF IN718 [274]. The results showed that specimens with a higher layer thickness possessed lower impact strength than thinner ones (59.6 J/cm² for 50 µm and 83.8 J/cm² for 30 µm, respectively). This highlighted that an increased layer thickness, with more lack-of-fusion defects and cracks in some sections of the specimen, can greatly diminish toughness.

In a study by Popovich et al., specimens built in the vertical direction showed a slightly higher impact toughness than the horizontal equivalents (91.3 ± 4.0 J/cm² and 83.8 ± 3.5 J/cm², respectively) [382]. Unlike Popovich et al., Hack et al. showed instead that the build direction had no evident impact on LPBF IN625 specimens toughness [381]. A common theme with comparing methodologies highlights the need for

uniformity in sample preparation to allow more meaningful comparison between results.

4.3.2. As-built specimens have better toughness than heat treated equivalents

Popovich et al. also evaluated the effects of a HT, consisting of homogenisation and ageing (HA), on the impact toughness of LPBF IN718 [68]. The impact toughness of AB specimens (58.7–79.3 J/cm²) was about two times higher than commercial hot rolled and HT equivalents (33–38 J/cm²). This was also observed by Hack et al., all specimens tested possessed superior impact and fracture toughness than their conventionally manufactured equivalents [381]. A possible explanation is that the specimens became more brittle after HT. Similarly to tensile testing results, the material impact strength presented clear signs of ductility in both AB and HT conditions as well as brittle fractures, especially where built-in defects were present [68].

4.4. Fatigue

Components used in critical applications, such as aerospace, are

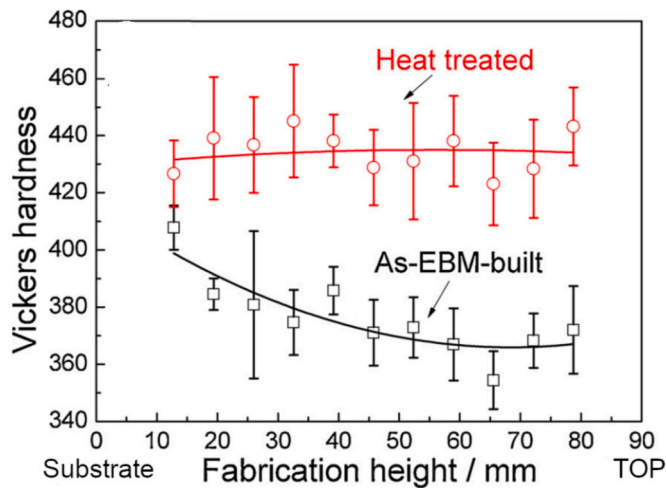


Fig. 56. Hardness distribution in as-built and heat-treated Electron Beam Melted specimens [308]. This shows a reduction in hardness as cooling regimes change with build height. This figure illustrates that although build height affects hardness, heat treatment can reduce or even eliminate that anisotropy.

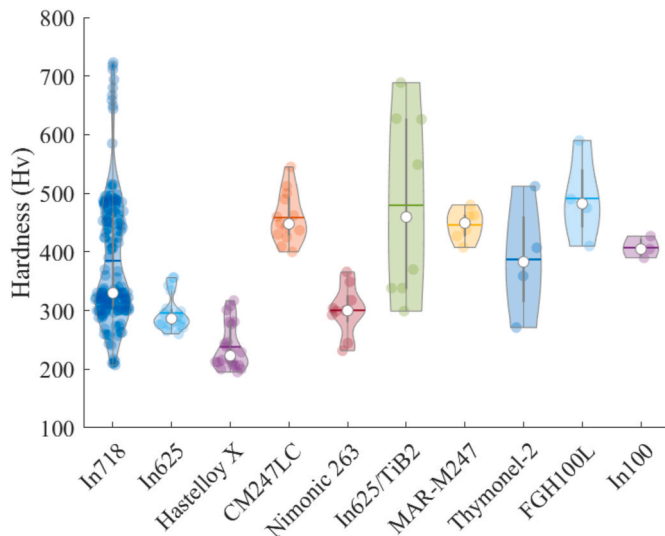


Fig. 57. Violin plots of research conducted in different nickel-based superalloys on Hardness properties, from 79 papers. The white dot is the median, horizontal lines are the mean, the height represents the range, the width is the amount of data, and the vertical lines in the middle are the interquartile range. The materials are arranged in order of how much data was available. These figures include the vast range of sample conditions used in works covered in this review. This shows that Inconel 718 and Inconel 625 have been studied most comprehensively within the literature. The violin plots were created from free-access matlab code [419].

subjected to dynamic cyclic mechanical and thermo-mechanical loads, meaning that their fatigue properties must be carefully considered [420]. This presents a distinct set of performance characteristics as compared to other approaches simulating near static loading conditions. LPBF IN718 damage evolution during monotonic and cyclic loading was monitored and showed accelerated damage evolution in LPBF materials compared to forged [337] as shown in Fig. 59. LPBF process defects result in worse fatigue performance and deteriorate the fatigue crack growth behaviour [327]. This is a universally reported observation and much effort has been invested in better accommodating defects or engineering these out of the process.

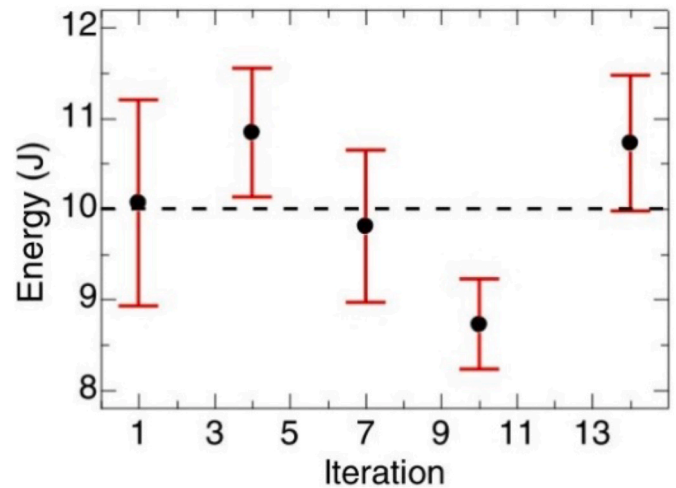


Fig. 58. Results from Charpy impact test by Ardila et al. [113]. These results highlight the consistency challenges associated with Powder Bed Fusion apparatus through material recycling procedures.

Fig. 60 shows the materials and PBF parameters investigated in Fatigue studies up to date. IN718 is by far the most studied material and the effect of thermal treatments, build orientation and surface condition are some of the most studied parameters. This figure also highlights materials and areas which would require more attention and study, such as the effect of powder composition and laser power on fatigue properties.

4.4.1. Grain morphology and orientation affect fatigue performance

A variety of fatigue performance studies focus on the effects of different processing parameters. Among them, the build direction was heavily investigated [176,252,255,296,312,319,384,385,387,402]. For example, two studies compared the fatigue performance of specimens built in the 0°, 45° and 90° directions [384,385]. Brodin et al. reported that LPBF Hastelloy X specimens built at 90° possessed the best fatigue strength [384]. The same result was found for HIP EBM specimens (Fig. 61) [296] (see Fig. 62).

Regarding fatigue life, LPBF Hastelloy X built at 0° performed better than those built at 90°, when the load was higher than 600 MPa. Under that stress, it was found a negligible difference in performance [255]. Konečná et al. obtained similar results and reported that the large surface roughness of notched 90° specimens may be the reason for their poor fatigue life [387]. Furthermore, for LPBF nickel-based superalloy K536, the fatigue performance anisotropy was not apparent at elevated temperatures (between 400 °C and 600 °C) [319]. However, in another study at low strain amplitudes, IN718 specimens built at 45° possessed longer fatigue lifetimes than the 0° samples [176]. A possible explanation is that the 45° built specimens have a longer mean free path for dislocation movement.

Grain structure also has an important impact on fatigue performance. Indeed, Zhou et al. and Kirka et al. carefully studied the effect of grain features on the fatigue performance of LPBF IN718 specimens [296, 396]. It was found that the build direction had a lesser influence on specimens with equiaxed grains, whereas specimens with columnar grains could withstand much lower cyclic stress amplitude. It was suggested that a columnar grains structure was more suitable for turbine blades - in order to provide directional preferential performance - while an equiaxed grains structure was more useful in turbine disks to comply with a distinct loading condition.

4.4.2. Laser driven effects on fatigue performance

The effects of input energy on specimens fatigue resistance have also been investigated [388]. IN718 Specimens manufactured using an input

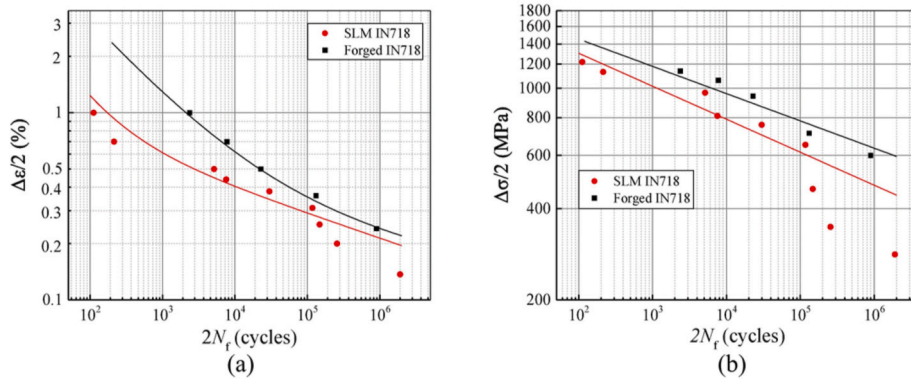


Fig. 59. A typical fatigue life curves for Laser Powder Bed Fused and forged alloys, demonstrated for Inconel 718 [337]. (a) Strain vs. number of cycles. (b) Stress vs. number of cycles. It is universally accepted that Laser Powder Bed Fusion process defects result in worse fatigue performance and deteriorate the fatigue crack growth behaviour, compared to conventionally manufactured materials.

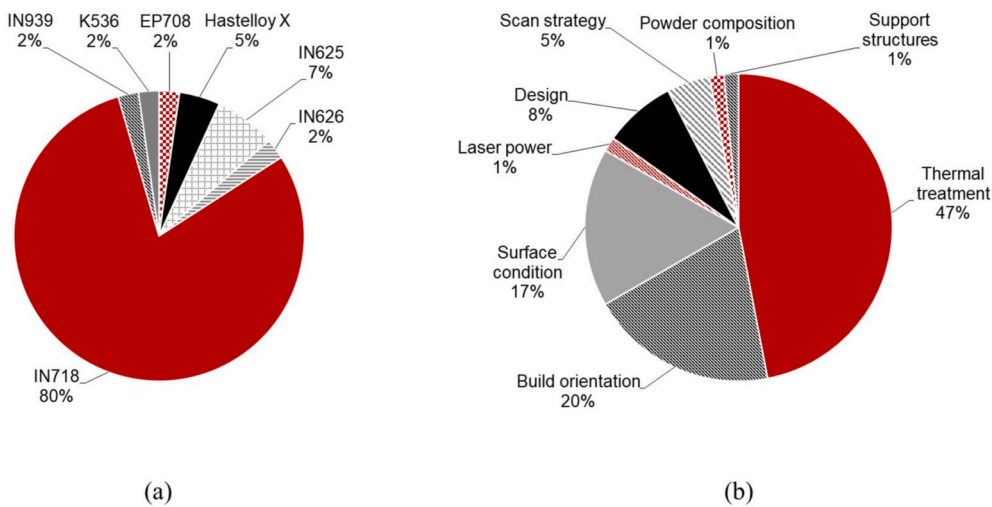


Fig. 60. Pie charts highlighting the materials and Powder Bed Fusion parameters investigated in Fatigue studies up to date, from 44 papers. (a) Materials studied. (b) Parameters studied. Inconel 718 is clearly the most studied material and the effect of thermal treatments and build orientation on the fatigue performance of powder bed fused nickel-based superalloys have been studied the most.

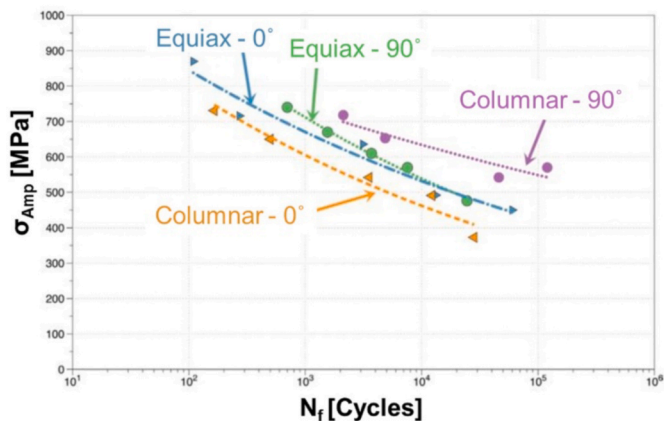


Fig. 61. S-N curves for Electron Beam Melted Inconel 718 of varying textures and orientations, equiaxed and columnar indicate specimens' grain structures that been controlled in the building process [296]. This shows that specimens built at 90° possess the best fatigue strength.

energy of 250 W (59.5 J/mm³) possessed less porosity and a higher fatigue resistance, than the ones produced at 950 W (59.4 J/mm³).

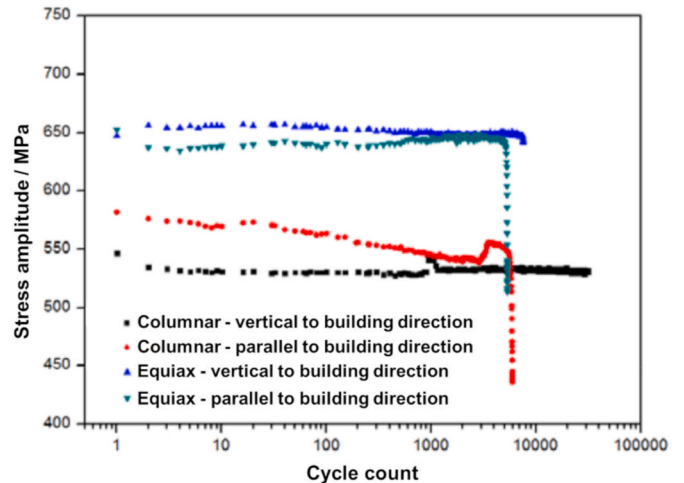


Fig. 62. Comparison of stress amplitude of specimens in different build directions [396]. This shows that the build direction had a lesser influence on specimens with equiaxed grains, whereas specimens with columnar grains could withstand much lower cyclic stress amplitude.

Interestingly, a functionally graded cylinder with a core processed at 950 W (59.4 J/mm^3), leading to coarse elongated grains, and a shell processed at 250 W (59.5 J/mm^3), resulting in fine equiaxed grains (Fig. 63). After HT, these cylinders showed the highest fatigue lifetime, which almost double that for HT 250 W (59.5 J/mm^3) specimen.

Kantzos et al. evaluated the influence of hatch spacing and of the corresponding cooling rates on fatigue performance [320]. Increasing the hatch spacing produced some lack of fusion defects, while decreasing the cooling rates resulted in a significant increase in pores size and number. The results highlighted that the fatigue performance was highly sensitive to the changes in porosity of the material.

The influence of scan strategies' contour regions were also considered [321]. The lack of fusion defects in the contour and contour-hatch interface significantly limited specimen fatigue performance and could not be eliminated by thermal post-processing. However, it was shown that this contour region could be mechanically removed, leading to significant improvements in fatigue performance. This challenge is well appreciated in the conventional machining world where surface integrity has been widely studied.

4.4.3. Heat treatments and machining strategy for fatigue performance

Post-processing can be used to reduce porosity and anisotropy in the material, in order to improve its fatigue performance. Wang et al. applied HIP to eliminate or reduce built-in defects, improving their fatigue limit from 500 MPa for AB specimens to 550 MPa [255]. In a study by Kanagarajah et al., a two-stage STA was applied to some LPBF IN939 specimens and found that the HT induced some brittleness in the material, dramatically decreasing specimens fatigue life [253]. In fact, it was found that higher brittleness was related to higher sensitivity to crack initiation and crack growth. A standard HT was instead applied to stress-relieved LPBF IN718 specimens. Fig. 64 shows the strain distribution overlaid with grain boundary maps for stress-relieved and HT specimens after fatigue testing [254]. In the first, strain was evenly distributed, with dislocation pileups at the grain boundaries (Fig. 64a). These coupled with finer grains, reduced stress concentration and crack initiation, were considered as the main fatigue-strengthening mechanisms. HT specimens, at the opposite, showed more localised strain (Fig. 64b). Despite these differences, they also showed excellent fatigue resistance, mainly due to big contribution of precipitation hardening, controlled by γ' and γ'' [254]. The fatigue properties at 455 °C of homogenized STA samples was studied [328]. Similarly, Popovich et al. compared the thermomechanical fatigue life of AB and two-stage HT LPBF IN718 specimens [388]. HT specimens showed a higher fatigue resistance due to the dissolution of the brittle Laves phase and the presence of δ -phase on the grain boundaries.

Balachandramurthi et al. compared the effects of STA and HIP + STA on EBM specimens fatigue performance [321]. The results showed that the HIP + STA yielded much better fatigue resistance than STA only. This is because HIP + STA closed most of the built-in defects and completely dissolved the δ -phase, which can hinder the precipitation of γ'' phases. In another study, LPBF specimens possessed better fatigue performance than those produced by EBM, due to the more numerous lack of fusion defects introduced by EBM [397]. However, it was found

that HIP and HT were able to effectively close the built-in defects in both LPBF and EBM specimens.

Surface finish is another important factor that influences the fatigue performance. In fact, for both LPBF and EBM, the AB surfaces provided more fracture initiation sites than their machined equivalents [397]. Furthermore, it was shown that small-scale specimens show a higher number of surface and near-surface defects which result in reduced mechanical properties, including a 65% reduction in fatigue strength in the case of Kotzem et al. [422]. It is highly likely that components produced by PBF will require machining ahead of experiencing fatigue-based loading conditions. Surface roughness and built-in defects, such as embedded particles, were identified as the main cause of fatigue initiation points (Fig. 65), limiting the fatigue performance [252,384]. Indeed, Wan et al. observed a $\sim 50\%$ increase in fatigue strength after surface machining and polishing [423]. Koutiri et al. observed that the use of lower scan speeds and lower power led to higher surface roughness, particularly on the down-skin sides for large building angles [386,397]. Other polishing processes such as low-stress grinding, have instead been found valid in producing more neat surfaces, thus improving specimens fatigue life [386,397]. Witkin et al. discovered that the AB surfaces of notched fatigue specimen always contained critical-sized defects which may lead to faster fatigue failure than what estimated using notch stress concentration calculations [392]. A modified HT was developed in order to reduce LPBF IN718 anisotropy in fatigue performance [401]. The effects on fatigue performance of surface preparation technique (mechanical or electromechanical polishing) was investigated for LPBF IN718 [402]. The effect of dry or emulsion cutting conditions on the fatigue performance of LPBF IN718 were also investigated and using a dry machining condition resulted in better surface roughness and more compressive residual stress, leading to more cycles to failure [373].

4.4.4. Fatigue crack growth

Konečná et al. and Kim et al. compared the fatigue crack growth rate of conventional (such as rolled or forged material) and LPBF IN718 specimens (Fig. 66) [390]. The LPBF manufactured specimens and their conventional equivalents had similar crack growth resistance in the high ΔK region [390,424], whereas in the intermediate ΔK region, the LPBF samples had much higher fatigue crack growth rate than their conventionally built counterparts [424]. However, the threshold stress intensity factor was about $1 \times 10^{-7} \text{ mm/cycle}$ for LPBF samples, much lower than for conventional equivalents, highlighting the poor fatigue resistance of LPBF manufactured materials. Three main factors were found to be responsible: the lower boron content, the finer microstructure and the presence of residual stress in the LPBF manufactured materials.

Poulin et al. investigated the influence of build direction and post-processing on the crack propagation behaviour of LPBF IN625 specimens [312]. The fatigue crack growth results (Fig. 67) indicated that the crack growth rate of stress-relieved LPBF specimens was highly dependent on the build direction. Similar results by Ma et al. showed the dependence of crack growth rate on build direction at room and elevated temperatures [425]. Furthermore, in a study by Brynk et al., LPBF IN718

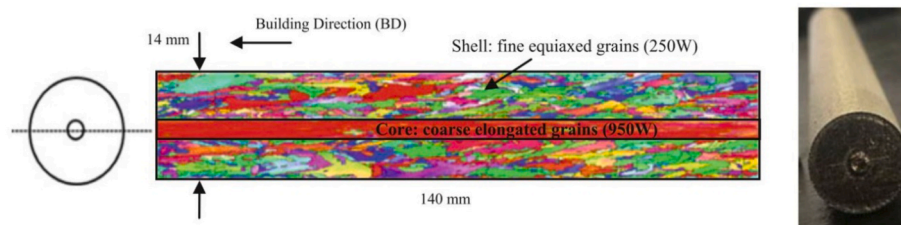


Fig. 63. Diagram of a functionally graded structure with fine equiaxed grains at the core encased by columnar grains. This showcases the degree of grain engineering possible by Powder Bed Fusion to obtain desired mechanical properties [388].

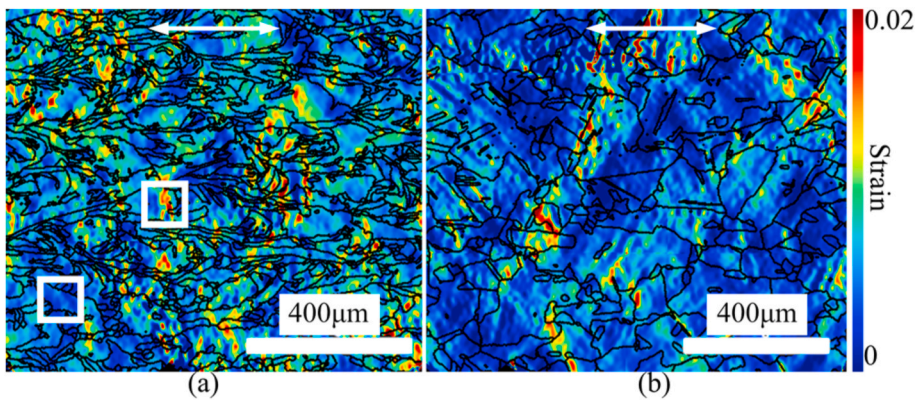


Fig. 64. The strain distribution overlaid with grain boundary maps of specimens after fatigue testing [254]. (a) Stress relieved specimens. (b) Heat treated specimens. Arrows indicate the loading direction. In the stress-relieved state, strain was evenly distributed, with dislocation pileups at the grain boundaries which reduced stress concentration and crack initiation and were considered as the main fatigue-strengthening mechanisms. The heat treated specimens showed more localised strain but showed excellent fatigue resistance, demonstrating the beneficial effects of heat treatment on Fatigue performance of Powder Bed Fused specimens.

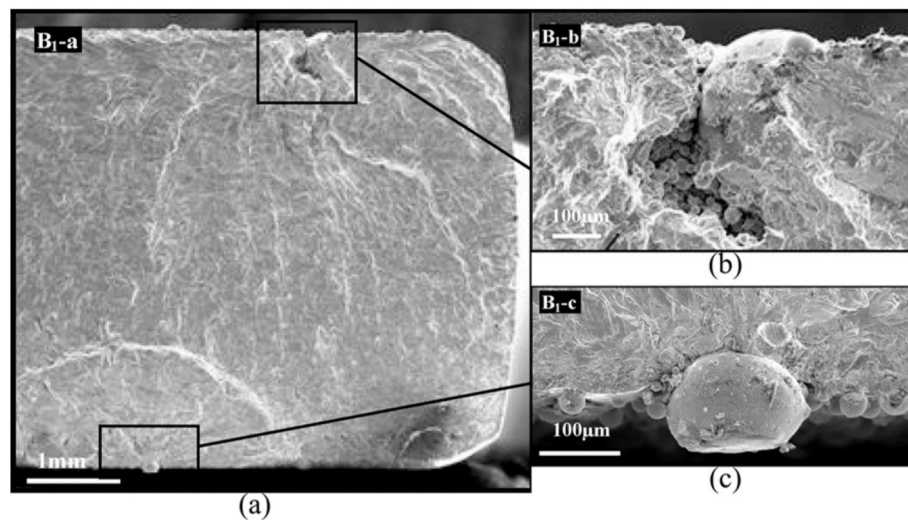


Fig. 65. Scanning Electron Microscopy image of the subsurface defect and Fatigue initiation sites in as-built Laser powder bed fused Inconel 625 [252]. (a) Low magnification. (b) High magnification. (c) Embedded particle on the as-built surface. Surface roughness and built-in defects, such as embedded particles, were identified as the main cause of fatigue initiation points.

specimens built at 45° were found to have the best fatigue crack growth resistance [385]. Post-processing HIP was also successfully used to eliminate the anisotropic behaviour. Finally, the fatigue crack growth rate of LPBF IN625 specimens seemed comparable to the wrought equivalents. Additionally, the effect of HT and loading direction on dwell-fatigue crack propagation resistance of LPBF IN718 at 550°C and 2160 s dwell holding period was investigated and showed that a creep mechanism was dominant [400,426]. The fatigue crack growth rate of LPBF IN625 was found to increase as the stress ratio increases [399]. Horizontal samples had a faster fatigue crack growth rate than vertical samples [399]. LPBF IN738 was built using different laser powers and scan speeds and it was found that small grains present along large grain boundaries act as crack initiation sites or affect crack propagation path [427].

4.5. Creep properties

Creep resistance defines component performance in high-temperature conditions. However, the creep performance of LPBF nickel-based superalloys has not been fully studied yet. Studies have focused mainly on IN718 (Fig. 68a) and the effect of thermal treatments and build orientation (Fig. 68b) on the creep properties. Fig. 68 also highlights the areas which require more research, such as the effect of surface condition and complex geometries on the creep properties of PBF nickel-based superalloys. Investigations to date also report significant

shortfalls with respect to counterparts machined from wrought material.

Creep testing can be categorized into two types: tensile loading tests [75,249,251,384,388,405–407] and compressive loading tests [190,275,295]. The former can normally provide information on creep fracture. For example, Brodin et al. observed the creep fracture surface of LPBF Hastelloy X tested at 815°C with a tensile load [384]. Compressive creep tests are performed to analyse specimens creep rate. The tests were usually interrupted when a predetermined plastic deformation was achieved.

Some non-standard creep specimens, such as 2 bar specimens are also used [75]. Small punch creep specimens are another commonly used specimen geometry, these tests are shown schematically in Fig. 69.

Wang et al. used a small punch creep test to compare the creep performance of forged, cast and LPBF material [411]. The results (Fig. 70) indicated that the AB LPBF specimens possessed similar creep lifetime to the forged ones, but far lower than the cast specimen. Laves phase at the grain boundaries may have led to poor creep performance in LPBF specimens. Moreover, the local tensile stress induced by the experimental loading in the fracture region was believed to be another reason for the reduced time to rupture. Another study also found that LPBF IN718 had a lower creep ductility than their wrought equivalent due to oxide contamination from powder surface [428].

Moreover, new AM 'specific' approaches for creep testing inspection have been investigated. Xu et al. conducted a new staged thermal-mechanical testing method which looked at the defect evolution in the

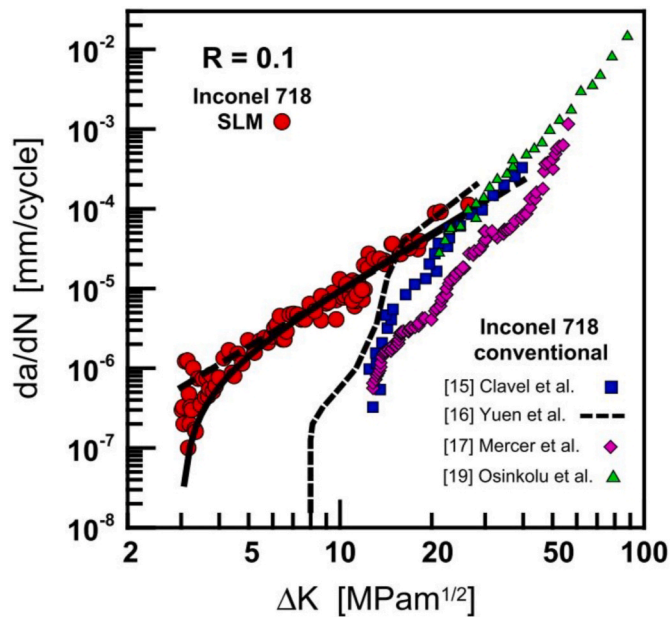


Fig. 66. Diagram showing the differences in fatigue crack growth between Laser Powder Bed Fused and conventionally manufactured Inconel 718 specimens [390]. The Laser Powder Bed Fused specimens and their conventional equivalents had similar crack growth resistance in the high ΔK region [390,424], whereas in the intermediate ΔK region, the Laser Powder Bed Fused samples had much higher fatigue crack growth rate than their conventionally built counterparts. This highlights that Powder Bed Fusion has the potential to have similar mechanical performance to conventional methods.

LPBF IN718 specimens during creep [75]. The idea was to interrupt the testing and characterise the defects using X-ray computed tomography. For example, Fig. 14 shows the porosity distribution in the specimens at the different stages where the test was stopped. This allowed the characterisation of the porosity accumulation during creep and the localisation of the position of the weakest point.

4.5.1. LPBF process parameters affect creep performance and failure

The effect of LPBF building orientation on specimens creep performance has been widely studied [249,251,384,405,406]. Rickenbacher et al. considered the creep performance of horizontally and vertically built LPBF IN738LC specimens [249]. The results indicated that the vertically built specimens had better creep resistance, with respect to cast equivalents. Hautfenne et al., Kuo et al. and Kunze et al. obtained similar results, explaining that vertical samples had the stress applied parallel to the columnar elongated grains, behaving similarly to the creep resistance strengthening mechanisms in directionally solidified and single crystal superalloys [251,405,406,429]. Small Punch Creep test of LPBF CM247LC with different process parameter (beam power, layer thickness and energy density) and build orientations (30° and 90°) found that 90° samples performed better for creep deformation [412]. Sanchez et al. also noted that the build orientation and the stress state were responsible for the different types of failure modes of creep specimens [414]. Shassere et al. also studied the influence of microstructure on creep performance of EBM IN718 specimens [409]. The results indicated that specimens with columnar grains possessed better creep performance than the ones with equiaxed grains, especially when the loading direction was parallel to the columnar grain growth direction. In fact, having the grain boundaries transverse to the loading direction was found to be particularly detrimental on creep resistance.

Laser power is also an important factor which can affect creep performance. Popovich et al. investigated the creep performance of LPBF IN718 specimens manufactured with two different laser power, namely 250 W (59.5 J/mm^3) and 950 W (59.4 J/mm^3). In general, ductile

fracture (Fig. 71a) dominated in specimens produced with lower power, except in some regions rich in brittle precipitates (Fig. 71b) [388]. On the other hand, specimens manufactured using higher power failed before reaching the required testing conditions. This was mainly due to the presence of a large number of built-in defects (Fig. 71c and d) caused by the excessive power. Sanchez et al. also showed that using multiple-laser scan strategies does not adversely affect the creep performance of LPBF IN718, with multi-laser vertically built samples even performing similarly to wrought material [415].

Assessing functional performance of functionally graded materials produced by AM is an interesting emergent research area. Popovich et al. analysed and compared the performance of post-treated LPBF IN718 specimens and functionally graded specimens [388].

4.5.2. Heat treatment for enhanced creep performance

To improve LPBF specimens creep performance, post-processing is still necessary at the present stage. Multiple studies compared the effects of HT on LPBF IN718 specimens [190,275,406,408,413]. Pröbstle et al. characterised the creep performance of cylindrical specimens subjected to different HTs, including direct ageing and STA [190]. The post-treated specimens showed an improved creep performance. As a confirmation, Hautfenne et al. [405] proved that the use of a solution temperature higher than 1000°C could contribute to better creep performance. Using a solution temperature of 1000°C followed by a two-stage ageing treatment resulted in better creep resistance than specimens directly aged [190,275]. However, when the solution temperature was decreased below 1000°C , direct aged specimens performed better [190,406]. Two possible reasons were identified to explain these results [190]. The first might be related to the strengthening phases composition. In nickel-based superalloys, Nb content is critical since it forms the main strengthening precipitates. When solution treated at 1000°C , δ -phase dissolves, releasing Nb in the surrounding matrix and hence allowing more γ'' precipitation. On the contrary, when treated at 930°C , more δ -phase is formed at the expense of γ'' phase. But since these precipitates contribute more to creep resistance than the δ particles, specimens treated at 1000°C perform better. The second possible reason might have been the size of γ'' (Fig. 72), with the largest average size of these precipitates was found in specimens treated at 1000°C ($13.4 \pm 5.8 \text{ nm}$), followed by direct aged ones ($9.4 \pm 3.2 \text{ nm}$) and lastly the 930°C treated ones ($9.1 \pm 5.8 \text{ nm}$) [190]. Wang et al. however, noted that using STA resulted in a shorter creep life than using homogenisation and ageing treatments [430]. Another study found that creep life and ductility was improved after HT by adding Y (yttrium) as Y-oxide (yttria) precipitated around the δ -phase instead of Al-oxides, which impeded δ -phase precipitate growth and improved creep properties [413]. (Table 11)

Similarly, Davies et al. tried two HT strategies with different solution temperatures (1150°C and 1275°C) to improve the creep performance of LPBF C263 and found that the higher solution temperature increased creep resistance [410]. This was because a higher solution temperature generated a more equiaxed microstructure, smaller average local misorientation, shorter random grain boundary network segment length and carbides (MC and M_6C) precipitation at grain boundaries. It was concluded that shorter random grain boundary network segment length, meant shorter potential intergranular crack paths. In turn carbides could hinder grain boundaries deformation, further improving creep resistance. However, despite HT increasing creep life of LPBF IN718 samples, Sanchez et al. scan lines were apparent on the fracture surface of vertically built HT samples (Fig. 73b-b',c-c'), showing that despite post-processing, an AM specific failure still occurred [414].

In summary, effort must be directed to understand and optimise post-processing to improve creep performance of LPBF manufactured nickel-based superalloys. Published data for the creep testing of LPBF manufactured nickel-based superalloys are compiled in Table 12 for the convenience of the reader.

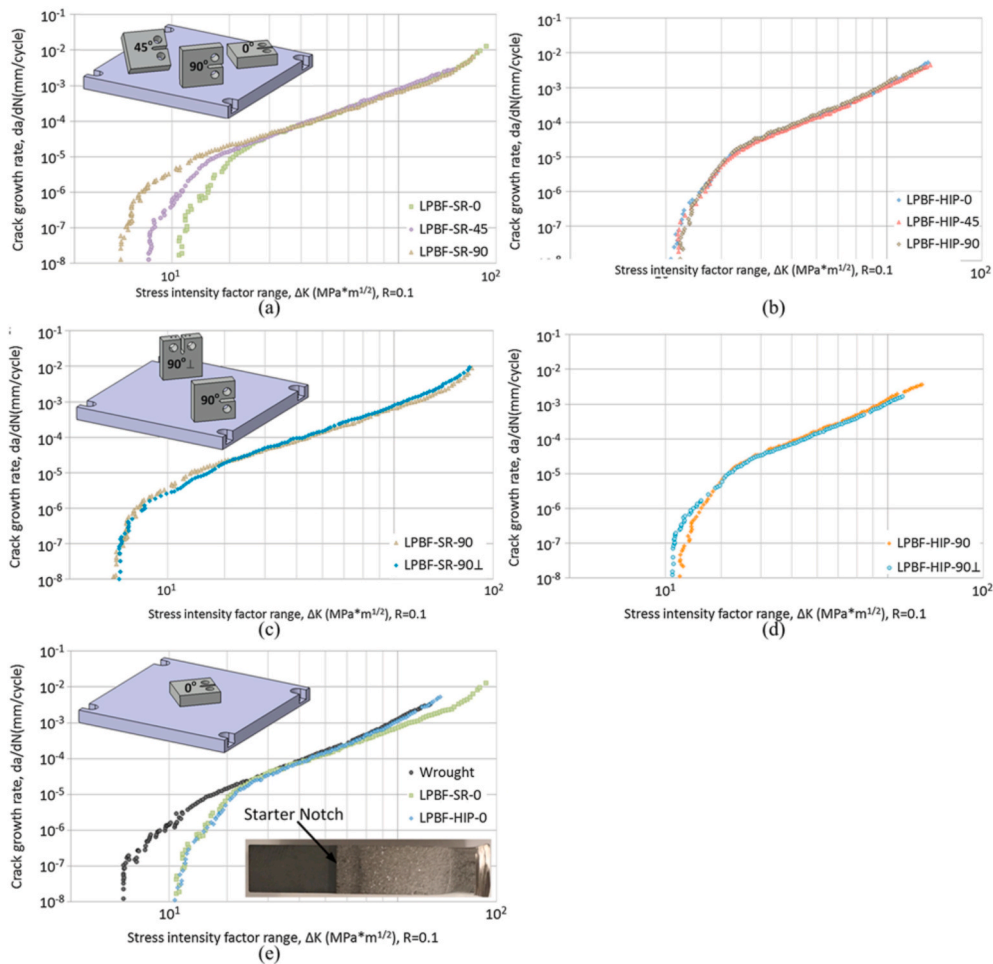


Fig. 67. Fatigue crack propagation diagrams of specimens in various heat treated conditions and build orientations [312]. They indicate that the crack growth rate of stress-relieved Laser Powder Bed Fused specimens was highly dependent on the build direction.

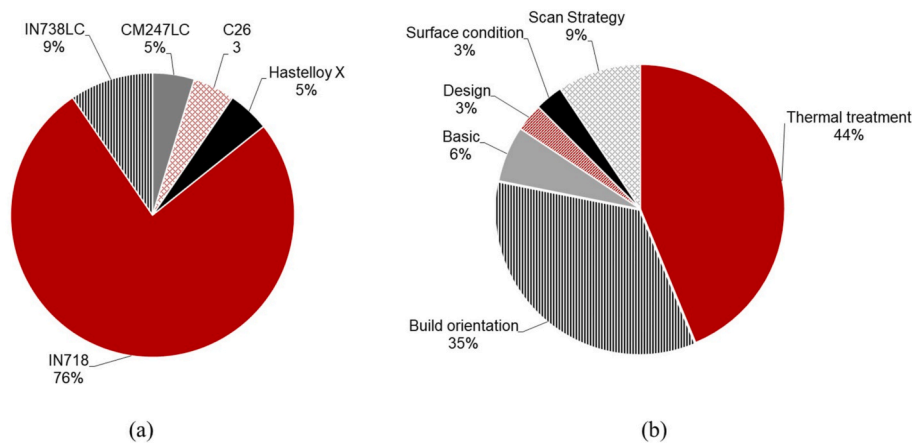


Fig. 68. Pie chart of the materials and the powder bed fusion parameters investigated in the creep studies to date, from 21 papers. (a) The materials studied. (b) The parameters studied (the label “Basic” refers to studies which only tested the material in one condition, focusing on performance without looking into the effect of a certain parameter.) Inconel 718 is the main material investigated and the effect of thermal treatments and build direction have been studied the most.

5. Toward more appropriate testing procedures for AM

Conventional approaches to mechanical testing of AM components are costly and can serve to undermine the use case for AM. As such alternate approaches are required. Small specimen testing techniques have the capability to characterise a localised mechanical response

while using only a small volume of materials [429]. For example, a small specimen testing method called “small punch test” exhibits potential in characterising LPBF nickel-based superalloys mechanical performance [430]. In fact, this method has been accepted as an approach to estimate mechanical properties from small quantities of materials only. The test is performed by deforming a disc specimen, typically 8 mm in diameter

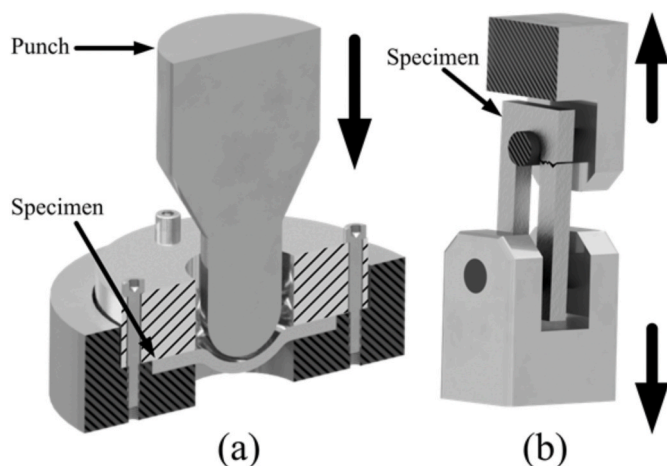


Fig. 69. Schematic showing tests on two non-standard specimens. (a) Small Punch test. (b) Two Bar Specimen test. This illustrates the potential of small and non-conventional specimen testing in Powder Bed Fusion.

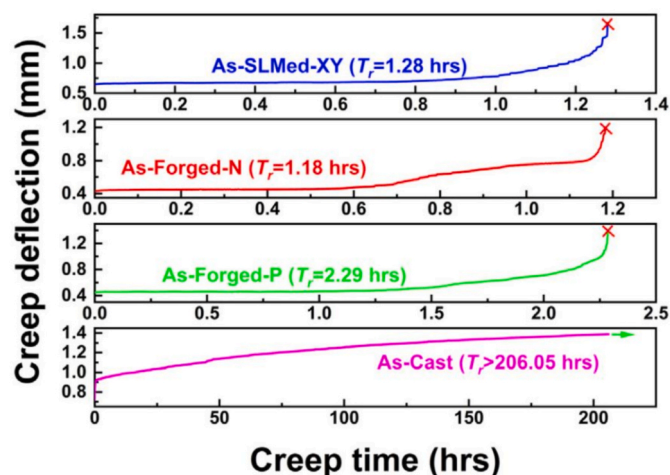


Fig. 70. Creep deflection vs creep time results for specimens in different conditions (Forged-N: loading direction parallel to the forging direction; Forged-P: loading direction perpendicular to the forging direction) [411]. Indicating that the as-built laser powder bed fused specimens possessed similar creep lifetime to the forged ones, but far lower than the cast specimen.

and 0.5 mm thick, under a hemispherical punch with a radius of 1–1.25 mm [431]. Two test configurations are available: constant load, which shows a creep-type response and is termed small punch creep test (SPCT); and constant displacement rate, which exhibits a tensile-type behaviour and is called small punch tensile test (SPTT) [432]. The specimen will deform biaxially and the data obtained can either be plotted on a displacement versus fracture time chart for SPCT [433] or load versus displacement chart for SPTT [434]. Both data sets can be correlated to the equivalent bulk mechanical properties through various means [419–422]. The small punch test method has been widely applied to evaluate the mechanical performance of various aerospace nickel-based superalloys [423–428]. Since only a small volume of material is required, this test offers a feasible option to study AM components mechanical properties when traditional testing methods are not possible, due to complex design geometries [429–431].

The anisotropic nature of PBF components has been highlighted on numerous occasions in this review. This is a major concern for the structural integrity of these materials. AB LPBF components usually exhibit microstructural and hence mechanical discrepancies between the build direction and the scanned planar direction. Even though

various strategies have been employed to minimise this tendency, it is inevitable to have anisotropic LPBF materials, mainly because of the layer-upon-layer approach. The community is exploring scanning and building strategies to ameliorate anisotropy however this will require maturation of process technology and control in unison with the development of our materials understanding.

It is generally observed that the material is mechanically weaker in the build direction (Z direction) as compared to in the X–Y plane. This is thought to be caused by poor bonding at the interface between individual layers. These anisotropies can also be evaluated through small specimen tests [431,432]. Small specimens can be sampled from different planes, allowing a localised investigation of the anisotropic behaviour of LPBF nickel-based superalloys. Using this technique, rapid adjustments on the process parameters can be done to minimise this tendency. This may allow researchers to have a better understanding of worst case scenarios.

However, there are applications where anisotropy is sought [433]. For example, one AM sector that can greatly benefit from LPBF components anisotropy is lattice structure design [434,435]. These structures allows for lightweight design and good mechanical properties in specific load conditions. PBF capability in manufacturing lattice structures outweighs traditional manufacturing processes. To date, studies concerning the effectiveness of lattice structure on bulk mechanical properties are few and future work in this area would benefit the AM community. In addition more complex testing configurations (e.g. triaxial approaches) are required in order to validate component performance in these cases.

Using more complex designs and lattice structures is quite clearly a research trend in AM [436]. For metal specific approaches a review of design and mechanical properties of metal lattice structures was written by Hanks et al. [437]. Here it is critical to ensure that methods are devised which can appropriately assess both the structural and material properties of AM components. A shortfall of many contributions made within the AM literature.

6. Conclusions

Regardless of the unique advantages PBF boasts compared to more traditional manufacturing processes it is widely recognized within the literature that morphological defects and suboptimal microstructures limit the performance of Nickel-based superalloys in current class PBF approaches. This is not confined to Nickel-based superalloys alone and remains a broader materials problem. However, the high sensitivity of Ni alloy performance to precipitate, phase, texture and grain size makes these systems particularly challenging when compared to Ti or Fe based alloys. Further, the primary application areas (including within turbo-machinery) mean that manufacturers require enhanced surety of the performance of these materials. This is particularly relevant for dynamic components subject to both thermal and mechanical loading cycles. As such many of the defects characteristic of PBF processes cannot be tolerated.

From the literature there is a desire to understand the influence of PBF process parameters - such as power density, scanning strategy and build direction - on specimen final mechanical properties. However, there is little evidence that product direct from machine will remotely match the performance of 'machined from wrought' equivalents. Hence there has been a significant body of work evaluating post-processing strategies which includes both thermomechanical techniques (to recover microstructural and in-built defects) and surface processing techniques to address stress concentration issues. This comes in the context of a rapidly developing machine tool market for AM which is seemingly improving month-to-month.

It is also evident that the extensive campaigns for mechanical evaluation of PBF nickel-based superalloys through traditional test methods is time-consuming and costly. Furthermore, PBF specimens often exhibit evolving microstructures and properties throughout the building

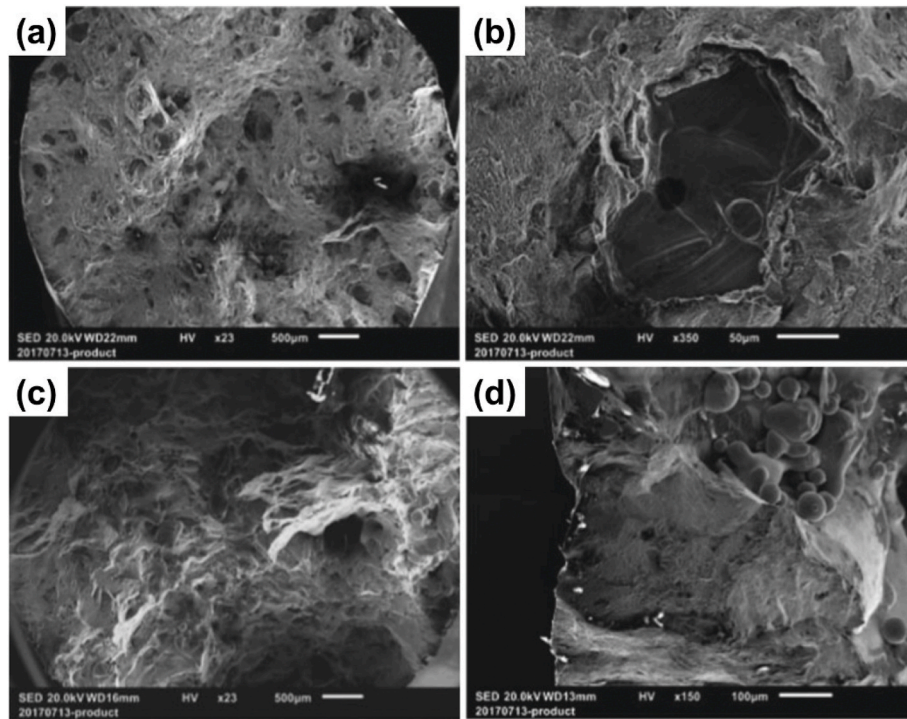


Fig. 71. Creep fracture surfaces of Laser Powder Bed Fused Inconel 718 specimen built with varying laser power [388]. (a),(b) Laser power of 250 W (59.5 J/mm^3). (c),(d) Laser power of 950 W (59.4 J/mm^3). This highlights the catastrophic failure associated with lack of fusion.

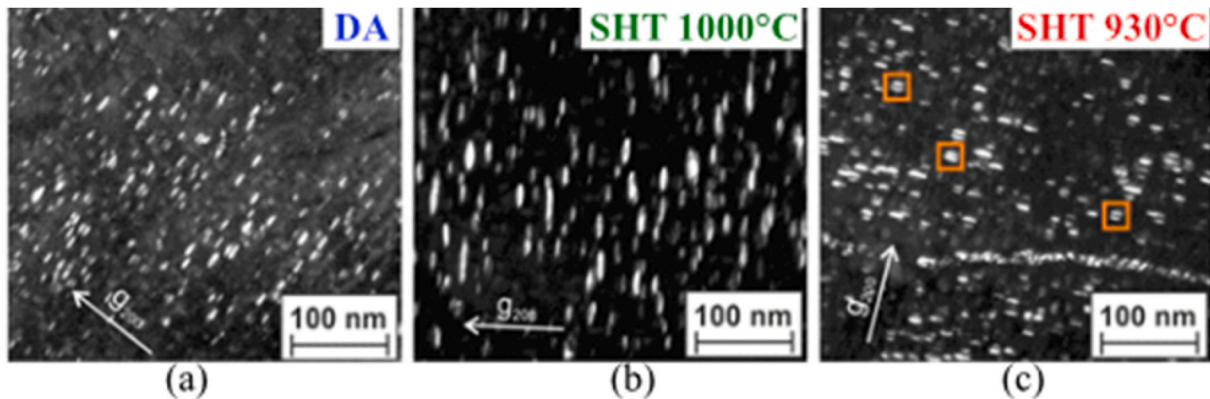


Fig. 72. Transmission Electron Microscopy images showing the γ' phase after different thermal treatments [190]. (a) Direct aged (DA). (b) Solution treated at $1000 \text{ }^\circ\text{C}$ then aged (SHT $1000 \text{ }^\circ\text{C}$). (c) Solution treated at $930 \text{ }^\circ\text{C}$ then aged (SHT $930 \text{ }^\circ\text{C}$) conditions. Using a solution temperature of $1000 \text{ }^\circ\text{C}$ followed by a two-stage ageing treatment resulted in better creep resistance than specimens directly aged, but when the solution temperature was decreased below $1000 \text{ }^\circ\text{C}$, direct aged specimens performed better.

process, while most of the traditional testing standards were designed for monolithic materials. Hence, these testing methods might not reflect the localised mechanical discrepancies in LPBF materials to equip designers with appropriate information. In some regards, particularly pre-HT, AM components are best considered as a continuous fabrication (a single weld constituting the whole component) as opposed to a monolithic and uniform component. They should therefore be analysed as such.

This review has highlighted a suite of Ni based materials which are explored in the literature. Many of these can be considered the 'low hanging fruit' in that they readily consolidate in PBF to realise components. However, the pallet of materials processable by AM is continually developing and much of this resides in proprietary knowledge and is not committed to the academic literature. The wider exploitation of materials within AM will require the development of several approaches to

accelerate this. Indeed the opportunities for materials development for PBF platforms may be inferred throughout this review.

Machine tool technology is also proving to be a limiting factor. Process control strategies commonly observed in even low cost conventional machine tools are not yet available for AM systems. As such the immaturity of PBF systems is apparent from many of the studies reported. The current state-of-the-art does indeed deliver parts but the repeatability and reliability of these is still very much a work in progress. The shortfalls of current platforms often make the use of PBF a tenuous decision. Similarly, to materials development this paper has highlighted numerous opportunities for machine tool innovation which will enhance the utility of nickel-based materials in AM.

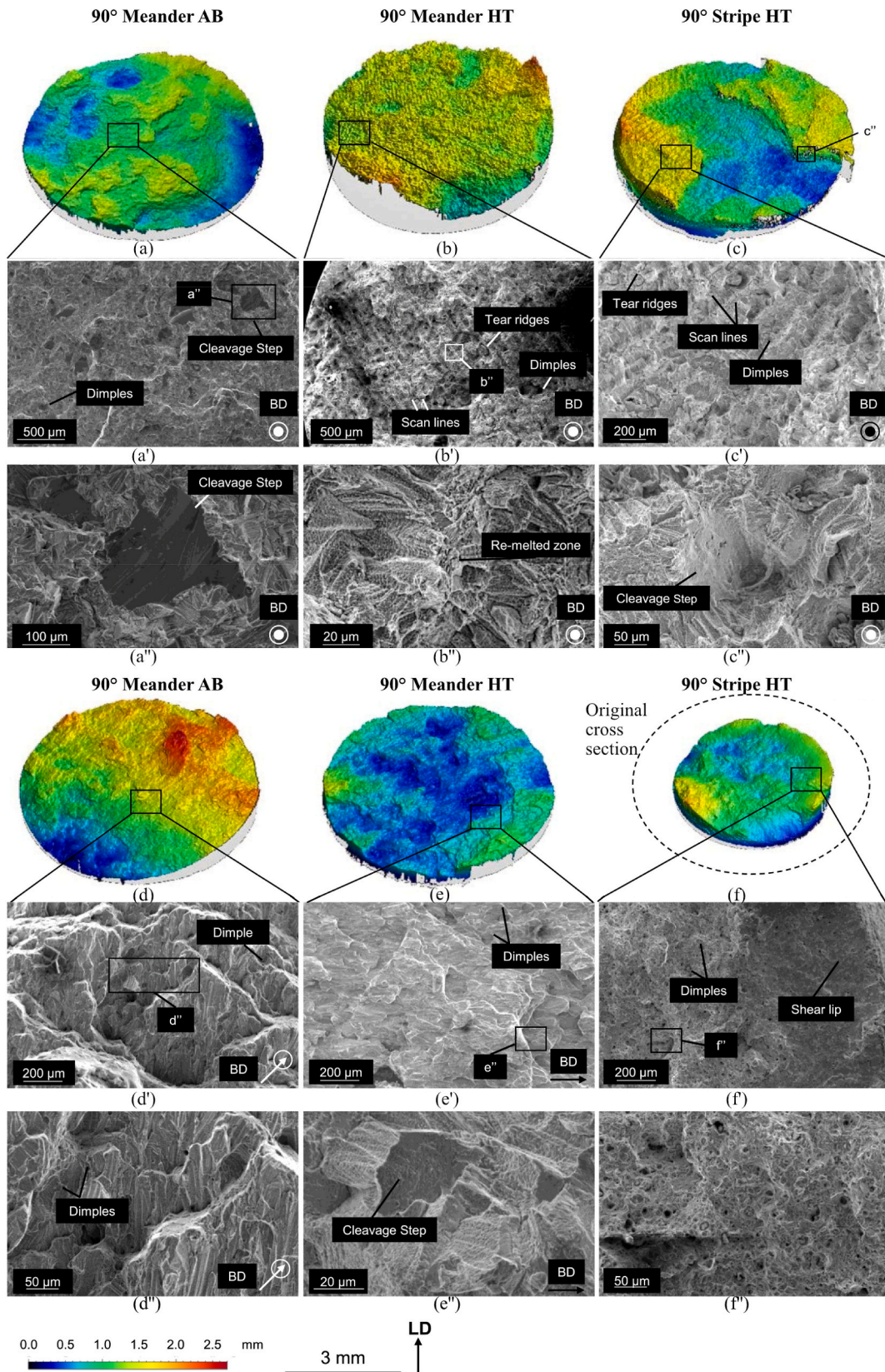


Fig. 73. Fracture surfaces of Laser Powder Bed Fused Inconel 718 after creep testing [414]. (a) – (a'') 90° Meander as-built; Heat treated (b) – (b'') 90° Meander; (c) – (c'') 90° Stripe; (d) – (d'') 45° Stripe; (e) – (e'') 0° Stripe and (f) – (f'') Wrought Inconel 718 specimens. All images oriented in line with the Loading Direction (LD). All surfaces showed signs of ductile fracture and apparent scan lines on the heat treated 90° samples, which indicates that heat treatments are still not optimised for Powder Bed Fused materials.

7. Research outlook

Based upon our assessment of the state-of-the-art, the authors propose the following key themes (summarised in Fig. 74) as being of primary interest to proliferate the manufacture of Ni superalloy components using PBF:

- **Heat treatments within-process** – post-processing of any description with reduce the already tenuous business case for deploying AM. As such there is a real need to arrive at desired integrity and microstructure within the process. This will be derived from enhanced process understanding and control. Where ‘post-processing’ cannot be achieved in process, which will be the case for some time, we must consider efficient methods for installing the properties and performance required by specification. These may not always be consistent with methods for processing wrought equivalents but will allow designers to make better and wider use of PBF Ni alloys.
- **Enhanced thermal management** - Advanced scan strategies, ‘new’ energy beam profiles and in-process monitoring have the potential to overcome cracking and stochastic pore formation in difficult to process materials. They may also allow users to introduce microstructure by design. These approaches present additional challenges as they are so rich in data generation that the role of the computer scientist will be important in gathering and interpreting this. This is analogous to process control which is far more mature in more established manufacturing technologies.
- **Modelling** – Allied to the development which will emerge in process control, it is essential that we develop higher fidelity but computationally lighter modelling approaches. To relate process to part performance there will be a significant need to predict recrystallisation phenomenon over longer ranges which deal with part

geometry at scale. In addition, machine tools must respond to complex events in process and as such ‘on-the-fly’ modelling approaches will be required to develop truly adaptive processes.

- **Design** – Exploitation of PBF (and all forms of AM for that matter) hinges upon designing for these techniques. It is foolish to expect that PBF will simply replace the preferred method of manufacturing for all components. Typically, such components will incorporate many processes whose effect upon tolerancing and microstructure are well understood. Our understanding of PBF in this regard is somewhat more juvenile and a holistic approach for PBF introduction is required.
- **Build environment** – It is apparent throughout the work presented here that build environment (pressure and species) drives the consolidation phenomena amongst other factors. In the opinion of the authors this feature of modern LPBF (this is less of an issue in EBM systems or course) is primed for further development and will be a feature of machine tools capable of achieving superior material properties in Nickel-based superalloys.
- **Standardisation** – Through groups such as the ASTM F42 committee, significant contributions have been made in standardisation descriptors and taxonomy. Much work remains however to allow direct comparison between machine technologies and resulting product. The reader will encounter this difficulty when assessing the extended appendices, the authors have compiled. It proves most difficult to draw meaningful conclusions without comparing like-with-like.
- **Alloy formulation** – This review has highlighted much work which attempts to process powdered specimens of existing and widely used Nickel-based superalloys. However, there is a tremendous opportunity within the Ni superalloy metallurgical fraternity to modify alloys specifically for AM processing. There is also an opportunity in

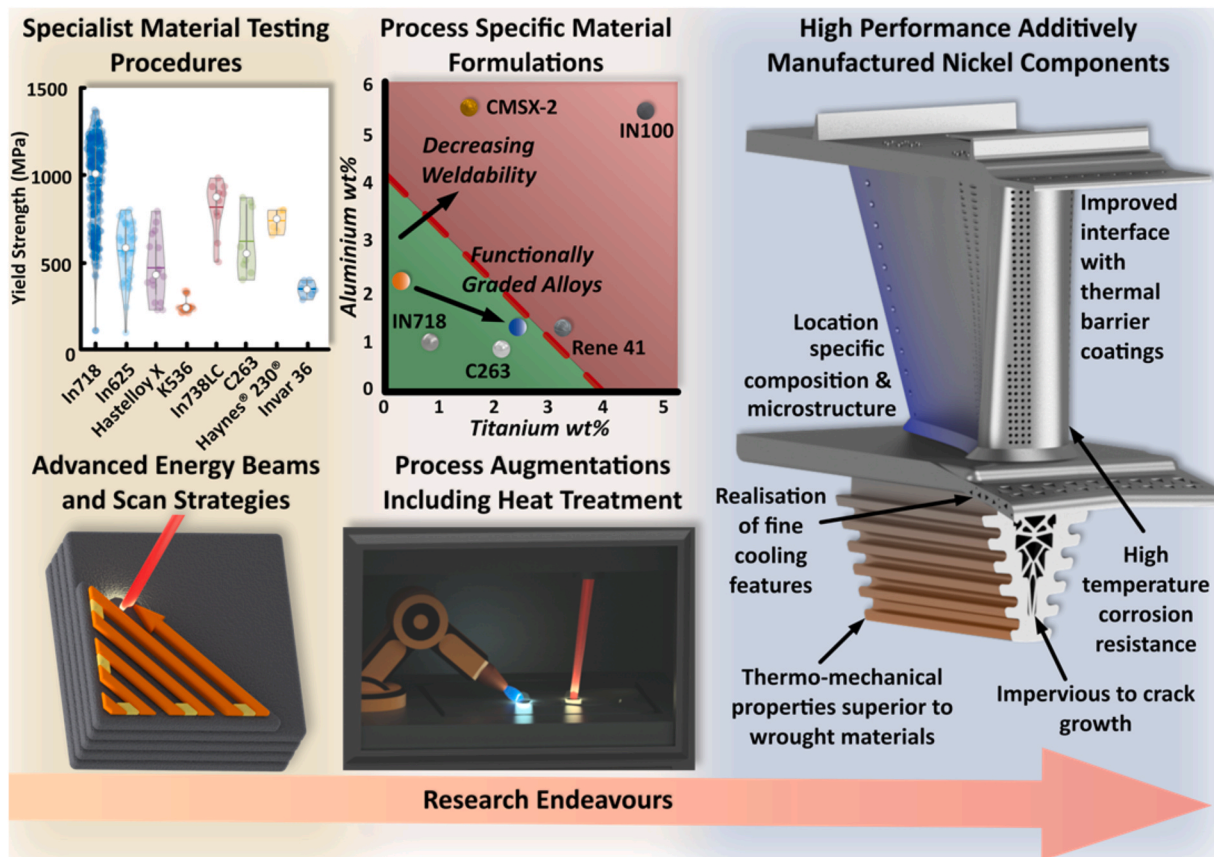


Fig. 74. Graphical representation of future research trends required to develop the next generation Powder Bed Fused nickel-based superalloys. Here an exemplar gas turbine blade is used to illustrate a vision for convergence of several new manufacturing capabilities.

this regard to devise new methods to enhance the longevity of Ni based materials through processing and devise reuse strategies in which alloy performance can be assured. The ability to reuse/recycle metal powder for PBF will therefore be hugely important in driving down process costs.

- **The role of AI** – Artificial intelligence as a discipline, while not new, is proving to be useful in materials and process design for AM. Through sophisticated decision making from suboptimal data sets it is possible to advance process and material development at pace. The authors propose that the role of AI will become more prevalent in AM given the experimental space which emerges when seeking to optimise composition and process parameter sets. Clearly automation and evaluation will be critical in driving this area when coupled to both experimental and modelling efforts.

The authors have had the privilege of exploring the AM literature from first efforts with powder bed fusion through to the state-of-the-art. It is fitting that Nickel-based superalloys were explored early in the development of AM but presented significant challenges as compared to the more readily processible Titanium and Iron based alloys which

'weld' well under PBF conditions. Many of the metallurgical challenges presented by nickel-based alloys persist and can trace their heritage back to the conception of these alloys as a family. As such we may suggest that AM practitioners continue to try to find new solutions to these established problems.

The rate of literature contributions to this domain is clearly increasing as researcher access to PBF techniques expands. As such, *this review will age much faster than a nickel-based superalloy in service* but the authors would hope that this contribution is of some value to our community providing a reference to common challenges and baseline performance while inspiring the pursuit of new research directions. We trust the work is of value and would welcome scientific dialogue on all topics contained here.

Declaration of competing interest

The authors declare that they have no known competing financial interests or personal relationships that could have appeared to influence the work reported in this paper.

Appendix A. Composition of IN718 and IN625

Table 8 below summarises the chemical composition of the most used nickel-based superalloys in PBF research: IN718 and IN625.

Table 8
Summary of the chemical composition (wt%) of the most used nickel-based superalloys in PBF (from CES EduPack software, Granta Design Limited, Cambridge, UK, 2009).

Elements (wt%)	IN718	IN625
Ni	50–55	58–69
Cr	17–21	20–23
Fe	11–25	<5
Mo	2.8–3.3	8–10
Nb	2.4–2.8	3–4
Ta	2.4–2.8	0.15
Ti	0.65–1.2	<0.4
Al	0.2–0.8	<0.4
Co	<0.1	<1
Mn	<0.35	<0.5
Si	<0.35	<0.5
Cu	<0.3	
C	<0.08	<0.1
P	<0.015	<0.015
S	<0.015	<0.015
B	<0.006	

Below are a summary of the mechanical properties reported in the literature.

Appendix B. Tensile properties of PBF Nickel-based superalloys

Table 9
Summary of tensile properties of PBF Nickel-based superalloys ('~' indicates that the data was obtained from the bar chart).

Technique	Material	Standard	Test condition	Sample Condition	Yield strength (MPa)	Tensile strength (MPa)	Elongation (%)	Young's modulus (GPa)	Ref
LPBF	C263		Small punch tensile test	90°/HT 1/20 °C	818	1100			[273]
				90°/HT 1/780 °C	401	409			
				0°/HT 1/20 °C	870	1045			
				0°/HT 1/780 °C	513	480			
				90°/HT 2/20 °C	843	886			
				90°/HT 2/780 °C	489	589			
				0°/HT 2/20 °C	590	1078			
LPBF	CM247LC	ASTM E8/E8M		0°/HT 2/780 °C	442	548			[270]
				90°	~790.8	~1012.7	~5.53		
LPBF	CM247LC			AB				220	[311]
				STA (1210 °C)				226	

(continued on next page)

Table 9 (continued)

Technique	Material	Standard	Test condition	Sample Condition	Yield strength (MPa)	Tensile strength (MPa)	Elongation (%)	Young's modulus (GPa)	Ref
LPBF	EP718			STA (1230 °C)				227	[173]
				STA (1240 °C)				226	
				STA (1260 °C)				227	
LPBF	FGH100L		Strain rate 10^{-3} s^{-1}	0°/AB	586	845	27		[324]
				0°/SA	1046	1301	6		
				0°/HIP + SA	1025	1306	24.4		
LPBF	FGH4096 M		Strain rate 10^{-3} s^{-1}	AB	761 ± 16	874 ± 12	3.25 ± 0.16		[341]
				HT	1094 ± 14	1232 ± 21	6.35 ± 0.28		
				HIP	879 ± 21	1146 ± 20	10.17 ± 0.11		
LPBF	GH648		Strain rate 10^{-3} s^{-1}	HIP + HT	1155 ± 17	1307 ± 15	5.59 ± 0.25		[143]
				AB	958.22	1204.13	24.97		
				DA	1459.46	1595.56	5.49		
LPBF	HastelloyX		Strain rate 1.5 mm/min	STA (1050 °C)	1039.86	1299.75	15.68		[178]
				STA (1130 °C)	1006.36	1322.02	14.44		
				Double Aging	1037.86	1325.72	10.74		
LPBF	HastelloyX		Strain rate 10^{-3} s^{-1}	325 W/annealed	890		~40		[255]
				0°/AB	480 ± 10	620 ± 15	40 ± 1	149 ± 9	
				0°/HIP	350 ± 6	560 ± 9	41 ± 4	150 ± 5	
LPBF	HastelloyX	ASTM E8/E8M	Strain rate 0.05 s^{-1}	AB (built in the centre of the building plate)/RT	~812.5	~924.5	~34.5		[179]
				AB (built in the corner of the building plate)/RT	~812.5	~924.5	~34.5		
				HIP (centre)/RT	~557	~839.5	~30		
				HIP (corner)/RT	~556.5	~841.5	~29.5		
				AB (centre)/750 °C	~544	~756	~22.5		
				AB (corner)/750 °C	~544	~757.5	~21.5		
				HIP (centre)/750 °C	~416	~729	~18.5		
				HIP (corner)/750 °C	~412.5	~726	~19		
				0°/AB	~650.15	698.59	8.79		
				90°/AB	601.26	784.98	27.67		
LPBF	Original Hastelloy X (OHX) Modified Hastelloy X (MHX)	ASTM E21	Strain rate 0.015 mm/min	0°/HT	413.73	672.30	22.5		[284]
				90°/HT	417.14	717.37	36.98		
				0°/HIP	468.85	807.51	39.83		
				90°/HIP	431.16	754.93	41.90		
				0°/HIP + HT	430.53	777.47	49.14		
				90°/HIP + HT	400.33	739.91	55.6		
				OHX/RT	~727.88	889.38	22.63		
LPBF	Hastelloy X	ASTM E8	Strain rate 0.005 mm/min	MHX/RT	723.45	882.74	24.74		[180]
				OHX/1033K	384.96	482.30	46.11		
				MHX/1033K	400.44	502.21	15.68		
				90°/AB/RT	663 ± 12	773 ± 9	22		
				90°/HT/RT	420	723	42		
				90°/HIP/RT	440	730	48		
				0°/AB/RT	792 ± 1	923 ± 9	25		
LPBF	Hastelloy X	ASTM E8	Strain rate 2 mm/min	0°/HT/RT	370	793 ± 20	50 ± 2		[334]
				0°/HIP/RT	400	800 ± 10	45		
				90°/AB/750 °C	386 ± 19	453	11		
				90°/HT/750 °C	270	420	40		
				90°/HIP/750 °C	270	410	38		
				0°/AB/750 °C	460 ± 17	543 ± 17	12		
				0°/HT/750 °C	230	450 ± 2	38		
LPBF	Hastelloy X	ASTM E8	Strain rate 1.33 × 10 ⁻³ s ⁻¹	0°/HIP/750 °C	230	440 ± 2	38		[340]
				AB	730 ± 20		14 ± 1		
				0.2% less Si, Mn and C (than above)/AB	590 ± 5		37 ± 2		
LPBF	Hastelloy X		Strain rate 0.05 s ⁻¹	Hastelloy X/AB	584	734	19 ± 2.8		[117]
				Hastelloy X + 1 wt% TiC	682 ± 5.6	849 ± 1	15 ± 4.2		
LPBF	Haynes® 230®	DIN 50125 A-5x25	Strain rate 0.05 s ⁻¹	Various build orientations and high temperature tensile test	See Fig. 5 in the original reference paper				[279]
				0°/Energy density 116 J/mm ³	798 ± 5	1102 ± 3	28 ± 1	205 ± 4	
				90°/116 J/mm ³	656 ± 4	941 ± 2	32 ± 3	152 ± 1	
				0°/77 J/mm ³	794 ± 6	1087 ± 5	25 ± 2	201 ± 2	
				90°/77 J/mm ³	681 ± 2	979 ± 5	25 ± 4	165 ± 3	
				0°/66 J/mm ³	798 ± 10	1077 ± 11	21 ± 2	201 ± 3	
				90°/66 J/mm ³	702 ± 6	991 ± 19	16 ± 4	179 ± 4	
LPBF	IN100	ASTM E8/E8M		AB	~821.95	1029.27	8.98		[280]

(continued on next page)

Table 9 (continued)

Technique	Material	Standard	Test condition	Sample Condition	Yield strength (MPa)	Tensile strength (MPa)	Elongation (%)	Young's modulus (GPa)	Ref		
Micro laser aided AM				SA/RT SA/600 °C	956.10	1048.78 904.88	4.96				
1063.41 LPBF	5.00 IN625		Strain rate, 10^{-3} s^{-1}	10°/AB 35°/AB	711 727	976 971	35%RA 35%RA	177 179	[252]		
LPBF	IN625		Strain rate 10^{-3} s^{-1}	0°/AB/RT 90°/AB/RT 0°/SR/RT 90°/SR/RT 0°/ST/RT 90°/ST/RT 0°/HIP/RT 90°/HIP/RT 0°/AB/760 °C 90°/AB/760 °C 0°/SR/760 °C 90°/SR/760 °C 0°/ST/760 °C 90°/ST/760 °C 0°/HIP/760 °C 90°/HIP/760 °C			~27.3 ~36.9 ~30 ~39.3 ~48.3 ~52.7 ~53.0 ~58.7 ~6.0 ~22.1 ~12.3 ~37.7 ~15.0 ~12.3 ~24.8 ~21.6		[263]		
LPBF	IN625		Strain rate $\sim 10^{-3} \text{ s}^{-1}$	90°/HIP 0°/HIP	360 380	880 900	58 58		[264]		
LPBF	IN625	ASTM E8/E8M	Strain rate 0.5 mm/min	AB AB carbon nanotube strengthened HT carbon nanotube strengthened	641.5 ± 23.5 788 ± 29 585 ± 10	878.5 ± 1.5 998 ± 34 1000 ± 3	30 ± 2 19.1 ± 0.1 31.5 ± 0.5	196 ± 12 378 ± 12 293 ± 5	[266]		
LPBF	IN625		Strain rate 10^{-3} s^{-1}	90°/AB 90°/SR 90°/RA 90°/ST 90°/HIP V 0°/AB 0°/SR 0°/RA 0°/ST 0°/HIP 45°/AB 45°/SR 45°/RA 45°/ST 45°/HIP 90°/AB/760 °C 90°/SR/760 °C 90°/RA/760 °C 90°/ST/760 °C 90°/HIP/760 °C 0°/AB/760 °C 0°/SR/760 °C 0°/RA/760 °C 0°/ST/760 °C 0°/HIP/760 °C 45°/AB/760 °C 45°/SR/760 °C 45°/RA/760 °C 45°/ST/760 °C 45°/HIP/760 °C			~0.60 0.55 0.48 0.4 0.35 0.65 0.58 0.51 0.4 0.35 0.67 0.62 0.52 0.40 0.36 0.35 0.36 0.30 0.26 0.23 0.36 0.37 0.32 0.26 0.21 0.39 0.40 0.34 0.28 0.24	0.82 0.81 0.78 0.79 0.78 0.85 0.89 0.83 0.81 0.78 0.87 0.93 0.83 0.80 0.36 0.39 0.32 0.31 0.34 0.37 0.40 0.34 0.32 0.32 0.35 0.41 0.41 0.35 0.33 0.35	36.6 39 43.1 52.5 58.7 27.5 29.8 37.5 48.2 53.1 30.8 34.7 41.7 52.9 53.8 22.4 37.9 36.6 12.4 21.5 5.9 12.2 11.7 15.1 25.0 7.0 11.1 9.9 11.1 23.5		[269]
LPBF	IN625	ASTM E8/E8M	Strain rate 0.015 min ⁻¹	0°	~765.86	~1068.99	~33.86	~185.60	[272]		
LPBF	IN625	ISO-7500/1	Strain rate 1 mm/min	0° 90°	800 ± 20 720 ± 30	1030 ± 50 1070 ± 60	~8-10 ~8-10		[282]		
LPBF	IN625	EN-10002/ISO-6892		0° 90°	734 ± 3 579 ± 5	1036 ± 3 888 ± 6	36 ± 0.3 40 ± 1	200 ± 3 159 ± 5	[288]		
LPBF	IN625	ASTM E8/E8M	Strain rate 8.10^{-3} s^{-1}	AB DA STA ST	783 ± 23 1012 ± 54 722 ± 7 396 ± 9	1041 ± 36 1222 ± 56 1116 ± 6 883 ± 15	33 ± 1 23 ± 1 35 ± 5 55 ± 1		[303]		
LPBF	IN625			0° 90°	396 ± 33 349 ± 5	906 ± 28 842 ± 29	62.34 ± 1.98 56.3 ± 6.24	561 ± 14 539 ± 58	[100]		
LPBF	IN625		Strain rate 10^{-3} s^{-1}	0°/SR 90°/SR 0°/HIP	718 ± 13 685 ± 87 442 ± 6	1069 ± 11 1009 ± 56 933 ± 14	37 ± 2 43 ± 5 43 ± 4	202 ± 3 195 ± 12 212 ± 7	[312]		

(continued on next page)

Table 9 (continued)

Technique	Material	Standard	Test condition	Sample Condition	Yield strength (MPa)	Tensile strength (MPa)	Elongation (%)	Young's modulus (GPa)	Ref
LPBF		IN625		90°/HIP 0.5 mN at 1/10 of layer thickness	425 ± 9 AB/0 dpa [376]	923 ± 21 AB/0.1 dpa AB/0.5 dpa AB/1 dpa ~215	46 ± 5	214 ± 7 ~225	~220 ~220 ~210
AB/3 dpa LPBF	IN625		Strain rate 10 ⁻³ s ⁻¹	AB AB + 90 °C/1h AB + 1100 °C/1h	652 ± 10 567 ± 15 409 ± 14	925 ± 13 869 ± 7 886 ± 11	32 ± 3 38 ± 1 56 ± 5	145 ± 4 142 ± 11 114 ± 8	[325]
LPBF	IN625		815 °C Average load: 1021 N 815 °C Average load: 1147 N	ST Welding zone		355.6 392.5			[329]
LPBF	IN625		Strain rate 10 ⁻³ s ⁻¹	Along the laser scanning Normal to laser scanning	686.7 747.9	967.5 1077.8	11.5 9		[416]
LPBF	IN625	ISO 6892-1:2009	Strain rate 2.5 × 10 ⁻⁴ s ⁻¹	Build orientation on X-axis; 90° interlayer rotation Build orientation on X-axis; 67° interlayer rotation Build orientation on X-axis; 45° interlayer rotation Build orientation on Y-axis; 90° interlayer rotation Build orientation on Y-axis; 67° interlayer rotation Build orientation on Y-axis; 45° interlayer rotation Build orientation on Z-axis; 90° interlayer rotation Build orientation on Z-axis; 67° interlayer rotation Build orientation on Z-axis; 45° interlayer rotation Build orientation at 45°; 90° interlayer rotation Build orientation at 45°; 67° interlayer rotation Build orientation at 45°; 45° interlayer rotation	560 ± 5 619 ± 11 627 ± 11 559 ± 5 616 ± 11 630 ± 9 518 ± 5 546 ± 10 551 ± 6 551 ± 6 583 ± 5 643 ± 5	877 ± 8 962 ± 11 991 ± 6 874 ± 10 946 ± 11 993 ± 5 814 ± 4 825 ± 3 824 ± 5 870 ± 7 910 ± 7 990 ± 9	39 ± 3 43 ± 2 42 ± 2 38 ± 5 42 ± 3 43 ± 2 50 ± 41 53 ± 1 53 ± 1 48 ± 1 48 ± 2 46 ± 2		[417]
LPBF	IN625	ASTM E8M	Strain rate 10 ⁻³ s ⁻¹	HIP and tested at RT HIP and tested at 650 °C	459.5 ± 6.5 246.2 ± 3.7	926.0 ± 12.7 637.5 ± 15.4	74.9 ± 2.9 38.7 ± 4.6		[438]
LPBF LPBF	IN625 IN625	ISO 6892-1:2009		Different notches Various temperatures (20 °C, 540 °C, 760 °C, 815 °C, 870 °C, 950 °C and 1000 °C)	See the original reference paper See Figs. 6 and 7 in the original reference paper				[439] [331]
LPBF	IN718	Chinese grain boundaries/T 228	Strain rate 10 ⁻³ s ⁻¹	0° 90°	780 634	1069.6 980	30.9		[247]
LPBF	IN718		Strain rate 4.25 × 10 ⁻⁴ s ⁻¹	AB/RT SA/RT AB/650 °C SA/650 °C	677 1271 594 1042	1023 1425 862.0 1142	28.1 18.6 25.1 10.1		[250]
LPBF	IN718	ASTM E8/E8M		Top left corner (TL), laser focus 3 mm	1234	1455	14.4	19.2% RA	[315]

(continued on next page)

Table 9 (continued)

Technique	Material	Standard	Test condition	Sample Condition	Yield strength (MPa)	Tensile strength (MPa)	Elongation (%)		Young's modulus (GPa)	Ref
				above the building plate (+3 mm)						
				TL, laser focus on the building plate (0 mm)	1207	1455	14.5	16.7% RA		
				TL, laser focus 3 mm below the building plate (-3 mm)	1207	1207	1372	3.6	12.2%RA	
				Middle left (ML), +3 mm	1179	1179	1475		13.9	
				25.4%RA						
				ML, 0 mm	1200	1200	1448		15.5	
				30.3%RA						
				ML, -3 mm	1213	1213	1434		10.2	
				18.0%RA						
				Top right corner (TR), +3 mm	1213	1213	1420	6.9	14.4%RA	
RT, 0 mm	1213	1427	9.3		15.1%RA					
RT, -3 mm	1220	1406	5.7	10.1%RA						
Middle right (MR), 3 mm	1207	1448	12.2	18.0%RA						
MR, 0 mm	1213	1455	10.8	13.1%RA						
MR, -3 mm	1179	1358	4.4	13.9%RA						
LPBF (DMLS)	IN718	ASTM-E8/E8M		Lattice dog bone specimen	1005.8	1220.8	22.3		166.5	[220]
LPBF	IN718		Strain rate $4 \times 10^{-3} \text{ s}^{-1}$	AB	580	845				[172]
				ST	535	870				
				SA	1240	1400				
				HIP	430	875				
				HIP + Aging	1100	1315				
				Arc-PVD + HIP	420	815				
				Arc-PVD + HIP + Aging	1185	1300				
LPBF	IN718	ASTM-E8/E8M	Strain rate 2 mm/min	AB	596 ± 30	943 ± 8	35 ± 1		170 ± 9	[256]
				HT A	924 ± 11	1186 ± 2	25 ± 5		158 ± 17	
				HT B	951 ± 3	1210 ± 23	23 ± 1		195 ± 2	
				HT C	1158 ± 14	1339 ± 30	7 ± 1		138 ± 6	
				HT D	558 ± 7	933 ± 3	43 ± 1		170 ± 7	
LPBF (DMLS)	IN718	ASTM-E8/E8M	Strain rate 102 µm/s	0°/Powder I #1	1070	1316	18		195	[257]
				90°/Powder I #2	1082	1331	20		199	
				90°/Powder I #5	1071	1322	20		198	
				0°/Powder I #6	1059	1293	17		191	
				0°/Powder II #2	789	1059	31		174	
				90°/Powder II #3	868	1162	26		182	
				0°/Powder II #4	787	1034	31		185	
				90°/Powder II #5	854	1148	26		172	
LPBF	IN718	ASTM-E8/E8M	24 °C or 650 °C	0°/STA/24 °C	1295	1484				[258]
				45°/STA/24 °C	1368	1521				
				90°/STA/24 °C	1240	1398				
				0°/STA/650 °C	1033	1139				
				45°/STA/650 °C	1124	1187				
				90°/STA/650 °C	978	1114				
LPBF	IN718			90°/AB	711 ± 14	1110 ± 11	24.5 ± 1.1			[259]
				0°/AB	858 ± 12	1167 ± 10	21.5 ± 1.3			
LPBF	IN718		Strain rate $3 \times 10^{-3} \text{ s}^{-1}$	0°/RT	1186	1440	18.5			[261]
				450 °C	1033	1216	12.4			
				650 °C	870	1011	3.6			
				90°/RT	1180	1400	20.4			
				450 °C	1026	1160	15.9			
				650 °C	860	992	14.2			
				45°/RT	1190	1450	16.9			
				450 °C	1080	1255	12.8			
				650 °C	855	1074	5.8			
LPBF	IN718	ASTM-E8/E8	Strain rate 0.5 mm/min	AB	~614	~957	~28.9			[66]
				SA (Standard)	~1211	~1391	~18.0			
				SA (single step ageing)	~1211	~1391	~18.9			
				SA (solution at 1100 °C)	~1142	~1304	~17.8			
					~822	~1121	~21.5			

(continued on next page)

Table 9 (continued)

Technique	Material	Standard	Test condition	Sample Condition	Yield strength (MPa)	Tensile strength (MPa)	Elongation (%)	Young's modulus (GPa)	Ref
LPBF		IN718	ASTM-E8/E8M	SA (solution at 1200 °C) Strain rate 10^{-4} s^{-1}	Raw powder	1210 ± 25	1404 ± 32	18.5 ± 1.6	
Recycled powder LPBF (DMLS)	1178 ± 31	1369 ± 35	17.4 ± 1.7		[115]				
LPBF (DMLS)	IN718	ASTM-E8/E8M		90°/SA 45°/SA 0°/SA SA + HIP	1215 1305 1290 1125			165 215 195 200	[74]
LPBF (DMLS)	IN718	ISO 6892-1		AB Rolled with 15% deformation 30% def. 50% def. 15% def. + SA 30% def. + SA 50% def. + SA	666 694 826 925 753 886 977	1065 1144 1446 1594 1405 1578 1623	24 22 20 17 13 8 5		[268]
LPBF	IN718	ASTM-E8/E8M		AB SA	646.50 1211.33	940.10 1408.50	35.47 14.83		[271]
	IN718/TiC			AB SA	774.26 1144.00	1029.00 1380.86	12.32 9.08		
LPBF	IN718			AB/20 °C HA/20 °C AB/1000 °C HA/1000 °C	569–646 1160 112 113	851–1002 1350 114 116	9.8–31.7 17.6 47.4–53.5 58.1		[68]
LPBF	IN718	ISO 6892-1		0°/50 µm layer thickness 90°/50 µm layer thickness 0°/30 µm layer thickness 90°/30 µm layer thickness	646 609 807 675	1049 949 1051 957	27.2 31.7 21.9 27.7		[274]
LPBF	IN718	EN 10002		0°/AB/RT 90°/AB/RT 0°/HT1/RT 90°/HT1/RT 0°/HT2/RT 90°/HT2/RT 0°/HT 1/450 °C 90°/HT 1/450 °C 0°/HT 2/450 °C 90°/HT 2/450 °C 0°/HT 1/650 °C 90°/HT 1/650 °C 0°/HT 2/650 °C 90°/HT 2/650 °C	816 ± 24 737 ± 4 1227 ± 1 1136 ± 16 1222 ± 26 1186 ± 23	1085 ± 11 1010 ± 10 1447 ± 10 1357 ± 5 1417 ± 4 1387 ± 12 ~1287.00 1224.22 1228.70 1183.86 1107.62 1029.15 1134.53 1121.08	19.1 ± 0.7 20.6 ± 2.1 10.1 ± 0.6 13.6 ± 0.2 15.9 ± 1.0 17.4 ± 0.4 ~13.06 15.77 14.75 15.43 8.78 18.8 12.61 17.57		[277]
LPBF	IN718			90°/AB 0°/AB 45°/AB D45°/AB 90°/SA 0°/SA 45°/SA D45°/SA	572 ± 44 643 ± 63 590 ± 15 723 ± 55 1074 ± 42 1159 ± 32 1152 ± 24 1241 ± 68	904 ± 22 991 ± 62 954 ± 15 1117 ± 45 1320 ± 6 1377 ± 66 1371 ± 5 1457 ± 55	19 ± 4 13 ± 6 20 ± 1 16 ± 3 19 ± 2 8 ± 6 15 ± 5 14 ± 5	162 ± 18 193 ± 24 200 ± 23 208 ± 48 163 ± 30 199 ± 15 188 ± 19 209 ± 44	[95]
LPBF	IN718	Nano indentation		90°/top 90°/middle top 90°/middle bottom 90°/bottom 0°/top 0°/middle top 0°/middle bottom 0°/bottom				188.9 210.6 211.1 202.8 193.7 193.4 201.2 196.2	[278]
LPBF	IN718		Strain rate 1.5 mm/min	90°/250 W/AB 90°/950 W/AB Zone 1–250 W Matrix and Zone 2 - two lines of 950 W Zone 1–950 W Matrix and Zone 2 - two lines of 250 W	668 ± 16 531 ± 9 574 ± 6 591 ± 14 585 ± 7	1011 ± 27 866 ± 33 873 ± 14 920 ± 23 880 ± 17	22 ± 2 21 ± 7 13 ± 2 15 ± 3 14 ± 1	173 ± 13 113 ± 3 136 ± 13 131 ± 3 155 ± 11	[281]

(continued on next page)

Table 9 (continued)

Technique	Material	Standard	Test condition	Sample Condition	Yield strength (MPa)	Tensile strength (MPa)	Elongation (%)	Young's modulus (GPa)	Ref
LPBF	IN718	grain boundaries/T 228-2002		Zone 1–250 W Matrix and Zone 2 – four lines of 950 W					
				Zone 1–950 W Matrix and Zone 2 – four lines of 250 W	586 ± 16	920 ± 7	18 ± 2	137 ± 12	
				AB	889–907	1137–1148	19.2–25.9	204	[283]
				SA	1102–1161	1280–1358	10–22	201	
LPBF	IN718			HSA	1046	1371	12.3		[216]
LPBF	IN718			HA	1174	1451	13.5		
LPBF	IN718			AB	849	1126	22.8		[165]
				SA	1084	1371	10.1		
LPBF	IN718		Strain rate 2 mm/s	HSA	1046	1371	12.3		
				Island size 2 × 2 mm ²	804.0 ± 49.5	1076.5 ± 28.9	16.85 ± 0.07		[286]
				3 × 3 mm ²	800.5 ± 7.80	1075.0 ± 8.50	21.05 ± 0.21		
				5 × 5 mm ²	770.5 ± 2.10	1064.5 ± 3.50	22.35 ± 0.21		
				7 × 7 mm ²	772.5 ± 2.20	1065.0 ± 1.40	25.25 ± 0.35		
LPBF (DMLS)	IN718	ASTM-E8/E8M	Strain rate 0.0185/min	HT	1170	1380	9.0	188	[287]
				HIP + HT	1090	1310	8.2	210	
				HT + shot peen	1110	1340	4.3	196	
				HIP + HT + shot peen	1080	1350	7.5	220	
LPBF	IN718		Strain rate 0.10%/s	0°/AB	~789.19	1075.09	31.16	200.38	[289]
				90°/AB	627.03	995.22	36.05	204.19	
				0°/DA	1356.76	1523.55	15.24	203.24	
				90°/DA	1194.59	1425.26	15.51	205.15	
				0°/SA	1232.43	1492.83	18.91	211.83	
				90°/SA	1167.57	1400.68	23.67	197.52	
				0°/HA	1248.65	1449.83	19.73	220.42	
				90°/HA	1178.38	1376.11	25.31	208.97	
				0°/HSA	1248.65	1443.68	19.86	205.15	
				90°/HSA	1200	1382.25	23.95	205.15	
LPBF	WC/IN718			Scan speed 400 mm/s		1299.6	22.12		[65]
				500 mm/s		~1339.94	~20.94		
				600 mm/s		~1408.84	~20.50		
				700 mm/s		1464.6	19.74		
LPBF	IN718		Strain rate 1 mm/min	0°/AB	912 ± 15.2	1072 ± 38.6	11.27 ± 2.14		[299]
				90°/AB	1102 ± 34.5	889 ± 20.5	30.42 ± 1.68		
LPBF	IN718			90°/HIP + SA/31.75 J/mm ³	~1128.18	~1340.16	~19.82		[300]
				90°/HIP + SA/39.7 J/mm ³	~1085.78	~1376.00	~19.96		
				90°/HIP + SA/40.8 J/mm ³	~1100.99	~1373.54	~20.10		
				90°/HIP + SA/47.6 J/mm ³	~1124.13	~1376.50	~19.71		
				90°/HIP + SA/51 J/mm ³	~1096.59	~1354.00	~18.62		
				90°/HIP + SA/61.2 J/mm ³	~1099.76	~1349.60	~17.61		
				0°/HIP + SA/31.75 J/mm ³	~1137.78	~1389.21	~19.45		
				0°/HIP + SA/39.7 J/mm ³	~1132.70	~1386.67	~23.58		
				0°/HIP + SA/40.8 J/mm ³	~1140.32	~1394.29	~25.25		
				0°/HIP + SA/47.6 J/mm ³	~1132.70	~1386.67	~23.63		
				0°/HIP + SA/51 J/mm ³	~1114.92	~1373.97	~18.26		
				0°/HIP + SA/61.2 J/mm ³	~1120	~1384.13	~23.25		
LPBF	IN718	ASTM E8	Strain rate 0.13 cm/min	HT # 554	698.2 ± 15.2	995.2 ± 12.8	33.21 ± 1.10		[301]
				HT # 528	1204.1 ± 8.6	1392 ± 8.9	17.32 ± 0.71		
				HT # 527	1268.5 ± 27.0	1739.5 ± 17.7	15.44 ± 2.00		
				HT # 522	1237.8 ± 13.4	1379.3 ± 10.4	19.49 ± 0.54		
				HT # 553	859.5 ± 22.9	1171.4 ± 12.8	34.34 ± 1.52		

(continued on next page)

Table 9 (continued)

Technique	Material	Standard	Test condition	Sample Condition	Yield strength (MPa)	Tensile strength (MPa)	Elongation (%)	Young's modulus (GPa)	Ref
				HT # 515	1124.4 ± 18.9	1330.8 ± 21.4	21.34 ± 0.80		
				HT # 514		1200.6 ± 9.5			
				1330.8 ± 21.4	20.78 ± 0.25				
				HT # 509	1203.3 ± 5.5	1390.2 ± 8.1	21.96 ± 0.37		
				HT # 507	1087.2 ± 7.5	1384.7 ± 6.2	23.36 ± 0.62		
HT # 506	1110.9 ± 7.4	1395.7 ± 4.2	23.61 ± 0.36						
LPBF	IN718	ASTM E8M	Strain rate 10 ⁻⁴ s ⁻¹	No WC	771 ± 4	1073 ± 1	29.4 ± 0.6	159 ± 12	[302]
				+5% WC	980 ± 16	1195 ± 12	21.6 ± 1.5	215 ± 17	
				+10% WC	1078 ± 14	1287 ± 15	15.1 ± 1.1	223 ± 15	
				+15% WC	974 ± 21	1104 ± 19	7.8 ± 1.1	225 ± 21	
LPBF	IN718	ASTM E8/E8M and ASTM E21	Strain rate 0.005/min	Sample orientation: XYZ/RT	694.77	1007.04	28.64	134.61	[306]
				YZX/RT	662.90	1004.21	27.92	127.01	
				ZXY/RT	604.43	912.63	33.63	82.16	
				XYZ/200 °C	702.82	1016.54	25.08	120.70	
				YZX/200 °C	634.35	968.86	24.51	121.23	
				ZXY/200 °C	539.90	850.76	31.43	90.27	
				XYZ/350 °C	667.97	955.15	26.45	108.44	
				YZX/350 °C	615.30	931.03	24.98	121.64	
				ZXY/350 °C	517.93	786.57	31.39	70.03	
LPBF	IN718 + Nano TiC		Simulation	225 J/m				117.506	[307]
				250 J/m				120.824	
				275 J/m				207.491	
				300 J/m				225.402	
LPBF	IN718	ISO 6892-2	Loading rate 1.5 mm/min	250 W/AB	668 ± 16	1011 ± 27	22 ± 2	173 ± 13	[67]
			Strain rate 2 mm/min	950 W/AB	531 ± 9	866 ± 33	21 ± 5	113 ± 3	
				250 W/HT	875 ± 11	1153 ± 4	17 ± 2	190 ± 11	
				950 W/HT	668 ± 7	884 ± 80	7 ± 2	138 ± 5	
				250 W/HIP	645 ± 6	1025 ± 14	38 ± 1	188 ± 8	
				950 W/HIP	481 ± 11	788 ± 12	34 ± 3	183 ± 19	
				250 W/HIP + HT	1145 ± 16	1376 ± 14	19 ± 1	190 ± 6	
				950 W/HIP + HT	1065 ± 20	1272 ± 12	15 ± 4	188 ± 20	
				AB	574 ± 6	873 ± 14	13 ± 2	136 ± 13	
				HT	704 ± 8	920 ± 53	4 ± 2	167 ± 13	
				HIP	500 ± 6	817 ± 16	21 ± 1	187 ± 8	
				HIP + HT	1041 ± 47	1154 ± 68	7 ± 1	196 ± 15	
				250 W/AB/650 °C	650 ± 11	845 ± 9	28 ± 4		
				950 W/AB/650 °C	543 ± 2	782 ± 6	31 ± 6		
				250 W/HIP/650 °C	626 ± 8	857 ± 14	29 ± 1		
				950 W/HIP/650 °C	479 ± 5	665 ± 7	28 ± 2		
				250 W/HIP + HT/ 650 °C	942 ± 11	1078 ± 8	20 ± 2		
				950 W/HIP + HT/ 650 °C	872 ± 13	1005 ± 12	17 ± 4		
LPBF	IN718		Strain rate ~10 ⁻³ s ⁻¹	90°/HIP + annealed/ Ar	850	1140	28		[64]
				0°/HIP + annealed/Ar	890	1200	28		
				0°/AB/N ₂	830	1120	25		
				90°/HIP + annealed/ N ₂	880	1140	30		
				0°/HIP + annealed/N ₂	930	1200	27		
LPBF	IN718 Lattice structure			Body Centred Cubic (BCC) 2 mm	7.28			354.61	[309]
				BCC 3 mm	1.56			56.73	
				BCC 4 mm	0.52			26.50	
				Body Centred Cubic-Z Struts (BCCZ) 2 mm	16.21			859.47	
				BCCZ 3 mm	4.13			522.85	
				BCCZ 4 mm	1.83			276.58	
				Face Centred Cubic (FCC) 2 mm	8.97			610.71	
				FCC 3 mm	2.16			150.92	
				FCC 4 mm	0.86			54.14	
				Face Centred Cubic-Z Struts (FCCZ) 2 mm	16.21			1267.26	
				FCCZ 3 mm	4.86			639.84	
				FCCZ 4 mm	2.16			365.80	
LPBF	IN718	ASTM-E8/E8M		Nominal	973.82	1265.84	18.01		[320]

(continued on next page)

Table 9 (continued)

Technique	Material	Standard	Test condition	Sample Condition	Yield strength (MPa)	Tensile strength (MPa)	Elongation (%)	Young's modulus (GPa)	Ref
Decreased cooling rate LPBF	940.98 IN718	1253.89	21.29	Strain rate 0.01 s ⁻¹	Increased hatch spacing	956.46	1256.55	12.29	
				Decreased hatch spacing	1229.98	20.94	904.85		
				Increased cooling rate	910.36	1233.97	20.05		
LPBF	IN718			Material A/90°/HT	1284	1432	29.2	29.7% RA	[313]
				Material A/0°/HT	1329	1499	31.8	30.7% RA	
				Material B/90°/HT Material B/0°/HT	1227 1300	1366 1467	13.6 27.3	8.6%RA 20%RA	
LPBF	IN718		Strain rate 5 × 10 ⁻⁴ s ⁻¹	AB SA HA HSA	~559.82 ~1016.63 ~986.18 ~1082.92	~781.96 ~1147.41 ~1163.53 ~1152.78		[322]	
LPBF	IN718			AB STA		1021–1035 1428	31–34 14	[335]	
LPBF	IN718		Strain rate 10 ⁻³ s ⁻¹	Homogenisation + AMS 5663 STA	1211 ± 24	1406 ± 21	13.6 ± 4	191 ± 3.1	[337]
LPBF	IN718 (AMS 5662)		Strain rate 8.3 × 10 ⁻³ s ⁻¹	Test at 20 °C Test at 550 °C Test at 600 °C Test at 6500 °C Test at 700 °C	1175 1064 1042 1025 957	1364 1176 1185 1126 1011	20.9 ± 0.5 16.9 ± 0.3 16.0 ± 0.7 19.5 ± 1.0 19.3 ± 1.3		[339]
LPBF	IN718	Compressive test	Strain rate 0.005 mm/min	Island/30° interlayer rotation/500 mm/s scan speed Island/30° interlayer rotation/700 mm/s scan speed Island/30° interlayer rotation/1000 mm/s scan speed Meander/90° interlayer rotation/500 mm/s scan speed Meander/90° interlayer rotation/700 mm/s scan speed Meander/90° interlayer rotation/1000 mm/s scan speed	595 580 580 680 660 630				[148]
LPBF	IN718	ASTM E8 and ASTM E21	Tests at 23 °C and 650 °C	90°/STA (954 °C)/23 °C 90°/STA (954 °C)/650 °C 90°/STA (1066 °C)/650 °C 0°/STA (954 °C)/23 °C 0°/STA (954 °C)/650 °C 45°/STA (954 °C)/23 °C 45°/STA (954 °C)/650 °C	1023 896 972 1053 958 1053 876	1368 1107 1145 1409 1127 1405 1134	28 26 20 24 23 21 24		[326]
LPBF	IN718	Tensile test Compressive test	Strain rate 10 ⁻⁴ s ⁻¹ Strain rate 10 ⁻⁴ s ⁻¹	0° 0° Specimen built at 90°	1211 ± 24 1248 ± 8 1120 ± 10	1406 ± 21	13.6 ± 4	191.0 ± 3.1 208.5 ± 1.1 213.0 ± 3.0	[327]
LPBF	IN718		Strain rate 10 ⁻⁴ s ⁻¹ and 10 ³ s ⁻¹	AB Stress Relieved STA	compression: 618 tension: 524 compression: 892 tension: 1055 compression: 1220 tension: 1100	894 1110 1314	30 42 23		[440]

(continued on next page)

Table 9 (continued)

Technique	Material	Standard	Test condition	Sample Condition	Yield strength (MPa)	Tensile strength (MPa)	Elongation (%)	Young's modulus (GPa)	Ref
				HIP	compression: 930 tension: 1167	1470	24		
LPBF		IN718		Strain rate $5 \times 10^{-4} \text{ s}^{-1}$	Various surface conditions	<i>See the original reference paper</i>			
[423] LPBF	IN718			ST STA	<i>See the original reference paper</i>				[314]
LPBF	IN718	Compression test	Strain rate 0.1 s^{-1}	HIP + STA 1000 °C 1050 °C 1000 °C 1050 °C	<i>See the original reference paper</i>				[317]
LPBF	IN718			Stress Relieved	<i>See the original reference paper</i>				[254]
LPBF	IN718			Post-processed 0° 30° 45° 60° 90°	<i>See Fig. 1 in the original reference paper</i>				[248]
LPBF (DMLS)	IN718		Strain rate $4.25 \times 10^{-4} \text{ s}^{-1}$	0°/AB/RT 90°/AB/RT 0°/STA/RT 90°/STA/RT 0°/STA/650 °C 90°/STA/650 °C	<i>See Fig. 6 in the original reference paper</i>				[92]
LPBF	IN718	ASTM E8/E8M		Various thermal treatments and build orientation	<i>See Fig. 4 in the original reference paper</i>				[176]
LPBF	IN718		Strain rate 1 mm/min	Pure IN718 IN718 + 0.25%GRP IN718 + 1.0%GRP	<i>See Fig. 6 in the original reference paper</i>				[262]
LPBF	IN718			Various HTs	<i>See Fig. 4 in the original reference paper</i>				[275]
LPBF	IN738LC	ISO 6892,	Strain rate ~4%/min	0°/RT 90°/RT 0°/850 °C 90°/850 °C	933 ± 8 786 ± 4 610 ± 1 503 ± 2	1184 ± 112 1162 ± 35 716 ± 1 688 ± 7	8.4 ± 4.6 11.2 ± 1.9 8.0 ± 1.2 14.2 ± 3.9	233 ± 9 158 ± 3 157 ± 4 110 ± 2	[249]
LPBF	IN738LC		Strain rate ~4%/min	0°/HT/23 °C 90°/HT/23 °C 0°/HT/850 °C 90°/HT/850 °C				237 ± 7 158 ± 3 159 ± 4 110 ± 2	[251]
LPBF	IN738LC		Strain rate $4 \times 10^{-3} \text{ s}^{-1}$	90°/SA 90°/HIP + SA	981 ± 12 932 ± 4	1450 ± 16 1350 ± 22	14 ± 1.1 14 ± 1.3		[58]
LPBF	IN738LC		Strain rate 4%/min	XY (single)/AB/23 °C XY (triple)/AB/23 °C XY (single)/AB/850 °C XY (single)/HT/23 °C XY (triple)/HT/23 °C XY (single)/HT/850 °C Z/AB/23 °C Z/HT/23 °C Z/HT/850 °C				148 225 183 148 222 173 108 164 134 190 225 210 197 228 204 141 164 154 141 138 196 200 143	[267]
LPBF	IN738LC	EN 10002		90° 0° H45°	765 ± 10 853 ± 16 893 ± 4			141 ± 3 141 ± 4 215 ± 7	[276]
LPBF	IN738LC	ASTM E8	Strain rate 4%/min	AB HIP HIP + DA/RT HIP + DA/850 °C	895 560 ± 1	1010 1010 720 ± 1	1.6 ± 0.2 3.9 14.4 ± 1		[323]

(continued on next page)

Table 9 (continued)

Technique	Material	Standard	Test condition	Sample Condition	Yield strength (MPa)	Tensile strength (MPa)	Elongation (%)		Young's modulus (GPa)	Ref		
LPBF	IN939			Various HTs	See Fig. 7 in the original reference paper					[253]		
LPBF	Invar 36		Strain rate 10^{-3} s^{-1}	0°/3200 mm/s	~397.7	~509.7	~15.3			[260]		
				90°/3200 mm/s	~352.5	~381.7	~3.25					
				90°/3200 mm/s/HIP	~288.3	~346.3	~4.7					
				90°/1000 mm/s	~342.5	~453	~29.5					
				0°/1000 mm/s	~400	~536.5	~19.5					
				0°/1000 mm/s/HT	~318	~443.5	~30.5					
LPBF	K418		Strain rate 1 mm/min	No graphene nanoplatelets (GNPs)	912	1200				[338]		
LPBF	K536	ASTM E8/E8M and ASTM E21	Strain rate 0.005/min	10.1 wt% GNPs	1018	1078						
					0°/RT/SR	338 ± 1.7	800 ± 2.1	36.9 ± 0.1	38.4% RA	193.3 ± 3.8	[319]	
					90°/RT/SR	325 ± 2.5	775 ± 1.2	41.3 ± 0.7	46.3% RA	188.7 ± 1.2		
					0°/400 °C/SR	250 ± 17.9	683 ± 6.7	40.7 ± 0.9	41.4% RA	143.8 ± 21.4		
					90°/400 °C/SR	243 ± 13.1	667 ± 0.7	45.2 ± 0.8	45.7% RA	129.1 ± 31.1		
					0°/500 °C/SR	249 ± 2.6	670 ± 2.6	40.3 ± 2.0	40.9% RA	118.3 ± 11.5		
					90°/500 °C/SR	237 ± 5.0	657 ± 4.0	43.3 ± 0.7	47.3% RA	114.4 ± 7.1		
					0°/600 °C/SR	242 ± 4.5	635 ± 2.1	41.6 ± 0.8	42.4% RA	117.2 ± 12.6		
					90°/600 °C/SR	228 ± 4.6	616 ± 0.7	44.6 ± 2.8	46.0% RA	103.9 ± 1.4		
					0°/700 °C/SR	218 ± 1.7	482 ± 3.2	27.2 ± 0.4	26.7% RA	129.8 ± 27.9		
					90°/700 °C/SR	213 ± 4.4	463 ± 3.1	32.0 ± 1.8	32.4% RA	104.4 ± 30.9		
LPBF	K536				Strain rate 0.005 mm/min	0°/RT	338 ± 1.7	800 ± 2.1	36.9 ± 0.1		193 ± 3.8	[319]
						90°/RT	325 ± 2.5	775 ± 1.2	41.3 ± 0.7		188.7 ± 1.2	
						0°/400 °C	250 ± 17.9	683 ± 6.7	40.7 ± 0.9		143.8 ± 21.4	
			90°/400 °C	243 ± 13.1		667 ± 0.7	45.2 ± 0.8		129.1 ± 31.1			
			0°/500 °C	249 ± 2.6		670 ± 2.6	40.3 ± 2		118.3 ± 11.5			
			90°/500 °C	237 ± 5		657 ± 4	43.3 ± 0.7		114.4 ± 7.1			
			0°/600 °C	242 ± 4.5		635 ± 2.2	41.6 ± 0.8		117.2 ± 12.6			
			90°/600 °C	228 ± 4.6		616 ± 0.7	44.6 ± 2.8		103.9 ± 1.4			
			0°/700 °C	218 ± 1.7		482 ± 3.2	27.2 ± 0.4		129.8 ± 27.9			
			90°/700 °C	213 ± 4.4		463 ± 3.1	32 ± 1.8		104.4 ± 30.9			
LPBF	Nimonic 263	French Aeronautical standard CEAT TP5		90°/AB	818 ± 8	1085 ± 11	24 ± 24		163	[285]		
				0°/AB	653 ± 11	860 ± 8	70 ± 1		191			
				90°/DA	834 ± 13	1136 ± 26	29 ± 2		150			
				0°/DA	697 ± 16	910 ± 4	52 ± 12		142			
				90°/SA	843 ± 20	1268 ± 7	29 ± 3		199			
				0°/SA	709 ± 7	981 ± 4	53 ± 2		206			
LPBF	Oxide dispersion strengthened nickel-based superalloy		Strain rate 10^{-3} s^{-1} Temperature between 25 °C and 1000 °C	Different process parameters	See Table 4 in the original reference paper					[336]		
LPBF	Steel/Ni				See Fig. 4 in the original reference paper					[265]		
EBM	IN625		Strain rate $\sim 10^{-3} \text{ s}^{-1}$	90°	410	750	44			[264]		
				90°/HIP	330	770	69					
				EBM, 0°	367 ± 33	849 ± 37	44.32 ± 4.95		484 ± 52	[100]		
				EBM, 90°	369 ± 7	723 ± 29	26.92 ± 5.49		459 ± 36			
				Binder jetting, 0°	320 ± 14	707 ± 12	58.74 ± 2.14		524 ± 47			
EBM	IN625 Mesh	Compression test	Strain rate 76 mm/min	Binder jetting, 90°	393 ± 2	708 ± 22	27.02 ± 5.39		506 ± 51			
					Load parallel or perpendicular to the build direction/specimens with different density	See the original reference paper					[318]	
EBM	IN625			AB/RT	410	750	44			[292]		

(continued on next page)

Table 9 (continued)

Technique	Material	Standard	Test condition	Sample Condition	Yield strength (MPa)	Tensile strength (MPa)	Elongation (%)		Young's modulus (GPa)	Ref					
EBM	IN625		Strain rate $\sim 10^{-3} \text{ s}^{-1}$	HIP/RT	330	770	69		0.76 1.68 4.17	[293]					
				AB/538 °C HIP/538 °C Relative density 0.16 0.21 0.31	230	300 610	590 70								
EBM	IN625		Strain rate 10^{-3} s^{-1}	AB	793	952 ± 18			[305]						
EBM	In690		Strain rate 0.075 mm/min	RT	527 ± 19	670 ± 44.5	21 ± 2.0		[310]						
EBM	In690		Strain rate 0.075 m/min	Cladding On Build plate	527 ± 19 377 ± 39	670 ± 44.5 603 ± 34	21 ± 2 23 ± 8		[330]						
EBM	IN718		Strain rate 0.1%/s	90° 0°				~100 ~142	[291]						
EBM	IN718		Strain rate 0.10%/s	90°/AB	~923.91	1113.05	31.51		98.69	[294]					
				90°/DA	1128.26	1268.98	22.08		108.03						
				90°/SA (930 °C)	1132.61	1218.36	24.89		106.28						
				90°/SA (980 °C)	1089.13	1180.83	22.08		107.15						
				90°/SA (1080 °C)	1119.57	1201.49	28.10		108.32						
				0°/AB	771.74	1002.51	40.35		144.23						
				0°/DA	1041.30	1200.62	31.31		135.18						
				0°/SA (930 °C)	941.30	1029.27	14.05		138.10						
				0°/SA (980 °C)	867.39	1095.02	38.34		124.67						
				0°/SA (1080 °C)	934.78	1073.49	35.33		141.02						
				EBM	IN718			Control case	568 ± 5		818 ± 43	16.9 ± 2.9		[183]	
EBM	IN718	ASTM E8/E8M		In-situ HT	Premature failure										
				Fast cooling	590.13	941.76	34.3		151.68	[97]					
EBM	IN718	Swedish standard SS112111-7A35		Slow cooling	868.87	1108.37	22.1		149.82	[295]					
				0°/AB	822 ± 25	1060 ± 26	22 %EL		192 ± 11						
EBM	IN718	German standard DIN 50125-B 4620		90°/AB	744 ± 44	929 ± 20	5.5 %EL		180 ± 6						
				0°/SA	1154 ± 46	1238 ± 22	7% EL		198 ± 12						
				90°/SA	1187 ± 27	1232 ± 16	1.1 %EL		198 ± 8						
EBM	IN718	ASTM E8/E8M		0°/Gas atomized (GA)- fast cool, 50 µm layer thickness	590 ± 40	942 ± 61	34 ± 2.6		[118]						
				0°/GA - slow cool, 50 µm	869 ± 32	1108 ± 50	22 ± 1.8								
				90°/GA - fast, 50 µm, on the cold powder bed	887 ± 16	1003 ± 21	5.4 ± 1.7								
				90°/GA - fast, 50 µm	822 ± 12	1082 ± 10	20 ± 0.6								
				0°/Rotary atomized (RA) - slow, 70 µm	957 ± 30	1142 ± 41	19 ± 4.6								
				0°/RA - slow, 50 µm	974 ± 20	1186 ± 34	20 ± 1.3								
				0°/Plasma rotated electrode process (PREP) - fast, 50 µm	967 ± 28	1186 ± 19	20 ± 1.4								
				90°/PREP - fast cool, 50 µm	632 ± 88	1069 ± 44	17 ± 2.4								
				EBM	IN718 (HIPed)	ASTM E606-12		90°/Columnar grains/ 650 °C		1009	1082	38		88	[296]
								0°/Columnar grains/ 650 °C		752	834	17		122	
90°/Equiaxed grains/ 650 °C	834	1055	20					174							
0°/Equiaxed grains/ 650 °C	827	1048	8.5					177							
EBM	IN718	ASTM E8/E8M and ASTM E21		90°/RT	925 ± 20	1138 ± 24	15.7 ± 4.3		[297]						
				0°/RT	894 ± 24	1061 ± 83	11.5 ± 6.9								
				90°/HIP + SA/RT	1061 ± 16	1266 ± 44	21.1 ± 1.1								
EBM	IN718	ASTM E8/E8M and ASTM E21	RT and 650 °C	0°/HIP + SA/RT	1035 ± 17	1240 ± 19	21.8 ± 2.4		[298]						
EBM	IN718		Strain rate 0.0056 s^{-1}	Various build orientations and scan strategies	See Fig. 8 in the original reference paper					[304]					
				AB/parameter set 1	980	1160	8.2								
				AB/parameter set 2	980	1160	8.2								
				AB/parameter set 3	980	1160	8.2								

(continued on next page)

Table 9 (continued)

Technique	Material	Standard	Test condition	Sample Condition	Yield strength (MPa)	Tensile strength (MPa)	Elongation (%)	Young's modulus (GPa)	Ref
EBM	IN718			HT/parameter set 1	1180	1350	6.5		[316]
				HT/parameter set 2	1290	1440	7.1		
				HT/parameter set 3	1180	1350	7.1		
				Focus offset 1 mA at 25 °C	988.8 ± 3.7	1144.0 ± 1.5	31.5 ± 4.3		
				3 mA	1010.5 ± 5.5	1157.5 ± 5.5	25.3 ± 2.6		
				6 mA	1050.0 ± 5.5	1187.3 ± 8.4	25.1 ± 5.7		
				9 mA	1122.3 ± 17.4	1300.6 ± 22.5	25.3 ± 0.9		
				12 mA	1095.1 ± 32.1	1278.4 ± 26.8	25.3 ± 0.7		
				15 mA	1112.3 ± 35.6	1276.6 ± 14.2	26.4 ± 0.4		
				18 mA	978.9 ± 8.3	1053.9 ± 11.6	9.3 ± 1.1		
				21 mA	989.8 ± 6.1	1046.3 ± 17.1	8.6 ± 0.9		
				24 mA	946.3 ± 5.8	958.7 ± 20.9	6.2 ± 0.3		
				30 mA	674.3 ± 47.8	680.5 ± 38.9	6.1 ± 0.8		
				40 mA	443.5 ± 16.4	455.4 ± 6.1	4.3 ± 0.2		
				Focus offset 1 mA at 650 °C	820.8 ± 2.5	952.1 ± 14.9	19.5 ± 6.4		
				3 mA	827.8 ± 2.6	955.5 ± 3.2	18.8 ± 1.1		
				6 mA	840.0 ± 10.8	967.8 ± 12.4	17.2 ± 0.8		
				9 mA	943.3 ± 27.2	1051.8 ± 12.4	29.8 ± 2.5		
				12 mA	917.0 ± 4.9	1037.5 ± 2.1	30.3 ± 1.1		
				15 mA	922.3 ± 12.4	1041.3 ± 7.4	22.8 ± 3.2		
				18 mA	862.8 ± 7.4	988.8 ± 2.5	17.8 ± 0.4		
				21 mA	866.3 ± 2.5	994.3 ± 4.9	17.8 ± 1.1		
				24 mA	868.0 ± 14.8	967.8 ± 51.9	14.5 ± 11.3		
				30 mA	516.3 ± 86.6	537.3 ± 57.1	4.5 ± 0.9		
EBM	IN718		Strain rate $1.5 \times 10^{-4} \text{ s}^{-1}$	40 mA	264.3 ± 17.3	320.7 ± 7.1	5.8 ± 3.2		[308]
				0°	793 ± 4	809 ± 14	1 ± 0.5		
				45°	757 ± 8	776 ± 12	16.2 ± 5.5		
				55°	843 ± 13	951 ± 10	11.4 ± 2.7		
EBM	IN718		Strain rate 10^{-3} s^{-1}	As-build	920 ± 16	1075 ± 46	10 ± 3	138 ± 5	[321]
				STA	1096 ± 6	1172 ± 30	6 ± 1	137 ± 7	
				HIP + STA	1100 ± 13	1190 ± 33	14 ± 1	142 ± 4	
								220 ± 125	
EBM	IN718	Procedure from [441]		0°				220	[442]
				90°				125	
EBM	IN718	Quasi-static tensile tests	Speed control 0.0025 mm/s	AB	406 ± 17	427 ± 28	0.7 ± 0.2		[422]
		ASTM-E8/E8M, ASTM-E21, Strain rate 0.005 (mm/mm)/min	RT and 650 °C	Polished	982 ± 52	1174 ± 29	27.8 ± 1.4		
EBM	IN718			Various build heights	See Fig. 11 in the original reference paper				[96]

Appendix C. Hardness properties of PBF Nickel-based superalloys

Table 10

Summary of hardness properties of PBF Nickel-based superalloys ('~' indicates that the data was obtained from the bar chart).

Technique	Material	Standard	Test condition	Sample condition	Hardness	Ref
LPBF	CM247LC	Vickers hardness	5 kgf	AB	400 ± 9 HV	[184]
				SA	512 ± 9HV	
LPBF	CM247LC	Vickers hardness	5 kgf	AB	409 ± 7 HV	[311]
					442 ± 16 HV	

(continued on next page)

Table 10 (continued)

Technique	Material	Standard	Test condition	Sample condition	Hardness	Ref
				Solution @ 1210 °C + ageing		
				Solution @ 1230 °C + ageing	437 ± 19 HV	
				Solution @ 1240 °C + ageing	448 ± 2 3HV	
				Solution @ 1260 °C + ageing	462 ± 13 HV	
LPBF	CM247LC	Vickers Hardness	1 kg	HT at 450 °C/2h	430 HV	[195]
				HT at 600 °C/2h	425 HV	
				HT at 700 °C/2h	460 HV	
				HT at 750 °C/2h	490 HV	
				HT at 850 °C/2h	545 HV	
				HT at 975 °C/2h	500 HV	
LPBF	FGH100L	Vickers Hardness		AB	~410 HV	[324]
				HT	~490 HV	
				HIP	~475 HV	
LPBF	FGH4096 M	Hardness		HIP + HT	~590 HV	[341]
				AB	~280 HB	
				DA	~445 HB	
				STA (1050 °C)	~390 HB	
				STA (1130 °C)	~425 HB	
				Double Aging	~385 HB	
LPBF	Hastelloy X	Vickers hardness	5 kgf	0°/AB	~246.07 HV	[179]
				90°/AB	~243.37 HV	
				0°/HT	~212.36 HV	
				90°/HT	~211.69 HV	
				0°/HIP	~205.62 HV	
				90°/HIP	~206.29 HV	
				0°/HIP + HT	~217.08 HV	
				90°/HIP + HT	~215.73 HV	
LPBF	Hastelloy X	Vickers hardness	500 gf	Original material	277.1 ± 3.9 HV	[284]
LPBF	Hastelloy X	Vickers Hardness (HV 0.5) Room temperature	200 gf/15 s RT	Modified material	280.9 ± 4.0 HV	[180]
				90°/AB	301 ± 8 HV	
				90°/HT	~195 HV	
				90°/HIP	~231 HV	
				0°/AB	308 ± 12 HV	
				0°/HT	~208 HV	
				0°/HIP	~238 HV	
			200 gf/15 s 750 °C	90°/AB	280 ± 6 HV	
				90°/HT	~229 HV	
				90°/HIP	~200 HV	
				0°/AB	317 ± 20 HV	
				0°/HT	~212 HV	
				0°/HIP	~200 HV	
LPBF (SLE)	IN100	Vickers hardness	2000 gf/10–15s	Substrate	~389.95 HV	[351]
				Interface	~404.90 HV	
				Deposited materials	~426.96 HV	
LPBF	IN625/TiB ₂	Vickers hardness	300 gf/15s	Linear energy density (LED) 1200 J/m/IN625	~299.02 HV	[346]
				LED 1200 J/m/ IN625+TiB ₂	~626.23 HV	
				LED 800 J/m/IN625	~338.24 HV	
				LED 800 J/m/ IN625+TiB ₂	~549.02 HV	
				LED 600 J/m/IN625	~338.24 HV	
				LED 600 J/m/ IN625+TiB ₂	~627.45 HV	
				LED 400 J/m/IN625	~370.10 HV	
				LED 400 J/m/ IN625+TiB ₂	~688.73 HV	
LPBF	IN625	Vickers hardness	500 gf/30s	AB	343 HV	[348]
				Solution @ 700 °C	~334.17 HV	
				Solution @ 800 °C	~356.20 HV	
				Solution @ 900 °C	~356.23 HV	
				Solution @ 1000 °C	~276.02 HV	
				Solution @ 1100 °C	~265.06 HV	
				Solution @ 1200 °C	~260.20 HV	
LPBF	IN625	Brinell hardness	2.5 mm WC ball, 62.5 kg/15s	Hardness vs Porosity	Fig. 52b	[353]
LPBF	IN625	Nano-indentation	0.5 mN at 1/10 layer thickness	90 W/AB/0 dpa	~5.75 GPa	[376]
				90 W/AB/0.1 dpa	~6.10 GPa	
				90 W/AB/0.5 dpa	~6.05 GPa	
				90 W/AB/1 dpa	~5.6 GPa	
				90 W/AB/3 dpa	~5.8 GPa	

(continued on next page)

Table 10 (continued)

Technique	Material	Standard	Test condition	Sample condition	Hardness	Ref					
LPBF	IN625	Brinell hardness	62.5 kgf/15s	AB	~283.25 HBW	[303]					
				DA @ 600 °C for 2h	~275.04 HBW						
				DA @ 700 °C for 2h	~311.70 HBW						
				DA @ 800 °C for 2h	~395.91 HBW						
				DA @ 900 °C for 2h	~282.37 HBW						
				DA @ 600 °C for 8h	~288.75 HBW						
				DA @ 700 °C for 8h	~319.78 HBW						
				DA @ 800 °C for 8h	~322.03 HBW						
				DA @ 900 °C for 8h	~298.91 HBW						
				DA @ 600 °C for 24h	~306.80 HBW						
				DA @ 700 °C for 24h	~349.39 HBW						
				DA @ 800 °C for 24h	~348.55 HBW						
				DA @ 900 °C for 24h	~316.96 HBW						
				Solution @ 1000 °C for 1h	~212.12 HBW						
				Solution @ 1150 °C for 1h	~186.22 HBW						
				Solution @ 1000 °C for 2h	~209.88 HBW						
				Solution @ 1150 °C for 2h	~188.96 HBW						
				Solution @ 1150 °C for 2h + Ageing @ 600 °C for 2h	~198.90 HBW						
				Solution @ 1150 °C for 2h + Ageing @ 700 °C for 2h	~209.92 HBW						
				Solution @ 1150 °C for 2h + Ageing @ 800 °C for 2h	~194.87 HBW						
				Solution @ 1150 °C for 2h + Ageing @ 900 °C for 2h	~188.75 HBW						
				Solution @ 1150 °C for 2h + Ageing @ 600 °C for 8h	~206.95 HBW						
				Solution @ 1150 °C for 2h + Ageing @ 700 °C for 8h	~259.97 HBW						
				Solution @ 1150 °C for 2h + Ageing @ 800 °C for 8h	~210.97 HBW						
				Solution @ 1150 °C for 2h + Ageing @ 900 °C for 8h	~188.75 HBW						
				Solution @ 1150 °C for 2h + Ageing @ 600 °C for 24h	~227.94 HBW						
				Solution @ 1150 °C for 2h + Ageing @ 700 °C for 24h	~279.91 HBW						
				Solution @ 1150 °C for 2h + Ageing @ 800 °C for 24h	~234.94 HBW						
				Solution @ 1150 °C for 2h + Ageing @ 900 °C for 24h	~192.95 HBW						
				LPBF	IN625		Vickers hardness	30 kgf	90°/Powder 1/90 J/mm ³	~289.79 HV	[121]
									0°/Powder 1/90 J/mm ³	~275.58 HV	
									90°/Powder 3/90 J/mm ³	~303.18 HV	
0°/Powder 3/90 J/mm ³	~287.03 HV										
90°/Powder 1/100 J/mm ³	~281.83 HV										
0°/Powder 1/100 J/mm ³	~275.58 HV										
90°/Powder 3/100 J/mm ³	~295.31 HV										
0°/Powder 3/100 J/mm ³	~285.73 HV										
90°/Powder 1/110 J/mm ³	~277.86 HV										
	~271.20 HV										

(continued on next page)

Table 10 (continued)

Technique	Material	Standard	Test condition	Sample condition	Hardness	Ref
				0°/Powder 1/110 J/ mm ³		
				90°/Powder 3/110 J/mm ³	~298.47 HV	
				0°/Powder 3/110 J/ mm ³	~286.22 HV	
LPBF	IN625 and cast iron substrate	Micro Hardness	500 gm/20 s	Cast iron substrate	~200 HV	[371]
				HAZ	~375 HV	
				Sample-substrate interface	~350 HV	
				IN625 sample	~300 HV	
LPBF	IN625	Microhardness	100g/10 s	See the original reference paper		[416]
LPBF	IN718	Vickers hardness	1 kgf	250 W/AB	320 HV	[67]
				950 W/AB	287 HV	
				250 W/HT	360 HV	
				950 W/HT	338 HV	
				250 W/HIP	310 HV	
				950 W/HIP	262 HV	
				250 W/HIP + HT	468 HV	
				950 W/HIP + HT	451 HV	
				Zone 1–250 W	330 HV	285 HV
				Matrix and zone 2 - two lines of 950 W/ AB		
				Zone 1–250 W	370 HV	335 HV
				Matrix and zone 2 - two lines of 950 W/ HT		
				Zone 1–250 W	310 HV	260 HV
				Matrix and zone 2 - two lines of 950 W/ HIP		
				Zone 1–250 W	478 HV	462 HV
				Matrix and zone 2 - two lines of 950 W/ HIP + HT		
LPBF	IN718	Vickers hardness	1 kgf	Zone 1–250 W	330 HV	285 HV [281]
				Matrix and Zone 2 - two lines of 950 W		
				Zone 1–950 W and Zone 2 – two lines of 250 W	322 HV	300 HV
				Zone 1–250 W and Zone 2 – four lines of 950 W	318 HV	285 HV
				Zone 1–950 W and Zone 2 – four lines of 250 W	311 HV	289 HV
LPBF	IN718+WC	Vickers hardness	200 gf	Scan speed 400 mm/ s	~385.30 HV	[65]
				Scan speed 500 mm/ s	~402.47 HV	
				Scan speed 600 mm/ s	~445.39 HV	
				Scan speed 700 mm/ s	~480.26 HV	
LPBF	WC _{1-x} reinforced IN718	Vickers hardness	100 gf/15s	Linear energy density	Fig. 53a	[343]
LPBF	IN718	Vickers hardness	100 gf/10s	Linear energy density	Fig. 53b	[344]
LPBF	IN718	Vickers hardness	500 gf/20s	Scan speed 100 mm/ s	~290.85 HV	[59]
				Scan speed 200 mm/ s	~303.19 HV	
				Scan speed 400 mm/ s	~312.98 HV	
				Scan speed 800 mm/ s	~318.51 HV	
				Scan speed 1200 mm/s	~294.26 HV	
				Scan speed 1600 mm/s	~213.40 HV	
LPBF	IN718+WC	Vickers hardness	100 gf	Scan speed 650 mm/ s	317.5 HV	[345]
				Scan speed 550 mm/ s	348.6 HV	

(continued on next page)

Table 10 (continued)

Technique	Material	Standard	Test condition	Sample condition	Hardness	Ref	
LPBF	IN718	Vickers hardness	100 gf/12s	Scan speed 450 mm/s	393.2 HV	[286]	
				Scan speed 350 mm/s	381.6 HV		
				Island size 2 × 2 mm ²	~339.68 HV		
				Island size 3 × 3 mm ²	~327.17 HV		
				Island size 5 × 5 mm ²	~329.91 HV		
LPBF (DMLS)	IN718	Rockwell Hardness, scale C		Island size 7 × 7 mm ²	~321.94 HV	[287]	
				90°/AB	30 HRC		416 HV
				0°/AB	43 HRC		416 HV
				90°/SA	26 HRC		260 HV
				0°/SA	42 HRC		404 HV
LPBF	IN718	Vickers hardness	300 gf/15s	0°/AB	~331.05 HV	[289]	
				90°/AB	~325.40 HV		
				0°/DA	~497.49 HV		
				90°/DA	~495.18 HV		
				0°/SA	~485.04 HV		
				90°/SA	~489.40 HV		
				0°/HA	~485.94 HV		
				90°/HA	~495.85 HV		
				0°/HSA	~491.27 HV		
				90°/HSA	~486.74 HV		
LPBF	IN718	Vickers hardness	1 kgf	0°/AB	297 ± 5 HV	[95]	
				XZ plane/AB	319 ± 10 HV		
				YZ plane/AB	322 ± 10 HV		
LPBF	IN718	Vickers hardness	100 gf	90°/SA	463 ± 8 HV	[72]	
				AB	273.2 ± 11.9 HV		
				Solution	262.7 ± 6.8 HV		
LPBF	IN718	Rockwell C-scale hardness for macro hardness, Vickers hardness for micro hardness	1.5 N for Rockwell C/ 0.25 N for Vickers	SA	482.7 ± 21.4 HV	[64]	
				HIP	258.8 ± 8.2 HV		
				0°/AB/HV/Argon	3.8/3.9 GPa		
				90°/HIP + annealed/HV/Argon	5.6/5.8 GPa		
				0°/HIP + annealed/HV/Argon	5.5/5.8 GPa		
				0°/annealed (4 h)/HV/Argon	4.5/4.7 GPa		
				0°/AB/HRC/Argon	30/33 HRC		
				90°/HIP + annealed/HRC/Argon	38/39 HRC		
				0°/HIP + annealed/HRC/Argon	33/35 HRC		
				0°/annealed (4 h)/HRC/Argon	39/40 HRC		
				90°/HIP + annealed/HV/Nitrogen	5.5/5.6 GPa		
				0°/HIP + annealed/HV/Nitrogen	5.4/5.6 GPa		
				90°/HIP + annealed/HRC/Nitrogen	35/38 HRC		
				0°/HIP + annealed/HRC/Nitrogen	36/38 HRC		
				LPBF (DMLS)	IN718		Vickers hardness
Ageing + shot peening	470 ± 8 HV						
LPBF	IN718	Rockwell hardness		AB	32.5 HRC	[165]	
				SA	43 HRC		424 HV
				HSA	42.5 HRC		406 HV
LPBF	IN718	Rockwell hardness		HSA	42.5 HRC	[216]	
LPBF	IN718	Vickers hardness	10 kgf	SA	45 HRC	[185]	
				0°/AB	304 ± 9 HV		
				90°/AB/top	288 ± 7 HV		
				90°/AB/bottom	301 ± 6 HV		
				0°/1100 °C/1h	258 ± 8 HV		
			5 kgf	0°/1100 °C/7h	217 ± 4 HV		
				0°/1250 °C/1h	210 ± 7 HV		

(continued on next page)

Table 10 (continued)

Technique	Material	Standard	Test condition	Sample condition	Hardness	Ref
LPBF HSA LPBF	IN718	IN718 463 ± 17 HV Vickers hardness	Vickers hardness 100 gf/15s	0°/1250 °C/7h 200 gf AB [349]	207 ± 6 HV 309 ± 12 HV	
LPBF	IN718	Vickers hardness	200 gf/10s	90°/AB 90°/STA (940 °C) 90°/STA (980 °C) 90°/STA (1020 °C) 90°/STA (1060 °C) 0°/AB 0°/STA (940 °C) 0°/STA (980 °C) 0°/STA (1020 °C) 0°/STA (1060 °C)	~366.74 HV ~318.33 HV ~322.01 HV ~312.67 HV ~299.93 HV ~243.31 HV ~241.05 HV	[355]
LPBF	IN718	Vickers hardness	0.98 N	Keyhole mode Conduction mode	Fig. 54d Fig. 54e	[369]
LPBF	IN718	Vickers hardness	9.8 gf	0°/AB 0°/SA	~325.93 ± 8.8 HV ~356.10 ± 10.6 HV	[350]
LPBF	IN718 (GA)	Vickers hardness	9.8 gf	AB Solution @ 550 °C Solution @ 650 °C Solution @ 700 °C Solution @ 750 °C Solution @ 775 °C Solution @ 800 °C Solution @ 825 °C Solution @ 850 °C Solution @ 900 °C Solution @ 950 °C Solution @ 1000 °C Solution @ 1050 °C STA (550 °C) STA (700 °C) STA (1000 °C)	~316.94 HV ~307.28 HV ~374.90 HV ~384.56 HV ~363.09 HV ~323.92 HV ~328.21 HV ~296.01 HV ~290.64 HV ~278.30 HV ~260.05 HV ~251.47 HV ~253.61 HV ~440.91 HV ~437.16 HV ~477.41 HV	[275]
LPBF	IN718	Rockwell hardness & Vickers hardness	150 kP (1471 N)/ Rockwell 10 kP (1471 N)/Vickers	90°/AB 0°/AB 90°/SA 0°/SA 90°/HSA 0°/HSA	341 HV 35 HRC 307 HV 30 HRC 452 HV 45 HRC 453 HV 45 HRC 439 HV 44 HRC 448 HV 44 HRC	[277]
LPBF	IN718		5 N/5s	90°/Top #1 90°/#2 90°/#3 90°/Bottom #4 0°/Top #5 0°/#6 0°/#7 0°/Bottom #8	6.64 667.1 HV GPa 6.47 659.7 HV GPa 6.67 680.1 HV GPa 7.09 723 HV GPa 6.81 694.4 HV GPa 6.32 644.4 HV GPa 7.05 718.9 HV GPa 6.98 711.7 HV GPa	[278]
LPBF	IN718	Vickers hardness	200 gf	AB/31.75 J/mm ³ AB/39.7 J/mm ³ AB/40.8 J/mm ³ AB/47.6 J/mm ³ AB/51 J/mm ³ AB/61.2 J/mm ³ HIP + SA/31.75 J/mm ³	~322.48 HV ~310.08 HV ~327.13 HV ~328.68 HV ~330.23 HV ~336.43 HV ~485.27 HV	[300]

(continued on next page)

Table 10 (continued)

Technique	Material	Standard	Test condition	Sample condition	Hardness	Ref
				HIP + SA/39.7 J/ mm ³	~489.92 HV	
				HIP + SA/40.8 J/ mm ³	~482.17 HV	
				HIP + SA/47.6 J/ mm ³	~486.82 HV	
LPBF	IN718+WC	Vickers hardness	200 gf/15s	0% Matrix WC WC particle Interface	315 ± 8 HV 299 ± 5 HBN NA	[302]
				5% Matrix WC WC particle Interface	340 ± 12 HV 322 ± 7 HBN 2670 ± 97 HV 1250 ± 76 HV	
				10% Matrix WC WC particle Interface	364 ± 14 HV 345 ± 8 HBN 2635 ± 105 HV 1198 ± 52 HV	
				15% Matrix WC WC particle Interface	366 ± 21 HV 346 ± 15 HBN 2665 ± 121 HV 1204 ± 74 HV	
LPBF	IN718+TiC	Nanohardness	100 mN/10s	Linear energy density 225 J/m	3.87 GPa	[307]
				250 J/m	~4.19 GPa	
				275 J/m	~4.34 GPa	
				300 J/m	4.48 GPa	
LPBF	IN718	Vickers hardness	25 gf/15s	Hardness in the melt pool	Fig. 55	[368]
LPBF	IN718	Vickers hardness	5 kgf/15s	90°/AB 0°/AB 90°/HT 0°/HT 90°/machined/AB 0°/machined/AB 90°/machined/HT 0°/machined/HT	269 ± 5 HV 310 ± 5 HV 452 ± 5 HV 457 ± 5 HV 257 ± 5 HV 277 ± 5 HV 441 ± 5 HV 454 ± 5 HV	[370]
LPBF	Multi material IN718-Ti6Al4V	Microhardness	500 gf/15 s	IN718 10 wt%IN718 – Ti6Al4V 20 wt%IN718 – Ti6Al4V 30 wt%IN718 – Ti6Al4V 40 wt%IN718 – Ti6Al4V	255 ± 13 HV 381 ± 21 HV 477 ± 16 HV 684 ± 48 HV 582 ± 27 HV	[377]
LPBF	IN718	Vickers Hardness		AB STA	335 HV 1595 HV	[335]
LPBF	IN718	Vickers Hardness	0.025 kgf/15 s	AB Barell Finish Ultrasonic shot peening Ultrasonic impact treatment Shot peening	390 HV _{0.025} 445.4 HV _{0.025} 482.8 HV _{0.025} 585 HV _{0.025} 649.4 HV _{0.025}	[197]
LPBF	IN718	Vickers Hardness	30 kg/20 s	Island/30° interlayer rotation/500 mm/s scan speed Island/30° interlayer rotation/700 mm/s scan speed Island/30° interlayer rotation/1000 mm/s scan speed Meander/90° interlayer rotation/ 500 mm/s scan speed Meander/90° interlayer rotation/ 700 mm/s scan speed	300 HV 300 HV 300 HV 330 HV 320 HV	[148]

(continued on next page)

Table 10 (continued)

Technique	Material	Standard	Test condition	Sample condition	Hardness	Ref	
LPBF		IN718	Vickers Hardness	Meander/90° interlayer rotation/ 1000 mm/s scan speed 200 g/ AB 10 s [372]	315 HV DA STA-1	300-350 HV 490-540 HV 476-500 HV	
STA-2 LPBF	IN718	400-450 HV ASTM E384 Vickers Hardness	20 kg/15 s	AB HIP + HT	297 HV 433 HV	[373]	
LPBF	IN718	Vickers Hardness		Solution HT at 950 °C	476-500 HV	[374]	
LPBF	IN718	Vickers Hardness		AB DA STA (950 °C) STA (1050 °C)	300-350 HV 490-540 HV 476-500 HV 400-450 HV	[375]	
LPBF	IN718	Microhardness	500 gf/10 s	AB	Top: 313 ± 13 HV _{0.5} Bottom: 307 ± 15 HV _{0.5}	[443]	
LPBF (SLE)	MAR-M247	Vickers hardness	2000 gf (19.6 N)	HIP Double Ageing Hip + Double Ageing	210 ± 10 HV _{0.5} 470 ± 20 HV _{0.5} 440 ± 113 HV _{0.5}		
LPBF	Nickel-based superalloy	Microhardness	300 g spacing 300 µm	AB/substrate AB/interface AB/deposited HT/substrate HT/interface HT/deposited With supports Without supports	407.8 HV 437.7 HV 462.5 HV 427.2 HV 461.1 HV 480.1 HV 301 ± 8.24 VHN 316 ± 9.14 VHN	[347]	
LPBF	Nimonic 263	Vickers hardness	30 kgf	90°/VED 100 J/mm ³ 0°/VED 120 J/mm ³ 90°/VED 120 J/mm ³ 0°/VED 140 J/mm ³ 90°/VED 140 J/mm ³ 0°/VED 160 J/mm ³ 90°/VED 160 J/mm ³ 0°/VED 180 J/mm ³ 90°/VED 180 J/mm ³ 0°/VED 200 J/mm ³ 90°/VED 200 J/mm ³	~153.37 HV ~145.07 HV ~150.86 HV ~148.11 HV ~147.28 HV ~148.16 HV ~148.07 HV ~146.10 HV ~157.54 HV ~148.51 HV ~151.45 HV	[380]	
LPBF	Thymonel-2	Vickers hardness	300 gf	AB Solution @ 400 °C Solution @ 500 °C Solution @ 600 °C Solution @ 650 °C Solution @ 700 °C Solution @ 800 °C Solution @ 900 °C Solution @ 1000 °C	300 HV ~292.61 HV ~298.96 HV ~303.81 HV ~349.06 HV ~366.01 HV ~317.64 HV ~244.37 HV ~231.48 HV	[285]	
LPBF	247LC	Microhardness		AB Solution @ 1200 °C DA Solution @ 800 °C	271 HV 359 HV 407 HV 512 HV	[352]	
DMD	12N-01 alloy	Vickers Hardness	100 gf	Various process parameters Single track Double track	See Table in the original reference paper 350 - 400 HV 500-580 HV	[444]	
EBM	IN625	Vickers hardness	1 kgf/10s	AB	335 HV	[305]	
EBM	IN625	Vickers hardness		Mesh structure	2.9 GPa	[293]	
EBM	IN625	Vickers hardness and Rockwell C	100 gf/10s/Vickers	Powder 0°/AB 90°/AB 0°/HIP 90°/HIP 0°/AB/538 °C 90°/AB/538 °C 0°/HIP/538 °C 90°/HIP/538 °C	2.6 GPa 2.8 GPa 2.5 GPa 2.2 GPa 2.1 GPa 2.6 GPa 2.8 GPa 2.3 GPa 2.2 GPa	265.1 HV 285.5 HV 254.9 HV 224.3 HV 214.1 HV 265.1 HV 285.5 HV 234.5 HV 224.3 HV	[292]
			Rockwell C 150 kgf	AB HIP AB/538 °C	14 HRC 8 HRC 14 HRC	197 HV 175 HV 197 HV	

(continued on next page)

Table 10 (continued)

Technique	Material	Standard	Test condition	Sample condition	Hardness	Ref
EBM	In690	Vickers hardness	100 gf	HIP/538 °C	6 HRC 172 HV	[310]
EBM	In690	Hardness	100 gf with 2 mm intervals	Cladding	2.33 ± 0.12 GPa	[330]
EBM	IN718	Brinell hardness for macro hardness, Vickers hardness for microhardness	Brinell 187.5 kPa (1839 N)/Vickers: 0.5 N	On build plate	1.78 ± 0.04 GPa	[295]
				0°/Macro-hardness/AB	337 ± 354 HV	
				0°/Macro-hardness/HT	10 HB	
				0°/Micro-hardness/AB	430 ± 452 HV	
				90°/Micro-hardness/AB	10 HB	
				0°/Micro-hardness/HT	506 ± 26 HV	
				90°/Micro-hardness/HT	502 ± 29 HV	
EBM	IN718	Vickers hardness		AB	410 HV	[304]
EBM	IN718	Vickers hardness		HT	470 HV	[183]
				Fast cooled	324 ± 18 HV	
				Slow cooled	392 ± 15 HV	
				In-situ HT	478 ± 7 HV	
EBM	IN718	Vickers hardness	300 gf/15s	AB	427.5 HV	[294]
				DA	488.0 HV	
				STA (930 °C)	479.6 HV	
				STA (980 °C)	478.7 HV	
				STA (1080 °C)	472.7 HV	
EBM	IN718	Vickers hardness	N.A.	AB/HT	Fig. 56	[308]
EBM	IN718	Vickers hardness	500 gf/15s	AB	438.41 ± 8.35 HV	[160]
				HIP	199.37 ± 10.44 HV	
				HIP + HT	482.26 ± 7.83 HV	
EBM	IN718	Vickers hardness	1 kgf/15s	AB	421.80 HV	[321]
				STA	468.72 HV	
				HIP + STA	474.38 HV	
EBM	IN718	Vickers hardness	500 gf/15s	Set A	387.92 HV	[367]
				Set B	386.95 HV	
				Set C	391.08 HV	
				Set D	394.96 HV	
EBM	nickel-based superalloy	Vickers hardness	1 kgf	90°	Fig. 52a	[146]
EBM	Rene 142	Vickers hardness & Rockwell C	Vickers 100 gf/Rockwell 1.5 N	Powder	3.4 GPa 346.7 HV	[354]
				0°/AB	4.1 GPa 418.1 HV	
				90°/AB	4.2 GPa 428.3 HV	
				0°/AB	39 HRC 379 HV	
				90°/AB	42 HRC 406 HV	

Appendix D. Fatigue properties of PBF Nickel-based superalloys

Table 11

Summary of fatigue properties of PBF Nickel-based superalloys (~ indicates that the data was obtained from the bar chart).

Technique	Material	Standard	Test condition	Load ratio (R)	Frequency	Sample condition	Ref
LPBF	EP708		Fatigue endurance study at room temperature, load from 340 to 380 MPa, cycles from 2·10 ⁶ to sample failure			Hot rolling + HT	[395]
LPBF	Hastelloy X		Low cycle fatigue test at RT in strain control with triangular wave shape, Strain ratio = 1			HIP + HT	[384]
			Thermomechanical fatigue test elevated temperature using a trapezoid waveform, Strain ratio = 0			Specimens were built in the 0°, 45° and 90° direction	
LPBF	Hastelloy® X		Four-point bend fatigue test, stress amplitude range 450 MPa–900 MPa	0.1	110 Hz	Specimens were built in the 0° and 90° direction. AB/HIP	[255]
			S–N tension–tension fatigue test, stress amplitude range 500 MPa–800 MPa	0.1	117 Hz		
LPBF	IN625	ASTM E647	Fatigue test at RT	0.1	20 Hz	0°/SR	[312]
						45°/SR	
						90°/SR	
						90°⊥/SR	
						0°/HIP	
						45°/HIP	
						90°/HIP	
						90°⊥/HIP	
LPBF	IN625		Fatigue Crack Growth at RT	Varied	20 Hz	Different R ratios	[399]
LPBF	IN625	ASTM E466	Fatigue Limit (10 ⁷ cycles) test at RT and at 650 °C	0.1	20	HIP	[438]

(continued on next page)

Table 11 (continued)

Technique	Material	Standard	Test condition	Load ratio (R)	Frequency	Sample condition	Ref
LPBF	IN626		Stress amplitude range 200 MPa–300 MPa	–1	20 Hz	AB, polished specimens	[252]
LPBF (DMLS)	IN718	ASTM E606	Low cycle fatigue at RT with strain amplitudes at 0.6%, or 0.8%, or 1.0%, or 1.2%, or 1.4% and a mean strain of 0.5%, strain rate $4 \times 10^{-3} \text{ s}^{-1}$		0.15 Hz	Specimens were built in the 0° and 45° direction, SA/HIP	[176]
LPBF	IN718		The crack growth rate study	0.1	25 Hz	Modified with Re. Specimens were built in the 0°, 45° and 90° direction, SA	[385]
LPBF	IN718	ASTM E647	High cycle fatigue, fatigue test at RT, 800 °F and 1200 °F	0.01	40 Hz	SR + HIP + HSA. AB surface condition, LSG surface condition	[386]
LPBF	IN718		High cycle fatigue plane bending testing	0	20 Hz	Specimens were built in the 0° and 90° direction, SR + ageing	[387]
LPBF	IN718		Thermomechanical Fatigue Testing, temperature cycling between 350 and 650 °C with a strain amplitude of $\pm 0.45\%$. Strain rate = –1			AB - 250, 950 W or Functionally Graded (FGM)	[388]
LPBF	IN718		Low-cycle fatigue tests at ambient temperature. Strain amplitudes of $\Delta\epsilon/2 = \pm 0.35\%$, $\Delta\epsilon/2 = \pm 0.5\%$ and $\Delta\epsilon/2 = \pm 0.8\%$. Strain rate = $6 \times 10^{-3} \text{ s}^{-1}$			Heat treated - HA	[172]
LPBF	IN718	ASTM E466	Fatigue test at RT	0.1	15 Hz	HT 1–1200 °C for 1 h under argon atmosphere HT 2 - Max temperature of 980 °C following the heat/hold/cool cycle for 24 h	[256]
LPBF (DMLS)	IN718		High cycle fatigue test, vibration bending testing, chord-wise bending (or two-stripe) mode		1600 Hz	AB	[257]
LPBF	IN718		Fatigued samples were pre-streined to 1% then tested	0.05	1 Hz	SR/SR + HSA	[254]
LPBF (DMLS)	IN718	ASTM E466	Fatigue test at RT	0.1	0.5 Hz	Dog bone structure, lattice structure. SR + SA	[220]
LPBF	IN718	ASTM E647	The crack growth rate study	0.1	80 to 60 Hz	AB, compact tension specimen with crack growth plane parallel to the build direction	[389]
LPBF	IN718	ASTM E647	The crack growth rate study	0.1	80 to 60 Hz	AB, compact tension specimen with crack growth plane parallel to the build direction	[390]
LPBF	IN718	ASTM E649	Fatigue Crack Growth at RT and 650 °C	0.1	10 Hz	AB	[424]
LPBF	IN718	ASTM E466	High cycle fatigue at RT	–1		SR + Defective specimen, LSG, HIP + built in 0°	[391]
				0.1		SA Non-defective specimen LSG, built in 90° LSG, built in 0° AB, built in 0°	
		ASTM E647	The crack growth rate study	0.1&0.7		Compact tension specimen with crack growth plane perpendicular to the build direction	
LPBF	IN718		Low cycle fatigue at 650 °C, strain amplitude of 0.40%	–1		SA HT to obtain columnar grains HA HT to obtain equiaxed grains	[396]
LPBF	IN718	ASTM E466	Fatigue test at 25 °C, maximum stress 827.4 MPa	0	30 Hz	Nominal Increased hatch spacing Decreased hatch spacing Increased cooling rate Decreased cooling rate	[320]
LPBF	IN718		Tension compression fatigue test	–1	30 Hz	Material A Material B	[313]
LPBF	IN718	ASTM E466	High cycle fatigue at RT	0.1	40 Hz	0°/HIP + SA/U notch 90°/HIP + SA/U notch 0°/HIP + SA/V notch type 1 90°/HIP + SA/V notch type 1 0°/HIP + SA/V notch type 2 90°/HIP + SA/V notch type 2 0°/HIP + SA/V notch type 2 with machined surfaces 90°/HIP + SA/V notch type 2 with machined surfaces	[392]
LPBF	IN718		Four-point bending fatigue test at RT	0.1	20 Hz	HIP + HT/Machined surface HIP + HT/AB surface HT/machined surface HT/AB surface	[397]
LPBF	IN718		Fatigue test at RT	0	10 Hz	Unnotched Semi-circular notch	[393]

(continued on next page)

Table 11 (continued)

Technique	Material	Standard	Test condition	Load ratio (R)	Frequency	Sample condition	Ref
LPBF	IN718		Fatigue test at RT	0	10 Hz	v-shaped notch with notch radius equal to 1 mm v-shaped notch with notch radius equal to radius 0.1 mm Unnotched Semi-circular V-shaped notch	[394]
LPBF	IN718		Fatigue test at RT	0.1	30 Hz	AB SA HA HSA	[322]
LPBF	IN718	ASTM E466	Fatigue test at RT, with maximum stress 900 MPa	0.1	20 Hz	Scan strategy-controlled group Processing parameters-controlled group	[398]
LPBF	IN718	ASTM E647	N-type Fatigue test at 550 °C and 2160 s dwell time P-type Fatigue test at 550 °C and 2160 s dwell time	0.05	10 Hz	STA/Homogenisation + DA/ Homogenisation + STA	[400]
LPBF	IN718	ASTM E647	Fatigue test at 550 °C and 2160 s dwell time	0.05	10 Hz	1h Homogenisation/48h Homogenisation	[426]
LPBF	IN718		Fatigue test at RT	-1		Homogenisation + STA (AMS 5663)	[337]
LPBF	IN718		Fatigue test at RT	0.1	10 Hz	Specimens built at 0°, 45° and 90°	[401]
LPBF	IN718		Fatigue test at RT	-1		Homogenisation + STA	[327]
LPBF	IN718		Fatigue limit (10 ⁵ cycles) test		20 Hz	Specimen built at 0° and 90° Dry machining Emulsion machining	[373]
LPBF	IN718	ASTM E606/E606 M And ASTM E739	Strain controlled at RT until 43200 cycles	Varied	0.5 Hz	Specimens built at 0°, 45° and 90° AB/DA/SA	[445]
LPBF	IN718		Fatigue Crack Growth at RT and 650 °C	0.1	2 Hz	Specimens built at 0° and 90° and HT	[425]
LPBF	IN718		Incremental step Fatigue test at RT	-1		Specimens built at 0°, 45° and 90° Different support structures Different surface preparation (mechanical or electromechanical polishing)	[402]
LPBF	IN718		Fatigue Limit (10 ⁷ cycles) test at RT	-1	10	Mechanically polished/HIP + HT	[446]
LPBF	IN718		Stress controlled fatigue test at 650 °C	0.1	1	Various surface conditions	[423]
LPBF	IN939		Low-cycle fatigue at RT and 750 °C, total strain amplitude 0.5%, strain rate 6 × 10 ⁻³	-1		AB/SA	[253]
LPBF	K536	ASTM E466	Tested at 400 °C Tested at 600 °C	0.1	100 Hz	SR/built in 0° SR/built in 90° SR/built in 0° SR/built in 90°	[319]
LPBF	K536		Stress controlled at 400 °C and 600 °C	0.1	100 Hz	Specimens built at 0° and 90°	[319]
EBM	IN718		Constant amplitude Fatigue Limit (10 ⁶ cycles) test at RT	-1	10	AB/Polished	[422]
EBM	IN718		Four-point bending fatigue test at RT	0.1	20 Hz	HIP + HT/Machined surface HIP + HT/AB surface HT/machined surface HT/AB surface	[397]
EBM	IN718	ASTM E647	Fatigue test at 550 °C and 2160 s dwell time	0.05	10 Hz	1h Homogenisation/48h Homogenisation	[426]
EBM	IN718	ASTM E606	Low cycle fatigue at 650 °C	-1	0.5 Hz	Specimens were built in the 0° and 90° direction. AB/HIP + SA	[296]
EBM	IN718		Four-point bending fatigue test at room temperature	0.1	20 Hz	STA + HIP/AB surface/cross-section 10 × 10 mm ² (with contour) STA + HIP/machined surface/cross-section 10 × 10 mm ² (with contour) STA + HIP/machined surface/cross-section 6 × 6 mm ² (without contour) STA/AB surface/cross-section 10 × 10 mm ² (with contour) STA/machined surface/cross-section 10 × 10 mm ² (with contour) STA/machined surface/cross-section 6 × 6 mm ² (without contour)	[321]

Appendix E. Creep properties of PBF Nickel-based superalloys

Table 12

Summary of creep properties of PBF Nickel-based superalloys ('~' indicates that the data was obtained from the bar chart).

Technique	Material	Standard	Test condition	Sample condition	Ref
LPBF	CM247LC		Small Punch creep test at 950 °C and 150 N	HIP + STA	[412]
LPBF	C263		Small punch testing, tested at 780 °C	Specimens are built in 0° and 90°. Solution (1150 °C) + ageing, Solution (1275 °C) + ageing	[410]
LPBF	Hastelloy X		Creep test at 815 °C	Specimens are built in 0°, 45° and 90°	[384]
LPBF	IN718		Creep test under the constant compressive stress of 725 MPa at 630 °C	DA & SA	[275]
LPBF	IN718		Creep test under the constant compressive stress of 900 MPa at 630 °C. Stress-change tests were performed at stresses between 900 and 1100 MPa. The load was step-wise increased by 50 MPa.	DA, solution at 930 °C + ageing, solution at 1000 °C + ageing	[190]
LPBF	IN718	ISO 204	Creep test at 700 °C, stress range from 250 to 375 MPa	Specimens are built in 0° and 90°. SR, SR + solution (980 °C) + ageing, SR + solution (1065 °C) + ageing	[405]
LPBF	IN718		Creep test at 650 °C and 550 MPa	AB, SA	[250]
LPBF	IN718		Creep test at 650 °C and 550 MPa	Specimens are built in 0° and 90°. AB, SA, DA	[406]
LPBF	IN718		Creep test at 650 °C and 650 MPa	AB, 2 bar specimens	[75]
LPBF	IN718	ASTM E139	Creep test at 650 °C and 690 MPa	AB, SA, functionally graded built	[388]
LPBF	IN718		Creep test at 650 °C and 650 MPa	AB, HSA, CNC/WEDM machined, 2 bar specimens	[407]
LPBF	IN718		Creep test at 650 °C and 550 MPa	AB Solution @ 980 °C for 1 h + ageing Solution @ 1045 °C for 1 h + ageing Solution @ 1065 °C for 1 h + ageing Solution @ 1120 °C for 1 h + ageing Solution @ 1180 °C for 1 h + ageing Solution @ 1180 °C for 4 h + ageing HIP	[408]
LPBF	IN718		Small punch testing, creep test at 650 °C and 600 N	HIP + ageing Forged-N: loading direction parallel to the forging direction Forged-P: loading direction perpendicular to the forging direction Casted LPBF specimen: Loading direction parallel to the build direction	[411]
LPBF	IN718	ASTM E139	650 °C and 620 MPa	1 different STA	[326]
LPBF	IN718	CEN 15627	Small Punch creep test at 650 °C and 400 N	Specimens built at 0° or 90° and STA or Homogenisation + Ageing	[430]
LPBF	IN718	ASTM E139	650 °C and 600 MPa	Specimens built at 0°, 90° and 45° AB/STA	[414]
LPBF	IN718	ASTM E139	650 °C and 600 MPa	Meander/Stripe strategy Specimens built at 0°, 90° and 45° + STA	[415]
LPBF	IN738LC	ISO 204	The creep machine used was a Unisteel multipoint machine with a load capacity of 30 kN and a 20:1 lever ratio. Creep test at 850 °C.	Single or Multi-laser Specimens are built in 0° and 90°	[249]
LPBF	IN738LC	ISO204	Creep test at 850 °C. A similar procedure respect to [249]	Specimens are built in 0° and 90°	[251]
LPBF	nickel-based superalloy		Creep test at 650 °C and 550 MPa	Specimens built in 90°/solution and aging treatment (980 °C/1 h/AC+718 °C/8 h/FC+621 °C/10 h/AC) Specimens built in 90°/Yttrium addition/solution and aging treatment (980 °C/1 h/AC+718 °C/8 h/FC + 621 °C/10 h/AC) Specimens built in 90°/Yttrium addition/direct aging treatment (718 °C/8 h/FC + 621 °C/10 h/AC) Specimens built in 0°/direct aging treatment (718 °C/8 h/FC + 621 °C/10 h/AC) Specimens built in 0°/Yttrium addition/direct aging treatment (718 °C/8 h/FC + 621 °C/10 h/AC)	[413]
EBM	IN718		Compression + Tension creep test at 800 °C. Load increased stepwise in a compression test	SA, Specimens are built in 0° and 90°.	[295]
EBM	IN718	ASTM E319	Creep test at 580 MPa and 600 MPa, at 650 °C	Specimens are built in 0° and 90° with point net fill scan strategy and standard melt fill scan strategy, post-treated with HIP + STA	[409]

Appendix F. Sample preparation

A summary of commonly used etchants for PBF manufactured nickel-based superalloys in literature is given in [Table 13](#).

Table 13
Commonly used etchants for PBF manufactured nickel-based superalloys in literature.

Alloys	Chemical etching	Electrolytic etching
IN718	<ul style="list-style-type: none"> Marble's reagent (10 g CuSO₄, 50 ml HCl and 50 ml H₂O) and 5% nitric acid in alcohol [173]. HNO₃, CH₃COOH and HCl in a ratio of 1:1:1 [132,183,297,447]. Glyceria reagent (15 ml HCl, 10 ml glycerol and 5 ml HNO₃) [67, 95,281,388]. Kalling's reagent No. 2 (40 ml HCl, 2 g CuCl₂ and 40 ml ethanol/methano) [67,165,216,220,385,389,390]. H₂O₂ (1.5–3 ml) and HCl (10 ml) for 10 s [65,228,229,289,344,345, 387,448]. 25 ml H₂O + 45 ml HCl + 15 ml HNO₃ + 15 ml HF [70]. Beraha III (colour etching) and Kalling No. 2 (micro-etching) [72, 172]. Dilute aqua regia solution (HNO₃ and HCl in a proportion of 1:3) [59,259,283]. 5 g FeCl₃, 100 ml HCl acid, and 100 ml ethanol [262]. 30 ml HCl + 5g FeCl₃ at RT [286]. 20 ml HCl, 20 ml HNO₃ and 1 g CuCl₂ [278]. 	<ul style="list-style-type: none"> Etch in 10% oxalic acid for 5–10 s [73–75]. Etch in a mixture of 70 ml of phosphoric acid and 30 ml of water at RT, using 5 V and last for 5–120 s at RT [76,77]. Etch in a solution of 12 ml H₃PO₄ + 40 ml HNO₃ + 48 ml H₂SO₄ at 6 V for 5 s [78]. Etch in a solution of 50 ml lactic acid, 3 g oxalic acid and 150 ml hydrochloric acid for 10–20 s at a voltage of 2 V (DC) [79]. Etch in a solution of 50 ml hydroxypropionic acid, 150 ml HCl acid, and 3 g oxalic acid with a constant current of 2 V for a few seconds [80].
IN625	<ul style="list-style-type: none"> Etch with aqua regia solution (HNO₃ and HCl in a proportion of 1:3) for 10–60 s [449,450]. Lactic acid-HCl mixture [451]. Etch with Kalling's No.2 etchant for 1–2 s [452]. Etch in 10 ml HNO₃, 10 ml HCl and 15 ml CH₃COOH for 30 s [348]. Kalling's No.2 reagent (5 g CuCl₂ in 100 ml HCl and 100 ml CH₃CH₂OH) for about 2 min [353]. Etch with 15 ml HCl, 10 ml CH₃COOH and 10 ml HNO₃ for 15 s [353]. 45 ml HCl, 2.2 ml HNO₃, 2.5 ml H₂SO₄ and 0.5 ml HF [318]. 5 ml HNO₃, 10 ml HCl, and 300 ml water for about 1s [453]. 30 ml HCl, 20 ml CH₃COOH and 20 ml HNO₃ [117,179]. Kalling's No.2 reagent (5 g CuCl₂ in 100 ml HCl and 100 ml CH₃CH₂OH) [147]. 	<ul style="list-style-type: none"> Etch in 7.5% oxalic acid for approx. 10 s [454]. Etch in a solution of 70 ml phosphoric acid and 30 ml H₂O using 1–5 V for 5 s–2 min at RT [264,266,269,292].
Hastelloy X	<ul style="list-style-type: none"> Kalling's No.2 reagent (5 g CuCl₂ in 100 ml HCl and 100 ml CH₃CH₂OH) [147]. 	<ul style="list-style-type: none"> Etch in a solution of 10 g oxalic acid in 100 ml of water at 6 V over 8 s [284,455].
IN939		<ul style="list-style-type: none"> Etch in HF at 3 V for 3–5 s [456].
IN738LC	<ul style="list-style-type: none"> Molybdc acid (0.5 g MoO₃, 200 ml H₂O, 50 ml HCl and 50 ml HNO₃) at 40 °C [457]. Adler reagent (50 ml H₂O, 100 ml HCl, 30 g FeCl₃, 6 g (NH₄)₂[CuCl₄]) for few seconds [249,251]. 	<ul style="list-style-type: none"> Etch with 10% H₂PO₄ [119]. Etch in a solution of 10 vol % oxalic acid with 6 V and 0.4 A for 26 s [58].
CMSX-4	<ul style="list-style-type: none"> V2A etchant at 338 K–343 K (65–70 °C) [458]. 	
CM247LC	<ul style="list-style-type: none"> Marble's reagent (50 ml HCl, 50 ml H₂O and 10.0 g CuSO₄) [459]. Kalling's No. 2 reagent (5 g CuCl₂, 100 ml HCl, and 100 ml ethanol) [38]. Etch for 3–5 s in Kalling's reagent (5 g CuCl₂ +100 ml HCl +100 ml distilled water) [184,460]. 	

Author statement

AC devised the underlying project alongside IA and CH, the main conceptual ideas and proof outline. ZX initiated the collection of resources and first draft which were developed to completion and substantially augmented by SS, HC GG, WW, AC, CH all contributed sections to the work and provided insight to the literature and contributions to date. PS generated all original graphics and illustrations. Conclusions and perspectives are a compound of efforts from all authors.

References

- [1] S.H. Huang, P. Liu, A. Mokasdar, L. Hou, "Additive manufacturing and its societal impact: a literature review, *Int. J. Adv. Manuf. Technol.* 67 (5) (2013) 1191–1203, 2013/07/01.
- [2] A. Liu, C.K. Chua, K.F. Leong, Properties of test coupons fabricated by selective laser melting, *Key Eng. Mater.* 447 (448) (2010) 780–784.
- [3] C.Y. Yap, C.K. Chua, Z.L. Dong, Z.H. Liu, D.Q. Zhang, State-of-the-art review on selective laser melting of non-ferrous metals, *Proceedings of the International Conference on Progress in Additive Manufacturing* (2014) 193–201, 0.
- [4] J.J. Lewandowski, M. Seifi, Metal additive manufacturing: a review of mechanical properties, *Annu. Rev. Mater. Res.* 46 (2016) 151–186.
- [5] S.L. Sing, J. An, W.Y. Yeong, F.E. Wiria, Laser and electron-beam powder-bed additive manufacturing of metallic implants: a review on processes, materials and designs, *J. Orthop. Res.* 34 (3) (2016) 369–385.
- [6] S. Gorsse, C. Hutchinson, M. Gouné, R. Banerjee, Additive manufacturing of metals: a brief review of the characteristic microstructures and properties of steels, Ti-6Al-4V and high-entropy alloys, *Sci. Technol. Adv. Mater.* 18 (1) (2017) 584–610.
- [7] M. Grasso, B.M. Colosimo, "Process defects and in situ monitoring methods in metal powder bed fusion: a review," *Measurement Science and Technology, Review* 28 (no. 4) (2017). Art. no. 044005.
- [8] D. Zhang, et al., Metal alloys for fusion-based additive manufacturing, *Advanced Engineering Materials, Review* 20 (no. 5) (2018). Art. no. 1700952.
- [9] D. Herzog, V. Seyda, E. Wycisk, C. Emmelmann, "Additive manufacturing of metals, *Acta Mater.* 117 (2016) 371–392.
- [10] D.D. Gu, W. Meiners, K. Wissenbach, R. Poprawe, Laser additive manufacturing of metallic components: materials, processes and mechanisms, *Int. Mater. Rev.* 57 (3) (2012) 133–164.
- [11] Y. Zhang, et al., "Additive manufacturing of metallic materials: a review, *Journal of Materials Engineering and Performance, Review* 27 (no. 1) (2018).
- [12] C.Y. Yap, et al., "Review of selective laser melting: materials and applications," *applied physics reviews, Review* 2 (4) (2015). Art. no. 041101.
- [13] L.E. Murr, et al., Metal fabrication by additive manufacturing using laser and electron beam melting technologies, *J. Mater. Sci. Technol.* 28 (1) (2012) 1–14.
- [14] C. Körner, "Additive manufacturing of metallic components by selective electron beam melting - a review, *Int. Mater. Rev.* 61 (5) (2016) 361–377.
- [15] B. Song, et al., "Differences in microstructure and properties between selective laser melting and traditional manufacturing for fabrication of metal parts: a review, *Front. Mech. Eng.* 10 (2) (2015) 111–125.

- [16] W.J. Sames, F.A. List, S. Pannala, R.R. Dehoff, S.S. Babu, "The metallurgy and processing science of metal additive manufacturing," *International Materials Reviews*, vol. 61, no 5 (2016) 315–360.
- [17] A. Basak, S. Das, "Epitaxy and microstructure evolution in metal additive manufacturing," *annual review of materials research*, vol. 46, no 1 (2016) 125–149.
- [18] J.-P. Kruth, M. Badrossamay, E. Yasa, J. Deckers, L. Thijs, J. Van Humbeeck, Part and material properties in selective laser melting of metals," in: *The 16th International Symposium on Electromachining*, Shanghai, China, 2010, pp. 1–12.
- [19] J.J. Lewandowski, M. Seifi, "Metal additive manufacturing: a review of mechanical properties," *Annu. Rev. Mater. Res.* 46 (1) (2016) 151–186.
- [20] M. Qian, W. Xu, M. Brandt, H.P. Tang, "Additive manufacturing and postprocessing of Ti-6Al-4V for superior mechanical properties," *MRS Bull.* 41 (10) (2016) 775–784.
- [21] P. Li, D.H. Warner, A. Fatemi, N. Phan, "Critical assessment of the fatigue performance of additively manufactured Ti-6Al-4V and perspective for future research," *International Journal of Fatigue* 85 (2016) 130–143.
- [22] A. Yadollahi, N. Shamsaei, "Additive manufacturing of fatigue resistant materials: challenges and opportunities," *Int. J. Fatig.* 98 (2017) 14–31.
- [23] Z. Tian, et al., "A review on laser powder bed fusion of inconel 625 nickel-based alloy," *Appl. Sci.* 10 (no. 1) (2020).
- [24] O. Adegoke, J. Andersson, H. Brodin, R. Pederson, "Review of laser powder bed fusion of gamma-prime-strengthened nickel-based superalloys," *Metals*, Review 10 (8) (2020) 1–26. Art. no. 996.
- [25] X. Wang, X. Gong, K. Chou, "Review on powder-bed laser additive manufacturing of Inconel 718 parts," *Proc. IME B J. Eng. Manufact.* 231 (11) (2017) 1890–1903.
- [26] N.T. Aboulkhair, N.M. Everitt, I. Maskery, I. Ashcroft, C. Tuck, "Selective laser melting of aluminum alloys," *MRS Bull.* 42 (4) (2017) 311–319.
- [27] L.C. Zhang, H. Attar, "Selective laser melting of titanium alloys and titanium matrix composites for biomedical applications: a review," *Adv. Eng. Mater.* 18 (4) (2016) 463–475.
- [28] X. Wang, et al., "Topological design and additive manufacturing of porous metals for bone scaffolds and orthopaedic implants: a review," *Biomaterials* 83 (2016) 127–141.
- [29] Y. Brif, M. Thomas, I. Todd, "The use of high-entropy alloys in additive manufacturing," *Scripta Mater.* 99 (2015) 93–96.
- [30] W.E. Frazier, "Metal additive manufacturing: a review," *Journal of materials engineering and performance* 23 (6) (2014) 1917–1928, 2014/06/01.
- [31] D. Bourell, et al., "Materials for additive manufacturing," *CIRP Annals* 66 (2) (2017) 659–681, 2017/01/01/.
- [32] J. Zhang, S. Li, Q. Wei, Y. Shi, L. Wang, L. Guo, "Cracking behavior and inhibiting process of inconel 625 alloy formed by selective laser melting," *3D Printing* 39 (2015) 961–966, 11/01.
- [33] L. Criales, Y. Arisoy, B. Lane, S. Moylan, M. Donmez, T. Özel, "Predictive modeling and optimization of multi-track processing for laser powder bed fusion of nickel alloy 625," *Additive Manufacturing* 13 (2016), 11/11.
- [34] R.J. Smith, G.J. Lewi, D.H. Yates, "Development and application of nickel alloys in aerospace engineering," *Aircraft Eng. Aero. Technol.* 73 (2) (2001) 138–147.
- [35] R.R. Boyer, J.D. Cotton, M. Mohaghegh, R.E. Schafrik, "Materials considerations for aerospace applications," *MRS Bull.* 40 (12) (2015) 1055–1066.
- [36] T.M. Pollock, S. Tin, "Nickel-based superalloys for advanced turbine engines: chemistry, microstructure and properties," *J. Propul. Power* 22 (2) (2006) 361–374.
- [37] Rolls Royce, More efficient turbines, *Nickel* 7 (2007).
- [38] S. Catchpole-Smith, N. Aboulkhair, L. Parry, C. Tuck, I.A. Ashcroft, A. Clare, "Fractal scan strategies for selective laser melting of 'unweldable' nickel superalloys," *Additive Manufacturing* 15 (2017) 113–122.
- [39] J.R. Davis, *ASM Specialty Handbook: Nickel, Cobalt, and Their Alloys*, ASM International, Materials Park, OH, 2000.
- [40] E.O. Ezugwu, J. Bonney, Y. Yamane, "An overview of the machinability of aeroengine alloys," *J. Mater. Process. Technol.* 134 (2) (2003) 233–253.
- [41] E.O. Ezugwu, Z.M. Wang, A.R. Machado, "The machinability of nickel-based alloys: a review," *J. Mater. Process. Technol.* 86 (1) (1999) 1–16.
- [42] J.A. Bernstein, et al., "Fabrication and Analysis of Porous Superalloys for Turbine Components Using Laser Additive Manufacturing," Presented at the 49th AIAA/ASME/SAE/ASEE Joint Propulsion Conference, California, San Jose, 2013, <https://doi.org/10.2514/6.2013-4178>. Available.
- [43] I.A. Choudhury, M.A. El-Baradie, "Machinability of nickel-base super alloys: a general review," *J. Mater. Process. Technol.* 77 (1–3) (1998) 278–284.
- [44] N. Guo, M.C. Leu, "Additive manufacturing: technology, applications and research needs," *Frontiers of Mechanical Engineering*, journal article 8 (3) (2013) 215–243.
- [45] I. Yadroitsev, I. Shishkovsky, P. Bertrand, I. Smurov, "Manufacturing of fine-structured 3D porous filter elements by selective laser melting," *Appl. Surf. Sci.* 255 (10) (2009) 5523–5527.
- [46] L. Li, C. Diver, J. Atkinson, R. Giedl-Wagner, H.J. Helm, "Sequential laser and EDM micro-drilling for next generation fuel injection nozzle manufacture," *CIRP Annals* 55 (1) (2006) 179–182.
- [47] A. Gisario, M. Kazarian, F. Martina, M. Mehrpouya, "Metal additive manufacturing in the commercial aviation industry: a review," *Journal of Manufacturing Systems*, Review 53 (2019) 124–149.
- [48] C.K. Yong, G.J. Gibbons, C.C. Wong, G. West, "A critical review of the material characteristics of additive manufactured in718 for high-temperature application," *Metals*, Review 10 (12) (2020) 1–22. Art. no. 1576.
- [49] Balbright, *NASA tests more printed rocket engine parts*. Available, 22/01, <http://www.rapidreadytech.com/2014/11/nasa-tests-more-printed-rocket-engine-parts/>, 2014.
- [50] J. Newman, *MTU aero engines parts built using selective laser melting*. Available, 22/01, <http://www.rapidreadytech.com/2014/03/mtu-aero-engines-parts-built-using-selective-laser-melting/>, 2014.
- [51] W.W. Wits, S.J. Weitkamp, J. van Es, "Metal additive manufacturing of a high-pressure micro-pump," *Procedia CIRP* 7 (2013) 252–257.
- [52] J. Newman, *GE Aviation Continues to Push Ahead with Additive Manufacturing*, 22/01, 2015. Available, <http://www.rapidreadytech.com/2015/05/ge-aviation-continues-to-push-ahead-with-additive-manufacturing/>.
- [53] T. Kellner, *The FAA Cleared the First 3D Printed Part to Fly in A Commercial Jet Engine from GE*, 22/01, 2015. Available, <http://www.gereports.com/post/116402870270/the-faa-cleared-the-first-3d-printed-part-to-fly/>.
- [54] D. Adair, M. Kirka, D. Ryan, Additive manufacture of prototype turbine blades for hot-fired engine performance validation trials, in: *In Proceedings of the ASME Turbo Expo*, vol. 6, 2019.
- [55] J. Zhang, F. Li, H. Zhang, "Research progress on preparation of metallic materials by selective laser melting," *Laser and Optoelectronics Progress*, Article 56 (no. 9) (2019).
- [56] *Standard Test Method for Density of Powder Metallurgy (PM) Materials Containing Less than Two Percent Porosity*, 2017.
- [57] J.P. Reese, *New Nanotechnology Research*. Nova Science Publishers, 2006.
- [58] P. Nataliya, et al., "Optimisation of selective laser melting parameters for the Ni-based superalloy IN-738 LC using Doehlert's design," *Rapid Prototyp. J.* 23 (5) (2017) 881–892.
- [59] J.-P. Choi, et al., "Densification and microstructural investigation of Inconel 718 parts fabricated by selective laser melting," *Powder Technol.* 310 (2017) 60–66, 2017/04/01/.
- [60] M. Terner, J. Lee, G. Marchese, S. Biamino, H.U. Hong, "Electron backscattered diffraction to estimate residual stress levels of a superalloy produced by laser powder bed fusion and subsequent heat treatments," *Materials*, Article 13 (20) (2020) 1–18. Art. no. 4643.
- [61] J. Rossin, et al., "Assessment of grain structure evolution with resonant ultrasound spectroscopy in additively manufactured nickel alloys," *Mater. Char.* 167 (2020) 110501, 2020/09/01/.
- [62] R.J. Smith, M. Hirsch, R. Patel, W. Li, A.T. Clare, S.D. Sharples, "Spatially resolved acoustic spectroscopy for selective laser melting," *Journal of Materials Processing Technology*, 236 (2016) 93–102, 2016/10/01/.
- [63] B.D. Cullity, S.R. Stock, *Elements of X-Ray Diffraction*, third ed., Pearson, ESSEX, UK, 2014.
- [64] K.N. Amato, et al., "Microstructures and mechanical behavior of Inconel 718 fabricated by selective laser melting," *Acta Mater.* 60 (5) (2012) 2229–2239, 2012/03/01/.
- [65] M. Xia, D. Gu, C. Ma, H. Chen, H. Zhang, "Microstructure evolution, mechanical response and underlying thermodynamic mechanism of multi-phase strengthening WC/Inconel 718 composites using selective laser melting," *J. Alloys Compd.* 747 (2018) 684–695.
- [66] S. Raghavan, et al., "Effect of different heat treatments on the microstructure and mechanical properties in selective laser melted INCONEL 718 alloy," *Mater. Manuf. Process.* 32 (14) (2017) 1588–1595.
- [67] V.A. Popovich, E.V. Borisov, A.A. Popovich, V.S. Sufiiarov, D.V. Masaylo, L. Alzina, "Impact of heat treatment on mechanical behaviour of Inconel 718 processed with tailored microstructure by selective laser melting," *Mater. Des.* 131 (2017) 12–22.
- [68] A.A. Popovich, V.S. Sufiiarov, I.A. Polozov, E.V. Borisov, "Microstructure and mechanical properties of inconel 718 produced by SLM and subsequent heat treatment," *Key Eng. Mater.* 651–653 (2015) 665–670.
- [69] S. Goel, et al., "Residual stress determination by neutron diffraction in powder bed fusion-built Alloy 718: influence of process parameters and post-treatment," *Materials and Design*, Article 195 (2020), 109045.
- [70] C. Sanz, V. García Navas, "Structural integrity of direct metal laser sintered parts subjected to thermal and finishing treatments," *J. Mater. Process. Technol.* 213 (12) (2013) 2126–2136.
- [71] W. Sun, S.B. Brown, R.K. Leach, *An Overview of Industrial X-Ray Computed Tomography*, National Physical Laboratory, Teddington, National Physical Laboratory, Middlesex, 2012.
- [72] W. Tillmann, C. Schaak, J. Nellesen, M. Schaper, M.E. Aydinöz, K.P. Hoyer, "Hot isostatic pressing of IN718 components manufactured by selective laser melting," *Additive Manufacturing* 13 (2017) 93–102.
- [73] S. Tammam-Williams, H. Zhao, F. Léonard, F. Derguti, I. Todd, P.B. Prangnell, "XCT analysis of the influence of melt strategies on defect population in Ti-6Al-4V components manufactured by Selective Electron Beam Melting," *Mater. Char.* 102 (2015) 47–61, 2015/04/01/.
- [74] D.H. Smith, et al., "Microstructure and mechanical behavior of direct metal laser sintered Inconel alloy 718," *Mater. Char.* 113 (2016) 1–9.
- [75] Z. Xu, et al., "Staged thermomechanical testing of nickel superalloys produced by selective laser melting," *Mater. Des.* 133 (2017) 520–527.
- [76] S.K. Everton, M. Hirsch, P. Stravroulakis, R.K. Leach, A.T. Clare, "Review of in-situ process monitoring and in-situ metrology for metal additive manufacturing," *Mater. Des.* 95 (2016) 431–445, 2016/04/05/.
- [77] L.E. Criales, Y.M. Arisoy, B. Lane, S. Moylan, A. Donmez, T. Özel, "Laser powder bed fusion of nickel alloy 625: experimental investigations of effects of process parameters on melt pool size and shape with spatter analysis," *Int. J. Mach. Tool Manufact.* 121 (2017) 22–36.

- [78] J.C. Heigel, B.M. Lane, "Measurement of the melt pool length during single scan tracks in a commercial laser powder bed fusion process, *J. Manuf. Sci. Eng.* 140 (5) (2018), 51012–51012-7.
- [79] J.L. McNeil, et al., In-situ monitoring for defect identification in nickel alloy complex geometries fabricated by L-PBF additive manufacturing, *Metall. Mater. Trans.: Physical Metallurgy and Materials Science*, Article 51 (12) (2020) 6528–6545.
- [80] Y.M. Arsoy, L.E. Ciales, T. Özel, "Modeling and simulation of thermal field and solidification in laser powder bed fusion of nickel alloy IN625, *Opt Laser. Technol.* 109 (2019) 278–292.
- [81] R. Esmailizadeh, U. Ali, A. Keshavarzkermani, Y. Mahmoodkhani, E. Marzbanrad, E. Toyserkani, "On the effect of spatter particles distribution on the quality of Hastelloy X parts made by laser powder-bed fusion additive manufacturing, *J. Manuf. Process.* 37 (2019) 11–20.
- [82] S.J. Foster, et al., Process-defect-structure-property correlations during laser powder bed fusion of alloy 718: role of in situ and ex situ characterizations, *Metallurgical and Materials Transactions A*, journal article 49 (11) (2018) 5775–5798.
- [83] Z. Tan, Q. Fang, H. Li, S. Liu, W. Zhu, D. Yang, "Neural network based image segmentation for spatter extraction during laser-based powder bed fusion processing, *Opt Laser. Technol.* 130 (2020) 106347, 10/01.
- [84] L. Yang, L. Lo, S. Ding, T. Özel, "Monitoring and detection of molten pool and spatter regions in laser powder bed fusion of super alloy Inconel 625, *Progress in Additive Manufacturing*, Article 5 (4) (2020) 367–378.
- [85] L. Caprio, A.G. Demir, B. Previtali, "Observing molten pool surface oscillations during keyhole processing in laser powder bed fusion as a novel method to estimate the penetration depth, *Additive Manufacturing*, Article 36 (2020), 101470.
- [86] B. Lane, et al., "Transient laser energy absorption, Co-axial melt pool monitoring, and relationship to melt pool morphology, *Additive Manufacturing*, Article 36 (2020), 101504.
- [87] C. Arnold, J. Böhm, C. Körner, Operando monitoring by analysis of backscattered electrons during electron beam melting, *Advanced Engineering Materials*, Article 22 (no. 9) (2020), 1901102.
- [88] C.L.A. Leung, S. Marussi, M. Towrie, R.C. Atwood, P.J. Withers, P.D. Lee, The effect of powder oxidation on defect formation in laser additive manufacturing, *Acta Mater.* 166 (2018).
- [89] G. Marco, C. Bianca Maria, "Process defects and in situ monitoring methods in metal powder bed fusion: a review, *Meas. Sci. Technol.* 28 (4) (2017) 44005.
- [90] E. Malekipoor, H. El-Mounayri, "Common defects and contributing parameters in powder bed fusion AM process and their classification for online monitoring and control: a review, *The International Journal of Advanced Manufacturing Technology*, journal article 95 (1) (2018) 527–550. March 01.
- [91] E. Malekipoor, H. El-Mounayri, "Common defects and contributing parameters in powder bed fusion AM process and their classification for online monitoring and control: a review, *International Journal of Advanced Manufacturing Technology*, Article 95 (1–4) (2018) 527–550.
- [92] Y. Kuo, S. Horikawa, K. Kakehi, "The effect of interdendritic δ phase on the mechanical properties of Alloy 718 built up by additive manufacturing, *Mater. Des.* 116 (2017) 411–418.
- [93] M. Calandri, S. Yin, B. Aldwell, F. Calignano, R. Lupoi, D. Ugues, "Texture and microstructural features at different length scales in Inconel 718 produced by selective laser melting, *Materials*, Article 12 (8) (2019). Art. no. 1293.
- [94] P. Tao, H. Li, B. Huang, Q. Hu, S. Gong, Q. Xu, "The crystal growth, intercellular spacing and microsegregation of selective laser melted Inconel 718 superalloy, *Vacuum*, Article 159 (2019) 382–390.
- [95] E. Chlebus, K. Gruber, B. Kuźnicka, J. Kurzac, T. Kurzynowski, "Effect of heat treatment on the microstructure and mechanical properties of Inconel 718 processed by selective laser melting, *Mater. Sci. Eng., A* 639 (2015) 647–655, 2015/07/15/.
- [96] M.M. Kirka, K.A. Unocic, N. Raghavan, F. Medina, R.R. Dehoff, S.S. Babu, "Microstructure development in electron beam-melted Inconel 718 and associated tensile properties, *J. Occup. Med.* 68 (3) (2016) 1012–1020.
- [97] W.J. Sames, K.A. Unocic, R.R. Dehoff, T. Lolla, S.S. Babu, "Thermal effects on microstructural heterogeneity of Inconel 718 materials fabricated by electron beam melting, *J. Mater. Res.* 29 (17) (2014) 1920–1930.
- [98] D. Deng, R.L. Peng, H. Söderberg, J. Moverare, "On the formation of microstructural gradients in a nickel-base superalloy during electron beam melting, *Mater. Des.* 160 (2018) 251–261.
- [99] A.T. Polonsky, M.P. Echlin, W.C. Lenthe, R.R. Dehoff, M.M. Kirka, T.M. Pollock, Defects and 3D structural inhomogeneity in electron beam additively manufactured Inconel 718, *Mater. Char.* 143 (2018).
- [100] J.A. Gonzalez, J. Mireles, S.W. Stafford, M.A. Perez, C.A. Terrazas, R.B. Wicker, "Characterization of Inconel 625 fabricated using powder-bed-based additive manufacturing technologies, *J. Mater. Process. Technol.* 264 (2019) 200–210.
- [101] S. Griffiths, et al., "Combining alloy and process modification for micro-crack mitigation in an additively manufactured Ni-base superalloy, *Additive Manufacturing*, Article 36 (2020), 101443.
- [102] N. Kalentics, et al., "Healing cracks in selective laser melting by 3D laser shock peening, *Additive Manufacturing*, Article 30 (2019), 100881.
- [103] M. Vilanova, R. Escribano-garcía, T. Guraya, M.S. Sebastian, "Optimizing laser powder bed fusion parameters for IN-738LC by response surface method, *Materials*, Article 13 (21) (2020) 1–12, 4879.
- [104] K.A. Unocic, M.M. Kirka, E. Cakmak, D. Greeley, A.O. Okello, S. Dryepondt, "Evaluation of additive electron beam melting of haynes 282 alloy, *Materials Science and Engineering A*, Article 772 (2020), 138607.
- [105] X. Zhang, C.J. Yocom, B. Mao, Y. Liao, "Microstructure evolution during selective laser melting of metallic materials: a review, *Journal of Laser Applications, Review* 31 (3) (2019), 31201.
- [106] J.P. Oliveira, A.D. LaLonde, J. Ma, "Processing parameters in laser powder bed fusion metal additive manufacturing, *Materials and Design*, Article 193 (2020), 108762.
- [107] Z. Snow, A.R. Nassar, E.W. Reutzel, "Invited Review Article: review of the formation and impact of flaws in powder bed fusion additive manufacturing, *Additive Manufacturing, Review* 36 (2020), 101457.
- [108] C. Kumara, A.R. Balachandramurthi, S. Goel, F. Hanning, J. Moverare, "Toward a better understanding of phase transformations in additive manufacturing of Alloy 718, *Materialia* 13 (2020) 100862, 2020/09/01/.
- [109] C.K. Sudbrack, et al., Impact of powder variability on the microstructure and mechanical behavior of selective laser melted alloy 718, in *Minerals, Metals and Materials Series* 2018 (2018) 89–113.
- [110] A.T. Sutton, C.S. Kriewall, M.C. Leu, J.W. Newkirk, "Powder characterisation techniques and effects of powder characteristics on part properties in powder-bed fusion processes, *Virtual Phys. Prototyp.* 12 (1) (2017) 3–29.
- [111] J.H. Tan, W.L.E. Wong, K.W. Dalgarno, "An overview of powder granulometry on feedstock and part performance in the selective laser melting process, *Additive Manufacturing* 18 (2017) 228–255.
- [112] A.M. Mancisidor, F. Garciandia, P.M. García-Riesco, M. San Sebastian, Influence of Hastelloy X composition on cracking susceptibility during SLM, in *Euro PM 2018 Congress and Exhibition* (2020). EID: 2-s:2-0-85084161546.
- [113] L.C. Ardila, et al., "Effect of IN718 recycled powder reuse on properties of parts manufactured by means of selective laser melting, *Physics Procedia* 56 (2014) 99–107.
- [114] P. Nandwana, et al., "Recyclability study on inconel 718 and Ti-6Al-4V powders for use in electron beam melting, *Metallurgical and Materials Transactions B*, journal article 47 (1) (2016) 754–762.
- [115] Q.B. Nguyen, M.L.S. Nai, Z. Zhu, C.-N. Sun, J. Wei, W. Zhou, "Characteristics of inconel powders for powder-bed additive manufacturing, *Engineering* 3 (5) (2017) 695–700.
- [116] A.N.D. Gasper, et al., "Spatter and oxide formation in laser powder bed fusion of Inconel 718, *Additive Manufacturing* 24 (2018) 446–456.
- [117] D. Tomus, P.A. Rometsch, M. Heilmaier, X. Wu, "Effect of minor alloying elements on crack-formation characteristics of Hastelloy-X manufactured by selective laser melting, *Additive Manufacturing* 16 (2017) 65–72.
- [118] W.J. Sames, F. Medina, W.H. Peter, S.S. Babu, R.R. Dehoff, Effect of process control and powder quality on Inconel 718 produced using electron beam melting, in: *8th International Symposium on Superalloy 718 and Derivatives*, 2014, pp. 409–423.
- [119] R. Engeli, T. Etter, S. Hövel, K. Wegener, "Processability of different IN738LC powder batches by selective laser melting, *Journal of Materials Processing Technology*, Article 229 (2016) 484–491.
- [120] Y. Zhang, H. Wang, X. Song, Z. Nie, "Preparation and performance of spherical Ni powder for SLM processing, *Jinshu Xuebao/Acta Metallurgica Sinica* 54 (12) (2018) 1833–1842.
- [121] C. Pleass, S. Jothi, "Influence of powder characteristics and additive manufacturing process parameters on the microstructure and mechanical behaviour of Inconel 625 fabricated by Selective Laser Melting, *Additive Manufacturing* 24 (2018) 419–431.
- [122] M.L. Montero-Sistiaga, et al., Fast screening of modified powder compositions for selective laser melting, in *Euro PM 2018 Congress and Exhibition* (2020). https://lirmo.libis.be/primo-explore/fulldisplay?docid=LIRIAS2321653&context=L&vid=Lirias&search_scope=Lirias&tab=default_tab&lang=en_US&fromSite=emap=1.
- [123] T.M. Pollock, A.J. Clarke, S.S. Babu, Design and tailoring of alloys for additive manufacturing, *Metall. Mater. Trans.: Physical Metallurgy and Materials Science* 51 (12) (2020) 6000–6019.
- [124] L. Aota, P. Bajaj, H. Sandim, E. Jägler, "Laser powder-bed fusion as an alloy development tool: parameter selection for in-situ alloying using elemental powders, *Materials* 13 (2020) 3922, 09/04.
- [125] B. Poorganji, E. Ott, R. Kelkar, A. Wessman, M. Jamshidinia, "Review: materials ecosystem for additive manufacturing powder bed fusion processes, *J. Occup. Med.* 72 (1) (2020) 561–576.
- [126] S. Traore, et al., "Influence of gas atmosphere (Ar or He) on the laser powder bed fusion of a Ni-based alloy, *J. Mater. Process. Technol.* 288 (2021) 116851, 2021/02/01/.
- [127] A.N.D. Gasper, et al., "Oxide and spatter powder formation during laser powder bed fusion of Hastelloy X, *Powder Technology*, Article 354 (2019) 333–337.
- [128] Y. Zhao, K. Aoyagi, K. Yamanaka, A. Chiba, "Role of operating and environmental conditions in determining molten pool dynamics during electron beam melting and selective laser melting, *Additive Manufacturing*, Article 36 (2020), 101559.
- [129] H. Gruber, M. Henriksson, E. Hryha, L. Nyborg, Effect of powder recycling in electron beam melting on the surface chemistry of alloy 718 powder, *Metall. Mater. Trans.: Physical Metallurgy and Materials Science* 50 (9) (2019) 4410–4422.
- [130] S. Dryepondt, M.M. Kirka, F.A. List, Oxidation behavior of Ni-based alloys fabricated by additive manufacturing, in *NACE - International Corrosion Conference Series* 2019 (2019).
- [131] H. Yu, S. Hayashi, K. Kakehi, Y.L. Kuo, "Study of formed oxides in IN718 alloy during the fabrication by selective laser melting and electron beam melting, *Metals*, Article 9 (1) (2019), 19.

- [132] P. Nandwana, M. Kirka, A. Okello, R. Dehoff, "Electron beam melting of Inconel 718: effects of processing and post-processing, *Mater. Sci. Technol.* 34 (5) (2018) 612–619.
- [133] H. Wong, K. Dawson, G.A. Ravi, L. Howlett, R. Jones, C. Sutcliffe, "Multi-Laser powder bed fusion benchmarking—initial trials with inconel 625, *Int. J. Adv. Manuf. Technol.* 105 (2019), 12/01.
- [134] H. Yeung, B. Lane, "A residual heat compensation based scan strategy for powder bed fusion additive manufacturing, *Manufacturing Letters*, Article 25 (2020) 56–59.
- [135] R. Sebastian, S. Catchpole-Smith, M. Simonelli, A. Rushworth, H. Chen, A. Clare, "'Unit cell' type scan strategies for powder bed fusion: the Hilbert fractal, *Additive Manufacturing* 36 (2020) 101588, 2020/12/01/.
- [136] H. Helmer, A. Bauereiß, R.F. Singer, C. Körner, "Grain structure evolution in Inconel 718 during selective electron beam melting, *Mater. Sci. Eng., A* 668 (2016) 180–187.
- [137] P. Karimi, E. Sadeghi, J. Ålgårdh, J. Andersson, "EBM-manufactured single tracks of Alloy 718: influence of energy input and focus offset on geometrical and microstructural characteristics, *Mater. Char.* 148 (2019) 88–99.
- [138] P. Fernandez-Zelaia, M.M. Kirka, S.N. Dryepondt, M.N. Gussev, "Crystallographic texture control in electron beam additive manufacturing via conductive manipulation, *Materials and Design*, Article 195 (2020), 109010.
- [139] T.D. McLouth, et al., "The effect of laser focus shift on microstructural variation of Inconel 718 produced by selective laser melting, *Mater. Des.* 149 (2018) 205–213.
- [140] Y. Wang, J. Shi, "Developing very strong texture in a nickel-based superalloy by selective laser melting with an ultra-high power and flat-top laser beam, *Mater. Char.* 165 (2020) 110372, 2020/07/01/.
- [141] M.C. Sow, et al., "Influence of beam diameter on laser powder bed fusion (L-PBF) process, *Additive Manufacturing*, Article 36 (2020), 101532.
- [142] K. Peng, et al., "Cracking behavior of rene 104 nickel-based superalloy prepared by selective laser melting using different scanning strategies, *Materials*, Article 13 (9) (2020), 2149.
- [143] D. Grange, J.D. Bartout, B. Macquaire, C. Colin, "Processing a non-weldable nickel-base superalloy by Selective Laser Melting: role of the shape and size of the melt pools on solidification cracking, *Materialia*, Article 12 (2020), 100686.
- [144] I. Serrano-Munoz, et al., "The residual stress in as-built Laser Powder Bed Fusion IN718 alloy as a consequence of the scanning strategy induced microstructure, *Scientific Reports*, Article 10 (1) (2020), 14645.
- [145] V.R.K. Rajendran, K. Mamidi, B. Ravichander, B. Farhang, A. Amerinatanzi, N. Shayesteh Moghaddam, Determination of residual stress for Inconel 718 samples fabricated through different scanning strategies in selective laser melting, in: *Proceedings of SPIE - the International Society for Optical Engineering*, vol. 11377, 2020.
- [146] E. Chauvet, et al., "Hot cracking mechanism affecting a non-weldable Ni-based superalloy produced by selective electron Beam Melting, *Acta Mater.* 142 (2018) 82–94.
- [147] G. Marchese, et al., "Study of the microstructure and cracking mechanisms of Hastelloy X produced by laser powder bed fusion, *Materials* 11 (1) (2018) 106.
- [148] M. Amirjan, H. Sakiani, "Effect of scanning strategy and speed on the microstructure and mechanical properties of selective laser melted IN718 nickel-based superalloy, *International Journal of Advanced Manufacturing Technology*, Article 103 (5–8) (2019) 1769–1780.
- [149] C. Guo, et al., "Effect of processing parameters on surface roughness, porosity and cracking of as-built IN738LC parts fabricated by laser powder bed fusion, *Journal of Materials Processing Technology*, Article 285 (2020), 116788.
- [150] W. Wang, Y. Li, X. Li, L. Liu, F. Chen, "Microstructures and properties of Ni-Cr-B-Si alloy powders prepared by selective laser melting, *Cailiao Daobao/Materials Reports*, Article 34 (1) (2020) 2077–2082.
- [151] B. Attard, S. Cruchley, C. Beetz, M. Megahed, Y.L. Chiu, M.M. Attallah, "Microstructural control during laser powder fusion to create graded microstructure Ni-superalloy components, *Additive Manufacturing*, Article 36 (2020), 101432.
- [152] M.D. Jean, Y.F. Tzeng, "Use of Taguchi methods and multiple regression analysis for optimal process development of high energy electron beam case hardening of cast iron, *Surf. Eng.* 19 (2) (2003) 150–156, 2003/04/01.
- [153] J. Sun, Y. Yang, D. Wang, "Parametric optimization of selective laser melting for forming Ti6Al4V samples by Taguchi method, *Opt Laser. Technol.* 49 (2013) 118–124, 07/01.
- [154] M. Marrey, E. Malekipour, H. El-Mounayri, E.J. Faierson, "A framework for optimizing process parameters in powder bed fusion (PBF) process using artificial neural network (ANN), *Procedia Manufacturing* 34 (2019) 505–515, 2019/01/01/.
- [155] C.H. Lim, M. Krishnan, H. Li, Methods of residual stress reduction for metal parts manufactured using selective laser melting (A Review), in: *Proceedings of the International Conference on Progress in Additive Manufacturing*, vol. 2018, 2018, pp. 315–320.
- [156] Z. Xu, C.J. Hyde, C. Tuck, A.T. Clare, "Creep behaviour of inconel 718 processed by laser powder bed fusion, *J. Mater. Process. Technol.* 256 (2018).
- [157] M. Ahmad, R. Ignacio Picazo, B. Vladimir, J. Mohammad, M. Mamoun, "Structure, texture and phases in 3D printed IN718 alloy subjected to homogenization and HIP treatments, *Metals* 7 (6) (2017) 196.
- [158] A. Hilaire, E. Andrieu, X. Wu, "High-temperature mechanical properties of alloy 718 produced by laser powder bed fusion with different processing parameters, *Additive Manufacturing* 26 (2019) 147–160.
- [159] M. Azarbarmas, M. Aghaie-Khafri, J.M. Cabrera, J. Calvo, "Dynamic recrystallization mechanisms and twinning evolution during hot deformation of Inconel 718, *Mater. Sci. Eng.* 678 (C) (2016) 137–152.
- [160] S. Goel, M. Ahlfor, F. Bahbou, S. Joshi, Effect of different post-treatments on the microstructure of EBM-built alloy 718, *J. Mater. Eng. Perform.* 28 (2019) 673–680, <https://doi.org/10.1007/s11665-018-3712-0>.
- [161] S. Parizia, et al., "Effect of heat treatment on microstructure and oxidation properties of Inconel 625 processed by LPBF, *Journal of Alloys and Compounds*, Article 846 (2020), 156418.
- [162] Y.S.J. Yoo, T.A. Book, M.D. Sangid, J. Kacher, "Identifying strain localization and dislocation processes in fatigued Inconel 718 manufactured from selective laser melting, *Mater. Sci. Eng.* 724 (2018) 444–451.
- [163] W. Huang, J. Yang, H. Yang, G. Jing, Z. Wang, X. Zeng, "Heat treatment of Inconel 718 produced by selective laser melting: microstructure and mechanical properties, *Mater. Sci. Eng.* 750 (2019) 98–107.
- [164] S.G.K. Manikandan, D. Sivakumar, K.P. Rao, M. Kamaraj, "Effect of weld cooling rate on Laves phase formation in Inconel 718 fusion zone, *J. Mater. Process. Technol.* 214 (2) (2014) 358–364, 2014/02/01/.
- [165] D. Zhang, W. Niu, X. Cao, Z. Liu, "Effect of standard heat treatment on the microstructure and mechanical properties of selective laser melting manufactured Inconel 718 superalloy, *Mater. Sci. Eng., A* 644 (2015) 32–40, 2015/09/17/.
- [166] Y. Zhao, K. Li, M. Gargani, W. Xiong, "A comparative analysis of Inconel 718 made by additive manufacturing and suction casting: microstructure evolution in homogenization, *Additive Manufacturing*, Article 36 (2020), 101404.
- [167] R. Jiang, A. Mostafaei, J. Pauza, C. Kantzos, A.D. Rollett, "Varied heat treatments and properties of laser powder bed printed Inconel 718, *Mater. Sci. Eng.* 755 (2019) 170–180.
- [168] A.R. Balachandramurthi, J. Moverare, N. Dixit, D. Deng, R. Pederson, "Microstructural influence on fatigue crack propagation during high cycle fatigue testing of additively manufactured Alloy 718, *Mater. Char.* 149 (2019) 82–94.
- [169] T. Gundgire, S. Goel, U. Klement, S. Joshi, "Response of different electron beam melting produced Alloy 718 microstructures to thermal post-treatments, *Mater. Char.* 167 (2020) 110498, 2020/09/01/.
- [170] F3055–14a Standard Specification for Additive Manufacturing Nickel Alloy (UNS N07718) with Powder Bed Fusion, 2014.
- [171] Heat Treatment Wrought Nickel Alloy and Cobalt Alloy Parts, 2001.
- [172] M.E. Aydınöz, et al., "On the microstructural and mechanical properties of post-treated additively manufactured Inconel 718 superalloy under quasi-static and cyclic loading, *Mater. Sci. Eng., A* 669 (2016) 246–258, 2016/07/04/.
- [173] D. Ivanov, et al., "Evolution of structure and properties of the nickel-based alloy EP718 after the SLM growth and after different types of heat and mechanical treatment, *Additive Manufacturing* 18 (2017) 269–275.
- [174] S. Holland, X. Wang, X.Y. Fang, Y.B. Guo, F. Yan, L. Li, "Grain boundary network evolution in Inconel 718 from selective laser melting to heat treatment, *Mater. Sci. Eng., A* 725 (2018) 406–418, 2018/05/16/.
- [175] X.Y. Fang, H.Q. Li, M. Wang, C. Li, Y.B. Guo, "Characterization of texture and grain boundary character distributions of selective laser melted Inconel 625 alloy, *Mater. Char.* 143 (2018) 182–190.
- [176] S. Gribbin, J. Bicknell, L. Jorgensen, I. Tsukrov, M. Knezevic, "Low cycle fatigue behavior of direct metal laser sintered Inconel alloy 718, *Int. J. Fatig.* 93 (2016) 156–167, 2016/12/01/.
- [177] Z.J. Zhang, P. Zhang, L.L. Li, Z.F. Zhang, "Fatigue cracking at twin boundaries: effects of crystallographic orientation and stacking fault energy, *Acta Mater.* 60 (6) (2012) 3113–3127.
- [178] Q. Han, et al., "Laser powder bed fusion of Hastelloy X: effects of hot isostatic pressing and the hot cracking mechanism, *Mater. Sci. Eng., A* 732 (2018) 228–239.
- [179] D. Tomus, Y. Tian, P.A. Rometsch, M. Heilmaier, X. Wu, "Influence of post heat treatments on anisotropy of mechanical behaviour and microstructure of Hastelloy-X parts produced by selective laser melting, *Mater. Sci. Eng., A* 667 (2016) 42–53.
- [180] O. Sanchez-Mata, J.A. Muñoz-Lerma, X. Wang, S.E. Atabay, M. Attarian Shandiz, M. Brochu, "Microstructure and mechanical properties at room and elevated temperature of crack-free Hastelloy X fabricated by laser powder bed fusion, *Materials Science and Engineering A*, Article 780 (2020), 139177.
- [181] G. Marchese, et al., "Microstructural evolution of post-processed Hastelloy X alloy fabricated by laser powder bed fusion, *Materials*, Article 12 (3) (2019), 486.
- [182] H. Peng, Y. Shi, S. Gong, H. Guo, B. Chen, "Microstructure, mechanical properties and cracking behaviour in a γ' -precipitation strengthened nickel-base superalloy fabricated by electron beam melting, *Materials and Design*, Article 159 (2018) 155–169.
- [183] W.J. Sames, et al., "Feasibility of in situ controlled heat treatment (ISHT) of Inconel 718 during electron beam melting additive manufacturing, *Additive Manufacturing* 13 (2017) 156–165.
- [184] V.D. Divya, et al., "Microstructure of selective laser melted CM247LC nickel-based superalloy and its evolution through heat treatment, *Mater. Char.* 114 (2016) 62–74.
- [185] W.M. Tucho, P. Cuvillier, A. Sjolyst-Kverneland, V. Hansen, "Microstructure and hardness studies of Inconel 718 manufactured by selective laser melting before and after solution heat treatment, *Mater. Sci. Eng., A* 689 (2017) 220–232, 2017/03/24/.
- [186] A. Deshpande, S.D. Nath, S. Atre, K. Hsu, "Effect of post processing heat treatment routes on microstructure and mechanical property evolution of haynes 282 Ni-based superalloy fabricated with selective laser melting (SLM), *Metals*, Article 10 (5) (2020), 629.
- [187] M.R. Stoudt, et al., "The influence of annealing temperature and time on the formation of δ -phase in additively-manufactured inconel 625, *Metallurgical and Materials Transactions A*, journal article 49 (7) (2018) 3028–3037.

- [188] F. Zhang, et al., "Effect of heat treatment on the microstructural evolution of a nickel-based superalloy additive-manufactured by laser powder bed fusion, *Acta Mater.* 152 (2018) 200–214.
- [189] R.J. Vikram, A. Singh, S. Suwas, "Effect of heat treatment on the modification of microstructure of selective laser melted (SLM) IN718 and its consequences on mechanical behavior, *J. Mater. Res.* 35 (15) (2020) 1949–1962.
- [190] M. Pröbstle, et al., "Superior creep strength of a nickel-based superalloy produced by selective laser melting, *Mater. Sci. Eng., A* 674 (2016) 299–307, 2016/09/30/.
- [191] S. Sui, J. Chen, Z. Li, H. Li, X. Zhao, H. Tan, "Investigation of dissolution behavior of laves phase in inconel 718 fabricated by laser directed energy deposition, *Additive Manufacturing* 32 (2020) 101055, 2020/03/01/.
- [192] S. Sui, et al., "The influence of Laves phases on the room temperature tensile properties of Inconel 718 fabricated by powder feeding laser additive manufacturing, *Acta Mater.* 164 (2019) 413–427, 2019/02/01/.
- [193] H. Xiao, S. Li, X. Han, J. Mazumder, L. Song, "Laves phase control of Inconel 718 alloy using quasi-continuous-wave laser additive manufacturing, *Mater. Des.* 122 (2017) 330–339, 2017/05/15/.
- [194] D.I. Sukhov, N.V. Petrushin, D.V. Zaitsev, M.M. Tikhonov, "Features of VZhL21 nickel-base superalloy structure formation during selective laser melting, vacuum heat treatment, and hot isostatic compaction, *Metallurgist*, Article 63 (3–4) (2019) 409–421.
- [195] J.H. Boswell, D. Clark, W. Li, M.M. Attallah, "Cracking during thermal post-processing of laser powder bed fabricated CM247LC Ni-superalloy, *Materials and Design*, Article 174 (2019), 107793.
- [196] E. Ezugwu, Z.M. Wang, A. Machado, "The machinability of nickel-based alloys: a review, *J. Mater. Process. Technol.* 86 (1998) 1–16, 02/15.
- [197] D.A. Lesyk, S. Martinez, B.N. Mordiyuk, V.V. Dzhemelinskiy, A. Lamikiz, G. I. Prokopenko, "Post-processing of the Inconel 718 alloy parts fabricated by selective laser melting: effects of mechanical surface treatments on surface topography, porosity, hardness and residual stress, *Surface and Coatings Technology*, Article 381 (2020), 125136.
- [198] E. Sadeghi, P. Pant, R. Jafari, R.L. Peng, P. Karimi, "Subsurface grain refinement in electron beam-powder bed fusion of Alloy 718: surface texture and oxidation performance, *Mater. Char.* 168 (2020) 110567, 2020/10/01/.
- [199] D. Lesyk, S. Martinez, O. Pedash, V. Dzhemelinskiy, B. Mordiyuk, Combined thermo-mechanical techniques for post-processing of the SLM-printed Ni-Cr-Fe alloy parts, *Lecture Notes in Mechanical Engineering* (2020) 295–304.
- [200] M.C. Kuner, M. Romedenne, P. Fernandez-Zelaia, S. Dreyepont, "Quantitatively accounting for the effects of surface topography on the oxidation kinetics of additive manufactured Hastelloy X processed by electron beam melting, *Additive Manufacturing*, Article 36 (2020), 101431.
- [201] R. Karthick Raaj, et al., "Exploring grinding and burnishing as surface post-treatment options for electron beam additive manufactured Alloy 718, *Surface and Coatings Technology*, Article 397 (2020), 126063.
- [202] L. Yang, C. O'Neil, Y. Wu, The use of electropolishing surface treatment on IN718 parts fabricated by laser powder bed fusion process, in: *Solid Freeform Fabrication 2017: Proceedings of the 28th Annual International Solid Freeform Fabrication Symposium - an Additive Manufacturing Conference*, SFF, vol. 2017, 2020, pp. 2493–2502.
- [203] Y. Yin, et al., "Effect of microstructure on the passive behavior of selective laser melting-fabricated Hastelloy X in NaNO₃ solution, *Materials Characterization*, Article 165 (2020), 110370.
- [204] J. Fei, G. Liu, K. Patel, T. Özel, "Effects of machining parameters on finishing additively manufactured nickel-based alloy inconel 625, *Journal of Manufacturing and Materials Processing*, Article 4 (2) (2020), 4020032.
- [205] L. Yang, K.V. Patel, K. Jarosz, T. Özel, Surface integrity induced in machining additively fabricated nickel alloy Inconel 625, in *Procedia CIRP* 87 (2020) 351–354.
- [206] J. Fei, G. Liu, K. Patel, T. Özel, "Cutting force investigation in face milling of additively fabricated nickel alloy 625 via powder bed fusion, *International Journal of Mechatronics and Manufacturing Systems*, Article 12 (3–4) (2019) 196–210.
- [207] S. Periane, et al., Selection of machining condition on surface integrity of additive and conventional Inconel 718, in *Procedia CIRP* 87 (2020) 333–338.
- [208] S. Webster, H. Lin, F.M. Carter Iii, K. Ehmann, J. Cao, "Physical mechanisms in hybrid additive manufacturing: a process design framework, *J. Mater. Process. Technol.* 291 (2021) 117048, 2021/05/01/.
- [209] J.M. Flynn, A. Shokrani, S.T. Newman, V. Dhokia, "Hybrid additive and subtractive machine tools – research and industrial developments, *Int. J. Mach. Tool Manufact.* 101 (2016) 79–101, 2016/02/01/.
- [210] D. Qiu, et al., "Research progress of SLM forming nickel-based superalloys and the simulation, *Gongneng Cailiao/Journal of Functional Materials*, Article 50 (3) (2019) 3049–3058.
- [211] M. Markl, C. Körner, "Multiscale modeling of powder bed-based additive manufacturing, *Annu. Rev. Mater. Res.* 46 (2016) 93–123, 08/04.
- [212] P. Stavropoulos, P. Foteinopoulos, "Modelling of additive manufacturing processes: a review and classification, *Manufacturing Rev.*, 10.1051/mfreview/2017014 5 (2018).
- [213] J.H.K. Tan, S.L. Sing, W.Y. Yeong, "Microstructure modelling for metallic additive manufacturing: a review, *Virtual and Physical Prototyping*, Review 15 (1) (2020) 87–105.
- [214] S. Srivastava, et al., "Multi-physics continuum modelling approaches for metal powder additive manufacturing: a review, *Rapid Prototyping Journal*, Review 26 (4) (2020) 737–764.
- [215] M. Masoomi, S.M. Thompson, N. Shamsaei, "Laser powder bed fusion of Ti-6Al-4V parts: thermal modeling and mechanical implications, *Int. J. Mach. Tool Manufact.* 118–119 (2017) 73–90, 2017/08/01/.
- [216] D. Zhang, Z. Feng, C. Wang, W. Wang, Z. Liu, W. Niu, Comparison of microstructures and mechanical properties of Inconel 718 alloy processed by selective laser melting and casting, *Mater. Sci. Eng., A* 724 (2018).
- [217] X. Ding, Y. Koizumi, D. Wei, A. Chiba, "Effect of process parameters on melt pool geometry and microstructure development for electron beam melting of IN718: a systematic single bead analysis study, *Additive Manufacturing*, Article 26 (2019) 215–226.
- [218] T. Pinomaa, T. Andersson, A. Laukkanen, Process-to-structure mapping of selective laser melting of a nickel based superalloy via phase field modelling, in: *In Euro PM 2018 Congress and Exhibition*, 2020.
- [219] H.L. Wei, et al., "Mechanistic models for additive manufacturing of metallic components, *Prog. Mater. Sci.* 116 (2021) 100703, 2021/02/01/.
- [220] L. Huynh, J. Rotella, M.D. Sangid, "Fatigue behavior of IN718 microcrusces produced via additive manufacturing, *Mater. Des.* 105 (2016) 278–289.
- [221] N. Raghavan, et al., "Numerical modeling of heat-transfer and the influence of process parameters on tailoring the grain morphology of IN718 in electron beam additive manufacturing, *Acta Mater.* 112 (2016) 303–314, 2016/06/15/.
- [222] J. Yang, et al., "Microstructure and grain growth direction of SRR99 single-crystal superalloy by selective laser melting, *Journal of Alloys and Compounds*, Article 808 (2019), 151740.
- [223] Y.H. Zhou, et al., "Selective laser melting of typical metallic materials: an effective process prediction model developed by energy absorption and consumption analysis, *Additive Manufacturing*, Article 25 (2019) 204–217.
- [224] L. Zhang, et al., "Effect of processing parameters on thermal behavior and related density in GH3536 alloy manufactured by selective laser melting, *Journal of Materials Research*, Article 34 (8) (2019) 1405–1414.
- [225] W. Yan, et al., "Data-driven multi-scale multi-physics models to derive process-structure-property relationships for additive manufacturing, *Comput. Mech.* 61 (5) (2018) 521–541, 2018/05/01.
- [226] E. Kundakcioglu, I. Lazoglu, Ö. Poyraz, E. Yasa, N. Cizicioglu, "Thermal and molten pool model in selective laser melting process of Inconel 625, *The International Journal of Advanced Manufacturing Technology*, journal article 95 (9) (2018) 3977–3984.
- [227] L.E. Criales, Y.M. Arisoy, T. Özel, "Sensitivity analysis of material and process parameters in finite element modeling of selective laser melting of Inconel 625, *The International Journal of Advanced Manufacturing Technology*, journal article 86 (9) (2016) 2653–2666.
- [228] M. Xia, D. Gu, G. Yu, D. Dai, H. Chen, Q. Shi, "Porosity evolution and its thermodynamic mechanism of randomly packed powder-bed during selective laser melting of Inconel 718 alloy, *Int. J. Mach. Tool Manufact.* 116 (2017) 96–106.
- [229] M. Xia, D. Gu, G. Yu, D. Dai, H. Chen, Q. Shi, "Influence of hatch spacing on heat and mass transfer, thermodynamics and laser processability during additive manufacturing of Inconel 718 alloy, *Int. J. Mach. Tool Manufact.* 109 (2016) 147–157.
- [230] Y. Zhang, G. Guillemot, M. Bernacki, M. Bellet, "Macroscopic thermal finite element modeling of additive metal manufacturing by selective laser melting process, *Comput. Methods Appl. Mech. Eng.* 331 (2018) 514–535.
- [231] Y.S. Lee, W. Zhang, "Modeling of heat transfer, fluid flow and solidification microstructure of nickel-base superalloy fabricated by laser powder bed fusion, *Additive Manufacturing* 12 (2016) 178–188.
- [232] Z. Chen, et al., "Thermal dynamic behavior during selective laser melting of K418 superalloy: numerical simulation and experimental verification, *Applied Physics A*, journal article 124 (4) (2018) 313.
- [233] D. Gu, M. Xia, D. Dai, "On the role of powder flow behavior in fluid thermodynamics and laser processability of Ni-based composites by selective laser melting, *Int. J. Mach. Tool Manufact.* 137 (2019) 67–78.
- [234] J. Weirather, et al., "A Smoothed Particle Hydrodynamics Model for Laser Beam Melting of Ni-Based Alloy 718, *Computers & Mathematics with Applications*, 2018.
- [235] D. Zhang, P. Zhang, Z. Liu, Z. Feng, C. Wang, Y. Guo, "Thermofluid field of molten pool and its effects during selective laser melting (SLM) of Inconel 718 alloy, *Additive Manufacturing* 21 (2018) 567–578.
- [236] M. Xia, et al., "Fragmentation and refinement behavior and underlying thermodynamic mechanism of WC reinforcement during selective laser melting of Ni-based composites, *J. Alloys Compd.* 777 (2019) 693–702.
- [237] J. Kundin, L. Mushongera, H. Emmerich, "Phase-field modeling of microstructure formation during rapid solidification in Inconel 718 superalloy, *Acta Mater.* 95 (2015) 343–356.
- [238] Y. Zhang, J. Zhang, "Sintering phenomena and mechanical strength of nickel based materials in direct metal laser sintering process—a molecular dynamics study, *J. Mater. Res.* 31 (15) (2016) 2233–2243.
- [239] D. Gu, C. Ma, M. Xia, D. Dai, Q. Shi, "A multiscale understanding of the thermodynamic and kinetic mechanisms of laser additive manufacturing, *Engineering* 3 (5) (2017) 675–684.
- [240] R. Acharya, J.A. Sharon, A. Staroselsky, "Prediction of microstructure in laser powder bed fusion process, *Acta Mater.* 124 (2017) 360–371.
- [241] X. Wang, K. Chou, "Microstructure simulations of Inconel 718 during selective laser melting using a phase field model, *The International Journal of Advanced Manufacturing Technology*, journal article (2018). <https://link.springer.com/article/10.1007/s00170-018-2814-z>.
- [242] X. Wang, P.W. Liu, Y. Ji, Y. Liu, M.H. Horstemeyer, L. Chen, "Investigation on microsegregation of IN718 alloy during additive manufacturing via integrated

- phase-field and finite-element modeling, *Journal of Materials Engineering and Performance*, journal article (2018). <https://link.springer.com/article/10.1007/s11665-018-3620-3>.
- [243] K. An, L. Yuan, L. Dial, I. Spinelli, A.D. Stoica, Y. Gao, "Neutron residual stress measurement and numerical modeling in a curved thin-walled structure by laser powder bed fusion additive manufacturing, *Mater. Des.* 135 (2017) 122–132.
- [244] S. Tadano, T. Hino, Y. Nakatani, "A modeling study of stress and strain formation induced during melting process in powder-bed electron beam melting for Ni superalloy, *J. Mater. Process. Technol.* 257 (2018) 163–169.
- [245] L.M. Sochalski-Kolbus, et al., "Comparison of residual stresses in Inconel 718 simple parts made by electron beam melting and direct laser metal sintering, *Metallurgical and Materials Transactions A*, journal article 46 (3) (2015) 1419–1432.
- [246] P. Prabhakar, W.J. Sames, R. Dehoff, S.S. Babu, "Computational modeling of residual stress formation during the electron beam melting process for Inconel 718, *Additive Manufacturing* 7 (2015) 83–91.
- [247] L. Tang, C. Wu, Z. Zhang, J. Shang, C. Yan, "A lightweight structure redesign method based on selective laser melting, *Metals* 6 (11) (2016) 280.
- [248] B. De Jager, et al., "Texture and microstructure analysis of IN718 nickel superalloy samples additively manufactured by selective laser melting, in: *Lecture Notes in Engineering and Computer Science* vol. 2228, 2017, pp. 734–740.
- [249] L. Rickenbacher, T. Etter, S. Hövel, K. Wegener, "High temperature material properties of IN738LC processed by selective laser melting (SLM) technology, *Rapid Prototyp. J.* 19 (4) (2013) 282–290.
- [250] Y. Kuo, K. Kakehi, "Influence of powder surface contamination in the Ni-based superalloy Alloy718 fabricated by selective laser melting and hot isostatic pressing, *Metals* 7 (9) (2017) 367.
- [251] K. Kunze, T. Etter, J. Grässlin, V. Shklover, "Texture, anisotropy in microstructure and mechanical properties of IN738LC alloy processed by selective laser melting (SLM), *Mater. Sci. Eng., A* 620 (2015) 213–222.
- [252] I. Koutiri, E. Pessard, P. Peyre, O. Amlou, T. De Terris, "Influence of SLM process parameters on the surface finish, porosity rate and fatigue behavior of as-built Inconel 625 parts, *J. Mater. Process. Technol.* 255 (2018) 536–546.
- [253] P. Kanagarajah, F. Brenne, T. Niendorf, H.J. Maier, "Inconel 939 processed by selective laser melting: effect of microstructure and temperature on the mechanical properties under static and cyclic loading, *Mater. Sci. Eng., A* 588 (2013) 188–195, 2013/12/20/.
- [254] Y.S.J. Yoo, T.A. Book, M.D. Sangid, J. Kacher, "Identifying strain localization and dislocation processes in fatigued Inconel 718 manufactured from selective laser melting, *Mater. Sci. Eng., A* 724 (2018) 444–451.
- [255] F. Wang, "Mechanical property study on rapid additive layer manufacture Hastelloy® X alloy by selective laser melting technology, *Int. J. Adv. Manuf. Technol.* 58 (5) (2012) 545–551.
- [256] S. Bagherifard, S. Monti, M.V. Zuccoli, M. Riccio, J. Kondás, M. Guagliano, "Cold spray deposition for additive manufacturing of freeform structural components compared to selective laser melting, *Mater. Sci. Eng., A* 721 (2018) 339–350.
- [257] O. Scott-Emuakpor, J. Schwartz, T. George, C. Holycross, C. Cross, J. Slater, "Bending fatigue life characterisation of direct metal laser sintering nickel alloy 718, *Fatig. Fract. Eng. Mater. Struct.* 38 (9) (2015) 1105–1117.
- [258] F. Caiazzo, V. Alfieri, G. Corrado, P. Argenio, "Laser powder-bed fusion of Inconel 718 to manufacture turbine blades, *Int. J. Adv. Manuf. Technol.* 93 (9) (2017) 4023–4031.
- [259] M. Ni, et al., "Anisotropic tensile behavior of in situ precipitation strengthened Inconel 718 fabricated by additive manufacturing, *Mater. Sci. Eng., A* 701 (2017) 344–351, 2017/07/31/.
- [260] C. Qiu, N.J.E. Adkins, M.M. Attallah, "Selective laser melting of Invar 36: microstructure and properties, *Acta Mater.* 103 (2016) 382–395.
- [261] T. Trosch, J. Ströbner, R. Völkl, U. Glatzel, "Microstructure and mechanical properties of selective laser melted Inconel 718 compared to forging and casting, *Mater. Lett.* 164 (2016) 428–431.
- [262] Y. Wang, J. Shi, S. Lu, Y. Wang, "Selective laser melting of graphene-reinforced Inconel 718 superalloy: evaluation of microstructure and tensile performance, *J. Manuf. Sci. Eng.* 139 (4) (2016), 041005–041005-6.
- [263] A. Kreitzberg, V. Brailovski, S. Turenne, "Elevated temperature mechanical behavior of IN625 alloy processed by laser powder-bed fusion, *Mater. Sci. Eng., A* 700 (2017) 540–553.
- [264] Krista Amato, et al., "Comparison of microstructures and properties for a Ni-base superalloy (alloy 625) fabricated by electron beam melting, *J. Mater. Sci. Res.* 1 (2) (2012) 3–41.
- [265] Y. Zhou, X. Zhou, Q. Teng, Q.S. Wei, Y.S. Shi, "Investigation on the scan strategy and property of 316L stainless steel-Inconel 718 functionally graded materials fabricated by selective laser melting, in: *In the 26th Solid Freeform Fabrication Symposium*, Austin, USA, 2015, pp. 700–707.
- [266] P. Wang, et al., "Microstructural characteristics and mechanical properties of carbon nanotube reinforced Inconel 625 parts fabricated by selective laser melting, *Mater. Des.* 112 (2016) 290–299.
- [267] F. Geiger, K. Kunze, T. Etter, "Tailoring the texture of IN738LC processed by selective laser melting (SLM) by specific scanning strategies, *Mater. Sci. Eng., A* 661 (2016) 240–246.
- [268] K. Žaba, et al., "Comparative analysis of properties and microstructure of the plastically deformed alloy Inconel®718, manufactured by plastic working and direct metal laser sintering, *Arch. Metall. Mater.* 61 (1) (2016) 143.
- [269] A. Kreitzberg, V. Brailovski, S. Turenne, "Effect of heat treatment and hot isostatic pressing on the microstructure and mechanical properties of Inconel 625 alloy processed by laser powder bed fusion, *Mater. Sci. Eng., A* 689 (2017) 1–10.
- [270] X. Wang, L.N. Carter, B. Pang, M.M. Attallah, M.H. Loretto, "Microstructure and yield strength of SLM-fabricated CM247LC Ni-Superalloy, *Acta Mater.* 128 (2017) 87–95.
- [271] X. Yao, S.K. Moon, B.Y. Lee, G. Bi, "Effects of heat treatment on microstructures and tensile properties of IN718/TiC nanocomposite fabricated by selective laser melting, *Int. J. Precis. Eng. Manuf.* 18 (12) (2017) 1693–1701.
- [272] C.U. Brown, G. Jacob, M. Stoudt, S. Moylan, J. Slotwinski, A. Donmez, "Interlaboratory study for nickel alloy 625 made by laser powder bed fusion to quantify mechanical property variability, *Journal of Materials Engineering and Performance*, journal article 25 (8) (2016) 3390–3397.
- [273] S.J. Davies, S.P. Jeffs, R.J. Lancaster, G. Baxter, "Mechanical assessment of a LPBF nickel superalloy using the small punch test method, in: *the 28th Annual International Solid Freeform Fabrication Symposium – an Additive Manufacturing Conference*, 2017, pp. 178–185.
- [274] V.S. Sufiiarov, A.A. Popovich, E.V. Borisov, I.A. Polozov, D.V. Masaylo, A. V. Orlov, "The effect of layer thickness at selective laser melting, *Procedia Engineering* 174 (2017) 126–134.
- [275] F. Brenne, et al., "Microstructural design of Ni-base alloys for high-temperature applications: impact of heat treatment on microstructure and mechanical properties after selective laser melting, *Progress in Additive Manufacturing* 1 (3) (2016) 141–151, 2016/12/01.
- [276] M. Cloots, K. Kunze, P.J. Uggowitzer, K. Wegener, "Microstructural characteristics of the nickel-based alloy IN738LC and the cobalt-based alloy Mar-M509 produced by selective laser melting, *Mater. Sci. Eng., A* 658 (2016) 68–76.
- [277] J. Ströbner, M. Terock, U. Glatzel, "Mechanical and microstructural investigation of nickel-based superalloy IN718 manufactured by selective laser melting (SLM), *Adv. Eng. Mater.* 17 (8) (2015) 1099–1105.
- [278] X. Wang, T. Keya, K. Chou, "Build height effect on the Inconel 718 parts fabricated by selective laser melting, *Procedia Manufacturing* 5 (2016) 1006–1017.
- [279] T. Bauer, K. Dawson, A.B. Spierings, K. Wegener, "Microstructure and mechanical characterisation of SLM processed Haynes® 230®, in: *In 26th Annual International Solid Freeform Fabrication (SFF) Symposium*, Austin, TX, USA, 2015, pp. 813–822.
- [280] G. Bi, C.-N. Sun, H.-c. Chen, F.L. Ng, C.C.K. Ma, "Microstructure and tensile properties of superalloy IN100 fabricated by micro-laser aided additive manufacturing, *Mater. Des.* 60 (2014) 401–408.
- [281] V.A. Popovich, E.V. Borisov, A.A. Popovich, V.S. Sufiiarov, D.V. Masaylo, L. Alzina, "Functionally graded Inconel 718 processed by additive manufacturing: crystallographic texture, anisotropy of microstructure and mechanical properties, *Mater. Des.* 114 (2017) 441–449, 2017/01/15/.
- [282] I. Yadroitsev, L. Thivillon, P. Bertrand, I. Smurov, "Strategy of manufacturing components with designed internal structure by selective laser melting of metallic powder, *Appl. Surf. Sci.* 254 (4) (2007) 980–983.
- [283] Z. Wang, K. Guan, M. Gao, X. Li, X. Chen, X. Zeng, "The microstructure and mechanical properties of deposited-IN718 by selective laser melting, *J. Alloys Compd.* 513 (2012) 518–523.
- [284] N.J. Harrison, I. Todd, K. Mumtaz, "Reduction of micro-cracking in nickel superalloys processed by Selective Laser Melting: a fundamental alloy design approach, *Acta Mater.* 94 (2015) 59–68.
- [285] T. Vilaro, C. Colin, J.D. Bartout, L. Nazé, M. Sennour, "Microstructural and mechanical approaches of the selective laser melting process applied to a nickel-base superalloy, *Mater. Sci. Eng., A* 534 (2012) 446–451.
- [286] Y. Lu, et al., "Study on the microstructure, mechanical property and residual stress of SLM Inconel-718 alloy manufactured by differing island scanning strategy, *Opt Laser. Technol.* 75 (2015) 197–206.
- [287] B. Farber, et al., "Correlation of mechanical properties to microstructure in Inconel 718 fabricated by direct metal laser sintering, *Mater. Sci. Eng., A* 712 (2018) 539–547.
- [288] A.B. Spierings, T. Bauer, K. Dawson, A. Colella, K. Wegener, "Processing ODS Modified IN625 Using Selective Laser Melting," Presented at the Annual International Solid Freeform Fabrication Symposium, Texas, Austin, 2015.
- [289] D. Deng, R.L. Peng, H. Brodin, J. Moverare, "Microstructure and mechanical properties of Inconel 718 produced by selective laser melting: sample orientation dependence and effects of post heat treatments, *Mater. Sci. Eng., A* 713 (2018) 294–306.
- [290] Y.C. Yen, T.H. Kenneth, D. Zhenglin, C.C. Kai, D. Zhili, "Selective laser melting of nickel powder, *Rapid Prototyp. J.* 23 (4) (2017) 750–757.
- [291] C. Kumara, D. Deng, J. Moverare, P. Nylén, "Modelling of anisotropic elastic properties in alloy 718 built by electron beam melting, *Mater. Sci. Technol.* 34 (5) (2018) 529–537.
- [292] L.E. Murr, et al., "Microstructural architecture, microstructures, and mechanical properties for a nickel-base superalloy fabricated by electron beam melting, *Metallurgical and Materials Transactions A*, journal article 42 (11) (2011) 3491–3508.
- [293] L. Murr, S. Li, Y. Tian, K. Amato, E. Martinez, F. Medina, "Open-Cellular Co-base and Ni-base superalloys fabricated by electron beam melting, *Materials* 4 (4) (2011) 782–790.
- [294] D. Deng, J. Moverare, R.L. Peng, H. Söderberg, "Microstructure and anisotropic mechanical properties of EBM manufactured Inconel 718 and effects of post heat treatments, *Mater. Sci. Eng., A* 693 (2017) 151–163.
- [295] A. Ströndl, M. Palm, J. Gnauk, G. Frommeyer, "Microstructure and mechanical properties of nickel based superalloy IN718 produced by rapid prototyping with electron beam melting (EBM), *Mater. Sci. Technol.* 27 (5) (2011) 876–883.
- [296] M.M. Kirka, D.A. Greeley, C. Hawkins, R.R. Dehoff, "Effect of anisotropy and texture on the low cycle fatigue behavior of Inconel 718 processed via electron beam melting, *Int. J. Fatig.* 105 (2017) 235–243.

- [297] M.M. Kirka, F. Medina, R. Dehoff, A. Okello, "Mechanical behavior of post-processed Inconel 718 manufactured through the electron beam melting process, *Mater. Sci. Eng., A* 680 (2017) 338–346.
- [298] M.M. Kirka, et al., "Strategy for texture management in metals additive manufacturing, *JOM, journal article* 69 (3) (2017) 523–531.
- [299] Z. Chen, et al., "Anisotropy of nickel-based superalloy K418 fabricated by selective laser melting, *Prog. Nat. Sci.: Materials International* 28 (4) (2018) 496–504.
- [300] K. Moussaoui, W. Rubio, M. Mousseigne, T. Sultan, F. Rezai, "Effects of Selective Laser Melting additive manufacturing parameters of Inconel 718 on porosity, microstructure and mechanical properties, *Mater. Sci. Eng., A* 735 (2018) 182–190.
- [301] J. Schneider, B. Lund, M. Fullen, "Effect of heat treatment variations on the mechanical properties of Inconel 718 selective laser melted specimens, *Additive Manufacturing* 21 (2018) 248–254.
- [302] Q.B. Nguyen, Z. Zhu, B.W. Chua, W. Zhou, J. Wei, S.M.L. Nai, "Development of WC-Inconel composites using selective laser melting, *Archives of Civil and Mechanical Engineering* 18 (4) (2018) 1410–1420.
- [303] G. Marchese, et al., "Influence of heat treatments on microstructure evolution and mechanical properties of Inconel 625 processed by laser powder bed fusion, *Mater. Sci. Eng., A* 729 (2018) 64–75.
- [304] L.A. Al-Juboori, T. Niendorf, F. Brenne, "On the tensile properties of inconel 718 fabricated by EBM for as-built and heat-treated components, *Metallurgical and Materials Transactions B, journal article* 49 (6) (2018) 2969–2974.
- [305] Y. Gao, M. Zhou, "Superior mechanical behavior and fretting wear resistance of 3D-printed inconel 625 superalloy, *Appl. Sci.* 8 (12) (2018) 2439.
- [306] A. Alafaghani, A. Qattawi, M.A.G. Castañón, "Effect of manufacturing parameters on the microstructure and mechanical properties of metal laser sintering parts of precipitate hardenable metals, *The International Journal of Advanced Manufacturing Technology, journal article* 99 (9) (2018) 2491–2507.
- [307] D. Gu, H. Zhang, D. Dai, M. Xia, C. Hong, R. Poprawe, "Laser additive manufacturing of nano-TiC reinforced Ni-based nanocomposites with tailored microstructure and performance, *Compos. B Eng.* 163 (2019) 585–597.
- [308] S.-H. Sun, et al., "Electron beam additive manufacturing of Inconel 718 alloy rods: impact of build direction on microstructure and high-temperature tensile properties, *Additive Manufacturing* 23 (2018) 457–470.
- [309] M. Leary, et al., "Inconel 625 lattice structures manufactured by selective laser melting (SLM): mechanical properties, deformation and failure modes, *Mater. Des.* 157 (2018) 179–199.
- [310] I.A. Segura, et al., "Grain boundary and microstructure engineering of Inconel 690 cladding on stainless-steel 316L using electron-beam powder bed fusion additive manufacturing, *J. Mater. Sci. Technol.* 35 (2) (2019) 351–367.
- [311] R. Muñoz-Moreno, et al., "Effect of heat treatment on the microstructure, texture and elastic anisotropy of the nickel-based superalloy CM247LC processed by selective laser melting, *Mater. Sci. Eng., A* 674 (2016) 529–539.
- [312] J.R. Poulin, V. Brailovski, P. Terriault, "Long fatigue crack propagation behavior of Inconel 625 processed by laser powder bed fusion: influence of build orientation and post-processing conditions, *Int. J. Fatig.* 116 (2018) 634–647.
- [313] Y. Yamashita, T. Murakami, R. Mihara, M. Okada, Y. Murakami, "Defect analysis and fatigue design basis for Ni-based superalloy 718 manufactured by selective laser melting, *Int. J. Fatig.* 117 (2018) 485–495.
- [314] E.W. Hovig, A.S. Azar, F. Grytten, K. Sørby, E. Andreassen, "Determination of anisotropic mechanical properties for materials processed by laser powder bed fusion, *Advances in Materials Science and Engineering* 2018 (2018) 20, 7650303.
- [315] G.E. Bean, D.B. Witkin, T.D. McLouth, D.N. Patel, R.J. Zaldivar, "Effect of laser focus shift on surface quality and density of Inconel 718 parts produced via selective laser melting, *Additive Manufacturing* 22 (2018) 207–215.
- [316] H.-J. Lee, H.-K. Kim, H.-U. Hong, B.-S. Lee, "Influence of the focus offset on the defects, microstructure, and mechanical properties of an Inconel 718 superalloy fabricated by electron beam additive manufacturing, *J. Alloys Compd.* 781 (2019) 842–856.
- [317] A. Mostafa, D. Shahriari, I.P. Rubio, V. Brailovski, M. Jahazi, M. Medraj, "Hot compression behavior and microstructure of selectively laser-melted IN718 alloy, *Int. J. Adv. Manuf. Technol.* (2018). <https://link.springer.com/article/10.1007/s00170-017-1522-4>.
- [318] F.A. List, R.R. Dehoff, L.E. Lowe, W.J. Sames, "Properties of Inconel 625 mesh structures grown by electron beam additive manufacturing, *Mater. Sci. Eng., A* 615 (2014) 191–197.
- [319] Z.H. Jiao, L.M. Lei, H.C. Yu, F. Xu, R.D. Xu, X.R. Wu, "Experimental evaluation on elevated temperature fatigue and tensile properties of one selective laser melted nickel based superalloy, *International Journal of Fatigue, Article* 121 (2019) 172–180.
- [320] C. Kantzos, J. Pauza, R. Cunningham, S.P. Narra, J. Beuth, A. Rollett, "An investigation of process parameter modifications on additively manufactured inconel 718 parts, *Journal of Materials Engineering and Performance, journal article* (2018). <https://link.springer.com/article/10.1007/s11665-018-3612-3>.
- [321] A. Balachandramurthi, J. Moverare, S. Mahade, R. Pederson, "Additive manufacturing of alloy 718 via electron beam melting: effect of post-treatment on the microstructure and the mechanical properties, *Materials* 12 (1) (2018) 68.
- [322] H.-Y. Wan, Z.-J. Zhou, C.-P. Li, G.-F. Chen, G.-P. Zhang, "Enhancing fatigue strength of selective laser melting-fabricated inconel 718 by tailoring heat treatment route, *Adv. Eng. Mater.* 20 (10) (2018) 1800307.
- [323] H. Wang, et al., "Selective laser melting of the hard-to-weld IN738LC superalloy: efforts to mitigate defects and the resultant microstructural and mechanical properties, *Journal of Alloys and Compounds, Article* 807 (2019), 151662.
- [324] Z. Hao, et al., "Effect of post-treatments on microstructure and mechanical properties of a novel nickel-based powder metallurgy superalloy processed by selective laser melting, *Materials Research Express, Article* 6 (10) (2019), 1065e5.
- [325] J. Nguejio, F. Szymytka, S. Hallais, A. Tanguy, S. Nardone, M. Godino Martinez, "Comparison of microstructure features and mechanical properties for additive manufactured and wrought nickel alloys 625, *Materials Science and Engineering A, Article* 764 (2019), 138214.
- [326] D.B. Witkin, R.W. Hayes, T.D. McLouth, G.E. Bean, "Anomalous notch rupture behavior of nickel-based superalloy inconel 718 due to fabrication by additive manufacturing, *Metall. Mater. Trans.: Physical Metallurgy and Materials Science, Article* 50 (8) (2019) 3458–3465.
- [327] C. Pei, D. Shi, H. Yuan, H. Li, "Assessment of mechanical properties and fatigue performance of a selective laser melted nickel-base superalloy Inconel 718, *Mater. Sci. Eng., A* 759 (2019) 278–287, 2019/06/24/.
- [328] X. Lv, B. Wen, J. Du, "Effects of heat treatment on microstructure and mechanical properties of selective laser melting IN718, *Xiyou Jinshu Cailiao Yu Gongcheng/Rare Metal Materials and Engineering, Article* 48 (5) (2019) 1386–1393.
- [329] X. Hu, Z. Xue, G. Zhao, J. Yun, D. Shi, X. Yang, "Laser welding of a selective laser melted Ni-base superalloy: microstructure and high temperature mechanical property, *Materials Science and Engineering A, Article* 745 (2019) 335–345.
- [330] I.A. Segura, et al., "Grain boundary and microstructure engineering of Inconel 690 cladding on stainless-steel 316L using electron-beam powder bed fusion additive manufacturing, *Journal of Materials Science and Technology, Article* 35 (2) (2019) 351–367.
- [331] X.A. Hu, G.L. Zhao, F.C. Liu, W.X. Liu, "Microstructure and mechanical behavior of Inconel 625 alloy processed by selective laser melting at high temperature up to 1000 °C, *Rare Metals, Article* (2019), in: https://www.google.com/search?q=Microstructure+and+mechanical+behavior+of+Inconel+625+alloy+processed+by+selective+laser+melt+at+high+temperature+up+to+1000+%C2%B0C&rlz=1C1GCEB_enGB842GB842&oq=Microstructure+and+mechanical+behavior+of+Inconel+625+alloy+processed+by+selective+laser+melt+at+high+temperature+up+to+1000+%C2%B0C&aqs=chrome..69i57.604j0j4&sourceid=chrome&ie=UTF-8.
- [332] B. Cheng, J. Gu, M. Song, "An investigation of the microstructural evolution and tensile properties of a nickel-based GH648 superalloy manufactured through selective laser melting, *Materials Science and Engineering A, Article* 790 (2020), 139704.
- [333] X.A. Hu, et al., "Experimental investigation on the LCF behavior affected by manufacturing defects and creep damage of one selective laser melting nickel-based superalloy at 815 °C, *Acta Metallurgica Sinica (English Letters), Article* 33 (4) (2020) 514–527.
- [334] Q. Han, Y. Gu, S. Soe, F. Lacan, R. Setchi, "Effect of hot cracking on the mechanical properties of Hastelloy X superalloy fabricated by laser powder bed fusion additive manufacturing, *Optics and Laser Technology, Article* 124 (2020), 105984.
- [335] L.L. Chang, T. Wang, S.G. Shen, Y. Ma, Y.H. Xing, "Laser welding properties of In718 alloy prepared by selective laser melting, *Cailiao Rechuli Xuebao/Transactions of Materials and Heat Treatment, Article* 41 (3) (2020) 62–69.
- [336] G. Wang, et al., "Process optimization and mechanical properties of oxide dispersion strengthened nickel-based superalloy by selective laser melting, *Materials and Design, Article* 188 (2020), 108418.
- [337] C. Pei, W. Zeng, H. Yuan, "A damage evolution model based on micro-structural characteristics for an additive manufactured superalloy under monotonic and cyclic loading conditions, *International Journal of Fatigue, Article* 131 (2020), 105279.
- [338] Z. Chen, et al., "Graphene reinforced nickel-based superalloy composites fabricated by additive manufacturing, *Materials Science and Engineering A, Article* 769 (2020), 138484.
- [339] K.S. Mukhtarova, R.V. Shakhov, S.K. Mukhtarov, V.V. Smirnov, V.M. Imayev, "Microstructure and mechanical properties of the inconel 718 superalloy manufactured by selective laser melting, *Letters on Materials, Article* 9 (4) (2019) 480–484.
- [340] Q. Han, et al., "Additive manufacturing of high-strength crack-free Ni-based Hastelloy X superalloy, *Additive Manufacturing, Article* 30 (2019), 100919.
- [341] Z. Hao, et al., "Effect of heat treatment on microstructure and properties of FGH4096M superalloy processed by selective laser melting, *Metals and Materials International, Article* (2019). <https://link.springer.com/article/10.1007/s12598-019-01321-3>.
- [342] V.P. Sabelkin, G.R. Cobb, B.M. Doane, R.A. Kemnitz, R.P. O'Hara, "Torsional behavior of additively manufactured nickel alloy 718 under monotonic loading and low cycle fatigue, *Materials Today Communications* 24 (2020) 101256, 2020/09/01/.
- [343] T. Rong, D. Gu, "Formation of novel graded interface and its function on mechanical properties of WC1-x reinforced Inconel 718 composites processed by selective laser melting, *J. Alloys Compd.* 680 (2016) 333–342.
- [344] Q. Jia, D. Gu, "Selective laser melting additive manufacturing of Inconel 718 superalloy parts: densification, microstructure and properties, *J. Alloys Compd.* 585 (2014) 713–721.
- [345] T. Rong, D. Gu, Q. Shi, S. Cao, M. Xia, "Effects of tailored gradient interface on wear properties of WC/Inconel 718 composites using selective laser melting, *Surf. Coating. Technol.* 307 (2016) 418–427.
- [346] B. Zhang, G. Bi, S. Nai, C.-n. Sun, J. Wei, "Microhardness and microstructure evolution of TiB2 reinforced Inconel 625/TiB2 composite produced by selective laser melting, *Opt Laser. Technol.* 80 (2016) 186–195.

- [347] A. Basak, S. Das, "Microstructure of nickel-base superalloy MAR-M247 additively manufactured through scanning laser epitaxy (SLE), *J. Alloys Compd.* 705 (2017) 806–816.
- [348] S. Li, Q. Wei, Y. Shi, Z. Zhu, D. Zhang, "Microstructure characteristics of Inconel 625 superalloy manufactured by selective laser melting, *J. Mater. Sci. Technol.* 31 (9) (2015) 946–952.
- [349] Y. Tian, J.A. Muñiz-Lerma, M. Brochu, "Nickel-based superalloy microstructure obtained by pulsed laser powder bed fusion, *Mater. Char.* 131 (2017) 306–315.
- [350] K.-y. Feng, P. Liu, H.-x. Li, S.-y. Sun, S.-b. Xu, J.-n. Li, "Microstructure and phase transformation on the surface of Inconel 718 alloys fabricated by SLM under 1050°C solid solution + double ageing, *Vacuum* 145 (2017) 112–115.
- [351] A. Basak, S. Das, "Additive manufacturing of nickel-base superalloy IN100 through scanning laser epitaxy, *JOM*, journal article 70 (1) (2018) 53–59.
- [352] A. Domashenkov, et al., "Microstructure and physical properties of a Ni/Fe-based superalloy processed by Selective Laser Melting, *Additive Manufacturing* 15 (2017) 66–77.
- [353] G. Marchese, et al., "Characterization and comparison of Inconel 625 processed by selective laser melting and laser metal Deposition " advanced engineering materials, 19 3 (2017) 1600635.
- [354] L.E. Murr, et al., "Microstructures of Rene 142 nickel-based superalloy fabricated by electron beam melting, *Acta Mater.* 61 (11) (2013) 4289–4296.
- [355] M. Calandri, et al., "Solution treatment study of Inconel 718 produced by SLM additive technique in view of the oxidation resistance, *Adv. Eng. Mater.* 20 (11) (2018) 1800351.
- [356] J. Li, et al., "Microstructural evolution and mechanical properties of IN718 alloy fabricated by selective laser melting following different heat treatments, *J. Alloys Compd.* 772 (2019) 861–870.
- [357] R. Seede, A. Mostafa, V. Brailovski, M. Jahazi, M. Medraj, "Microstructural and microhardness evolution from homogenization and hot isostatic pressing on selective laser melted Inconel 718: structure, texture, and phases, *Journal of Manufacturing and Materials Processing* 2 (2) (2018) 30.
- [358] X. Li, et al., "Effect of heat treatment on microstructure evolution of Inconel 718 alloy fabricated by selective laser melting, *J. Alloys Compd.* 764 (2018) 639–649, 2018/10/05/.
- [359] A.A. Popovich, V.Sh. Sufiiarov, E.V. Borisov, I.A. Polozov, D.V. Masaylo, "Design and manufacturing of tailored microstructure with selective laser melting, *Mater. Phys. Mech.* 38 (2018) 1–10.
- [360] J.A. Muñiz-Lerma, Y. Tian, X. Wang, R. Gauvin, M. Brochu, "Microstructure evolution of Inconel 738 fabricated by pulsed laser powder bed fusion, *Progress in Additive Manufacturing*, journal article (2018). <https://link.springer.com/article/10.1007/s40964-018-0062-2>.
- [361] P. Karimi, E. Sadeghi, P. Åkerfeldt, J. Ålgårdh, J. Andersson, "Influence of successive thermal cycling on microstructure evolution of EBM-manufactured alloy 718 in track-by-track and layer-by-layer design, *Mater. Des.* 160 (2018) 427–441, 2018/12/15/.
- [362] L. Zhou, A. Mehta, B. McWilliams, K. Cho, Y. Sohn, "Microstructure, precipitates and mechanical properties of powder bed fused Inconel 718 before and after heat treatment, *J. Mater. Sci. Technol.* 35 (2018).
- [363] S. Holland, X. Wang, J. Chen, W. Cai, F. Yan, L. Li, "Multiscale characterization of microstructures and mechanical properties of Inconel 718 fabricated by selective laser melting, *J. Alloys Compd.* 784 (2019) 182–194.
- [364] N.H. Sateesh, G.C.M. Kumar, K. Prasad, S. C. K. A.R. Vinod, "Microstructure and mechanical characterization of laser sintered Inconel-625 superalloy, *Procedia Materials Science* 5 (2014) 772–779.
- [365] S.H. Kim, et al., "Thermo-mechanical improvement of Inconel 718 using ex situ boron nitride-reinforced composites processed by laser powder bed fusion, *Sci. Rep.* 7 (1) (2017) 14359.
- [366] F. Shengnan, J.H. Gong, L. Huixiang, W. Haoran, "Microstructural investigation of Inconel718 manufactured by SLM, *IOP Conf. Ser. Mater. Sci. Eng.* 452 (2) (2018) 22088.
- [367] P. Karimi, E. Sadeghi, D. Deng, H. Gruber, J. Andersson, P. Nylén, "Influence of build layout and orientation on microstructural characteristics of electron beam melted Alloy 718, *The International Journal of Advanced Manufacturing Technology*, journal article 99 (9) (2018) 2903–2913.
- [368] D. Gu, Q. Shi, K. Lin, L. Xi, "Microstructure and performance evolution and underlying thermal mechanisms of Ni-based parts fabricated by selective laser melting, *Additive Manufacturing* 22 (2018) 265–278.
- [369] H. Yang, J. Yang, W. Huang, Z. Wang, X. Zeng, "The printability, microstructure, crystallographic features and microhardness of selective laser melted Inconel 718 thin wall, *Mater. Des.* 156 (2018) 407–418.
- [370] M.D. Sangid, et al., "Role of heat treatment and build orientation in the microstructure sensitive deformation characteristics of IN718 produced via SLM additive manufacturing, *Additive Manufacturing* 22 (2018) 479–496.
- [371] R. Sebastian, A.K. Singh, M. Paliwal, A. Gautam, "Investigation of the interface between SLM processed nickel alloy on a cast iron substrate, *Progress in Additive Manufacturing*, Article 4 (2) (2019) 131–142.
- [372] P. Liu, J. Hu, S. Sun, K. Feng, Y. Zhang, M. Cao, "Microstructural evolution and phase transformation of Inconel 718 alloys fabricated by selective laser melting under different heat treatment, *Journal of Manufacturing Processes*, Article 39 (2019) 226–232.
- [373] S. Periane, et al., "Machining influence on the fatigue resistance of Inconel 718 fabricated by selective laser melting (SLM), in *Procedia Structural Integrity* 19 (2019) 415–422.
- [374] P. Liu, et al., "Effect of substitutional solid solution plus double ageing treatment on the microstructure of the X-Y surface of Inconel 718 alloy fabricated with selective laser melting (SLM), *Lasers in Engineering*, Article 43 (1–3) (2019) 47–58.
- [375] P. Liu, S. Sun, M. Cao, J. Gong, J. Hu, "Microstructural evolution and phase transformation on the X-Y surface of Inconel 718 Ni-based alloys fabricated by selective laser melting under different heat treatment, *High Temperature Materials and Processes*, Article 38 (2019) 229–236, 2019.
- [376] I. Cieślík, M. Duchna, T. Płociński, E. Wyszowska, A. Azarov, M. Zieniuk, "Ion irradiation effect on the microstructure of Inconel 625 obtained by Selective Laser Melting and by the metallurgical process, *Surface and Coatings Technology*, Article 396 (2020), 125952.
- [377] M.G. Scaramuccia, A.G. Demir, L. Caprio, O. Tassa, B. Previtali, "Development of processing strategies for multigraded selective laser melting of Ti6Al4V and IN718, *Powder Technology*, Article 367 (2020) 376–389.
- [378] J. Patalas-Maliszewska, E. Feldshtein, O. Devojno, M. Sliwa, M. Kardapolava, N. Lutsko, "Single tracks as a key factor in additive manufacturing technology-analysis of research trends and metal deposition behavior, *Materials*, Article 13 (5) (2020), 1115.
- [379] K.S. Mukhtarova, R.V. Shakhov, V.V. Smirnov, S.K. Mukhtarov, "Microstructure and microhardness studies of Inconel 718, manufactured by selective laser melting and subjected to severe plastic deformation and annealing, *IOP Conf. Ser. Mater. Sci. Eng.* 672 (2019).
- [380] H. Song, T. McGaughy, A. Sadek, W. Zhang, "Effect of structural support on microstructure of nickel base superalloy fabricated by laser-powder bed fusion additive manufacturing, *Additive Manufacturing* 26 (2019) 30–40.
- [381] H. Hack, R. Link, E. Knudsen, B. Baker, S. Olig, "Mechanical properties of additive manufactured nickel alloy 625, *Additive Manufacturing* 14 (2017) 105–115.
- [382] A.A. Popovich, V.S. Sufiiarov, E.V. Borisov, I.A. Polozov, D.V. Masaylo, A. V. Grigoriev, "Anisotropy of mechanical properties of products manufactured using selective laser melting of powdered materials, *Russ. J. Non-Ferrous Metals* 58 (4) (2017) 389–395.
- [383] H. Gruber, P. Karimi, E. Hryha, L. Nyborg, "Effect of powder recycling on the fracture behavior of electron beam melted alloy 718, (in English), *Powder metallurgy progress* 18 (1) (2018) 40.
- [384] Håkan Brodin, Olov Andersson, Sten Johansson, "Mechanical testing of a selective laser melted superalloy, in: 13th International Conference on Fracture, China, Beijing, 2013.
- [385] T. Brynk, et al., "Fatigue crack growth rate and tensile strength of Re modified Inconel 718 produced by means of selective laser melting, *Mater. Sci. Eng., A* 698 (2017) 289–301.
- [386] D.M. Lambert, "Evaluation of the Effect of Surface Finish on High-Cycle Fatigue of SLM-IN718," Presented at the JANNAP Propulsion Meeting, United States, Newport News, VA, 2016.
- [387] R. Konečná, G. Nicoletto, L. Kunz, A. Bača, "Microstructure and directional fatigue behavior of Inconel 718 produced by selective laser melting, *Procedia Structural Integrity* 2 (2016) 2381–2388.
- [388] V.A. Popovich, E.V. Borisov, V. Heurtebise, T. Riemsagel, A.A. Popovich, V. S. Sufiiarov, "Creep and thermomechanical fatigue of functionally graded Inconel 718 produced by additive manufacturing, in: Presented at the 147th Annual Meeting and Exhibition of the Minerals, Metals and Materials Society, TMS, 2018, p. 2018. Conference Paper. Available, https://www.scopus.com/inward/record.uri?eid=2-s2.0-85044480105&doi=10.1007%2f978-3-319-72526-0_9&partnerID=40&md5=3af9f811167f33299eb6f4a9780fdffe.
- [389] R. Konečná, L. Kunz, G. Nicoletto, A. Baca, "Fatigue crack growth behavior of Inconel 718 produced by selective laser melting, *Frat. Ed. Integrità Strutt.* 35 (2016) 31–40.
- [390] R. Konečná, L. Kunz, G. Nicoletto, A. Baca, "Long fatigue crack growth in Inconel 718 produced by selective laser melting, *Int. J. Fatig.* 92 (2016) 499–506.
- [391] A. Yadollahi, M.J. Mahtabi, A. Khalili, H.R. Doude, J.C. Newman, "Fatigue life prediction of additively manufactured material: effects of surface roughness, defect size, and shape, *Fatig. Fract. Eng. Mater. Struct.* 41 (7) (2018) 1602–1614.
- [392] D.B. Witkin, D.N. Patel, G.E. Bean, "Notched fatigue testing of Inconel 718 prepared by selective laser melting, *Fatig. Fract. Eng. Mater. Struct.* 42 (1) (2019) 166–177.
- [393] K. Solberg, F. Berto, "Notch-Defect interaction in additively manufactured Inconel 718, *Int. J. Fatig.* 122 (2018) 35–45.
- [394] K. Solberg, J. Torgersen, F. Berto, "Fatigue behaviour of additively manufactured Inconel 718 produced by selective laser melting, *Procedia Structural Integrity* 13 (2018) 1762–1767.
- [395] M.G. Khomutov, A.Y. Travyanov, P.V. Petrovskii, V.V. Cheverikin, A.I. Dubin, "Comparison of fatigue properties for alloy EP708 specimens prepared by selective laser melting and hot rolling, *Metallurgist*, journal article 62 (3) (2018) 283–288, July 01.
- [396] Z. Zhou, X. Hua, C. Li, G. Chen, "The effect of texture on the low cycle fatigue property of Inconel 718 by selective laser melting," *MATEC Web Conf.*, 165 (2018) 2007.
- [397] A.R. Balachandramurthi, J. Moverare, N. Dixit, R. Pederson, "Influence of defects and as-built surface roughness on fatigue properties of additively manufactured Alloy 718, *Mater. Sci. Eng., A* 735 (2018) 463–474.
- [398] L. Sheridan, O.E. Scott-Emuakpor, T. George, J.E. Gockel, "Relating porosity to fatigue failure in additively manufactured alloy 718, *Mater. Sci. Eng., A* 727 (2018) 170–176.
- [399] Z.Y. Xue, "Experiment and simulation of fatigue crack growth of SLM nickel base superalloy with different stress ratios and building directions," in *IOP Conf. Ser. Mater. Sci. Eng.* 490 (2019).
- [400] D. Deng, R. Eriksson, R.L. Peng, J. Moverare, "On the dwell-fatigue crack propagation behavior of a high-strength Ni-base superalloy manufactured by

- selective laser melting, *Metall. Mater. Trans.: Physical Metallurgy and Materials Science*, Article 51 (2) (2020) 962–972.
- [401] V.P. Sabelkin, et al., "Mitigation of anisotropic fatigue in nickel alloy 718 manufactured via selective laser melting, *Mater. Des.* 182 (2019) 108095, 2019/11/15/.
- [402] M. Scurria, B. Möller, R. Wagener, J. Pena, T. Bein, "Effects of surface preparation, support structures and build orientation on the cyclic stress-strain behavior of Inconel®718 produced by SLM," *SAE Technical Papers*, Conference Paper 2019 (April, 2019).
- [403] D.B. Witkin, D.N. Patel, G.E. Bean, "Notched fatigue testing of Inconel 718 prepared by selective laser melting, *Fatigue and Fracture of Engineering Materials and Structures*, Article 42 (1) (2019) 166–177.
- [404] A. Schoening, L. Sheridan, O. Scott-Emuakpor, T. George, A simplified investigation into fatigue viability of additively manufactured IN-718, 2020, pp. 97–100.
- [405] C. Hautfenne, S. Nardone, E.D. Bruycker, Influence of heat treatments and build orientation on the creep strength of additive manufactured IN718," presented at the 4th international ECCS Conference, Germany (2017).
- [406] Y. Kuo, S. Horikawa, K. Kakehi, "Effects of build direction and heat treatment on creep properties of Ni-base superalloy built up by additive manufacturing, *Scripta Mater.* 129 (2017) 74–78.
- [407] Z. Xu, C.J. Hyde, C. Tuck, A.T. Clare, "Creep behaviour of Inconel 718 processed by laser powder bed fusion, *J. Mater. Process. Technol.* 256 (2018) 13–24.
- [408] Y.-L. Kuo, T. Nagahari, K. Kakehi, "The effect of post-processes on the microstructure and creep properties of Alloy718 built up by selective laser melting, *Materials* 11 (6) (2018) 996.
- [409] B. Shassere, D. Greeley, A. Okello, M. Kirka, P. Nandwana, R. Dehoff, "Correlation of microstructure to creep response of hot isostatically pressed and aged electron beam melted Inconel 718, *Metallurgical and Materials Transactions A*, journal article 49 (10) (2018) 5107–5117.
- [410] S.J. Davies, S.P. Jeffs, M.P. Coleman, R.J. Lancaster, "Effects of heat treatment on microstructure and creep properties of a laser powder bed fused nickel superalloy, *Mater. Des.* 159 (2018) 39–46.
- [411] L.Y. Wang, Z.J. Zhou, C.P. Li, G.F. Chen, G.P. Zhang, "Comparative investigation of small punch creep resistance of Inconel 718 fabricated by selective laser melting, *Mater. Sci. Eng., A* 745 (2019) 31–38.
- [412] H. Hilal, R. Lancaster, S. Jeffs, J. Boswell, D. Stapleton, G. Baxter, "The influence of process parameters and build orientation on the creep behaviour of a laser powder bed fused ni-based superalloy for aerospace applications, *Materials*, Article 12 (9) (2019), 1390.
- [413] K. Kakehi, S. Banoth, Y.L. Kuo, S. Hayashi, "Effect of yttrium addition on creep properties of a Ni-base superalloy built up by selective laser melting, *Scripta Materialia*, Article 183 (2020) 71–74.
- [414] S. Sanchez, G. Gaspard, C.J. Hyde, I.A. Ashcroft, R. G. A. A.T. Clare, "The creep behaviour of nickel alloy 718 manufactured by laser powder bed fusion, *Mater. Des.* 204 (2021) 109647, 2021/06/01/.
- [415] S. Sanchez, C.J. Hyde, I.A. Ashcroft, R. G. A. A.T. Clare, "Multi-laser scan strategies for enhancing creep performance in LPBF, *Additive Manufacturing* 41 (2021) 101948, 2021/05/01/.
- [416] S.K. Nayak, S.K. Mishra, A.N. Jinoop, C.P. Paul, K.S. Bindra, "Experimental studies on laser additive manufacturing of Inconel-625 structures using powder bed fusion at 100 µm layer thickness, *Journal of Materials Engineering and Performance*, Article 29 (11) (2020) 7636–7647.
- [417] M.R. Condruz, G. Matache, A. Paraschiv, T.F. Frigioescu, T. Badea, "Microstructural and tensile properties anisotropy of selective laser melting manufactured in 625, *Materials*, Article 13 (21) (2020) 1–22, 4829.
- [418] A.V. Sotov, et al., "Investigation of the IN-738 superalloy microstructure and mechanical properties for the manufacturing of gas turbine engine nozzle guide vane by selective laser melting, *International Journal of Advanced Manufacturing Technology*, Article 107 (5–6) (2020) 2525–2535.
- [419] B. Bechtold, *Violin Plots for Matlab*, 2016. Github Project, <https://github.com/bastibe/Violinplot-Matlab>.
- [420] J. William D Callister, D.G. Rethwisch, *Materials Science and Engineering: an INTRODUCTION*, ninth ed., John Wiley & Sons, 2013.
- [421] E. Bassini, M. Calandri, S. Parizita, G. Marchese, S. Biamino, D. Ugues, "Optimization of processing parameters and heat treatment for components made of Inconel 625 and 718 via Selective Laser Melting (SLM), *Metallurgia Italiana*, Article 111 (6) (2019) 48–54.
- [422] D. Kotzem, P. Dumke, P. Sepehri, J. Tenkamp, F. Walther, "Effect of miniaturization and surface roughness on the mechanical properties of the electron beam melted superalloy Inconel®718, *Progress in Additive Manufacturing* 5 (3) (2020) 267–276, 2020/09/01.
- [423] H. Wan, et al., "Effects of surface roughness and build thickness on fatigue properties of selective laser melted Inconel 718 at 650, *Int. J. Fatig.* 137 (2020) 105654, 04/01.
- [424] S. Kim, H. Choi, J. Lee, S. Kim, "Room and elevated temperature fatigue crack propagation behavior of Inconel 718 alloy fabricated by laser powder bed fusion," *International Journal of Fatigue*, Article 140 (2020), 105802.
- [425] X.F. Ma, et al., "Fatigue short crack propagation behavior of selective laser melted Inconel 718 alloy by in-situ SEM study: influence of orientation and temperature, *International Journal of Fatigue*, Article 139 (2020), 105739.
- [426] D. Deng, R.L. Peng, J. Moverare, "A comparison study of the dwell-fatigue behaviours of additive and conventional IN718: the role of dislocation substructure on the cracking behaviour, *Materials Science and Engineering A*, Article 797 (2020), 140072.
- [427] C. Qiu, H. Chen, Q. Liu, S. Yue, H. Wang, "On the solidification behaviour and cracking origin of a nickel-based superalloy during selective laser melting, *Materials Characterization*, Article 148 (2019) 330–344.
- [428] N. Sato, S. Nakano, T. Nagahari, T. Nagoya, K. Kakehi, "Microstructure of nickel-based superalloy fabricated by selective laser melting in vacuum, *Funtai Oyobi Fumatsu Yakin/Journal of the Japan Society of Powder and Powder Metallurgy*, Article 67 (3) (2020) 121–124.
- [429] H.P. Tang, G.Y. Yang, W.P. Jia, W.W. He, S.L. Lu, M. Qian, "Additive manufacturing of a high niobium-containing titanium aluminide alloy by selective electron beam melting, *Mater. Sci. Eng.* 636 (C) (2015) 103–107.
- [430] L.Y. Wang, et al., "Small punch creep performance of heterogeneous microstructure dominated Inconel 718 fabricated by selective laser melting," *Materials and Design*, Article 195 (2020), 109042.
- [431] N. Okuda, R. Kasada, A. Kimura, "Statistical evaluation of anisotropic fracture behavior of ODS ferritic steels by using small punch tests, *J. Nucl. Mater.* 386–388 (2009) 974–978, 2009/04/30/.
- [432] E. Altstadt, M. Serrano, M. Houska, A. García-Junceda, "Effect of anisotropic microstructure of a 12Cr-ODS steel on the fracture behaviour in the small punch test, *Mater. Sci. Eng., A* 654 (2016) 309–316, 2016/01/27/.
- [433] H. Ragelle, et al., "Surface tension-assisted additive manufacturing, *Nat. Commun.* 9 (1) (2018) 1184, 2018/03/22.
- [434] A. Vyatskikh, S. Delalande, A. Kudo, X. Zhang, C.M. Portela, J.R. Greer, "Additive manufacturing of 3D nano-architected metals, *Nat. Commun.* 9 (1) (2018) 593, 2018/02/09.
- [435] J. Souza, A. Großmann, C. Mittelstedt, "Micromechanical analysis of the effective properties of lattice structures in additive manufacturing," *Additive Manufacturing*, 23 (2018) 53–69, 2018/10/01/.
- [436] M. Askari, et al., "Additive manufacturing of metamaterials: a review, *Additive Manufacturing*, Article 36 (2020), 101562.
- [437] B. Hanks, J. Berthel, M. Frecker, T.W. Simpson, "Mechanical properties of additively manufactured metal lattice structures: data review and design interface, *Additive Manufacturing*, Article 35 (2020), 101301.
- [438] K.-S. Kim, T.-H. Kang, M.E. Kassner, K.-T. Son, K.-A. Lee, "High-temperature tensile and high cycle fatigue properties of Inconel 625 alloy manufactured by laser powder bed fusion, *Additive Manufacturing* 35 (2020) 101377, 2020/10/01/.
- [439] G. Matache, A. Paraschiv, M.R. Condruz, "Tensile notch sensitivity of additively manufactured IN 625 superalloy, *Materials*, Article 13 (21) (2020) 1–24, 4859.
- [440] B.B. Babamiri, J. Indeck, G. Demeneghi, J. Cuadra, K. Hazeli, "Quantification of porosity and microstructure and their effect on quasi-static and dynamic behavior of additively manufactured Inconel 718, *Additive Manufacturing*, Article 34 (2020), 101380.
- [441] D. J, et al., in: M. Sokolov, E. Lucon (Eds.), *Micro-Tensile Test Technique Development and Application to Mechanical Property Determination Small Specimen Test Techniques: 6th Volume*, ASTM International, West Conshohocken, PA, 2015, pp. 30–2015.
- [442] M.R. Gotterbarm, et al., "Small scale testing of IN718 single crystals manufactured by EB-PBF, *Additive Manufacturing*, Article 36 (2020), 101449.
- [443] R. Jiang, et al., "Effect of heat treatment on microstructural evolution and hardness homogeneity in laser powder bed fusion of alloy 718, *Additive Manufacturing*, Article 35 (2020), 101282.
- [444] O. Adegoke, J. Andersson, H. Brodin, R. Pederson, "Influence of laser powder bed fusion process parameters on voids, cracks, and microhardness of nickel-based superalloy alloy 247LC, *Materials* 13 (no. 17) (2020), 3770.
- [445] A.R. Balachandramurthi, et al., "On the microstructure of laser beam powder bed fusion alloy 718 and its influence on the low cycle fatigue behaviour," *Materials*, Article, 13, no 22 (2020) 1–21, 5198.
- [446] Kevinsanny, et al., "Defect tolerance and hydrogen susceptibility of the fatigue limit of an additively manufactured Ni-based superalloy 718," *International Journal of Fatigue*, 139 (2020) 105740, 2020/10/01/.
- [447] N. Raghavan, et al., "Localized melt-scan strategy for site specific control of grain size and primary dendrite arm spacing in electron beam additive manufacturing," *Acta Materialia*, 140 (2017) 375–387, 2017/11/01/.
- [448] Q. Jia, D. Gu, Selective laser melting additive manufactured Inconel 718 superalloy parts: high-temperature oxidation property and its mechanisms, *Opt Laser. Technol.* 62 (2014) 161–171.
- [449] E.A. Lass, et al., formation of the Ni3Nb δ-phase in stress-relieved Inconel 625 produced via laser powder-bed fusion additive manufacturing, *Metallurgical and Materials Transactions A*, journal article 48 (11) (2017) 5547–5558.
- [450] Q. Lanlan, et al., The microstructure and mechanical properties of deposited-IN625 by laser additive manufacturing, *Rapid Prototyp. J.* 23 (6) (2017) 1119–1129.
- [451] D.B. Witkin, T.V. Albright, D.N. Patel, "Empirical approach to understanding the fatigue behavior of metals made using additive manufacturing, *Metall. Mater. Trans.* 47 (8) (2016) 3823–3836.
- [452] C. Li, Y.B. Guo, J.B. Zhao, "Interfacial phenomena and characteristics between the deposited material and substrate in selective laser melting Inconel 625, *J. Mater. Process. Technol.* 243 (2017) 269–281.
- [453] J. Hernandez, et al., "Microstructures and properties for a superalloy powder mixture processed by electron beam melting, *J. Mater. Sci. Res.* 1 (2) (2012) 124–144.
- [454] M.A. Anam, D. Pal, B. Stucker, Modeling and experimental validation of nickel-based super alloy (Inconel 625) made using Selective Laser Melting, in: *In 24th International SFF Symposium - an Additive Manufacturing Conference*, 2013, pp. 463–473.

- [455] Y. Tian, D. Tomus, P. Rometsch, X. Wu, "Influences of processing parameters on surface roughness of Hastelloy X produced by selective laser melting, Additive Manufacturing 13 (2017) 103–112.
- [456] W. Philpott, M.A.E. Jepson, R.C. Thomson, "Comparison of the effects of a conventional heat treatment between cast and selective laser melted IN939 alloy," presented at the 8th International Conference on Advances in Materials Technology for Fossil Power Plants, Algarve, PORTUGAL (2016).
- [457] M. Cloots, P.J. Uggowitzer, K. Wegener, "Investigations on the microstructure and crack formation of IN738LC samples processed by selective laser melting using Gaussian and doughnut profiles, Mater. Des. 89 (2016) 770–784.
- [458] M. Ramsperger, R.F. Singer, C. Körner, "Microstructure of the nickel-base superalloy CMSX-4 fabricated by selective electron beam melting," metallurgical and materials transactions A, journal article 47 (3) (2016) 1469–1480.
- [459] A. Basak, R. Acharya, S. Das, "Additive manufacturing of single-crystal superalloy CMSX-4 through scanning laser epitaxy: computational modeling, experimental process development, and process parameter optimization, Metallurgical and Materials Transactions A, journal article 47 (8) (2016) 3845–3859.
- [460] L.N. Carter, C. Martin, P.J. Withers, M.M. Attallah, "The influence of the laser scan strategy on grain structure and cracking behaviour in SLM powder-bed fabricated nickel superalloy, J. Alloys Compd. 615 (2014) 338–347.